

## PROJECTED SHELL MODEL AND HIGH-SPIN SPECTROSCOPY

KENJI HARA

*Physik-Department, Technische Universität München  
D-85747 Garching bei München, Germany*

YANG SUN

*Department of Physics and Atmospheric Science, Drexel University  
Philadelphia, Pennsylvania 19104, USA*

and

*Joint Institute for Heavy Ion Research, Oak Ridge National Laboratory  
Oak Ridge, Tennessee 37831, USA*

*Department of Physics and Astronomy, University of Tennessee,  
Knoxville, Tennessee 37996, USA*

*Physics Division, Oak Ridge National Laboratory,  
Oak Ridge, Tennessee 37831, USA*

Received 15 August 1995

Most of the nuclei in the nuclear chart are deformed except for those in the vicinity of the magic numbers. It is difficult to treat such nuclei within the framework of the standard (spherical) shell model. On the other hand, the necessity for a proper quantum mechanical treatment of high-spin states has been steadily growing ever since modern experimental techniques made it possible to measure the fine details of the high-spin states of heavy nuclei.

The present article reviews an approach based on the angular momentum projection technique which was initiated in the late seventies for the purpose of carrying out shell model configuration mixing calculations efficiently. A large number of examples is presented with an emphasis on the physical interpretation of the numerical results.

Computing time for the whole spectrum up to spin  $\approx 40$  of an axially symmetric rare-earth nucleus takes only a few minutes on a Mainframe, showing the efficiency of the method. Most of the present calculations were carried out on a Workstation, but computation on a modern PC also presents no problem, so that one can enjoy a genuine quantum mechanical analysis of high-spin data using a facility available everywhere. Detailed technical information which may be useful for programming purposes is given in an Appendix.

### 1. Introduction

#### 1.1. *Spherical shell model*

The standard (spherical) shell model is not an optimal way of describing deformed heavy nuclei because of the huge configuration space required. Although it may technically be attainable on a modern supercomputer, such a calculation is not of much interest from the physical point of view. Even if one could reproduce

experimental data in this way, one would not be able to uncover the physics hidden behind a vast amount of computer output. With increasing complexity of the system, it is essential to use an approximation to extract the underlying physics. The role of an approximation method is indeed not only to simplify the treatment of a complex problem, but also to establish a physical picture. Pursuing this line of thought, we will use an intrinsic basis which spontaneously violates the symmetries of the system and will restore them by the projection method. An advantage of this approach (referred to as the Projected Shell Model hereafter) is that the truncation of the configuration space can be done very efficiently. To clarify the main difference between the present and the conventional shell model approach, let us first look at the latter from a critical point of view.

There is no doubt that the shell model<sup>1</sup> is the most fundamental way of describing many-nucleon systems fully quantum mechanically, treating the fermion dynamics directly (i.e., no mapping to a Boson space, etc.). However, it has some drawbacks. In the first place, each basis state (Slater determinant) has to be coupled to a good angular momentum. This is because, even if the single-particle wave functions are generated by a spherically symmetric potential (e.g., spherical harmonic oscillator with a proper spin-orbit force), the Slater determinants constructed by them are no longer eigenstates of the angular momentum. Construction of a set of basis states corresponding to good angular momentum (the  $J$ -scheme) is done by using the so-called Coefficients of Fractional Parentage (CFP). Although the procedure for evaluating the CFP is mathematically well developed and technically long established, it very soon becomes too complex and time-consuming with increasing number of active nucleons and, therefore, the maximal number of active nucleons that can be treated in this way is strongly limited in practice. In the so-called Large Scale Shell Model,<sup>2</sup> one attempts to go beyond this limit by abandoning the  $J$ -scheme and simply using the  $M$ -scheme to construct the shell model basis. Therefore, in this method, various angular momenta  $J$  with  $J \geq |M|$  are admixed in a basis state. In other words, the basis is no longer irreducible with respect to the rotational transformation (i.e., the rotational symmetry is broken). Theoretically, this poses no problem. When the Hamiltonian is diagonalized in such a basis, its eigenstates are obtained for all possible angular momenta simultaneously. One has only to check which eigenstate corresponds to which representation (angular momentum) when the solution is obtained. In practice, however, this is true only if one uses a sufficiently large configuration space in order to cover the whole space of the relevant representations. Therefore, as the name of the approach suggests, one usually has to deal with an eigenvalue problem of a huge Hamiltonian matrix, which is obviously one of the reasons why this method also becomes inapplicable to heavier systems. All this indicates that there is no absolute advantage in using a spherical single-particle basis. The practical implication of this statement will become evident as we proceed.

Let us examine another drawback of the standard (normal as well as Large Scale) shell model. Most of the nuclei in the nuclear chart are deformed except for those

in the neighborhood of the closed shells. Use of the spherical single-particle basis is obviously disadvantageous in treating such systems because a simple shell model configuration does not correspond to any simple mode of excitation. This means that a large configuration space would be necessary to represent even the lowest eigenstate (yrast state) of the Hamiltonian. For well-deformed heavy nuclei, one might need millions of basis states just to describe the ground state. Consequently, the physics would be largely lost in the sense mentioned at the beginning. In order to be able to extract the essence of the physics, it is desirable to use a shell model basis which has a good classification scheme (hierarchy), such that a simple configuration corresponds (approximately) to a simple mode of excitation of the nucleus. Such a feature is obviously missing in the spherical basis. In particular, we have seen above that there is no overriding reason why one should insist on the spherical basis. All this suggests that one may use a deformed basis from the outset corresponding to the optimal set of basis states in the sense of the Hartree–Fock (–Bogolyubov) theory which spontaneously violates the rotational (and gauge) symmetry. These basis states describe the intrinsic states of the system. The symmetry thus broken has to be restored by projecting the intrinsic states onto good angular momenta (and particle number) to obtain the proper shell model basis.

### 1.2. Deformed shell model

In the long history of the shell model, Elliott was the first to point out the advantage of a deformed (intrinsic) many-body basis and developed the SU(3) Shell Model<sup>3</sup> for sd-shell nuclei. In this model, the classification of basis states and their projection onto good angular momenta can be carried out using the group theoretical method. It works nicely so long as the spin-orbit force is weak (L–S coupling scheme), which is the reason why it applies only to light nuclei. In heavier nuclei, where the presence of a strong spin-orbit force (*j*-*j* coupling scheme) is essential for the correct shell closures (magic numbers), the SU(3) scheme is no longer valid. For such systems, we may resort to the Nilsson Model<sup>4</sup> (more precisely the Nilsson + BCS scheme in order to take the strong pairing correlations into account) and project numerically the deformed (multi-quasiparticle) basis onto good angular momenta (and particle number). In this way, we come to the basic idea of the Projected Shell Model approach. It can be considered to be a natural extension of the SU(3) shell model to heavier systems. While it might not matter in theory how we prepare a shell model basis, it is crucial in practice to use the most efficient one. For the description of deformed nuclei, a deformed basis provides us with an efficient way of truncating the shell model basis. However, its economical feature is not necessarily our main interest. The most important aspect of the deformed basis lies in the fact that it allows us to interpret the results in simple physical terms, and this is one of the main reasons for introducing the Projected Shell Model which we wish to demonstrate in the present article.

As is well-known, high-spin spectroscopy began with the discovery of the backbending phenomenon in the early seventies.<sup>5,6</sup> Since then, the number of measurements has been growing year by year and the range of spins higher and higher, thanks to rapidly developing experimental techniques. Furthermore, an incredibly sharp energy resolution in the  $\gamma$ -ray measurement made it possible to detect an extremely delicate and fine inversion phenomenon in the signature-dependent spectra of doubly-odd nuclei, which is to be compared with the rather pronounced and wild one observed in odd-mass nuclei. As we will see later in greater detail, there is a common mechanism in these seemingly different phenomena (backbending, fine and wild signature dependence). Namely, all this is caused (directly or indirectly) by the specific orbital motion of particle(s) occupying an intruder subshell whose existence is an immediate consequence of a strong spin-orbit force. Eventually, this may imply that these phenomena are providing us with further important evidence for the presence of a strong spin-orbit force which was originally introduced by Mayer and Jensen to explain the magic numbers nearly half a century ago.

The Projected Shell Model<sup>7-10</sup> has been designed and developed, so to speak, in order to meet the quality of measurements made possible by modern experimental techniques. It has been our strong belief that only a proper quantum mechanical theory would be able to explain quantitatively the finest features of observed data, and could provide us with a unified understanding of ever accumulating high-spin data. In fact, the outcome<sup>11-13</sup> seems to indicate that this is the case.

### 1.3. *Outline*

The present article is a review of the Projected Shell Model including a large number of examples on the analysis of high-spin data. Theoretical issues are explained, while experimentalists are kept in mind. Detailed technical information is given in Appendix A, which contains a mathematical proof of the algorithm and various formulas that may be useful when developing one's own (or modifying our) Projected Shell Model Code.

In Sec. 2, we present the formal aspect of the theory. The single band projection theory is discussed in a large deformation limit and the importance of a multiband theory is pointed out. We then formulate the Projected Shell Model in full generality. The Hamiltonian used in the present article is specified, for which the HFB procedure leads essentially to the Nilsson + BCS scheme. Obviously, this is the main reason why the present model can describe various types of nuclei over a wide range of isotope or isotone chains quite accurately. A comparison between the Projected Shell Model and the MONSTER approach is attempted at the end. In fact, the two approaches are similar in framework but are based on very different philosophies.

In Sec. 3, we discuss the quantum mechanical aspects of the decoupled motion and rotational alignment and propose a generalized signature rule, which is also treated in Appendix B from a different point of view. We introduce the band

diagram, which is an indispensable tool for the analysis of data as it enables us to extract valuable physical information. We predict the existence of remarkable high- $K$  bands in some doubly-even rare-earth nuclei, which are an immediate consequence of the Nilsson + BCS scheme.

Sections 4 to 6 present applications of the Projected Shell Model to different types of rare-earth nuclei. Doubly-even (Sec. 4), doubly-odd (Sec. 5), and odd-mass nuclei (Sec. 6) are treated on a unified footing using the same Hamiltonian ( $Q \cdot Q$  + Monopole Pairing + Quadrupole Pairing Force model), which works surprisingly well despite its simplicity. The use of a schematic interaction is justified in Appendix B. Although these forces may be too restrictive for certain problems, we will not go into the well-justified question as to whether one should include other types of forces in the Hamiltonian. In fact, the question is not “whether” but “when”, since the nuclear deformation is limited to the (axial as well as triaxial) quadrupole shapes at the moment and the neutron–proton interaction exists only in the  $Q \cdot Q$  force. All this is an obvious shortcoming of the present model which certainly deserves serious consideration but is left for future investigations.

In Sec. 7, we show that the Projected Shell Model is furnished with a mechanism which leads to a  $\Delta I = 4$  bifurcation. This result follows without assuming any  $C_4$  type symmetry if a certain condition on the shell filling is met. However, at present, we reserve judgement as to whether or not it is an explanation of the recently discovered phenomenon in some superdeformed nuclei. This is still to be investigated in the future.

Section 8 concludes the present article. We summarize each chapter once again and point out that what we learn from a number of examples gives us a very good hint as to the reason why the present model works so well. This is mentioned on several occasions but we will clarify it once again as the main conclusion to the present article. As a perspective for the future, an extension of the present theory to triaxial nuclei is outlined. Finally, a possible application of the Projected Shell Model to spherical nuclei is suggested, which may be useful for the study of the multiphonon problem.

## 2. Shell Model in the Projected Basis

### 2.1. *Projection operator*

The projection operator associated with a compact Lie Group is a well-known concept in the theory of group representations.<sup>14</sup> To begin with, we summarize the important properties of the projection operator in order to make the present article selfcontained. In the present context, we are primarily interested in the Rotation or SU(2) Group whose elements are specified by the group parameter  $\Omega$ , which represents a set of Euler angles ( $\alpha, \gamma = [0, 2\pi]$  and  $\beta = [0, \pi]$ ). The explicit form of the group element is

$$\hat{R}(\Omega) = e^{-i\alpha \hat{J}_z} e^{-i\beta \hat{J}_y} e^{-i\gamma \hat{J}_z}, \quad (2.1)$$

where  $\hat{J}$ 's are the angular momentum operators. Its (unitary) representation is

$$\langle \mu IM | \hat{R}(\Omega) | \nu JK \rangle = \delta_{\mu\nu} \delta_{IJ} D_{MK}^{I*}(\Omega), \quad (2.2)$$

where the symbol  $*$  means the complex conjugation and  $D_{MK}^I(\Omega)$  is the  $D$ -function.<sup>15</sup> The  $D$ -functions form a complete set of functions in the parameter space of  $\Omega$ . For a state  $|\mu IM\rangle$  belonging to the angular momentum  $IM$ ,  $\mu$  designates a set of quantum numbers that specify the quantum state uniquely, so that the following closure holds:

$$\sum_{\mu IM} |\mu IM\rangle \langle \mu IM| = 1. \quad (2.3)$$

We need not specify details of the state  $|\mu IM\rangle$  for our purposes, except for the fact that it belongs to a complete set of orthonormal vectors in a Hilbert space in which the operator (2.1) acts. From (2.2) and (2.3), it follows that

$$\hat{R}(\Omega) | \nu IK \rangle = \sum_M |\nu IM\rangle D_{MK}^{I*}(\Omega), \quad (2.4)$$

which is the multiplet relation between the states belonging to a representation (angular momentum)  $I$ . Using (2.4) and the orthogonality of the  $D$ -functions

$$\int d\Omega D_{MK}^{I*}(\Omega) D_{M'K'}^{I'}(\Omega) = \frac{8\pi^2}{2I+1} \delta_{II'} \delta_{MM'} \delta_{KK'} \quad (2.5)$$

we obtain the relation

$$\hat{P}_{MK}^I | \nu I' K' \rangle = \delta_{II'} \delta_{KK'} | \nu IM \rangle, \quad (2.6)$$

where the operator  $\hat{P}_{MK}^I$  is defined by

$$\hat{P}_{MK}^I = \frac{2I+1}{8\pi^2} \int d\Omega D_{MK}^I(\Omega) \hat{R}(\Omega) \quad (2.7)$$

and is called the Angular Momentum Projection Operator. From (2.3) and (2.6), we obtain its spectral representation and the “sum rule”

$$\hat{P}_{MK}^I = \sum_{\nu} |\nu IM\rangle \langle \nu IK|, \quad \sum_{IM} \hat{P}_{MM}^I = 1. \quad (2.8)$$

Using the spectral representation, we can easily derive the properties

$$\hat{P}_{MK}^{I\dagger} = \hat{P}_{KM}^I \quad \text{and} \quad \hat{P}_{KM}^I \hat{P}_{M'K'}^{I'} = \delta_{II'} \delta_{MM'} \hat{P}_{KK'}^I. \quad (2.9)$$

In general, a set of projection operators must satisfy the relations  $P_i^\dagger = P_i$ ,  $P_i P_j = \delta_{ij} P_i$ , and  $\sum_i P_i = 1$ , so that  $\hat{P}_{MK}^I$  is a projection operator in the usual sense only if  $K \equiv M$ . We show later that it is more natural to consider  $\hat{P}_{MK}^I$  as an operator which transforms a body-fixed (or intrinsic) system into a space-fixed system.

Nevertheless, we continue referring to it as a projection operator, in accordance with the usual terminology.

In an analogous way, we can introduce the Particle Number Projection Operator in terms of a Gauge Group [element =  $\exp(-i\phi\hat{N})$  and representation =  $\exp(i\phi N)$ ] by

$$\hat{P}^N = \frac{1}{2\pi} \int_0^{2\pi} d\phi e^{-i\phi(\hat{N}-N)}, \quad (2.10)$$

where  $\hat{N}$  is the particle number operator. The group parameter  $\phi$  is called the gauge angle. The operator  $\hat{P}^N$  is a projection operator in the usual sense.

When projecting the angular momentum and particle number simultaneously, we can combine two projectors (2.7) and (2.10):

$$\hat{P}_{MK}^{IN} \equiv \hat{P}_{MK}^I \hat{P}^N = \frac{2I+1}{16\pi^3} \int d\Omega d\phi D_{MK}^I(\Omega) \hat{R}(\Omega) e^{-i\phi(\hat{N}-N)}. \quad (2.11)$$

It should be noted that  $\hat{P}_{MK}^I$  and  $\hat{P}^N$  commute with each other.

What is shown above is only a formal definition. We will therefore supplement it with a discussion which demonstrates how such an operator comes into play in a physical problem taking the angular momentum projection operator as an example.

Suppose that  $|\Phi\rangle$  is a “deformed” state which means that it is not an eigenstate of the angular momentum. Because of the rotational invariance of the Hamiltonian

$$\hat{R}^\dagger(\Omega) \hat{H} \hat{R}(\Omega) = \hat{H}, \quad (2.12)$$

the energy expectation value

$$\frac{\langle \Phi | \hat{H} | \Phi \rangle}{\langle \Phi | \Phi \rangle} \quad (2.13)$$

remains the same even if we rotate the state  $|\Phi\rangle$ . In other words, all states  $\hat{R}(\Omega)|\Phi\rangle$  having different orientation  $\Omega$  are mutually degenerate. We note that  $\hat{R}(\Omega)|\Phi\rangle$  can be linearly independent of  $|\Phi\rangle$  since deformed states do not satisfy a linear relation such as (2.4). We can thus construct a wider class of states by forming a superposition

$$|\Psi\rangle = \int d\Omega F(\Omega) \hat{R}(\Omega) |\Phi\rangle, \quad (2.14)$$

where  $F(\Omega)$  is a function to be determined by minimizing the energy expectation value

$$E = \frac{\langle \Psi | \hat{H} | \Psi \rangle}{\langle \Psi | \Psi \rangle}. \quad (2.15)$$

This procedure should and does give an energy lower than (2.13) because the space spanned by  $\hat{R}(\Omega)|\Phi\rangle$  is larger than that consisting of just a single state  $|\Phi\rangle$  which corresponds to  $\Omega = 0$ . We can simplify the variational procedure greatly by making

use of the completeness of the  $D$ -functions. We expand first the trial function  $F(\Omega)$  as

$$F(\Omega) = \sum_{IMK} \frac{2I+1}{8\pi^2} F_{MK}^I D_{MK}^I(\Omega) \quad (2.16)$$

and then insert this into (2.14) to obtain

$$|\Psi\rangle = \sum_{IMK} F_{MK}^I \hat{P}_{MK}^I |\Phi\rangle, \quad (2.17)$$

where  $\hat{P}_{MK}^I$  is the angular momentum projection operator defined by (2.7). The coefficients  $F_{MK}^I$  now play the role of the variational parameters in place of the variational function  $F(\Omega)$ . If we carry out the variational procedure with (2.17), the summation over  $I$  and  $M$  actually drops away (i.e., a sharp  $I$  and  $M$ ) due to (2.9) and (2.12). Note, in particular, that (2.12) implies that the Hamiltonian commutes with the projection operator. Thus, it is sufficient to carry out the variational calculation with

$$|\Psi\rangle = \sum_K F_K^I \hat{P}_{MK}^I |\Phi\rangle \quad (2.18)$$

by omitting the summation over  $I$  and  $M$ . This means that  $|\Psi\rangle$  becomes an eigenstate of the angular momentum. The rotational symmetry violated in the original state  $|\Phi\rangle$  is thus recovered in the new state  $|\Psi\rangle$ . The resulting variational equation takes the form of an eigenvalue equation (and a normalization condition) independent of  $M$ :

$$\sum_{K'} \{H_{KK'}^I - EN_{KK'}^I\} F_{K'}^I = 0, \quad \sum_{KK'} F_K^I N_{KK'}^I F_{K'}^I = 1, \quad (2.19)$$

where we defined the Hamiltonian and norm matrix, respectively, by

$$H_{KK'}^I = \langle \Phi | \hat{H} \hat{P}_{KK'}^I | \Phi \rangle \quad \text{and} \quad N_{KK'}^I = \langle \Phi | \hat{P}_{KK'}^I | \Phi \rangle. \quad (2.20)$$

If the state  $|\Phi\rangle$  is triaxial, a given spin  $I$  appears, in general, more than once in the whole spectrum,  $I=0$  being a trivial exception. On the other hand, if it is axially symmetric for which the relation  $\hat{J}_z |\Phi\rangle = K_0 |\Phi\rangle$  holds where  $K_0$  is the conserved  $K$ -quantum number, the problem is simple. The solution of (2.19) then becomes

$$E = \frac{H_{K_0 K_0}^I}{N_{K_0 K_0}^I} \quad \text{with} \quad F_{K_0}^I = \frac{1}{\sqrt{N_{K_0 K_0}^I}} \quad (2.21)$$

since only one term with  $K = K_0$  remains in the summation over  $K$ . This represents the most primitive form of the angular momentum projection theory. It does not allow admixture of excited bands and thus can describe only one “rotational band”, whose “rotational energy” is obtained by evaluating  $E$  as a function of spin  $I$ . In contrast to the triaxial case, a given spin  $I$  appears only once in the spectrum.

We note that, for an axially symmetric case, the projection operator  $\hat{P}_{MK}^I$  reduces effectively to

$$\left( I + \frac{1}{2} \right) \int_0^\pi d\beta \sin \beta D_{MK}^I(\beta) e^{-i\beta J_y} \quad (2.22)$$

since  $\alpha$  and  $\gamma$  can be integrated explicitly when evaluating the matrix elements.

The state  $|\Phi\rangle$  used in the above argument can be generated, in practice, in various ways. One may construct such a symmetry violating state using the Nilsson (or Hartree-Fock) single-particle basis or, if the pairing correlations are strong, the Nilsson + BCS (or Hartree-Fock-Bogolyubov) quasiparticle basis. The state  $|\Phi\rangle$  may violate various symmetries of the Hamiltonian because it represents an “intrinsic” state. We have seen above that such a symmetry violating state is highly degenerate and a better state  $|\Psi\rangle$  can be constructed by using this degeneracy. Moreover, we have shown that the violated symmetry is recovered in the new state. This implies that we can accept  $|\Psi\rangle$  as a possible approximate solution of the Hamiltonian. We will refer to  $|\Psi\rangle$  ( $|\Phi\rangle$ ) as a state in the “space-fixed” (“body-fixed”) system. This is the conventional terminology, whose origin can be traced back to the mathematical nature of the  $D$ -function appearing in the projection operator (2.7). As is well-known, there exist two sets of (mutually commuting) differential operators both representing the angular momentum, which are called, respectively, the space-fixed and body-fixed type, the latter being characterized by “wrong” signs in the angular momentum commutation relations. The quantum number  $M$  ( $K$ ) of  $D_{MK}^I(\Omega)$  originates from the former (latter). It is natural to associate  $M$  and  $K$  of the operator  $\hat{P}_{MK}^I$  with the same physical interpretation as those of  $D_{MK}^I(\Omega)$  and, as (2.18) shows, the quantum number  $M$  belongs to  $|\Psi\rangle$  and  $K$  to  $|\Phi\rangle$ . We refer to the former (latter) as the “space-fixed” (“body-fixed”) state in this sense. Thus, the projection operator transforms a “body-fixed” state into a “space-fixed” state. The contents of the projection theory are rather abstract. However, it is possible to use many concepts developed in the semiclassical theory, such as the rotor model,<sup>16</sup> also in the projection theory if we translate them using an analogy. For example, it should be clear from the structure of the wave functions that the rotational motion of the “body” as a whole is described phenomenologically by the  $D$ -function  $D_{MK}^I$  in the former and microscopically by the projection operator  $\hat{P}_{MK}^I$  in the latter.

## 2.2. Semiclassical limit

In the previous subsection, we gave a simple example projecting just one “configuration”  $|\Phi\rangle$  onto a good angular momentum. In the early days of the theory, the formula (2.21) represented, in fact, the whole contents of the angular momentum projection method.<sup>17</sup> A pioneering calculation<sup>18,19</sup> was carried out using the Nilsson + BCS quasiparticle vacuum state  $|0\rangle$  for  $|\Phi\rangle$  (with  $K_0 = 0$ ) which represents the ground state band or  $g$ -band of a doubly-even nucleus. Let us first examine the outcome of such a theory.

After the  $\alpha$ - and  $\gamma$ -integration, the matrix element  $\langle 0 | \hat{O} \hat{P}_{00}^I | 0 \rangle$  ( $\hat{O} = 1, \hat{H}$ ) becomes

$$(2I+1) \int_0^{\frac{\pi}{2}} d\beta \sin \beta P_I(\cos \beta) \langle 0 | \hat{O} e^{-i\beta \hat{J}_y} | 0 \rangle \quad \text{for } I = \text{even} \quad (2.23)$$

and 0 for  $I = \text{odd}$ . Here, we used  $d_{00}^I(\beta) = (-)^I d_{00}^I(\pi - \beta) = P_I(\cos \beta)$  and the symmetry of the integrand with respect to  $\beta = \frac{\pi}{2}$  due to  $e^{-i\pi \hat{J}_y} | 0 \rangle = e^{-i\pi \hat{J}_x} | 0 \rangle = | 0 \rangle$ .

We will estimate the above integral in the large deformation limit, which we refer to as the “semiclassical” limit. Since the fluctuation of the angular momentum is a good measure for the deformation, the result may be written as a power series in  $1/\Delta J_y^2$ .

First, we examine the overlap  $\langle 0 | e^{-i\beta \hat{J}_y} | 0 \rangle$ , which may be written in the form

$$\langle 0 | e^{-i\beta \hat{J}_y} | 0 \rangle = \exp \left\{ -i \int_0^\beta d\beta' \langle 0 | \hat{J}_y [\beta'] | 0 \rangle \right\}, \quad [\beta] \equiv \frac{e^{-i\beta \hat{J}_y}}{\langle 0 | e^{-i\beta \hat{J}_y} | 0 \rangle}, \quad (2.24)$$

as can be verified by differentiating both sides with respect to  $\beta$ . The left-hand side of (2.24) corresponds to the characteristic function and the exponent of the right-hand side to the cumulant function known in statistical physics. The required expansion in terms of moments is given by what is known as the cumulant expansion, which is a power series expansion of the cumulant function. In the present case, it is obtained easily from the power series expansion of the operator  $[\beta]$  for small  $\beta$ ,

$$[\beta] = 1 - i\beta(\hat{J}_y - J_y) - \frac{1}{2}\beta^2(\hat{J}_y^2 - \Delta J_y^2) + \dots \quad (2.25)$$

The first order moment  $J_y = \langle 0 | \hat{J}_y | 0 \rangle$  is zero due to the time reversal symmetry of  $| 0 \rangle$  (generally, all odd order moments vanish). We will stop at the second order moment  $\Delta J_y^2 = \langle 0 | (\hat{J}_y - J_y)^2 | 0 \rangle = \langle 0 | \hat{J}_y^2 | 0 \rangle$  which represents the fluctuation of the angular momentum. We thus obtain the following approximate relations:

$$\begin{cases} \langle 0 | e^{-i\beta \hat{J}_y} | 0 \rangle \approx e^{-\frac{1}{2}\Delta J_y^2 \beta^2} \\ [\beta] \approx 1 - i\beta \hat{J}_y - \frac{1}{2}\beta^2 : \hat{J}_y^2 : \end{cases} \quad (2.26)$$

where  $\hat{J}_y^2 := \hat{J}_y^2 - \Delta J_y^2$ . The overlap is strongly peaked at  $\beta = 0$  if  $\Delta J_y^2$  is large. The integral in (2.23) can be obtained in a closed form by using the approximation (2.26) as well as an asymptotic form  $P_I(\cos \beta) \approx J_0(\sqrt{I(I+1)}\beta)$  valid for small  $\beta$ , where  $J_0(x)$  is the Bessel function of order zero, and by extending the integration range to infinity

$$\int_0^\infty d\beta \beta J_0(\sqrt{I(I+1)}\beta) e^{-\frac{1}{2}\Delta J_y^2 \beta^2} \left\{ \langle 0 | \hat{O} | 0 \rangle - \frac{1}{2} \langle 0 | \hat{O} \hat{J}_y^2 : | 0 \rangle \beta^2 \right\}. \quad (2.27)$$

The relevant integration formula can be found in Ref. 20;

$$\int_0^\infty dx x^{2n+1} J_0(bx) \exp \left\{ -\frac{1}{2} a^2 x^2 \right\} = \frac{2^n n!}{a^{2n+2}} L_n \left( \frac{b^2}{2a^2} \right) \exp \left\{ -\frac{b^2}{2a^2} \right\}, \quad (2.28)$$

where  $L_n(x)$  is the Laguerre Polynomial of order  $n$ . The energy  $E_I = H_{00}^I/N_{00}^I$  and the norm  $N_{00}^I$  (for  $I = \text{even}$  only) are therefore obtained approximately as

$$E_I \approx E_0 + \frac{I(I+1)}{2\Im} \quad \text{and} \quad N_{00}^I \approx Q_I \equiv \frac{2I+1}{\Delta J_y^2} \exp \left\{ -\frac{I(I+1)}{2\Delta J_y^2} \right\}, \quad (2.29)$$

respectively, where we have defined the quantities

$$\Im = \frac{(\Delta J_y^2)^2}{\langle 0|\hat{H} : \hat{j}_y^2 : |0\rangle} \quad \text{and} \quad E_0 = \frac{H_{00}^0}{N_{00}^0} \approx \langle 0|\hat{H}|0\rangle - \frac{\Delta J_y^2}{\Im}. \quad (2.30)$$

Note that  $\Im$  is nothing other than the Peierls–Yoccoz moment of inertia<sup>17</sup> and also that the projected ground state energy  $E_0$  is lower than the unprojected one,  $\langle 0|\hat{H}|0\rangle$ , by an amount  $\Delta J_y^2/\Im$ . This energy gain is due to the fluctuation of the angular momentum which causes a “zero-point rotation”. In fact, since  $\Delta J_x^2 = \Delta J_y^2$ , it may be written as  $\frac{1}{2\Im}(\Delta J_x^2 + \Delta J_y^2)$ , which represents the fluctuation of the rotational energy.

The norm  $N_{00}^I$  represents the probability distribution of the angular momentum in the ground state  $|0\rangle$  as can be seen by using the spectral representation (2.8),  $N_{00}^I = \langle 0|\hat{P}_{00}^I|0\rangle = \sum_\nu |\langle 0|\nu I 0\rangle|^2$ . Its approximation  $Q_I$  is normalized to 1 under the replacement  $\sum_{I=\text{even}} \rightarrow \int_0^\infty \frac{dI}{2}$ . The metric  $\frac{1}{2}$  corresponds to the summation only over  $I = \text{even}$ . We point out that the formulas depend only on two quantities,  $E_I - E_0$  on  $\Im$  and  $N_{00}^I$  on  $\Delta J_y^2$ , namely, (2.29) is the same for any Hamiltonian which yields the same  $\Im$  and  $\Delta J_y^2$ . It means that the result does not depend on details of the Hamiltonian.

Let us test the accuracy of the formula (2.29) by comparing its results with those of the exact numerical calculations for the excitation energy  $E = E_I - E_0$  and the norm  $N_{00}^I$ . For the evaluation of  $\Im$  and  $H_{00}^I$ , we take the Hamiltonian which we use throughout the present article; see (2.40). Some selected results<sup>21</sup> are tabulated in Table 1. The approximate and exact rotational energies compare rather well if not perfectly. On the other hand, the results for the norm  $N_{00}^I$  are excellent. It means that the fluctuation of the angular momentum  $\Delta J_y^2 = \langle 0|\hat{j}_y^2|0\rangle$  determines essentially the distribution of the angular momentum in the state  $|0\rangle$ . Consequently, the distributions will be the same for different nuclei that have the same  $\Delta J_y^2$ . This can be seen in the case of <sup>164</sup>Dy and <sup>170</sup>Yb. The values of  $\Delta J_y^2$  are almost the same (40.74 and 40.64, respectively) and, in fact, the distributions are found to be identical. This shows that the angular momentum distribution is determined by the quantity  $\Delta J_y^2$  alone. The formula also shows that the peak of the distribution occurs at  $I \approx \sqrt{\Delta J_y^2}$ . We see that the peak of  $N_{00}^I$  is at  $I = 6$  for all nuclei listed in Table 1 and that the integral part of  $\sqrt{\Delta J_y^2}$  is indeed 6 for all of them. We may conclude that the semiclassical formula (2.29) is a good approximation to the exact projection for well-deformed nuclei.

Table 1. Comparison of (2.29) with the exact result (in parentheses).

$^{164}\text{Dy}$ : $\Im = 35.026 \text{ MeV}^{-1}$ , $\Delta J_y^2 = 40.744$				
Spin	2	4	6	8
E MeV	0.086 (0.085)	0.286 (0.263)	0.600 (0.593)	1.028 (1.016)
Norm	0.114 (0.116)	0.174 (0.174)	0.191 (0.190)	0.172 (0.170)
	10	12	14	16
	1.570 (1.549)	2.227 (2.190)	2.998 (2.934)	3.883 (3.774)
	0.134 (0.130)	0.090 (0.088)	0.054 (0.053)	0.029 (0.029)
$^{170}\text{Er}$ : $\Im = 34.863 \text{ MeV}^{-1}$ , $\Delta J_y^2 = 43.693$				
Spin	2	4	6	8
E MeV	0.086 (0.080)	0.289 (0.267)	0.602 (0.563)	1.033 (0.970)
Norm	0.107 (0.108)	0.164 (0.166)	0.184 (0.183)	0.171 (0.169)
	10	12	14	16
	1.578 (1.489)	2.237 (2.120)	3.012 (2.862)	3.901 (3.713)
	0.136 (0.134)	0.096 (0.094)	0.060 (0.059)	0.034 (0.034)
$^{170}\text{Yb}$ : $\Im = 33.467 \text{ MeV}^{-1}$ , $\Delta J_y^2 = 40.640$				
Spin	2	4	6	8
E MeV	0.090 (0.085)	0.299 (0.286)	0.627 (0.601)	1.076 (1.033)
Norm	0.114 (0.116)	0.173 (0.174)	0.191 (0.190)	0.172 (0.170)
	10	12	14	16
	1.643 (1.582)	2.331 (2.247)	3.137 (3.025)	4.064 (3.914)
	0.134 (0.131)	0.090 (0.088)	0.054 (0.053)	0.029 (0.029)

It is worth mentioning that the second order cumulant expansion used to derive (2.29) is fully equivalent to the use of the quasiboson approximation (or quasiparticle RPA) in evaluating the matrix element in the integrand of the exact expression (2.23). The result (2.29) will be used later to clarify the basic nature of the present theory.

The above result shows that, as far as the ground state band of a well-deformed doubly-even nucleus is concerned, this kind of projection theory contains no information other than the moment of inertia. The rotational spectrum is proportional to  $I(I+1)$  and is therefore essentially the same as that of the rotor model. The intraband  $BE2$  values<sup>8</sup> are also almost the same as the semiclassical values. It means that, although the theory itself is purely quantum mechanical, the physics one can learn from it is rather little. Moreover, its applicability to the realistic cases is limited to a relatively low spin region because the  $g$ -band will no longer be the lowest band beyond a moderate spin ( $I > 10$ ) due to the crossing of the  $g$ - and  $s$ -band (the first band crossing).

As it stands, the description of rotational states in terms of such a one-band theory is of a “static” nature. The dynamical features of the system will first become evident when more than one configuration (band) is taken into account. The most popular example is the mutual crossing and coupling between the  $g$ - and  $s$ -bands, which play a decisive role in the backbending phenomenon of doubly-even nuclei. Therefore, in order to take into account the interplay of various bands, it is necessary to carry out configuration mixing. This is exactly what the Projected Shell Model aims to do.

### 2.3. Projected Shell Model

We now formulate the Projected Shell Model by generalizing the single-band theory discussed above and derive its basic equations. Let us suppose that we have selected a set of multi-quasiparticle (multi-qp) states  $\{|\Phi_\kappa\rangle\}$  which we want to take into account in the shell model configuration space by projecting them onto good angular momentum  $I$  and particle number  $N$ , whose concrete specification will be given later for doubly-even, doubly-odd, and odd-mass nuclei; see (2.53).

Once the quasiparticle basis is prepared, we diagonalize the Hamiltonian in the shell model space spanned by  $\{\hat{P}_{MK}^{IN}|\Phi_\kappa\rangle\}$ . This leads to the eigenvalue equation

$$\sum_{\kappa' K'} \{H_{\kappa K \kappa' K'}^I - EN_{\kappa K \kappa' K'}^I\} F_{\kappa' K'}^I = 0 \quad (2.31)$$

with the normalization condition

$$\sum_{\kappa K \kappa' K'} F_{\kappa K}^I N_{\kappa K \kappa' K'}^I F_{\kappa' K'}^I = 1. \quad (2.32)$$

Note that (2.31) and (2.32) are the straightforward generalization of (2.19) to a multiconfiguration space. The Hamiltonian and norm elements are defined, respectively, by

$$H_{\kappa K \kappa' K'}^I = \langle \Phi_\kappa | \hat{H} \hat{P}_{KK'}^{IN} | \Phi_{\kappa'} \rangle \quad \text{and} \quad N_{\kappa K \kappa' K'}^I = \langle \Phi_\kappa | \hat{P}_{KK'}^{IN} | \Phi_{\kappa'} \rangle, \quad (2.33)$$

which is the generalization of (2.20). Sum rules involving these matrix elements can be derived using the second relation of (2.8); see (A.79) of Appendix A.

The eigenvalue Eq. (2.31) is most easily solved by using the method described in Appendix A.5. The normalized eigenstate is then given by

$$|\Psi_{IM}\rangle = \sum_{\kappa K} F_{\kappa K}^I \hat{P}_{MK}^{IN} |\Phi_\kappa\rangle, \quad (2.34)$$

which is the generalization of (2.18). We note that  $|\Phi_\kappa\rangle$  and its time reversal  $|\Phi_{\bar{\kappa}}\rangle$  yield the same projected state; see (3.24) for the proof of this statement. This halves the dimension of the configuration space.

To compute the matrix element of a tensor operator of rank  $\lambda$  with respect to the projected states, the matrix element of the operator  $\hat{P}_{K'M'}^{I'N'} \hat{T}_{\lambda\mu} \hat{P}_{MK}^{IN}$  has to be

evaluated. This is obtained as follows. On the one hand, we have the relation

$$\hat{P}_{K'M'}^{I'} \hat{T}_{\lambda\mu} \hat{P}_{MK}^I = (IM, \lambda\mu | I'M') \sum_{\nu} (IK' - \nu, \lambda\nu | I'K') \hat{T}_{\lambda\nu} \hat{P}_{K'-\nu K}^I, \quad (2.35)$$

which follows from the transformation property of a tensor operator of rank  $\lambda$  under the rotation as well as the reduction theorem of a product of two  $D$ -functions. The proof is given in Appendix B. On the other hand, we have analogously

$$\hat{P}^{N'} \hat{T}_{\lambda\mu} \hat{P}^N = \delta_{N' N + \Delta N} \hat{T}_{\lambda\mu} \hat{P}^N \quad \text{with} \quad [\hat{N}, \hat{T}_{\lambda\mu}] = \Delta N \hat{T}_{\lambda\mu}. \quad (2.36)$$

Here,  $\Delta N$  is an integer which represents the difference between the number of single-particle creation and annihilation operators that constitute the operator  $\hat{T}_{\lambda\mu}$ . Namely, it is given by  $\Delta N = 0$  ( $\pm 2$ ) for the electromagnetic (pairing type) multipole operator. Combining the above two results, we obtain the relation ( $\hat{P}_{MK}^{IN} \equiv \hat{P}_{MK}^I \hat{P}^N$ )

$$\hat{P}_{K'M'}^{I'N'} \hat{T}_{\lambda\mu} \hat{P}_{MK}^{IN} = \delta_{N' N + \Delta N} (IM, \lambda\mu | I'M') \sum_{\nu} (IK' - \nu, \lambda\nu | I'K') \hat{T}_{\lambda\nu} \hat{P}_{K'-\nu K}^{IN}. \quad (2.37)$$

We have so far given the mathematical framework of the Projected Shell Model in full generality. It is formulated in quite a general manner allowing for triaxiality of the quasiparticle basis and taking into account the simultaneous angular momentum and particle number projection. In practice, we can make some simplifications, for example, by omitting the particle number projection. Although the particle number projection may improve the result, the essential physics of the yrast spectroscopy can be described even without taking it into consideration. Therefore, most of the present calculations have been done by replacing  $\hat{P}_{MK}^{IN}$  with  $\hat{P}_{MK}^I$  ( $\hat{P}^N \rightarrow 1$ ). We will compare the calculations obtained with and without particle number projection in Sec. 4.3 and show to what extent the particle number projection can improve the results of the rotational spectra. Another simplification made in the present work is the use of the axially symmetric basis. We postpone the study of triaxial nuclei to the future.

The presence of axial symmetry and/or omission of particle number projection will simplify the equations and their numerical treatment. In particular, axial symmetry implies that the set of quantum numbers  $\kappa$  contains, amongst other things, the total intrinsic magnetic quantum number  $K$  implicitly. We can, therefore, omit writing  $K$  in the amplitude  $F_{\kappa K}^I$  for such a system. Moreover, the summations over  $K$  may also be omitted since only one specific  $K$  contributes to the sum for a given  $\kappa$ . This leads to the set of equations on which (most of) the present numerical calculations are based:

$$\sum_{\kappa'} \{H_{\kappa\kappa'}^I - EN_{\kappa\kappa'}^I\} F_{\kappa'}^I = 0, \quad \sum_{\kappa\kappa'} F_{\kappa}^I N_{\kappa\kappa'}^I F_{\kappa'}^I = 1, \quad (2.38)$$

$$H_{\kappa\kappa'}^I = \langle \Phi_{\kappa} | \hat{H} \hat{P}_{KK'}^I | \Phi_{\kappa'} \rangle, \quad N_{\kappa\kappa'}^I = \langle \Phi_{\kappa} | \hat{P}_{KK'}^I | \Phi_{\kappa'} \rangle.$$

Then the matrix element of a tensor operator of rank  $\lambda$  can be evaluated by

$$\begin{aligned}\langle \Psi_{I'M'} | \hat{T}_{\lambda\mu} | \Psi_{IM} \rangle &= (IM, \lambda\mu | I'M') \langle \Psi_{I'} | \hat{T}_\lambda | \Psi_I \rangle, \\ \langle \Psi_{I'} | \hat{T}_\lambda | \Psi_I \rangle &= \sum_{\nu\kappa\kappa'} (IK' - \nu, \lambda\nu | I'K') \langle \Phi_{\kappa'} | \hat{T}_{\lambda\nu} \hat{P}_{K'-\nu K}^I | \Phi_\kappa \rangle F_{\kappa'}^{I'} F_\kappa^I,\end{aligned}\quad (2.39)$$

which follows from the operator identity (2.35) and is, therefore, also valid for the triaxial case with an obvious extension of the formula for the triaxial basis. This result is to be compared with the corresponding matrix element of the particle-rotor model

$$(IM, \lambda\mu | I'M') \sum_{\nu\kappa\kappa'} (IK, \lambda\nu | I'K') \langle \Phi_{\kappa'} | \hat{T}_{\lambda\nu} | \Phi_\kappa \rangle F_{\kappa'}^{I'} F_\kappa^I.$$

Note that this result follows from (2.39) through the replacement

$$\langle \Phi_{\kappa'} | \hat{T}_{\lambda\nu} \hat{P}_{K'-\nu K}^I | \Phi_\kappa \rangle \rightarrow \delta_{K'-\nu K} \langle \Phi_{\kappa'} | \hat{T}_{\lambda\nu} | \Phi_\kappa \rangle$$

which shows the correspondence between the quantum mechanical and semiclassical expression. Note, in particular, that the latter does not depend on spin  $I$ .

#### 2.4. Choice of the Hamiltonian

We now describe the Hamiltonian which will be used throughout the present work. As mentioned before, our interaction consists of a sum of schematic (i.e.,  $Q \cdot Q$  + Monopole Pairing + Quadrupole Pairing) forces which represent different kinds of characteristic correlations between active nucleons. Justification for a schematic interaction to be used in conjunction with the harmonic oscillator single-particle Hamiltonian will be given in Appendix B. The total Hamiltonian of the present model assumes the form

$$\hat{H} = \hat{H}_0 - \frac{\chi}{2} \sum_\mu \hat{Q}_\mu^\dagger \hat{Q}_\mu - G_M \hat{P}^\dagger \hat{P} - G_Q \sum_\mu \hat{P}_\mu^\dagger \hat{P}_\mu. \quad (2.40)$$

The first term represents the harmonic oscillator single-particle Hamiltonian

$$\hat{H}_0 = \sum_\alpha c_\alpha^\dagger \varepsilon_\alpha c_\alpha (\varepsilon_\alpha \equiv \hbar\omega \{N - \kappa[2\mathbf{j} \cdot \mathbf{s} + \mu(\mathbf{l}^2 - \langle \mathbf{l}^2 \rangle)]_{Nj}\}), \quad (2.41)$$

where  $c_\alpha^\dagger$  and  $c_\alpha$  are, respectively, the single-particle creation and annihilation operator labeled by a set of the spherical harmonic oscillator quantum numbers  $\alpha = \{N, j, m\}$ . Note that  $\mathbf{l}$  is known when  $N$  and  $j$  are specified. The Fermi energy will be included in the single-particle energy ( $\varepsilon_\alpha \rightarrow \varepsilon_\alpha - \lambda$ ) for convenience and obvious dependence on the isospin degrees of freedom will be omitted for simplicity. We take three major shells for active nucleons, e.g.,  $N = 4, 5, 6$  (3, 4, 5) for neutrons (protons) in rare-earth nuclei.

The one-body operators in (2.40) are defined (for each kind of nucleons) by

$$\hat{Q}_\mu = \sum_{\alpha\beta} c_\alpha^\dagger Q_{\mu\alpha\beta} c_\beta, \quad \hat{P}^\dagger = \frac{1}{2} \sum_\alpha c_\alpha^\dagger c_\alpha^\dagger, \quad \hat{P}_\mu^\dagger = \frac{1}{2} \sum_{\alpha\beta} c_\alpha^\dagger Q_{\mu\alpha\beta} c_\beta^\dagger, \quad (2.42)$$

where  $\bar{\alpha}$  represents the time reversal of  $\alpha$  ( $c_{\bar{\alpha}} = \hat{T}c_{\alpha}\hat{T}^{\dagger} = (-)^{j-m}c_{N_j-m}$ ) while

$$Q_{\mu\alpha\alpha'} = \delta_{NN'}(Njm|Q_{\mu}|N'j'm') \quad (2.43)$$

is the matrix element of the SU(3) quadrupole generator, whose matrix elements are equal to those of the dimensionless mass quadrupole operator

$$\sqrt{\frac{4\pi}{5}} \left(\frac{r}{b}\right)^2 Y_{2\mu}$$

for  $N = N'$ , but vanish for  $N \neq N'$  where  $b$  is the harmonic oscillator length

$$b^2 = \frac{\hbar}{m\omega}.$$

Note the symmetry properties of the matrix element

$$Q_{\bar{\mu}\alpha\beta} \equiv Q_{\mu\bar{\alpha}\bar{\beta}} = Q_{\mu\beta\alpha} = (-)^{\mu} Q_{-\mu\alpha\beta} \quad (2.44)$$

which ensure the relations  $\hat{Q}_{\bar{\mu}} \equiv \hat{T}\hat{Q}_{\mu}\hat{T}^{\dagger} = \hat{Q}_{\mu}^{\dagger} = (-)^{\mu} \hat{Q}_{-\mu}$ .

The HFB single-particle Hamiltonian resulting from (2.40) is

$$\hat{H}_{HFB} = \hat{H}_0 - \chi \sum_{\mu} \langle \hat{Q}_{\mu} \rangle \hat{Q}_{\mu} - G_M \langle \hat{P} \rangle (\hat{P} + \hat{P}^{\dagger}) - G_Q \sum_{\mu} \langle \hat{P}_{\mu} \rangle (\hat{P}_{\mu} + \hat{P}_{\mu}^{\dagger}). \quad (2.45)$$

Here,  $\langle \cdots \rangle$  means the expectation value with respect to the HFB vacuum state  $|0\rangle$ . Note that  $\langle \hat{Q}_{\mu} \rangle$  vanishes for  $\mu = \text{odd}$ , due to the  $S$ -symmetry (cf. (A.6) of Appendix A) while  $\langle \hat{Q}_{\mu} \rangle = \langle \hat{Q}_{\bar{\mu}} \rangle$  if  $\mu = \text{even}$ , due to the time reversal symmetry. For axially symmetric nuclei, all vanish except for  $\mu = 0$ . The same applies to  $\langle \hat{P}_{\mu} \rangle$ . We remark in passing that it is crucial for an odd-particle system to require the correct particle number ( $N = \text{odd}$ ) in the number condition  $\langle \hat{N} \rangle = N$ . This is the usual prescription but is often misunderstood since  $|0\rangle$  contains even numbers of particles. If one used the particle number of a neighboring even-particle system (i.e.,  $N+1$  or  $N-1$ ), it would lead to an incorrect Fermi energy for the (odd-particle) system in question.

Before we go into the isospin dependence of the above forces, let us first adjust the nuclear size by using the conventional harmonic oscillator parameters

$$\omega_{\tau} = \omega_0 a_{\tau}, \quad b_{\tau}^2 = \frac{b_0^2}{a_{\tau}}, \quad b_0^2 = \frac{\hbar}{m\omega_0}, \quad a_{\tau} \equiv \left\{ 1 \pm \frac{N-Z}{A} \right\}^{\frac{1}{3}}, \quad (2.46)$$

with  $+$  ( $-$ ) for  $\tau = \text{neutron}$  ( $\text{proton}$ ). If we use the value  $\hbar\omega_0 = 41.4678A^{-\frac{1}{3}}$  MeV, for example, we find  $b_0^2 = A^{\frac{1}{3}}$  fm $^2$  which is not only easy to remember but also practical.

All pairing type forces are assumed to act only between like nucleons (i.e., the iso-vector type). The coupling constant for the Monopole Pairing force is taken as

$$G_M = \left( G_1 \mp G_2 \frac{N-Z}{A} \right) \frac{1}{A} \text{ MeV} \quad \text{with } - \text{ (+) for neutron (proton)}, \quad (2.47)$$

where  $G_1$  and  $G_2$  (respectively, 21.24 and 13.86 in the rare-earth region) are adjusted to yield the known odd–even mass differences. Another possible form will be  $G_M = G_\tau/A$  for  $\tau = \text{neutron}$  and  $\text{proton}$ . For the Quadrupole Pairing force, we assume for simplicity that the strength  $G_Q$  is simply proportional to  $G_M$  with an overall constant  $\gamma$ ,

$$G_Q = \gamma G_M . \quad (2.48)$$

According to our experience,  $\gamma$  is about 0.18 to 0.20 (0.16 to 0.18) in the lighter (heavier) part of the rare-earth region. For the  $Q \cdot Q$  force, the second term of (2.45) can be identified as the (stretched) Nilsson potential  $\frac{2}{3}\epsilon\hbar\omega\hat{Q}_0$ . Introducing  $x_\tau \equiv \hbar\omega_\tau\langle\hat{Q}_0\rangle_\tau$  and  $C_{\tau\tau'} \equiv \chi_{\tau\tau'}(\hbar\omega_\tau\hbar\omega_{\tau'})^{-1}$ , we obtain the selfconsistent condition

$$\begin{aligned} C_{nn}x_n(\epsilon_n, \epsilon_p) + C_{np}x_p(\epsilon_n, \epsilon_p) &= \frac{2}{3}\epsilon_n , \\ C_{pn}x_n(\epsilon_n, \epsilon_p) + C_{pp}x_p(\epsilon_n, \epsilon_p) &= \frac{2}{3}\epsilon_p , \end{aligned} \quad (2.49)$$

whose solutions  $\epsilon_n$  and  $\epsilon_p$  are, in general, different from each other.<sup>22</sup> We will assume as usual that the neutron and proton deformation parameters are equal to each other,  $\epsilon_n = \epsilon_p \equiv \epsilon$ . The necessary and sufficient condition for this is that two equations of (2.49) reduce to a single equation, namely, they have to be linearly dependent:

$$C_{nn}C_{pp} - C_{np}^2 = 0, \quad (C_{pn} = C_{np}) , \quad (2.50)$$

which is the condition for the determinant of (2.49) to vanish, so that (2.49) and (2.50) lead to the isoscalar coupling  $C_{nn} = C_{pp} = C_{np}$ . We, therefore, obtain the relation

$$\chi_{\tau\tau'} = \frac{\frac{2}{3}\epsilon\hbar\omega_\tau\hbar\omega_{\tau'}}{\hbar\omega_n\langle\hat{Q}_0\rangle_n + \hbar\omega_p\langle\hat{Q}_0\rangle_p} . \quad (2.51)$$

This is a very useful relation since the nuclear deformation is a well-studied quantity.<sup>23</sup> The  $Q \cdot Q$  force coupling constant corresponding to a given deformation parameter  $\epsilon$  is thus obtained by (2.51). We adopt this strategy to ensure that the  $Q \cdot Q$  force generates the correct nuclear deformation. Note, however, that  $\chi_{\tau\tau'}$  remains undetermined for  $\epsilon = 0$  (a spherical nucleus) since both  $\langle\hat{Q}_0\rangle_n$  and  $\langle\hat{Q}_0\rangle_p$  vanish.

The present force model works surprisingly well despite its simplicity. Nevertheless, it has obvious shortcoming. In the first place, the nuclear deformation is restricted to the quadrupole type only. Secondly, the neutron–proton interaction is present only in the (particle–hole type)  $Q \cdot Q$  force. Depending on the problem, all this might be too restrictive and one will have to introduce (schematic) forces of a more general type.

Let us summarize the logical structure of the theory. The calculation proceeds in the following sequence. For each nucleon, we diagonalize first the Nilsson Hamiltonian

$$\hat{H}_0 - \frac{2}{3}\epsilon\hbar\omega\hat{Q}_0 \quad (2.52)$$

for the known deformation parameter  $\epsilon$  and then carry out the usual BCS procedure to take the (static) Monopole Pairing force into account. This defines the Nilsson + BCS quasiparticle basis. In principle, we should use the HFB basis to take also the (static) Quadrupole Pairing force into account. In practice, however, this does not make much difference to the Nilsson + BCS basis after the final shell model diagonalization, so that the simpler procedure may be used to a good approximation (cf. a detailed discussion in Appendix A.1). Now, the strength of the  $Q \cdot Q$  force can be evaluated by the relation (2.51). This fixes the Hamiltonian (2.40), which is then diagonalized within the shell model space spanned by a selected set of projected multi-qp states. We list below the quasiparticle configurations used in the present work for different types of nuclei.

$$\begin{aligned} \text{Doubly-even nucleus: } & |0\rangle, a_{\nu_1}^\dagger a_{\nu_2}^\dagger |0\rangle, a_{\pi_1}^\dagger a_{\pi_2}^\dagger |0\rangle, a_{\nu_1}^\dagger a_{\nu_2}^\dagger a_{\pi_1}^\dagger a_{\pi_2}^\dagger |0\rangle, \\ \text{Doubly-odd nucleus: } & a_\nu^\dagger a_\pi^\dagger |0\rangle, \\ \text{Odd-neutron nucleus: } & a_\nu^\dagger |0\rangle, a_\nu^\dagger a_{\pi_1}^\dagger a_{\pi_2}^\dagger |0\rangle, \\ \text{Odd-proton nucleus: } & a_\pi^\dagger |0\rangle, a_\pi^\dagger a_{\nu_1}^\dagger a_{\nu_2}^\dagger |0\rangle, \end{aligned} \quad (2.53)$$

where  $\nu$ 's ( $\pi$ 's) denote the neutron (proton) Nilsson quantum numbers which run over properly selected (low-lying) quasiparticle states. We have discarded configurations that contain three or more like-nucleon quasiparticles because they have higher excitation energies due to mutual blocking of levels and thus affect the results little in the energy (and the spin) ranges that interest us. This restriction can be easily released if necessary.

The Projected Shell Model can be considered as a kind of Tamm-Dancoff Approximation to which the so-called Broken-Pair Approximation<sup>24</sup> also belongs. In the present theory, the violated rotational symmetry is restored by the angular momentum projection method. The effect of the rotation is described by the projection operator and the whole dependence of the wave functions on spin is contained in the eigenvectors since the quasiparticle basis is spin independent. It is this feature which makes not only the numerical treatment simple and stable but also the interpretation of the result easy and intuitive. Our central numerical problem is how to evaluate various projected matrix elements most efficiently. The technical details are given in Appendix A.

### 2.5. Comparison with other approaches

Besides the Projected Shell Model, another approach based on the projection method is the so-called MONSTER.<sup>25</sup> It will be worthwhile to devote the rest of this chapter to examining the main difference between the two. MONSTER is a procedure for carrying out the diagonalization in the number- and spin-projected 0- and 2-quasiparticle space and therefore applies exclusively to doubly-even nuclei. On the other hand, the Projected Shell Model can treat all types of nuclei while the particle number projection is not mandatory (i.e., it is done only if necessary).

There are two MONSTER versions which differ in the way in which the quasiparticle basis is constructed. One is based on the usual HFB procedure (in the sense of Variation Before Projection). This version is referred to as MONSTER(HFB).<sup>26</sup> The other is based on the quasiparticle basis optimized at each spin (in the sense of Variation After Projection). This version is referred to as MONSTER(VAMPIR)<sup>27</sup> since the procedure to determine the quasiparticle basis is called VAMPIR,<sup>28</sup> which has actually several variants<sup>29</sup> with varying degrees of sophistication. The quasiparticle basis of the MONSTER(VAMPIR) changes with spin while that of the MONSTER(HFB) does not. The Projected Shell Model also uses a spin independent basis. Note that, in a spin independent basis, the whole effect of the rotation arises from the projection operator. Table 2 compares the main features of the two approaches (naturally only) for doubly-even nuclei.

Table 2. Comparison between Projected Shell Model (PSM) and MONSTER.

Approach	SP Space	Deformation	SM Space	Interaction
PSM	= 3 Shells	Axial/Triax.	0-, 2-, 4-qp	$QQ + MP + QP$
MONSTER	< 2 Shells	Axial symm.	0-, 2-qp	General

The first item (SP Space) compares the size of the single-particle space. The symbol “= 3 Shells” implies three full major shells for each kind of nucleon while “< 2 Shells” means less than two major shells, e.g., one major shell plus a few subshells from the next major shell including, among others, an intruder subshell. The physical consequence of the difference in the size of the single-particle space will be discussed later. The next item (Deformation) compares the types of the deformation allowed for the quasiparticle (*qp*) basis. The Projected Shell Model can be, and has been, applied to triaxial nuclei<sup>30,31</sup> while MONSTER has been applied exclusively to axially symmetric nuclei.

The next item (SM Space) shows that the shell model space of MONSTER consists of projected 0- and 2-*qp* states. However, it is well known that a 4-*qp* band crosses the *s*-band (the second band-crossing) at a higher spin and becomes the yrast state. Unlike the Projected Shell Model, the MONSTER(HFB) cannot describe this mechanism since its shell model space contains no 4-*qp* configuration. It will, therefore, break down for spins beyond the second band-crossing. The MONSTER(VAMPIR) was introduced to overcome this weak point. Namely, the quasiparticle basis in the VAMPIR procedure is constructed such that the projected HFB vacuum state becomes the yrast state for any spin, at least in theory. Actually, to make the calculation feasible, it is assumed that the HFB vacuum state is axially symmetric and has  $K = 0$ ,  $K$  being the intrinsic magnetic quantum number. However, these approximations are inconsistent with the fact that a  $K = 1$  state (*s*-band) becomes the yrast state after a moderate spin ( $I = 12 \sim 14$ ) by crossing the *g*-band (the first band-crossing). Therefore, in order to achieve what was

originally intended, the VAMPIR procedure has to break time-reversal symmetry. To understand the role of time-reversal in this context, it should be noted that even a triaxial HFB vacuum state may contain only the  $K = \text{even}$  components if it preserves time-reversal. This kind of triaxiality is not sufficient for a rotating system. One also needs the admixtures of  $K = \text{odd}$  components (triaxiality of a general type) and, to achieve this, it is necessary to break time-reversal symmetry in the HFB procedure. As a guideline, one may recall that the degree of time-reversal violation (measured by the vacuum expectation value  $\langle \hat{J}_x \rangle$ ) increases with spin in the Cranked HFB<sup>32</sup> and this is possible only if both  $K = \text{even}$  and odd components are admixed in the HFB vacuum state. The same should also happen to the HFB vacuum state obtained by the VAMPIR should it represent the yrast state for an arbitrary spin. This is one requirement. Another requirement is that one has to take a superposition of a projected vacuum state over  $|K| \leq I$  (at least over a few smaller  $|K|$ -values) when constructing the trial wave function in order to include different  $K$ -values depending on spin. These two requirements are indeed formidable hurdles which make Variation After Projection (VAP) practically unattainable for a rapidly rotating system. One may recall that, starting from the VAP formalism, the Cranked HFB has attempted to make it tractable by means of a number of drastic approximations. Since the approximations used in the VAMPIR conflict with the above requirements, the resulting HFB vacuum is not necessarily the yrast state but is simply a continuation of the  $g$ -band optimized to a given spin. Thus, the nuclear deformation may change with spin. However, the Coriolis antipairing effect is still absent since time-reversal is not broken. As mentioned above, the HFB vacuum obtained by the VAMPIR procedure will no longer be the yrast state beyond the first band-crossing. Therefore, the latter can be obtained only through a subsequent MONSTER diagonalization, so that it is again of  $2\text{-}qp$  nature as in the case of the MONSTER(HFB). Moreover, beyond the second band-crossing, the MONSTER(VAMPIR) will suffer from the same problem as the MONSTER(HFB) because the yrast state may be accessible only through the  $4\text{-}qp$  configurations which are not contained in the MONSTER shell model space. Therefore, the MONSTER(VAMPIR) will eventually break down at higher spins exactly as the MONSTER(HFB) does. To escape from this dilemma, it is indeed necessary to find the VAMPIR solution which fulfills the two above-mentioned requirements. Since this is extremely difficult to achieve, projecting the Cranked HFB vacuum onto good angular momenta (Variation Before Projection) seems to be a more practical strategy for tackling this problem. In fact, this has been shown to be attainable.<sup>30</sup> Unfortunately, there is a strong suspicion that even such a simplified approach may fail to converge at very high spins because of a rapidly increasing level density. We will discuss this problem in Sec. 4.1 and show concrete evidence for this potential difficulty.

Let us next discuss the physical consequence of the differences in the size of single-particle space. Roughly speaking, the MONSTER uses not more than half the space taken into account in the Projected Shell Model (PSM). There is a single

case where one can compare the results of PSM<sup>9</sup> and MONSTER(HFB),<sup>26</sup> in which the spectrum of the <sup>164</sup>Er nucleus has been calculated using the same interaction ( $Q \cdot Q$  + Monopole Paring + Quadrupole Pairing) in both approaches. In this case, the main differences between PSM and MONSTER(HFB) are the size of the spaces (cf. SP and SM in Table 1) and treatment of the particle number projection. The above mentioned PSM calculation<sup>9</sup> was carried out within the projected 0- and 2-*qp* shell model space as in the MONSTER case but without particle number projection. The latter will further improve the result as we will show in Sec. 4.3. Therefore, the essential difference in the two calculations originates from the size of the single-particle space. While everything was done microscopically in PSM to obtain good agreement with data, it was necessary in the MONSTER(HFB) calculation to modify the spectrum by introducing a constant effective moment of inertia for the core,  $\mathfrak{I}_c = 5.8 \text{ MeV}^{-1}$ , with a justifying argument that the introduction of the core moment of inertia could have been avoided by a proper adjustment of the force parameters. However,  $5.8 \text{ MeV}^{-1}$  is more than 25 percent of the total moment of inertia, so that such a large adjustment may also modify other features of the spectrum. We emphasize that it is important to have large single-particle space in order to accommodate a sufficiently large number of active nucleons which define the “rotating body” microscopically. There should be a limit beyond which one cannot truncate the active space without changing the physical properties of the system, since the renormalization of the force parameters may no longer be able to compensate for all that is caused by the truncation of the number of active nucleons. Incidentally, the “trick” with the core moment of inertia is to shift the first band-crossing to a larger spin and this has often been used in the Cranked HFB calculations to get agreement with data. However, a quantum mechanical theory has to be able to describe the whole physical events solely in terms of the active nucleon’s degrees of freedom and there should be no room to introduce such a semiclassical quantity.

Finally, we comment on the last item (Interaction) of Table 2. The Projected Shell Model uses exclusively the  $Q \cdot Q$  + Monopole Pairing (MP) + Quadrupole Pairing (QP) Force model. There are several good reasons for this. The first two forces have been used since the early days of the microscopic theory of nuclear structure, so that we know their properties very well. The former ( $Q \cdot Q$ , responsible for the deformation) has been the essential ingredient of the SU(3) Model and the latter (MP, responsible for the pairing correlations) of the BCS theory. They lead to the Nilsson + BCS scheme which has been tested over many years. It is, therefore, assured that we obtain the correct shell filling for individual nuclei. Of course, such simple forces cannot describe everything that is taking place in the many-nucleon systems and thus have to be supplemented with other types of force whenever the necessity arises. We have included the Quadrupole Pairing (QP) force<sup>33</sup> which is a pairing type force acting between two like-nucleons coupled to spin 2, and may be considered to be a correction to the Monopole Pairing force. It is known that this force has an important effect on the rotational spectra.<sup>34,35</sup> Through intensive and

extensive studies, the presence of these three forces ( $QQ$ ,  $MP$ , and  $QP$ ) has been found to be very important, if not sufficient, to explain a large body of high-spin data. They simulate the essence of the most important correlations in nuclei, so that even the so-called realistic force has to contain at least these components implicitly in order for it to work successfully. In contrast, the MONSTER approach can deal with a general (realistic) force. On the one hand, only with such a formalism is it possible to investigate the effective interactions proposed in the literature or to make use of a more fundamental interaction such as Brueckner's  $G$ -matrix. Actually, it is not obvious whether or not a realistic interaction can also be applied successfully to nuclear structure problems other than the ground state (bulk) properties of the nucleus (e.g., the pairing correlations are too weak in the  $G$ -matrix). Above all, the usual realistic forces are not at all adjusted to the empirical shell structure and this might eventually cause a serious problem. Nevertheless, there is no doubt that this kind of approach is very useful in establishing the nuclear structure from the first principle using the basic nucleon-nucleon force. Especially, for the study of nuclei near the drip-lines in which the use of a schematic Hamiltonian hardly makes sense, this type of approach should be most useful. On the other hand, because of the generality of the force, the MONSTER approach has to rely upon a variational procedure (HFB or VAMPIR) to determine the mean field. This makes the treatment of heavy systems other than doubly-even nuclei untractable since then the mean field might no longer be axially symmetric while the MONSTER (and VAMPIR) cannot cope with the triaxial projection due to the large CPU time, especially in the case of heavy nuclei. One hopes that this problem will be resolved in the future owing to rapidly developing computer technology. On the other hand, the hardware requirement of the Projected Shell Model is minimal. The PSM code runs even on a PC<sup>a</sup> so that the analysis of data can be carried out at home.

### 3. Decoupled Motion and Rotational Alignment

#### 3.1. The case of the particle-rotor model

The physics of angular momentum projection seems to be rather abstract. Therefore, in order to translate the results into simple physical terms, it will be helpful if certain analogies to the semiclassical theory can be established. For this purpose, we will first review some facts known in the particle-rotor model.<sup>16</sup> In the following, the intrinsic (i.e., body-fixed) coordinate system will be referred to as the 1-, 2-, and 3-axis.

We consider a particle coupled to an axially symmetric rotor whose moment of inertia is  $\mathfrak{J}$ . The total Hamiltonian is thus given by

$$H = \frac{\mathbf{R}^2}{2\mathfrak{J}} + H_N = \frac{\mathbf{J}^2 - 2\mathbf{J} \cdot \mathbf{j} + \mathbf{j}^2}{2\mathfrak{J}} + H_N, \quad \mathbf{R} = \mathbf{J} - \mathbf{j} \quad (3.1)$$

<sup>a</sup>The execution time is 20 minutes on a 486DX4/100MHz DOS Machine compiled with the full optimization by the NDP Fortran (R) of MicroWay.

where  $\mathbf{J}$  is the (body fixed) angular momentum operator of the total system and  $H_N$  the intrinsic (Nilsson) Hamiltonian of the particle whose angular momentum operator is denoted by  $\mathbf{j}$ . Since the rotor is axially symmetric, the eigenvalue of the operator  $\mathbf{R}$  along the symmetry axis ( $R_3 = J_3 - j_3$ ) is zero. This means that the angular momentum of the body  $\mathbf{R}$  always points in the direction of the axis of rotation ( $\mathbf{R}^2 = R_1^2 + R_2^2$ ). The Hamiltonian (3.1) is diagonalized in the so-called strong-coupling basis

$$|\Psi_{iK}^{IM}\rangle = \sqrt{\frac{2I+1}{16\pi^2}} [D_{MK}^I(\Omega)|\Phi_{iK}\rangle + (-)^{I-K} D_{M-K}^I(\Omega)|\Phi_{i\bar{K}}\rangle] \quad (3.2)$$

with  $K > 0$  where  $|\Phi_{i\bar{K}}\rangle$  is the time reversal of the intrinsic (Nilsson) state  $|\Phi_{iK}\rangle$

$$H_N|\Phi_{iK}\rangle = E_{iK}|\Phi_{iK}\rangle, \quad j_3|\Phi_{iK}\rangle = K|\Phi_{iK}\rangle.$$

As is well known,  $D_{MK}^I(\Omega)$  is an eigenfunction of  $\mathbf{J}^2$  and  $J_3$  with respective eigenvalues  $I(I+1)$  and  $K$ . We are not interested in the whole diagonalization problem but only in the expectation value of the Hamiltonian (3.1) with respect to the state (3.2):

$$\langle \Psi_{iK}^{IM} | H | \Psi_{iK}^{IM} \rangle = \frac{1}{2\Im} [I(I+1) - (-)^{I-K}(2I+1)d_{iK} - 2K^2 + \langle \mathbf{j}^2 \rangle_{iK}] + E_{iK}, \quad (3.3)$$

where  $\langle \mathbf{j}^2 \rangle_{iK}$  is the expectation value of  $\mathbf{j}^2$  with respect to  $|\Phi_{iK}\rangle$ . We have defined here a quantity which is known as the decoupling factor

$$d_{iK} = \langle \Phi_{iK} | j_1 + \imath j_2 | \Phi_{i\bar{K}} \rangle. \quad (3.4)$$

The presence of the pairing correlations will not affect the formula (3.4), i.e., it is also valid in the Nilsson + BCS representation. It measures the degree of decoupling of the particle motion from the rotational motion of the body. We note that, in the particle-rotor model, the decoupling factor does not appear in the energy expectation value (3.3) if  $|K| \neq \frac{1}{2}$  (i.e., no spin alignment), since the matrix element (3.4) vanishes, nor will it occur if the particle (or quasiparticle) number is different from one. All this will be modified in the Projected Shell Model as we will see in the next section.

The decoupling factor can be evaluated by the expression

$$d_{iK} = \delta_{K\frac{1}{2}} \sum_j (-)^{j-K} \left( j + \frac{1}{2} \right) |W_{ji}^K|^2 \quad (3.5)$$

which is obtained by the explicit use of the Nilsson state  $|\Phi_{iK}\rangle = \sum_j |\psi_{jK}\rangle W_{ji}^K$  in (3.4) where  $|\psi_{jK}\rangle$  is the spherical single-particle wave function. The summation in (3.5) runs from  $j = \frac{1}{2}$  to  $N + \frac{1}{2}$  for a major shell  $N$  and contains alternating signs, so that a partial cancellation occurs in the sum especially when the deformation

is large (a strong  $j$ -admixture). In such a case, the particle strictly follows the rotational motion of the deformed potential, namely, it is coupled strongly to the deformed body (rotor). However, if the summation almost consists of a single term ( $W_{ji}^K \approx \delta_{ji}$ ), we obtain

$$d_{iK} \approx \delta_{K\frac{1}{2}} (-)^{i-K} \left( i + \frac{1}{2} \right). \quad (3.6)$$

This happens indeed for an intruder subshell  $i = N + \frac{1}{2}$ . Note that  $i + \frac{1}{2} = N + 1$  is the maximal magnitude of the decoupling factor (for a given major shell  $N$ ). Such a subshell appears far away from the other subshells of the same major shell in heavy nuclei due to strong spin-orbit force so that the admixture of the latter to the former wave function is indeed very weak. The Nilsson states of an intruder subshell are thus very close to the spherical ones and are almost independent of the deformation,  $|\Phi_{iK}\rangle \approx |\psi_{iK}\rangle$  (not only for  $K = \frac{1}{2}$ ). This means that a particle in an intruder subshell does not feel the deformed potential and its motion is decoupled from that of the rotor. This causes various prominent high-spin phenomena as we will see later.

The expression (3.3) represents the rotational energy of a “band” labeled by  $iK$  as a function of spin  $I$  ( $I \geq K$ ). If  $K \neq \frac{1}{2}$  (or  $K = \frac{1}{2}$  with a very small decoupling factor), its spin dependent part becomes (using  $I(I+1) = (I + \frac{1}{2})^2 - \frac{1}{4}$ )

$$E = \frac{\Lambda^2}{2\Im}, \quad (3.7)$$

where  $\Lambda \equiv I + \frac{1}{2}$  is the WKB form of the angular momentum  $I$ . The rotational frequency, which is defined by the slope of the rotational energy,

$$\omega = \frac{dE}{d\Lambda} = \frac{\Lambda}{\Im} \quad (3.8)$$

is positive definite, which means that the rotational energy increases monotonically with spin as in the classical case. What is more interesting is the  $K = \frac{1}{2}$  (i.e., well aligned) band in an intruder (i.e., well decoupled) subshell. Its rotational energy becomes

$$E_{\pm} = \frac{(\Lambda \pm \lambda)^2}{2\Im} \quad \text{with} \quad +(-) \text{ for } I - i = \text{odd (even)}, \quad (3.9)$$

where  $\lambda \equiv i + \frac{1}{2}$  and we used the expression (3.6) for the decoupling factor. Note that, in this case, the particle degree of freedom is contributing to the rotational energy explicitly through  $\lambda$ . The spectrum (3.9) may be divided into two branches according to  $I - i = \text{odd}$  (unfavored band  $E_+$ ) and even (favored band  $E_-$ ). This is the so-called signature splitting. The rotational frequency becomes

$$\omega_{\pm} = \frac{dE_{\pm}}{d\Lambda} = \frac{\Lambda \pm \lambda}{\Im}, \quad (3.10)$$

which shows quite different behavior for unfavored and favored bands. In the former case ( $\omega_+$ ), it is again positive definite and can be large even if the spin ( $\Lambda$ ) is small

due to the contribution from the particle ( $\lambda$ ). In the latter case ( $\omega_-$ ), it can be negative (i.e., the rotational energy decreases with spin) if the spin is small and becomes positive (i.e., the rotational energy increases with spin) after passing the critical point  $\Lambda = \lambda$  where the rotational frequency vanishes. This means that the system stops rotating at  $\Lambda = \lambda$  and that the spin of the system comes solely from that of the particle ( $I = i$ ) which is the amount of particle spin aligned to the axis of rotation. In other words, the amount of spin alignment is the value of spin  $I$  at which the rotational frequency of the favored band vanishes, i.e.,

$$\omega_- = \frac{dE_-}{d\Lambda} = 0. \quad (3.11)$$

Let us now give the geometrical interpretations to these results. To study the geometry of the vector addition  $\mathbf{R} = \mathbf{J} - \mathbf{j}$ , we consider the expectation value of the scalar product  $\mathbf{J} \cdot \mathbf{j}$  with respect to the state (3.2). Using (3.6), we find<sup>13</sup>

$$\langle \mathbf{J} \cdot \mathbf{j} \rangle = \begin{cases} K^2 & \text{for a band coupled to the body} \\ K^2 + \delta_{K\frac{1}{2}}(-)^{I-i}\Lambda\lambda & \text{for a well decoupled band} \end{cases}$$

which is the basic relation for our discussion. It shows that, in a band coupled strongly to the body or in a band with  $K > \frac{1}{2}$  (i.e., not aligned), the angular momentum of the particle points in the direction of the symmetry axis ( $\langle j_1 \rangle = \langle j_2 \rangle = 0$ ), namely, the particle spin is on average perpendicular to the axis of rotation and its length  $\lambda$  is effectively equal to  $K$ . On the other hand, in a decoupled band with  $K = \frac{1}{2}$  (i.e., aligned), the cosine of the angle between  $\mathbf{J}$  and  $\mathbf{j}$  is equal to  $(-)^{I-i}$  if we neglect a small term  $K^2 = \frac{1}{4}$ . In this case, since  $\mathbf{J} \cdot \mathbf{R} = \mathbf{J}^2 - \mathbf{J} \cdot \mathbf{j}$  and  $\mathbf{j} \cdot \mathbf{R} = \mathbf{J} \cdot \mathbf{j} - \mathbf{j}^2$ , we find

$$\langle \mathbf{J} \cdot \mathbf{R} \rangle = \Lambda^2 - (-)^{I-i}\Lambda\lambda = \begin{cases} \Lambda(\Lambda + \lambda) & \text{for a unfavored band} \\ \Lambda(\Lambda - \lambda) & \text{for a favored band} \end{cases}$$

and

$$\langle \mathbf{j} \cdot \mathbf{R} \rangle = (-)^{I-i}\Lambda\lambda - \lambda^2 = \begin{cases} -\lambda(\Lambda + \lambda) & \text{for a unfavored band} \\ +\lambda(\Lambda - \lambda) & \text{for a favored band} \end{cases}$$

which show the geometrical relations of  $\mathbf{J}$  and  $\mathbf{j}$  to the axis of rotation ( $\mathbf{R}$ ), respectively. In the case of a favored band, for example, both scalar products are negative (positive) if  $\Lambda < \lambda$  ( $\Lambda > \lambda$ ). This means that, if the spin of the system  $I$  is smaller (larger) than the spin  $i$  of the aligned particle,  $\mathbf{J}$  and  $\mathbf{j}$  are antiparallel (parallel) to the axis of rotation  $\mathbf{R}$ , so that the sense of rotation of the body is negative (positive) with respect to the orientation of  $\mathbf{J}$ . This is the geometrical significance of the sign of the angular frequency. In all other cases, the sense of rotation will be positive since the sign of the scalar product  $\langle \mathbf{J} \cdot \mathbf{R} \rangle$  becomes positive. Table 3

summarizes all these results. We can understand all this more intuitively by looking at Fig. 1 which shows the four cases tabulated above. Note that the sign of  $\omega$  represents the sense of the rotation.

Table 3. The vector addition  $\mathbf{J} = \mathbf{j} + \mathbf{R}$  in the particle–rotor model.

Particle State (Band)	$\mathbf{j}$ against $\mathbf{R}$	Sense of the Rotation	Fig. 1
Coupled to the Rotor	orthogonal	positive	a
Decoupled, unfavored	antiparallel	positive	b
"", favored ( $I < i$ )	antiparallel	negative	c
"", favored ( $I > i$ )	parallel	positive	d

In this section, we recapitulated some known results of the particle–rotor model and gave them visual interpretations. In the next section, we will present corresponding examples from the angular momentum projection calculations and show that the theory contains more features. It will be seen that concepts such as the decoupled particle motion and the rotational alignment of the particle also play an essential role in the interpretation of the numerical results. These concepts are almost equivalent to each other in the particle–rotor model. This will no longer be the case in the present theory. In the following, we will use the term “decoupled” for a (multi- $qp$ ) band if its intrinsic wave function is close to a spherical one, which is a measure of the  $j$ -admixture in the Nilsson wave function, and “aligned” for a decoupled (multi- $qp$ ) band if its  $K$ -value is small, which is a measure of the orientation of the particle spin with respect to the axis of rotation. A clear distinction between these two concepts is necessary because the rotational alignment will be present appreciably beyond  $K = \frac{1}{2}$  although the amount of the alignment decreases if the  $K$ -value increases. It is an effect originating from the quantum mechanical feature of the theory, which plays an essential role in understanding various high-spin phenomena, as we will see in later sections.

### 3.2. The case of the Projected Shell Model

The Nilsson + BCS (or HFB) vacuum describes the “rotating body” when projected. We refer to it as the intrinsic state of the ground band ( $g$ -band) and to the multi- $qp$  states built on it as the intrinsic states of excited bands. It should be noted that, in a theory based on angular momentum projection, we cannot simply separate the angular momentum of the rotating body and that of the quasiparticles because there are no such (quantum mechanical) operators. To interpret the numerical results, it is quite important to look for analogies with the semiclassical theory as much as possible. The discussions given in the previous section will be of great help here. For example, the amount of spin alignment (or the decoupling factor) would be difficult to define in terms of quantum mechanics. However, we can find it simply by searching for the spin at which the rotational energy reaches a minimum

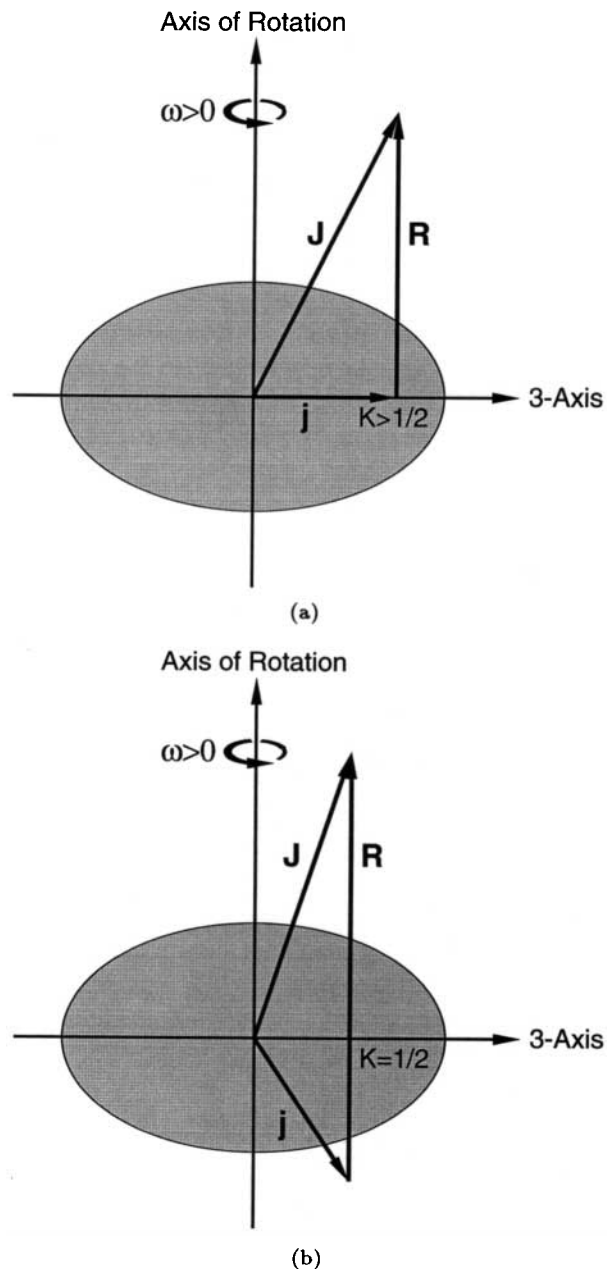


Fig. 1. Geometry of the vector addition  $J = j + R$  in the particle-rotor model. (a) The particle spin is orthogonal to the axis of rotation ( $j \cdot R = 0$ ) and the sense of rotation is positive ( $J \cdot R > 0$ ). (b) The particle spin is antiparallel to the axis of rotation ( $j \cdot R < 0$ ) and the sense of rotation is positive ( $J \cdot R > 0$ ). (c) The particle spin is antiparallel to the axis of rotation ( $j \cdot R < 0$ ) and the sense of rotation is negative ( $J \cdot R < 0$ ). (d) The particle spin is parallel to the axis of rotation ( $j \cdot R > 0$ ) and the sense of rotation is positive ( $J \cdot R > 0$ ).

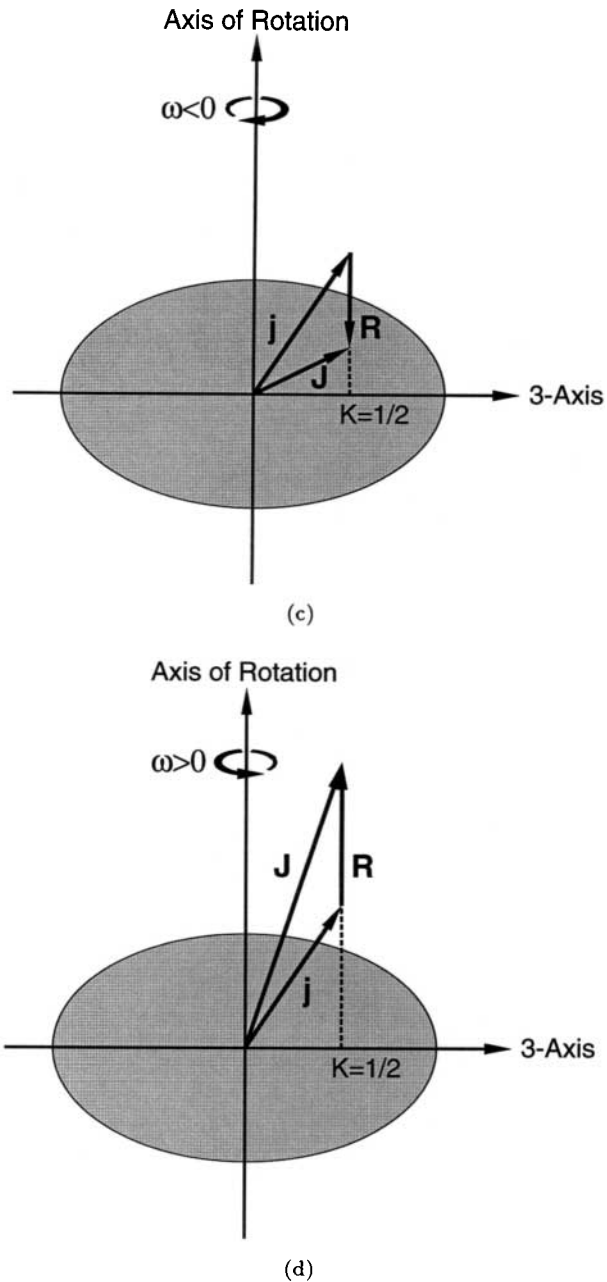


Fig. 1. (Continued)

(vanishing rotational frequency) according to the relation (3.11). The usefulness of a phenomenological theory lies not only in its simplicity but also in the richness of the concepts it provides.

In the present case, the rotational energy of a band (or simply “band energy”) is defined by the expectation value of the Hamiltonian with respect to a projected quasiparticle state  $\hat{P}_{MK}^I |\Phi_\kappa\rangle$  (we omit writing  $I$  in  $H_{\kappa\kappa'}^I$  and  $N_{\kappa\kappa'}^I$  for simplicity):

$$E_\kappa(I) = \frac{H_{\kappa\kappa}}{N_{\kappa\kappa}} = \frac{\langle \Phi_\kappa | \hat{H} \hat{P}_{KK}^I | \Phi_\kappa \rangle}{\langle \Phi_\kappa | \hat{P}_{KK}^I | \Phi_\kappa \rangle}. \quad (3.12)$$

In particular, if  $|\Phi_\kappa\rangle$  is a 1-*qp* state, it corresponds to (3.3) of the particle-rotor model. In the following, we examine some 1-*qp* bands numerically. Multi-quasiparticle bands will be studied in the next section.

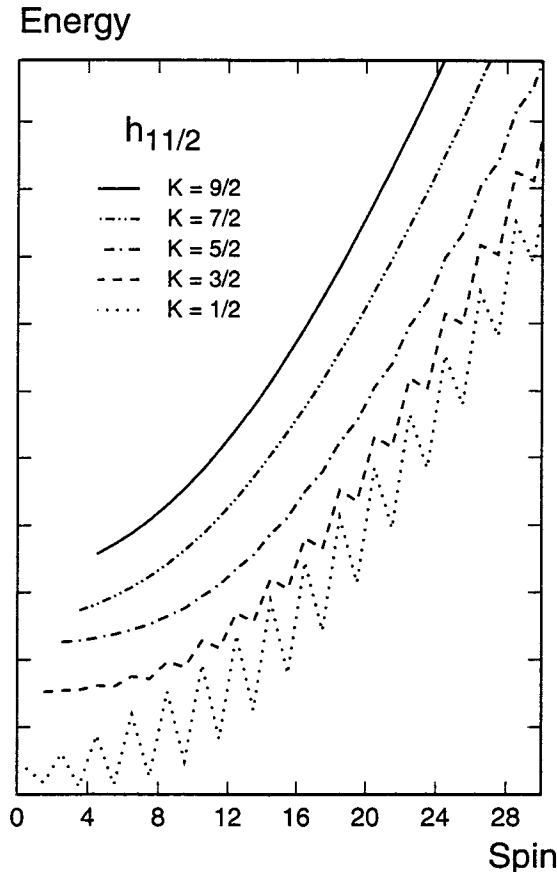


Fig. 2. Decoupled 1-*qp* bands with  $|K| = \frac{1}{2}$  to  $\frac{9}{2}$  in the intruder subshell  $h_{11/2}$ . Stronger signature splitting is seen in the bands with smaller  $K$ -values. The sequence  $I = \frac{3}{2}, \frac{7}{2}, \dots (\frac{1}{2}, \frac{5}{2}, \dots)$  belongs to the favored (unfavored) band.

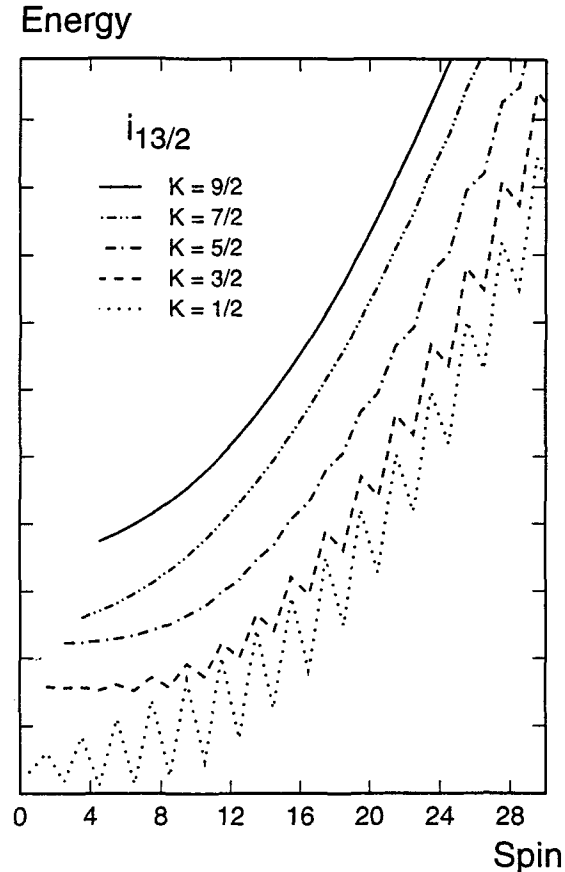


Fig. 3. Decoupled 1-*qp* bands with  $|K| = \frac{1}{2}$  to  $\frac{9}{2}$  in the intruder subshell  $i_{13/2}$ . Stronger signature splitting is seen in the bands with smaller  $K$ -values. The sequence  $I = \frac{1}{2}, \frac{5}{2}, \dots (\frac{3}{2}, \frac{7}{2}, \dots)$  belongs to the favored (unfavored) band.

Figure 2 (3) shows the band energies of decoupled 1-*qp* bands with various  $K$ -values which originate from the intruder subshell of  $N = 5$ ,  $h_{11/2}$  ( $N = 6, i_{13/2}$ ). Their mutual positions are shifted up or down so as to avoid crossings between diagrams of different bands (band-crossing will be discussed later). In the first place, we observe that signature dependence is also present beyond  $|K| = \frac{1}{2}$  and that such bands split clearly into favored and unfavored ones. Note that the higher the  $K$ -values the weaker the signature dependence. This means that the rotational alignment also occurs in the bands having  $|K| > \frac{1}{2}$  although it diminishes rapidly when the  $K$ -value increases (i.e., when the particle spin becomes less aligned to the axis of rotation). We observe also that the phases of the signature dependence in Fig. 2 ( $N = 5, h_{11/2}$  intruder subshell) and Fig. 3 ( $N = 6, i_{13/2}$  intruder subshell) are mutually opposite. In fact, as we can verify, this is in agreement with the

“classical” signature rule

$$I - i = \pm \begin{cases} \text{even favored band} \\ \text{odd unfavored band} \end{cases} \quad (3.13)$$

discussed in Sec. 3.1 since  $i$  is equal to  $\frac{11}{2}$  in the former and to  $\frac{13}{2}$  in the latter.

Let us study how all this comes about in the present (quantum mechanical) theory.<sup>12</sup> The diagonal matrix element appearing in (3.12) is equal to (with  $\hat{O} = 1$  or  $\hat{H}$ )

$$\begin{aligned} O &= \left( I + \frac{1}{2} \right) \int_0^\pi d\beta \sin \beta d_{KK}^I(\beta) \langle \Phi_\kappa | \hat{O} e^{-i\beta j_y} | \Phi_\kappa \rangle = \left( I + \frac{1}{2} \right) \int_0^{\pi/2} d\beta \sin \beta \\ &\quad \{ d_{KK}^I(\beta) \langle \Phi_\kappa | \hat{O} e^{-i\beta j_y} | \Phi_\kappa \rangle + (-)^{I-K} d_{K-K}^I(\beta) \langle \Phi_\kappa | \hat{O} e^{-i\beta j_y} | \Phi_{\bar{\kappa}} \rangle \} \end{aligned} \quad (3.14)$$

where  $|\Phi_{\bar{\kappa}}\rangle$  is the time reversal of  $|\Phi_\kappa\rangle$ , namely,

$$|\Phi_{\bar{\kappa}}\rangle \equiv \hat{T}|\Phi_\kappa\rangle = e^{-i\pi j_y} |\Phi_\kappa\rangle. \quad (3.15)$$

The integral (3.14) is thus written as (cf. (2.24) for the definition of  $[\beta]$ )

$$\begin{aligned} O &= O_1 + (-)^{I-K} O_2, \\ O_1 &\equiv \left( I + \frac{1}{2} \right) \int_0^{\pi/2} d\beta \sin \beta d_{KK}^I(\beta) \langle \Phi_\kappa | \hat{O}[\beta] | \Phi_\kappa \rangle \langle e^{-i\beta j_y} \rangle, \\ O_2 &\equiv \left( I + \frac{1}{2} \right) \int_0^{\pi/2} d\beta \sin \beta d_{K-K}^I(\beta) \langle \Phi_\kappa | \hat{O}[\beta] | \Phi_{\bar{\kappa}} \rangle \langle e^{-i\beta j_y} \rangle. \end{aligned} \quad (3.16)$$

Therefore, the band energy (3.12) can be evaluated by letting  $\hat{O} = 1$  and  $\hat{H}$ , namely,

$$\begin{aligned} E &= \frac{H}{N} = \frac{H_1 + (-)^{I-K} H_2}{N_1 + (-)^{I-K} N_2} = E_1 - (-)^{I-K} E_2, \\ E_1 &\equiv \frac{H_1 N_1 - H_2 N_2}{N_1^2 - N_2^2}, \quad E_2 \equiv \frac{H_1 N_2 - H_2 N_1}{N_1^2 - N_2^2}. \end{aligned} \quad (3.17)$$

Now, since a decoupled state has a weak  $j$ -admixture, it is close to a spherical one. A 1- $qp$  state, for example, may be written approximately as (with  $j = i$  and  $m = K$ )

$$|\Phi_\kappa\rangle = a_{iK}^\dagger |0\rangle, \quad |\Phi_{\bar{\kappa}}\rangle = \hat{T}a_{iK}^\dagger |0\rangle = (-)^{i-K} a_{i-K}^\dagger |0\rangle.$$

The matrix element  $O_2$  (i.e.,  $H_2$  as well as  $N_2$ ) contains the phase  $(-)^{i-K}$ , which together with  $(-)^{I-K}$  gives  $(-)^{I-i}$ . We may therefore write  $(-)^{I-K} O_2 = (-)^{I-i} \bar{O}_2$  so that

$$E = E_1 - (-)^{I-i} \bar{E}_2, \quad \bar{E}_2 \equiv \frac{H_1 \bar{N}_2 - \bar{H}_2 N_1}{N_1^2 - N_2^2}. \quad (3.18)$$

$E_1$  and  $\bar{E}_2$  are smooth functions of spin  $I$ . Thus, the signature dependence of  $E$  arises from the phase  $(-)^{I-i}$  if the amplitude  $|\bar{E}_2|$  is not too small. It turns out that  $\bar{E}_2$  is a positive quantity for 1- $qp$  states (which is not necessarily the case for multi- $qp$  states as we will see in the next section) and this leads to the signature rule (3.13).

We note that the magnitude of  $O_2$  in (2.16) is a decreasing function of  $K(>0)$ . The reason is as follows.<sup>12</sup> On the one hand, the overlap  $\langle e^{-i\beta J_\nu} \rangle$  is strongly peaked at  $\beta = 0$ ; cf. (2.26) of Sec. 2.2. On the other hand, in the limit of a small  $\beta$ , the leading term of  $d_{K-K}^I(\beta)\langle a_{iK}\hat{O}[\beta]a_{i-K}^\dagger \rangle$  in  $O_2$  is proportional to  $\beta^{4K}$  while that of  $d_{KK}^I(\beta)\langle a_{iK}\hat{O}[\beta]a_{iK}^\dagger \rangle$  in  $O_1$  is unity. This means that  $|\bar{E}_2|$  is a decreasing function of  $K$ . This is the reason why the signature dependence is weaker for a less aligned state. See Appendix B for an alternative approach to the signature problem.

### 3.3. Generalized signature rule

It is straightforward to extend the above argument to the case of a decoupled multi- $qp$  state ( $i \equiv i_1 + i_2 + \dots$  and  $K \equiv K_1 + K_2 + \dots$ )

$$|\Phi_\kappa\rangle = a_{i_1 K_1}^\dagger a_{i_2 K_2}^\dagger \cdots |0\rangle, \quad |\Phi_{\bar{\kappa}}\rangle = \hat{T}|\Phi_\kappa\rangle = (-)^{i-K} a_{i_1 - K_1}^\dagger a_{i_2 - K_2}^\dagger \cdots |0\rangle.$$

The band energy again takes the form (3.18) with  $i = i_1 + i_2 + \dots$ . One might thus expect the signature rule of the form (3.13) to hold again. But, generally, this is not necessarily the case. Depending on the configuration, it may happen that the quantity  $\bar{E}_2$  of (3.18) becomes negative or even changes its sign dynamically at certain value(s) of  $I$ . If  $\bar{E}_2$  is negative, the favored and unfavored sequence will be interchanged. If  $\bar{E}_2$  changes its sign, the band energy will show spontaneous signature inversion (or “self-inversion”) in which case  $\bar{E}_2$  becomes positive definite only asymptotically at large  $I$ , as we will see below. Representing the sign of  $\bar{E}_2$  by  $(-)^{\sigma}$ , where the value of  $\sigma$  is either 0 or 1 and is in general spin dependent, we obtain a generalized signature rule

$$I - i_1 - i_2 - \cdots + \sigma = \pm \begin{cases} \text{even} & \text{favored band} \\ \text{odd} & \text{unfavored band} \end{cases} \quad (3.19)$$

which is the extension of (3.13). We will give some numerical examples below.

Let us first consider a doubly-odd nucleus. The quasiparticle state in this case is

$$|\Phi_\kappa\rangle = a_\nu^\dagger a_\pi^\dagger |0\rangle \quad (3.20)$$

according to (2.53). As for the Nilsson states  $\nu$  ( $\pi$ ), we consider two cases. In the first case, we choose those states which belong to the neutron ( $\nu$ ) and proton ( $\pi$ ) intruder subshells  $\nu i_{13/2}$  and  $\pi h_{11/2}$ . In the second case, we take a set of states from the subshells  $\nu i_{13/2}$  and  $\pi h_{9/2}$ . The latter is the spin-orbit partner of the proton intruder  $\pi h_{11/2}$ . We have selected this case because it is known that the

spin-orbit partner of an intruder is also relatively well decoupled. In both cases, we pick up well aligned states (i.e., small  $|K|$ -values), namely, states with  $K_{\nu(\pi)} = \pm \frac{1}{2}$  and  $\pm \frac{3}{2}$ . In each case, there are eight possible bands ( $4^2/2 = 8$ ; not sixteen bands because, as mentioned before,  $|\Phi_\kappa\rangle$  and its time reversal  $|\Phi_\kappa\rangle$  generate the same projected state). Figures 4 and 5 show eight band energies corresponding to the above-mentioned two cases, respectively. Again, the diagrams have been shifted up or down in order to avoid mutual overlap.

In the first place, we note that the overall zigzag phases in Figs. 4 and 5 are opposite to each other. This is due to the difference in the proton subshells ( $h_{11/2}$  and  $h_{9/2}$ ). In both figures, the bands with  $K_\pm = |K_\nu| \pm |K_\pi|$  are plotted pair-wise. We see clearly that the signature dependence of the  $K_+$  ( $K_-$ ) bands is of the normal

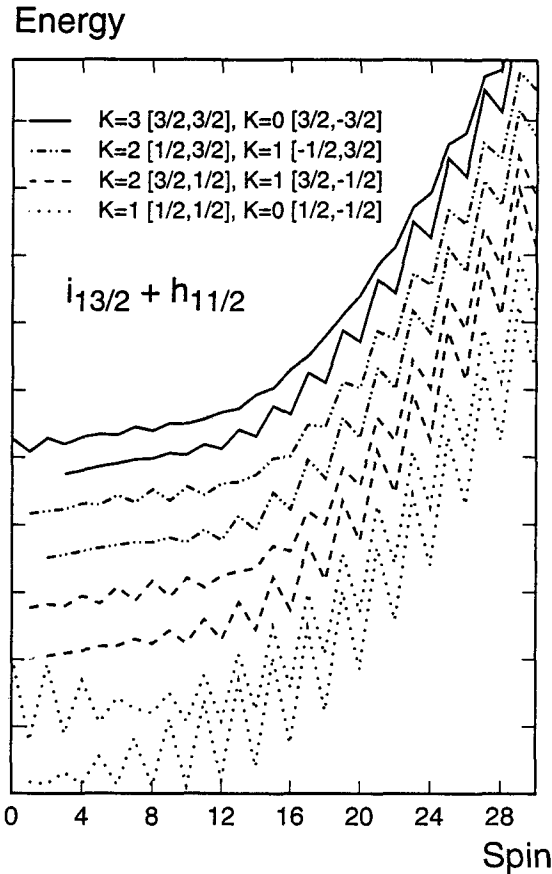


Fig. 4. Decoupled  $1\nu \otimes 1\pi$  bands with  $|K| = 0$  to 3 in the subshell  $\nu i_{13/2} \otimes \pi h_{11/2}$ . Eight bands are shown for  $K[K_\nu, K_\pi] = 0[\frac{1}{2}, -\frac{1}{2}], 1[\frac{1}{2}, \frac{1}{2}], 1[\frac{1}{2}, -\frac{3}{2}], 2[\frac{1}{2}, \frac{3}{2}], 1[-\frac{3}{2}, \frac{1}{2}], 2[\frac{3}{2}, \frac{1}{2}], 0[-\frac{3}{2}, \frac{3}{2}],$  and  $3[\frac{3}{2}, \frac{3}{2}]$ . It is seen that the signature dependence of the bands with  $K = |K_\nu| - |K_\pi|$  ( $|K_\nu| + |K_\pi|$ ) is of the selfinversion (normal) type. Note that the overall zigzag phase is opposite to that of Fig. 5. This is due to different proton subshell, ( $\pi h_{11/2}$  vs.  $\pi h_{9/2}$ ); cf. the signature rule (3.21).

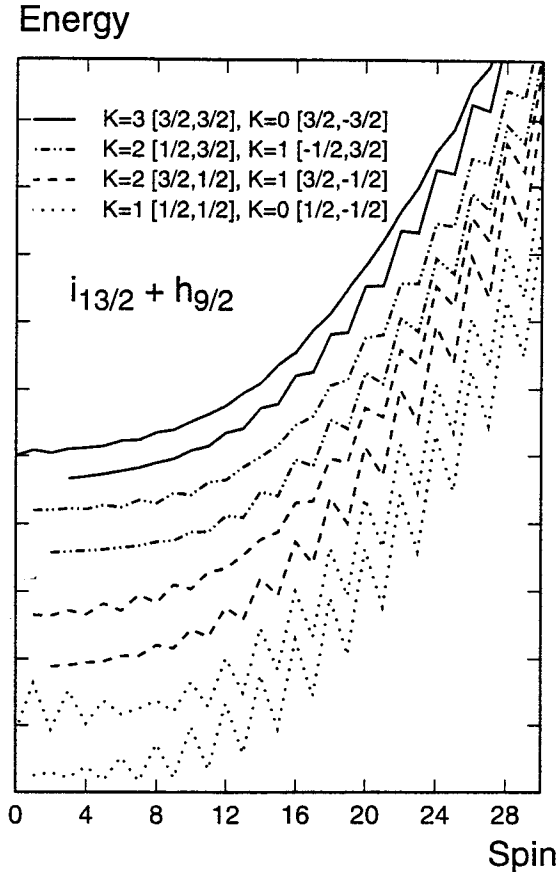


Fig. 5. Decoupled  $1\nu \otimes 1\pi$  bands with  $|K| = 0$  to 3 in the subshell  $\nu i_{13/2} \otimes \pi h_{9/2}$ . Eight bands are shown for  $K[K_\nu, K_\pi] = 0[\frac{1}{2}, -\frac{1}{2}], 1[\frac{1}{2}, \frac{1}{2}], 1[\frac{1}{2}, -\frac{3}{2}], 2[\frac{1}{2}, \frac{3}{2}], 1[-\frac{3}{2}, \frac{1}{2}], 2[\frac{3}{2}, \frac{1}{2}], 0[-\frac{3}{2}, \frac{3}{2}],$  and  $3[\frac{3}{2}, \frac{3}{2}]$ . It is seen that the signature dependence of the bands with  $K = |K_\nu| - |K_\pi| (|K_\nu| + |K_\pi|)$  is of the selfinversion (normal) type. Note that the overall zigzag phase is opposite to that of Fig. 4. This is due to different proton subshell, ( $\pi h_{9/2}$  vs.  $\pi h_{11/2}$ ); cf. the signature rule (3.21).

(selfinversion) type. In particular, we can confirm that the normal types follow the signature rule

$$I - i_\nu - i_\pi = \pm \begin{cases} \text{even} & \text{favored band} \\ \text{odd} & \text{unfavored band} \end{cases} \quad (3.21)$$

which corresponds to  $\sigma = 0$  of (3.19). In the selfinversion cases, however, we have  $\sigma = 0$  asymptotically only in the high spin region while  $\sigma = 1$  applies in the low spin region. Namely,  $\sigma$  changes from 1 to 0 dynamically as the spin increases. We will refer to the signature rule as “normal” if  $\sigma = 0$  and as “anomalous” if  $\sigma = 1$ . From the numerical results, we find that the signature dependence is of the normal (selfinversion) type if the signs of  $K_\nu$  and  $K_\pi$  are the same (opposite).

The signature rule (3.21) also applies to the decoupled like-nucleon 2-*qp* states if two quasiparticles occupy different subshells. However, if they are in the same subshell, the result becomes quite different. Let us take the like-nucleon 2-*qp* states

$$|\Phi_\kappa\rangle = a_{\nu_1}^\dagger a_{\nu_2}^\dagger |0\rangle \quad (3.22)$$

and consider various configurations in the intruder subshell  $\pi h_{11/2}^2$  and  $\nu i_{13/2}^2$ . The results of these two cases are shown in Figs. 6 and 7, respectively. Both cases are described by the signature rule (3.19) with  $\sigma = 1$  (anomalous signature dependence), namely,  $\bar{E}_2$  is negative definite. It means that the signature rule becomes

$$I = \begin{cases} \text{even} & \text{favored band} \\ \text{odd} & \text{unfavored band} \end{cases} \quad (3.23)$$

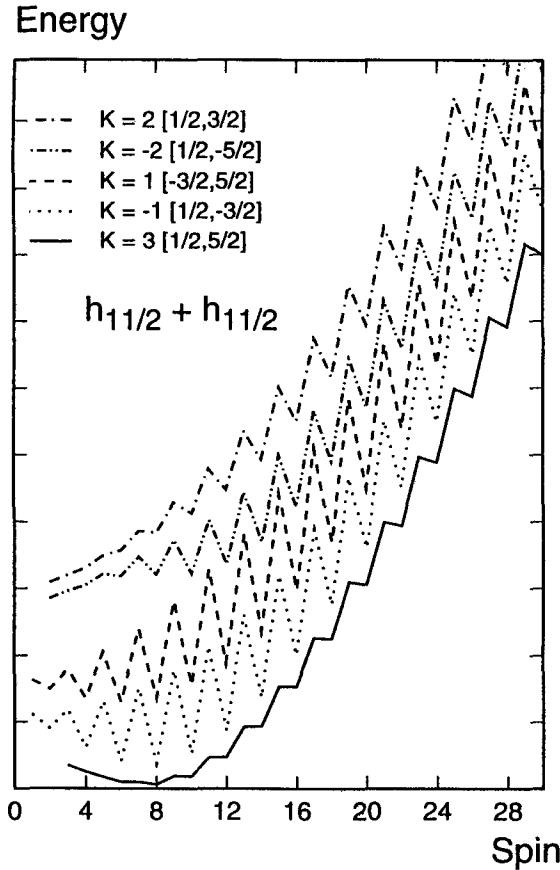


Fig. 6. Decoupled like-nucleon 2-*qp* bands with  $|K| = 1$  to 3 in the subshell  $(h_{11/2})^2$ . Five bands are shown for  $K[K_1, K_2] = 1[\frac{1}{2}, -\frac{3}{2}], 1[-\frac{3}{2}, \frac{5}{2}], 2[\frac{1}{2}, -\frac{5}{2}], 2[\frac{1}{2}, \frac{3}{2}], \text{ and } 3[\frac{1}{2}, \frac{5}{2}]$ . Stronger signature splitting is seen in the bands with smaller  $|K|$ -values. The sequence  $I = 0, 2, \dots (1, 3, \dots)$  belongs to the favored (unfavored) band.

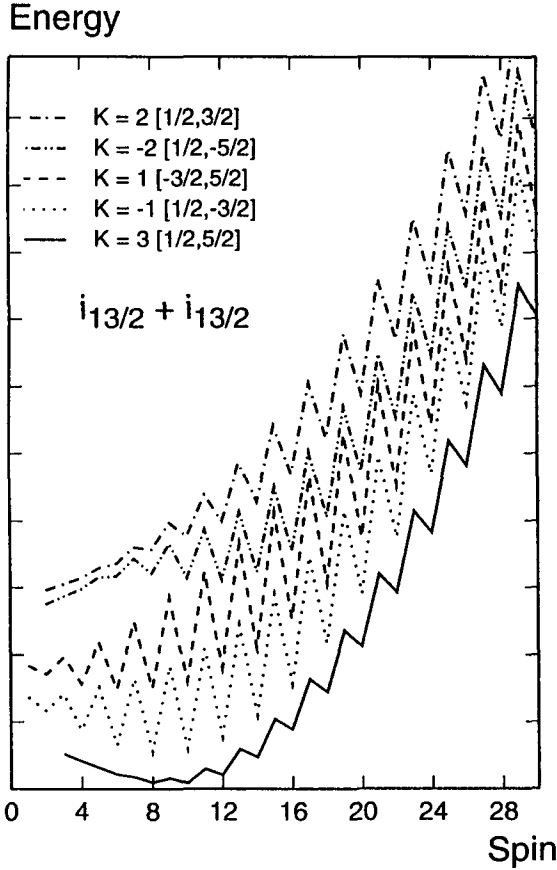


Fig. 7. Decoupled like-nucleon 2-*qp* bands with  $|K| = 1$  to 3 in the subshell  $(i_{13/2})^2$ . Five bands are shown for  $K[K_1, K_2] = 1[\frac{1}{2}, -\frac{3}{2}], 1[-\frac{3}{2}, \frac{5}{2}], 2[\frac{1}{2}, -\frac{5}{2}], 2[\frac{1}{2}, \frac{3}{2}],$  and  $3[\frac{1}{2}, \frac{5}{2}]$ . Stronger signature splitting is seen in the bands with smaller  $|K|$ -values. The sequence  $I = 0, 2, \dots (1, 3, \dots)$  belongs to the favored (unfavored) band.

for the like-nucleon 2-*qp* states filling the same intruder subshell ( $i_1 = i_2 = \text{odd}/2$ ) with  $K \neq 0$ . A special consideration is in order in the case of  $K = 0$ , namely,  $a_\nu^\dagger a_{\bar{\nu}}^\dagger |0\rangle$ . Actually, we can discuss this case in a more general context. We will refer to a state  $|\Phi_\kappa\rangle$  as “selfconjugate” if it has the property  $|\Phi_\kappa\rangle \equiv \hat{T}|\Phi_\kappa\rangle = |\Phi_\kappa\rangle$ . It belongs necessarily to  $K = 0$  if the system is axially symmetric. Such a state carries no (intrinsic) angular momentum as we will see below. Simple examples of selfconjugate states are the quasiparticle vacuum state  $|0\rangle$  and a quasiparticle pair (*qp*-pair) state  $a_\nu^\dagger a_{\bar{\nu}}^\dagger |0\rangle$ . The latter is in fact the state in question.

Let us first note that, for an arbitrary state  $|\Phi_\kappa\rangle$ , the following identity holds:

$$\hat{P}_{MK}^I |\Phi_\kappa\rangle = \hat{P}_{MK}^I \hat{T}^\dagger \hat{T} |\Phi_\kappa\rangle = (-)^{I-K} \hat{P}_{M-K}^I |\Phi_\kappa\rangle, \quad (3.24)$$

i.e., a state  $|\Phi_\kappa\rangle$  and its time reversal  $|\bar{\Phi}_\kappa\rangle$  generate the same projected state. It follows from (3.24) that projected selfconjugate states vanish for  $I = \text{odd}$  and  $K = 0$ :

$$\hat{P}_{M0}^I |\Phi_\kappa\rangle = 0 \quad \text{if} \quad |\Phi_\kappa\rangle = |\bar{\Phi}_\kappa\rangle \quad \text{and} \quad I = \text{odd}. \quad (3.25)$$

For  $I = \text{even}$ , the corresponding band energy reduces to the expression

$$E = \frac{H_1}{N_1} \quad (I = 0, 2, 4, \dots), \quad (3.26)$$

which is a monotonically increasing function of spin and shows no signature dependence. This means that a selfconjugate state does not carry the angular momentum to cause alignment. Therefore, we may regard the  $qp$ -pair in question,  $a_\nu^\dagger a_\nu^\dagger$ , as the counterpart of a  $qp$ -pair coupled to the angular momentum 0 of the spherical system. We note that the results obtained here are also valid in the case of triaxial systems so long as the time reversal invariance of the intrinsic system is preserved.

As we saw above, the signature dependence is due not only to the phase  $(-)^{I-i}$  but also to the sign of  $\bar{E}_2$  in (3.18), which contains the Hamiltonian explicitly. It therefore seems that the signature rule depends on the Hamiltonian in the present theory while this is not the case in the particle-rotor model. This apparent difference poses an interesting question which touches one of the basic features of the present theory and is therefore investigated in Appendix B. We will show that the signature rule indeed arises from the kinematics of the rotational motion alone and does not depend on details of the Hamiltonian in the present theory either. Strictly speaking, however, it still remains an “empirical rule” deduced numerically since the value of  $\sigma$  in (3.19) has not been derived with a mathematical rigor. This is an open problem at present. Nevertheless, several important physical aspects of the decoupled particle motion are clarified there.

### 3.4. Two-quasiparticle high- $K$ bands

There are cases where the simple semiclassical interpretations discussed above do not apply at all. Interesting examples are the like-nucleon 2- $qp$  high- $K$  bands in which the quasiparticles fill the same intruder subshell (see the  $|K| = 3$  bands in Figs. 6 and 7). A number of 2- $qp$  bands having  $|K| > 2$  in the intruder subshell configurations  $i_{13/2}^2$  are presented in Fig. 8. Note that these bands are well decoupled but less aligned.

The figure clearly shows that the rotational energies of the odd- $K$  bands behave quite differently from those of the even- $K$  bands. Namely, they decrease in the low spin region and turn to increase at a certain spin. The odd- $K$  bands in question can thus dive into the yrast region as the spin increases, which makes these bands particularly interesting. This does not occur if two quasiparticles are filling different subshells. The most striking feature is that the rotational energy decreases for the even as well as odd values of spin and, accordingly, shows no signature splitting (a smooth spin dependence). Thus, this remarkable behavior is not due to

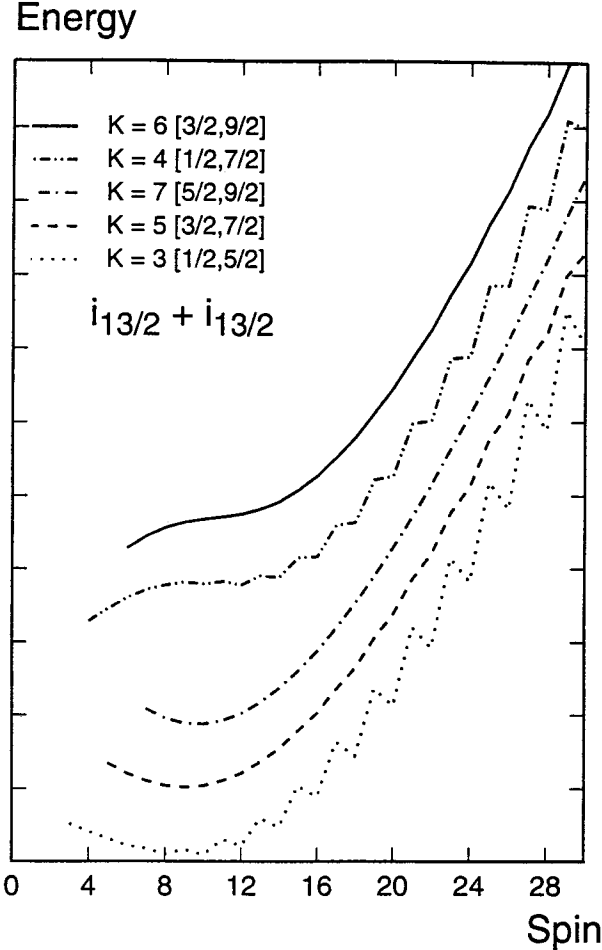


Fig. 8. Decoupled like-nucleon 2-*qp* bands with  $|K| > 2$  in the subshell  $(i_{13/2})^2$ . Rotational energies of the odd-*K* bands  $K = 3[\frac{1}{2}, \frac{5}{2}]$ ,  $5[\frac{3}{2}, \frac{7}{2}]$ , and  $7[\frac{5}{2}, \frac{9}{2}]$  behave quite differently from those of the even-*K* bands  $K = 4[\frac{1}{2}, \frac{7}{2}]$  and  $6[\frac{3}{2}, \frac{9}{2}]$  in the low-spin region. Note, however, that both types of bands obey the signature rule (3.23) in the high-spin region if the *K*-value is not too large ( $K = 3$  and  $4$ ).

the spin alignment mechanism and we can find no simple physical explanation in semiclassical terms.

To understand this unexpected feature, we will investigate a like-nucleon 2-*qp* state of  $K = K_1 + K_2 > 2$  in the intruder subshells  $j_1$  and  $j_2$  by reformulating the theory, see Appendix B for details. Since a well-decoupled 2-*qp* state can be decomposed into a sum of the irreducible representations  $\hat{A}_{JK}^\dagger \equiv (a_{j_1}^\dagger \otimes a_{j_2}^\dagger)_{JK}$  as

$$a_{j_1 K_1}^\dagger a_{j_2 K_2}^\dagger = \sum_J (j_1 K_1, j_2 K_2 | JK) \hat{A}_{JK}^\dagger, \quad (3.27)$$

we can rewrite the projected matrix element of  $\hat{O}$  ( $= 1$  or  $\hat{H}$ ) in the form

$$\begin{aligned} & \langle a_{j_2 K_2} a_{j_1 K_1} \hat{O} \hat{P}_{KK}^I a_{j_1 K_1}^\dagger a_{j_2 K_2}^\dagger \rangle \\ &= \sum_J (j_1 K_1, j_2 K_2 | JK) (j_1 K'_1, j_2 K'_2 | JK) \\ &\quad \times \sum_L (JK, L0 | IK)^2 \langle a_{j_2 K_2} a_{j_1 K_1} \hat{O} a_{j_1 K'_1}^\dagger a_{j_2 K'_2}^\dagger \hat{P}_{00}^L \rangle \end{aligned} \quad (3.28)$$

with the help of (B.1) of Appendix B, where  $L$  is summed only over even integers since  $\hat{P}_{M0}^L |0\rangle = 0$  for  $L = \text{odd}$ . Also, the selection rule  $J = \text{even}$  holds if two quasiparticles fill the same subshell ( $j_1 = j_2$ ) in which case the lower limit of  $J$  is not  $|K|$  but  $|K| + 1$  for an odd- $K$  band. It is a condition due to the symmetry with respect to the exchange of identical particles (like-nucleons in the same subshell) which arises in conjunction with the symmetry property of the Clebsch-Gordan coefficient  $(j_1 K_1, j_2 K_2 | JK)$ .

In the case of  $\hat{O} = \hat{H}$ , we rewrite the matrix element using

$$\hat{H} a_{j_1 K'_1}^\dagger a_{j_2 K'_2}^\dagger = [\hat{H}, a_{j_1 K'_1}^\dagger a_{j_2 K'_2}^\dagger] + a_{j_1 K'_1}^\dagger a_{j_2 K'_2}^\dagger \hat{H}. \quad (3.29)$$

We note that two quasiparticles (1 and 2) do not interact with each other due to the condition  $K'_1 + K'_2 = K > 2$  since our interaction contains at most the quadrupole type forces ( $|\Delta K| \leq 2$ ). However, each of them can interact with the particles that constitute the rotating body. We will neglect the (dynamical) disturbance on the single-particle motion exerted by the rotating body and make the approximation

$$[\hat{H}, a_{j_1 K'_1}^\dagger a_{j_2 K'_2}^\dagger] \approx [\hat{H}_{HFB}, a_{j_1 K'_1}^\dagger a_{j_2 K'_2}^\dagger] = (E_{j_1 K'_1} + E_{j_2 K'_2}) a_{j_1 K'_1}^\dagger a_{j_2 K'_2}^\dagger, \quad (3.30)$$

which is the same assumption as made in Appendix B. The band energy becomes

$$\frac{H_{KK}}{N_{KK}} = E_{j_1 K_1} + E_{j_2 K_2} + \sum_L E_L p_L^I(K_1, K_2) \quad (3.31)$$

where the bandhead energy  $E_{j_1 K_1} + E_{j_2 K_2}$  is spin independent. The quantity

$$p_L^I(K_1, K_2) = \frac{\sum_J [1 + (-)^J \delta_{j_1 j_2}] (j_1 K_1, j_2 K_2 | JK)^2 (JK, L0 | IK)^2 N_{00}^L}{\sum_{JL} [1 + (-)^J \delta_{j_1 j_2}] (j_1 K_1, j_2 K_2 | JK)^2 (JK, L0 | IK)^2 N_{00}^L} \quad (3.32)$$

is the probability of finding various 2- $qp$  angular momenta  $J$  and a possible  $L$  of the rotor being coupled to spin  $I$ . The factor  $[1 + (-)^J \delta_{j_1 j_2}]$  is due to the exchange symmetry mentioned above. In (3.31) and (3.32),  $E_L = \langle \hat{H} \hat{P}_{00}^L \rangle / \langle \hat{P}_{00}^L \rangle$  and  $N_{00}^L = \langle \hat{P}_{00}^L \rangle$  are the rotational energy of the rotor and the probability of finding the rotor angular momentum  $L$  (= even), respectively. Note that the axis

of rotation (i.e., the orientation of  $\mathbf{L}$ ) is always perpendicular to the symmetry axis of the body since the projection of  $\mathbf{L}$  onto that axis is zero as indicated by the Clebsch–Gordan coefficient ( $JK, L0|IK$ ). The (space-fixed) axis of quantization can be defined by the direction of  $\mathbf{I}$  ( $M = I$ ).

The above formulation shows clearly that two quasiparticles are nothing other than “spectators” whose role is simply to supply their angular momenta to the system. This means that, for an understanding of the remarkable behavior of the  $|K| > 2$  bands, the kinematics of the angular momentum coupling plays an important role. We will treat the addition of the angular momenta quantum mechanically but describe the rotational motion of the rotor in a semiclassical (i.e., a large deformation) limit for simplicity. Namely, we evaluate  $E_L$  and  $N_{00}^L$  by the formula (2.29) derived in Sec. 2.2

$$E_L \approx E_0 + \frac{L(L+1)}{2\Im} \quad \text{and} \quad N_{00}^L \approx Q_L \equiv \frac{2L+1}{\Delta J_y^2} \exp \left\{ -\frac{L(L+1)}{2\Delta J_y^2} \right\} \quad (3.33)$$

in order to avoid an exact numerical evaluation of the angular momentum projection. Under this approximation, the spin dependent part of the band energy becomes

$$E_I(K_1, K_2) \approx \frac{1}{2\Im} \sum_L L(L+1) p_L^I(K_1, K_2) \quad (3.34)$$

in which we evaluate  $p_L^I(K_1, K_2)$  of (3.32) using the approximate formula  $Q_L$  given in (3.33). The result depends essentially on a single parameter  $\Delta J_y^2$  ( $\approx 40$ ; cf. Table 2) since the moment of inertia  $\Im$  is just a scaling factor of the rotational energy (3.34). In other words,  $2\Im E_I(K_1, K_2)$  does not depend on the details of the Hamiltonian. This is namely the result (B.10) of Appendix B. In contrast to (3.31), the expression (3.34) is valid only in the large deformation limit because of the approximation (3.33).

Figure 9 shows the spin dependence of the quantity  $2\Im E_I(K_1, K_2)$  evaluated by the formula (3.34) using a typical value of  $\Delta J_y^2 = 40$  for those configurations  $[K_1, K_2]i_{13/2}^2$  which correspond to the ones presented in Fig. 8 ( $|K_1 + K_2| > 2$ ). It is seen that the present approximation reproduces the exact projection calculation quite well. Namely, the rotational energies of the odd- $K$  bands decrease with spin until they turn to increase at spin  $I \approx 10$ , while those of the even- $K$  bands increase monotonically, which is the main feature of Fig. 8. Therefore, the clue to the underlying physics should be hidden in the simple formula (3.34). This makes our task much easier.

Let us now come to the conclusion. The answer to our question is incredibly simple. We can understand the remarkable behavior of the like-nucleon high- $K$  bands in terms of the exchange symmetry of two identical particles. In fact, if we omit the aforementioned factor  $[1 + (-)^J \delta_{j_1 j_2}]$  which allows only  $J = \text{even}$  when  $j_1 = j_2$ , the whole difference between the odd- and even- $K$  bands disappears. We

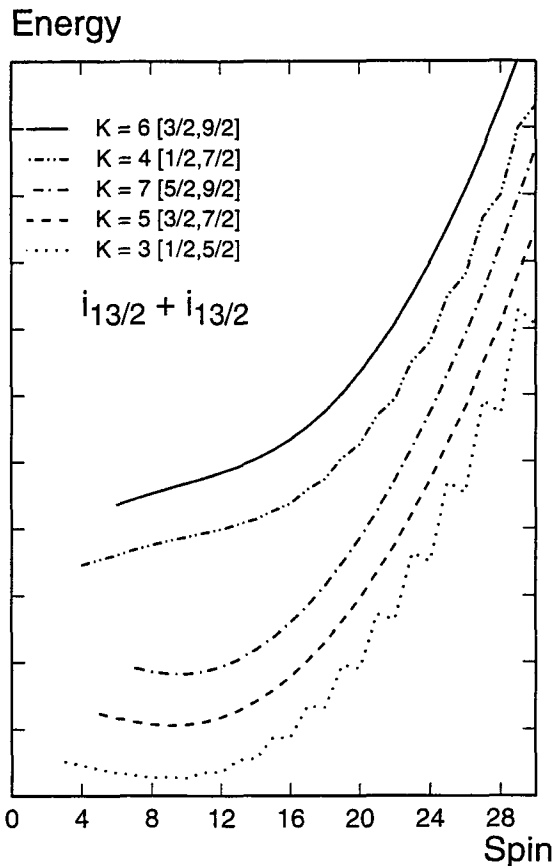


Fig. 9. Same as Fig. 8 obtained by the Formula (3.34). The figure shows that the result obtained by the formula (3.34) is a good approximation to the exact projection calculation (Fig. 8). The vertical axis is properly scaled.

demonstrate this in Fig. 10 which shows the same quantities as Fig. 9 but is obtained by omitting this  $J$ -selection rule despite  $j_1 = j_2 (= \frac{13}{2})$ . It may thus be regarded as the result for two quasinucleons of different kinds ( $1\nu \otimes 1\pi$ -qp states).

Therefore, it is the indistinguishability of identical particles which makes the odd- $K$  bands so different from the even- $K$  bands. The residual interaction thereby plays no role. But this is not the whole story. We can also construct another type of odd- $K$  bands using configurations such as  $[\frac{1}{2}, -\frac{7}{2}]$  and  $[-\frac{3}{2}, \frac{9}{2}]$ , although such high-lying ( $|K| = 3$ ) bands are less interesting in practice. It turns out that their rotational energies increase monotonically and exhibit nothing unusual. Thus, there are two types of odd- $K$  bands depending on whether  $K_1$  and  $K_2$  are of the same or opposite signs. This is obviously due to the Clebsch-Gordan coefficient ( $j_1 K_1, j_2, K_2 | JK \rangle$ ). In the high spin region ( $I > 10$ ), on the other hand, all bands behave more or less normally. Figure 8 even shows the presence of signature

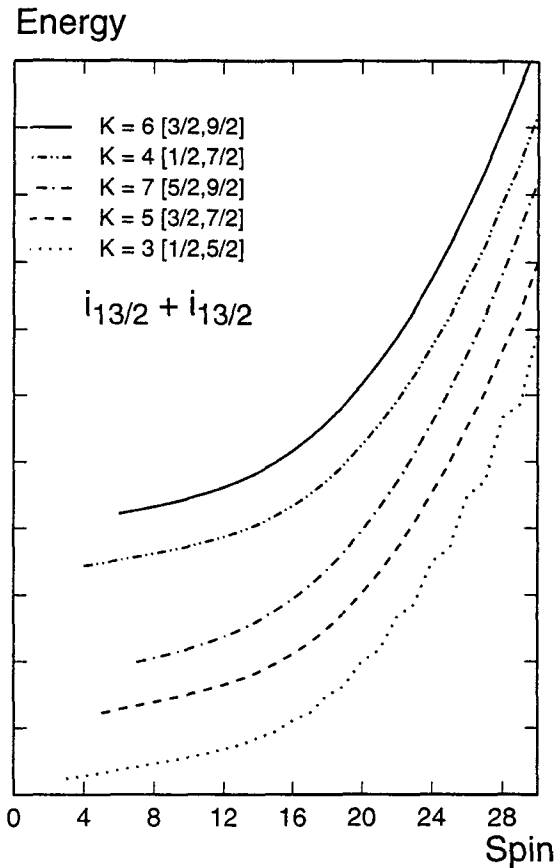


Fig. 10. Same as Fig. 9 without the Selection Rule “ $J = \text{even}$ ”. The figure shows that the remarkable behavior of the odd- $K$  bands disappears if the selection rule “ $J = \text{even}$ ” is released. The figure corresponds to  $1\nu \otimes 1\pi$  bands.

dependence if the  $K$ -values are not too large (i.e.,  $|K| = 3$  and 4). This means that the spin alignment, which was absent in the low spin region, develops in the high spin region, to which the usual signature rule (3.23) applies.

To summarize, all the features of the high- $K$  bands arise from the kinematics (the angular momentum coupling and its selection rule for identical particles) alone since the dynamics (the effect of residual interaction) plays no role; see also Appendix B.

We now discuss what these odd- $K$  bands would actually look like. As Fig. 8 suggests, such an odd- $K$  band might be seen as if it were a (low-lying excited) high- $K$  band since its bandhead appears around spin  $I \approx 10^b$  although it actually

<sup>b</sup>This applies to the  $i_{13/2}^2$  configuration. For the  $h_{11/2}^2$  configuration, the bandhead is around  $I \approx 8$ ; cf. two  $|K| = 3$  bands shown in Figs. 6 and 7.

continues to the low spin region down to  $I = |K|$  where the rotational energy goes up as the spin decreases so that the low spin portion of the band would remain practically undetected. We may expect that one of the high- $K$  bands appears low when the Fermi energy of the nucleus happens to be at the middle point of two Nilsson levels of  $\Omega = \frac{1}{2}$  and  $\frac{5}{2}$  ( $|K| = 3$  band),  $\Omega = \frac{3}{2}$  and  $\frac{7}{2}$  ( $|K| = 5$  band), etc. We note that there is a difference between these high- $K$  bands. The  $|K| = 3$  band shows an appreciable signature dependence in the high spin region ( $I > 10$ ). Therefore, the  $I = \text{odd}$  members may hardly be detected since such a state would decay primarily into the  $I' = I - 1$  (= even) state by an  $M1$  decay and the latter into the subsequent even spin states by the stretched  $E2$  transitions ( $\Delta I = 2$ ). On the other hand, the  $|K| = 5$  (or higher) band has essentially no signature dependence because of a larger  $K$ -value. Consequently, both even and odd spin members would be equally populated through the successive  $M1$  decays.

### 3.5. The band diagram

So far, we have shown the spin dependence of various band energies by shifting their positions to avoid mutual overlap or crossing. If we plot them by keeping their relative positions correctly, we obtain a figure called the Band Diagram which depends sensitively on the shell-filling of the nucleus in question. It shows the crossing of various bands, where some prominent phenomena may take place, and therefore plays a central role in the interpretation of the numerical results. Needless to say, one should not plot too many bands in a single band diagram but select carefully those which are essential for the description of the physics of interest. In addition, the Nilsson diagram marked with the actual position of the Fermi energy will often be a great help in understanding the mechanism of a particular phenomenon. One must thus keep track of the configuration of each band when plotting the band diagram. A useful fact to remember is that the  $K$ -value of a band can easily be identified in the band diagram as the lowest possible value of the spin ( $|K| \leq I$ ), i.e.,  $|K|$  is equal to the spin where a band starts. However, it is not necessarily equal to the spin of the bandhead since the band energies are not always increasing functions of the spin. We now show some demonstrative examples.

Figure 11 is a band diagram for the nucleus  $^{160}\text{Er}$  showing five band-energies. The neutron ( $\nu$ ) Fermi energy lies in the intruder subshell  $N = 6, i_{13/2}$  and the proton ( $\pi$ ) Fermi energy in the intruder subshell  $N = 5, h_{11/2}$ . Plotted are the  $g$ -band (which exists only for  $I = \text{even}$ ), the lowest two  $2\nu\text{-}qp$   $|K| = 1$  bands, the lowest  $2\nu\text{-}qp$   $|K| = 3$  band, and the lowest  $2\pi\text{-}qp$   $|K| = 1$  band. The  $|K| = 3$  band has the configuration  $[\frac{1}{2}, \frac{5}{2}]$  and appears quite low since the neutron Fermi energy is at about the middle point of the Nilsson levels  $\Omega = \frac{1}{2}$  and  $\frac{5}{2}$  (cf. the previous section). It should also be noted that two  $2\nu\text{-}qp$   $|K| = 1$  bands  $[\frac{1}{2}, -\frac{3}{2}]$  and  $[-\frac{3}{2}, \frac{5}{2}]$  are very close to each other at this particular Fermi energy since their quasiparticle energies are about the same. The implication of such a particular Fermi energy will be discussed in greater detail later. Another example with a different configuration will be shown in a moment.

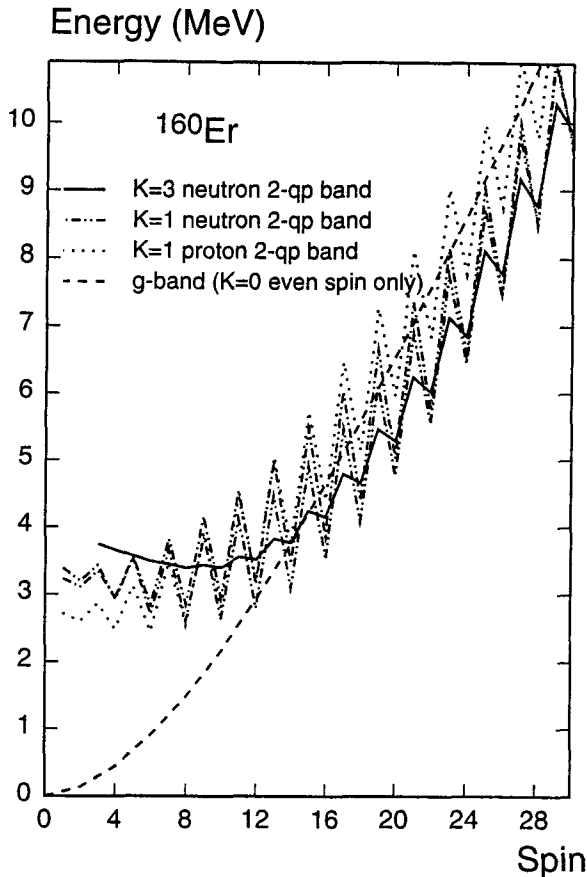


Fig. 11. Band diagram for the nucleus  $^{160}\text{Er}$ . Band energies are plotted against spin for the  $g$ -band (even spin only), the lowest two  $K = 1$  and a  $K = 3$   $2\nu\text{-}qp$  bands of  $(i_{13/2})^2$ , and the lowest  $K = 1$   $2\pi\text{-}qp$  band of  $(h_{11/2})^2$ . Two  $K = 1$  bands are nearly degenerate in this nucleus and cross the  $g$ -band at  $I = 12$ , namely, the  $g$ - $s$  crossing takes place between three bands. The  $K = 1$   $2\pi\text{-}qp$  band does not come close to the yrast region due to smaller alignment. The  $K = 3$   $2\nu\text{-}qp$  band appears relatively low.

In the figure, two  $2\nu\text{-}qp$  bands and a  $2\pi\text{-}qp$  band having  $|K| = 1$  show clearly the signature splitting between  $I = \text{even}$  and  $\text{odd}$  states and the rotational energies for  $I = \text{even}$  states decrease in the low spin region. This is due to the spin alignment. Note that, although the intrinsic energy of the  $2\pi\text{-}qp$  state is lower than that of the  $2\nu\text{-}qp$  states, the proton band does not come close to the yrast region due to smaller alignment ( $\pi h_{11/2}$  vs.  $\nu i_{13/2}$ ). The latter (we can actually see two nearly degenerate  $|K| = 1$  bands) even crosses the  $g$ -band at  $I = 12$  and thereafter becomes the yrast state. This is the so-called  $s$ -band. As is well known, the  $g$ - $s$  band-crossing leads to the backbending (or upbending depending on the crossing condition) of the moment of inertia. Very interesting is the  $2\nu\text{-}qp$   $|K| = 3$  band. It becomes the yrast band for

the  $I = \text{odd}$  states starting from  $I = 11$ . However, because of signature dependence, such a state will mostly decay to the  $I - 1 = \text{even}$  state by an  $M1$  transition so that it will be rather difficult to detect all members of the  $I = \text{odd}$  sequence. The  $I = \text{even}$  sequence, on the other hand, will be populated through the stretched  $E2$  transitions and may be observed as if it were an excited high- $K$  band ( $|K| \approx 10$ ) since the lowest state (i.e., the bottom) of the band occurs at spin  $I \approx 10$ , as can be seen in Fig. 11.

Figure 12 shows a similar band diagram for the nucleus  $^{164}\text{Er}$ . The two lowest  $2\nu\text{-}qp$   $|K| = 1$  bands have, respectively, the configurations  $[-\frac{3}{2}, \frac{5}{2}]$  and  $[\frac{5}{2}, -\frac{7}{2}]$  in this case, which cross the  $g$ -band at  $I = 14$ . They are again very close to each

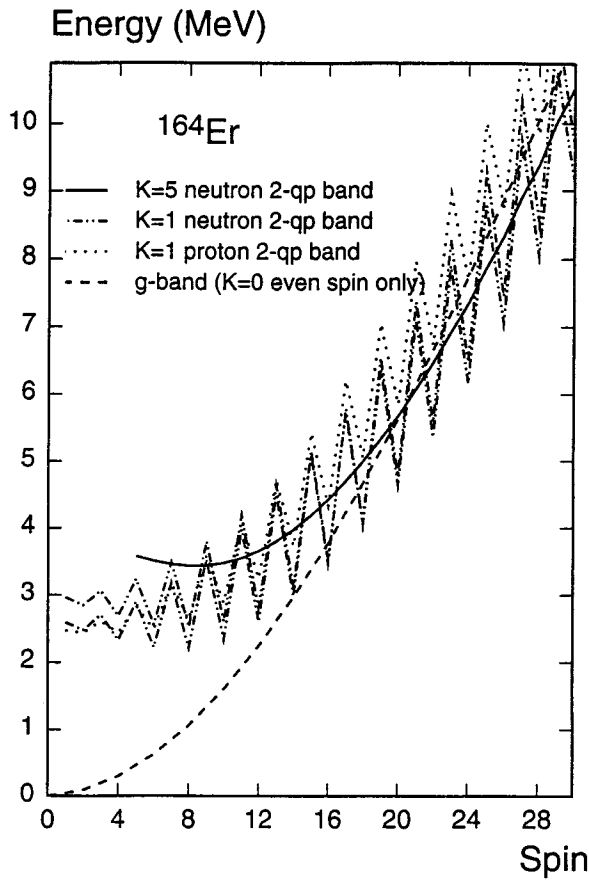


Fig. 12. Band diagram for the nucleus  $^{164}\text{Er}$ . Band energies are plotted against spin for the  $g$ -band (even spin only), the lowest two  $K = 1$  and a  $K = 5$   $2\nu\text{-}qp$  bands of  $(i_{13/2})^2$ , and the lowest  $K = 1$   $2\pi\text{-}qp$  band of  $(h_{11/2})^2$ . Two  $K = 1$  bands are nearly degenerate in this nucleus and cross the  $g$ -band at  $I = 14$ , namely, the  $g$ - $s$  crossing takes place between three bands. The  $K = 1$   $2\pi\text{-}qp$  band does not come closely to the yrast region due to smaller alignment. The  $K = 5$   $2\nu\text{-}qp$  band appears relatively low.

other (nearly degenerate) since the neutron Fermi energy lies at about the middle point of the Nilsson levels  $\Omega = \frac{3}{2}$  and  $\frac{7}{2}$ . At the same time, the  $|K| = 5$  [ $\frac{3}{2}, \frac{7}{2}$ ] band appears quite low. This situation is very similar to the case of  $^{160}\text{Er}$  in which the  $|K| = 3$  band appears rather low (cf. Fig. 11). But we note that, in contrast to the  $|K| = 3$  band, the  $|K| = 5$  band shows no signature dependence because of a larger  $K$ -value. This means that both  $I =$  even and odd members will be equally populated through the successive  $M1$  decays. This band would also be observed as if it were an excited high- $K$  band ( $|K| \approx 10$ ) since  $I \approx 10$  is the lowest state (i.e., the bottom) of the band as we can see in Fig. 12.

We will now clarify the implication of the “particular” Fermi energies in the above examples. Consider two like-nucleon quasiparticles in an intruder subshell. If the Fermi energy is at the middle point between Nilsson levels  $\Omega - 1$  and  $\Omega + 1$ , the quasiparticle energies of two  $|K| = 1$  (2-qp) states  $[\Omega - 1, -\Omega]$  and  $[-\Omega, \Omega + 1]$  become degenerate and that of the  $|K| = 2\Omega$  (2-qp) state  $[\Omega - 1, \Omega + 1]$  is at its minimum. The former ( $|K| = 1$ ) states represent two degenerate  $s$ -bands and the latter ( $|K| = 2\Omega = \text{odd}$ ) the high- $K$  band. This situation is repeated for  $\Omega = \frac{3}{2}, \frac{5}{2}, \dots$ <sup>c</sup>. Namely, such a constellation occurs “periodically” as the Fermi energy (or the particle number) increases.

In order to demonstrate these features, we consider the three lowest ( $K \neq 0$ ) 2-qp energies that correspond to the configurations  $[\Omega - 1, -\Omega]$ ,  $[-\Omega, \Omega + 1]$  and  $[\Omega - 1, \Omega + 1]$

$$\begin{aligned} E_1 &= \sqrt{(\varepsilon_{\Omega-1} - \lambda)^2 + \Delta^2} + \sqrt{(\varepsilon_{-\Omega} - \lambda)^2 + \Delta^2} \quad (K = -1), \\ E_2 &= \sqrt{(\varepsilon_{\Omega+1} - \lambda)^2 + \Delta^2} + \sqrt{(\varepsilon_{-\Omega} - \lambda)^2 + \Delta^2} \quad (K = +1), \\ E_3 &= \sqrt{(\varepsilon_{\Omega-1} - \lambda)^2 + \Delta^2} + \sqrt{(\varepsilon_{\Omega+1} - \lambda)^2 + \Delta^2} \quad (K = 2\Omega). \end{aligned} \quad (3.35)$$

They represent, respectively, the intrinsic energies of two  $s$ -bands and the high- $K$  band. The actual value of  $\Omega$  depends on the shell filling, namely, on the Fermi energy  $\lambda$ .

In Fig. 13, the quantities  $|E_1 - E_2|$  and  $E_3$  are plotted as functions of the Fermi energy. We can see that the degeneracy of the lowest two  $s$ -bands ( $|E_1 - E_2| = 0$ ) and a local minimum of high- $K$  band ( $E_3 = \text{minimum}$ ) occur simultaneously whenever the Fermi energy is at the middle point of two Nilsson energies  $\varepsilon_{\Omega-1}$  and  $\varepsilon_{\Omega+1}$ , namely, at

$$\lambda = \frac{1}{2}(\varepsilon_{\Omega-1} + \varepsilon_{\Omega+1}) \quad \text{for } \Omega = \frac{3}{2}, \frac{5}{2}, \dots \quad (3.36)$$

Moreover, the figure shows clearly the periodicity in question. We stress that this simple mechanism is an immediate consequence of the Nilsson + BCS scheme.

What is remarkable is the fact that the above-mentioned particular Fermi energies coincide with those values which lead to the yrare–yrast degeneracy at the

<sup>c</sup>The sequence of  $\Omega$  will be reversed if the deformation is oblate.

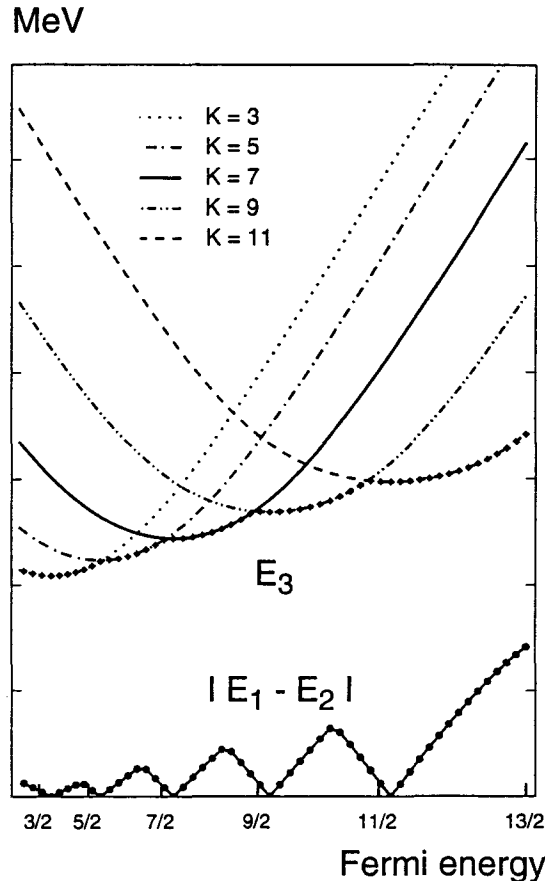


Fig. 13.  $|E_1 - E_2|$  (lower curve) and  $E_3$  (upper curve) plotted as functions of the Fermi energy in the intruder subshell ( $i_{13/2}$ )<sup>2</sup>. The degeneracy of two  $s$ -bands ( $E_1 = E_2$ ) occurs periodically whenever the Fermi energy is at the middle point of two Nilsson energies  $\varepsilon_{\Omega-1}$  and  $\varepsilon_{\Omega+1}$ . At the same time, this is where the intrinsic energy ( $E_3$ ) of the high- $K$  band ( $K = 2\Omega$ ) becomes a minimum. The actual  $K$ -value of the lowest high- $K$  band changes from 3 to 11 in step of 2 units as the Fermi energy increases. A prolate shape is assumed; cf. footnote b.

$g-s$  crossing point. This kind of degeneracy was first discussed in the Cranked Shell Model<sup>36</sup> with the conclusion that the  $g-s$  band coupling vanishes<sup>d</sup> periodically as the Fermi energy increases. A similar periodic occurrence of the yrare-yrast degeneracy is also obtained in the Projected Shell Model. However, it is difficult for us to understand why the coupling matrix elements in the shell model should vanish periodically since they are expected to be rather slowly varying functions of the Fermi energy (or particle number). This conflict can be immediately resolved if we recall the simple mechanism described above, which indicates that the level

<sup>d</sup>This interpretation is based on a degenerate two-level model.

crossing actually takes place between three (i.e., between the  $g$ - and two  $s$ -) bands rather than two (the  $g$ - and an  $s$ -band) when the Fermi energy happens to be close to one of the particular values. In fact, such three-level crossing can be seen in Figs. 11 (at  $I = 12$ ) and 12 (at  $I = 14$ ). It means that, at the band crossing point, we have to take into account three interacting levels whenever the Fermi energy is close to one of the particular values (3.36), which takes place “periodically” as the Fermi energy increases. This picture leads naturally to a conclusion different from that deduced from the usual two-level model, namely, the coupling matrix elements need not (and should not) vanish for the lowest two eigenvalues to become degenerate. In fact, in a three-level crossing model, the yrare–yrast degeneracy takes place if the coupling matrix elements between three crossing bands satisfy the relations

$$|V_{12}| = |V_{23}| = |V_{31}| \quad \text{and} \quad V_{12}V_{23}V_{31} > 0; \quad (3.37)$$

see Appendix C for proof. Therefore, in light of the present theory, none of the coupling matrix elements should vanish and the periodicity in question is simply due to the periodic occurrence of the particular Fermi energies for which three (unperturbed) rotational bands become degenerate at the crossing point. The coupling matrix elements may thus depend rather weakly on the particle number.

As concluded in the Cranked Shell Model,<sup>36</sup> the occurrence of yrare–yrast degeneracy is certainly one of the important conditions for the occurrence of strong backbending. In addition, the present theory predicts relatively low-lying high- $K$  bands in such nuclei. In nuclei whose Fermi energies are not so close to these particular values, the high- $K$  bands in question will appear correspondingly at higher energies and there will be a competition between two bands corresponding to  $|K| = 3$  and 5 (or 5 and 7).

Finally, we mention that the concept of the band diagram discussed here is based on first order perturbation theory (the expectation value of the Hamiltonian), so that the coupling between various bands is not yet taken into account. To obtain the final result, the Hamiltonian has to be diagonalized, as described in Sec. 2.3. In fact, this procedure corresponds to configuration mixing in the usual shell model (or band mixing in the particle–rotor model). Nevertheless, the band diagram is a useful tool for gaining physical insights and is also indispensable for the interpretation of the numerical results. It will often be helpful also to plot in the band diagram the yrast energies obtained by the diagonalization procedure. These yrast levels will appear below the energies of the lowest band in the band diagram according to the Ritz Theorem (recall the variational principle). If their displacement from the lowest (unperturbed) band is large, it means that the coupling between bands is substantial and thus the band mixing is large. Such information is quite useful and can cover to a certain extent the inconvenient aspect of the Projected Shell Model which arises from the fact that the projected basis is not orthonormal and thus the eigenvectors  $\{F_{\kappa K}^I\}$  of the PSM equation (2.31) are not the usual probability amplitudes.

In the following three chapters, we will apply the shell model diagonalization (or the configuration mixing) to doubly-even, doubly-odd, and odd-mass nuclei. In the present theory, all nuclei are treated on an equal footing using the same Hamiltonian (2.40) with the standard set of parameters for the harmonic oscillator Hamiltonian, i.e.,  $\kappa$  and  $\mu$  in (2.41). The distinction between different types of nuclei is made by the choice of the shell model basis (2.53).

#### 4. Application to Doubly-Even Nuclei

##### 4.1. *Yrast levels*

A large body of experimental data is available for yrast levels of doubly-even nuclei. We shall apply our theory first to the yrast levels of some rare-earth nuclei and then turn to side bands. The yrast bands of doubly-even nuclei are usually compared with data using the backbending plot, on which we will comment briefly below.

In analogy to the classical relation  $\omega = \frac{dE(I)}{dI}$ , we define the rotational frequency by

$$\omega = \frac{E(I) - E(I - \Delta I)}{\Delta I} \quad (4.1)$$

with  $\Delta I = 2$ . Recall that the  $g$ -band consists only of even values of spin. This quantity is directly related to the measured  $\gamma$ -ray energy and multipolarity and represents the slope of  $E(I)$  as a function of  $I$ . We note that the signature dependence of the spectrum, which may show up if we take  $\Delta I = 1$ , is suppressed by the choice  $\Delta I = 2$ .

The rotational frequency of the yrast band will decrease suddenly at a band crossing point since, in the band diagram, the slope of the crossing band (e.g., the  $s$ -band) is smaller than that of the crossed band (e.g., the  $g$ -band). Otherwise no crossing can occur. This means that the rotational frequency suddenly becomes smaller if a band crossing takes place. Also, the weaker the strength of the ( $g-s$ ) band coupling, the stronger the suddenness, because the transition from the crossed ( $g$ -) band to the crossing ( $s$ -) band occurs abruptly if the coupling is small. A diagram in which the spin  $I$  is plotted against the rotational frequency  $\omega$  is called an Alignment Diagram.

The moment of inertia is usually defined by the classical relation

$$\Theta = \frac{I}{\omega}. \quad (4.2)$$

To evaluate this quantity, the absolute value of the spin must be known. Therefore, it is sometimes convenient to define the so-called dynamic moment of inertia

$$\Theta^{(2)} = \frac{\Delta I^2}{E(I + \Delta I) - 2E(I) + E(I - \Delta I)} \quad (4.3)$$

corresponding to the inverse of  $\frac{d\omega}{dI} = \frac{d^2E(I)}{dI^2}$ , which contains only the measured  $\gamma$ -ray energies and multipolarity. These two definitions are totally different from

each other. In the present work, we will deal exclusively with the moment of inertia (4.2).

A remark is in order before we proceed further. If we apply the above formulas to the spectrum of an axially symmetric rotor  $E(I) = \frac{1}{2\Im}I(I+1)$ , the rotational frequency (4.1) and the moment of inertia (4.2) become, respectively,

$$\omega = \frac{1}{\Im} \left( I - \frac{\Delta I - 1}{2} \right) \quad \text{and} \quad \Theta = \Im + \frac{\Delta I - 1}{2\omega}.$$

While  $\omega$  increases with spin,  $\Theta$  decreases as a function of  $\omega$  or  $I$ . This is no surprise as it arises from the finite difference  $\Delta I = 2$ . In fact, if we choose  $\Delta I = -2$ ,  $\Theta$  becomes an increasing function of  $\omega$ . This would actually be a better approximation to the moment of inertia defined by using  $\omega = \frac{dE(I)}{dI}$  (i.e.,  $\Delta I \rightarrow 0$ ) which is also an increasing function of  $\omega$ . (Such an  $\omega$  dependence of the moment of inertia has of course nothing to do with the shape change of the rotor.) At any rate, the above consideration shows that there is a qualitative difference between two definitions (i.e.,  $\Delta I = 2$  and  $-2$ ) for the spectrum of an axial (and in general of a triaxial) rotor. In practice, however, it does not really matter which definition one uses for  $\omega$  so far as the comparison between theory and experiment is done consistently using the same definition. The choice  $\Delta I = 2$  is the usual convention. In this connection, we note that the symmetrized definition

$$\omega = \frac{E(I + \Delta I) - E(I - \Delta I)}{2\Delta I}$$

is exactly equal to  $\frac{dE(I)}{dI}$  for an axial rotor, so that the above mentioned conflict does not occur. Moreover, it represents a better approximation to  $\frac{dE(I)}{dI}$  also for a general spectrum since all odd order terms of  $\Delta I$  are absent. This kind of definition is rarely used but may be more appropriate from the theoretical point of view.

A diagram in which twice the moment of inertia  $2\Theta$  is plotted as a function of  $\omega^2$  is called a Backbending Plot, which is known to disclose the finest feature of the yrast levels in an exaggerated manner. When looking at such a diagram, it is worth remembering that a horizontal line in the plot corresponds to the rotational limit ( $E \propto I^2$ ) while a vertical line corresponds to the vibrational limit ( $E \propto I$ ). As mentioned earlier, a well decoupled and aligned 2-qp band (*s*-band) will eventually cross the *g*-band since the rotational energy of the *s*-band has a smaller slope ( $\omega$ ) relative to the *g*-band. If a band crossing takes place with appreciably different rotational frequencies, something remarkable occurs in the backbending plot. The moment of inertia increases suddenly according to (4.2) and the plot bends in the backward direction due to a sudden decrease of the rotational frequency. This leads to an S-shaped (backbending) diagram. The sharpness of the backbending depends essentially on the ratio of the rotational frequencies of the *g*- and *s*-band at the crossing point, which is a good measure for the crossing angle of two bands. This ratio depends not only on the amount of the spin alignment but also on the deformation of the nucleus, as we will see later.

We now show a few demonstrative examples. As mentioned in Sec. 2.4, cf. (2.53), the quasiparticle configuration for doubly-even nuclei is taken to be

$$|\Phi_\kappa\rangle = \{|0\rangle, a_{\nu_1}^\dagger a_{\nu_2}^\dagger |0\rangle, a_{\pi_1}^\dagger a_{\pi_2}^\dagger |0\rangle, a_{\nu_1}^\dagger a_{\nu_2}^\dagger a_{\pi_1}^\dagger a_{\pi_2}^\dagger |0\rangle\}, \quad (4.4)$$

where the neutron ( $\nu$ ) and proton ( $\pi$ ) Nilsson quantum numbers run over appropriately selected low-lying quasiparticle states. This can be done most conveniently by consulting the Nilsson diagrams in the vicinity of the neutron and proton Fermi energies.

Let us first focus on the low spin region ( $I < 10$  or  $\omega^2 < 0.08$ ) in which the  $g$ -band is the dominant band ( $g$ -dominant). In the lighter isotopes of Figs. 14–16, the slope of the experimental backbending plot (circles) is steeper than that of the theoretical one (dots) although the agreement between theory and experiment improves rapidly as the neutron number increases. The opposite trend is seen in Fig. 17 and will be discussed later. Note that the discrepancy in the low spin region is attributed exclusively to the problem in the  $g$ -band. Since it is quite possible that the nucleus may stretch as the spin increases, we have tried first to reproduce the experimental data by adjusting the nuclear shape for each spin. However, the result<sup>11</sup> was hardly acceptable because it was necessary to increase the deformation

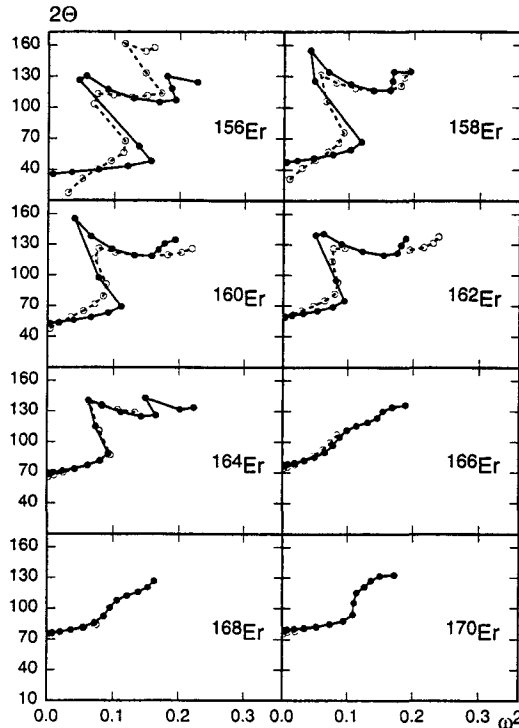


Fig. 14. Backbending plots for Er isotopes. The dots represent the theoretical predictions and the circles the experimental results. The data are taken from Refs. 37–44.

parameter  $\epsilon$  by as much as 10% for every spin increment of two units, which is rather difficult to understand. We give therefore another more plausible reasoning.<sup>11</sup> On the one hand, we recall that a horizontal (vertical) line in the backbending plot represents the rotational (vibrational) limit. In this sense, the experimental result slants slightly towards the vibrational side in comparison with the theoretical prediction. On the other hand, the yrast spectrum of a triaxial rotor<sup>66</sup> is known to change from the (purely) rotational spectrum to a (more or less) vibration-like spectrum as the triaxiality parameter  $\gamma$  increases from 0 to 30°. We demonstrate the  $g$ -band (i.e., low spin) “backbending plot” of a triaxial rotor for various values of  $\gamma$  in Fig. 18 (using the choice  $\Delta I = -2$  for the reason mentioned earlier), which shows clearly that the slope of the plot becomes steeper as the triaxiality increases.

Therefore, our conjecture is that the present ( $g$ -band) problem may be resolved by allowing certain amount of triaxiality in these nuclei. In fact, the presence of (static) triaxiality is not so unlikely for the nuclei in question since their neutron numbers are not very far from 90, around which many  $\gamma$ -soft nuclei are known to exist. While this is for nuclei at the beginning (lighter part) of the rare-earth region, there is another prominent transitional region at the other end (heavier part), towards which the triaxiality will again develop.<sup>31</sup> We thus expect that a similar ( $g$ -band) problem should occur in this region. Indeed, in the low spin region

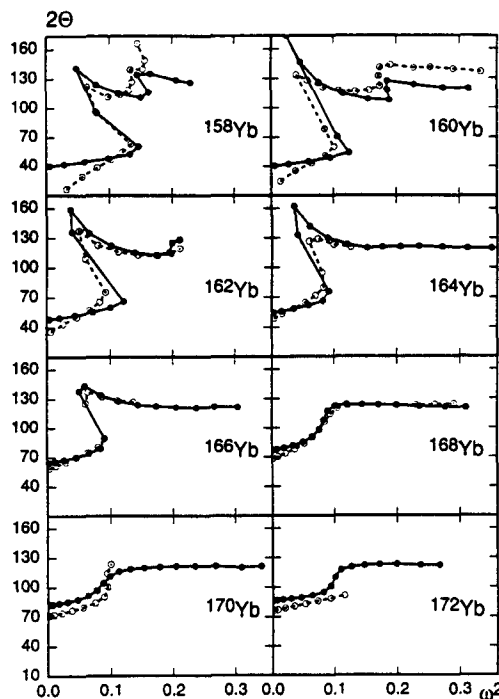


Fig. 15. Backbending plots for Yb isotopes. The dots represent the theoretical predictions and the circles the experimental results. The data are taken from Refs. 45–52.

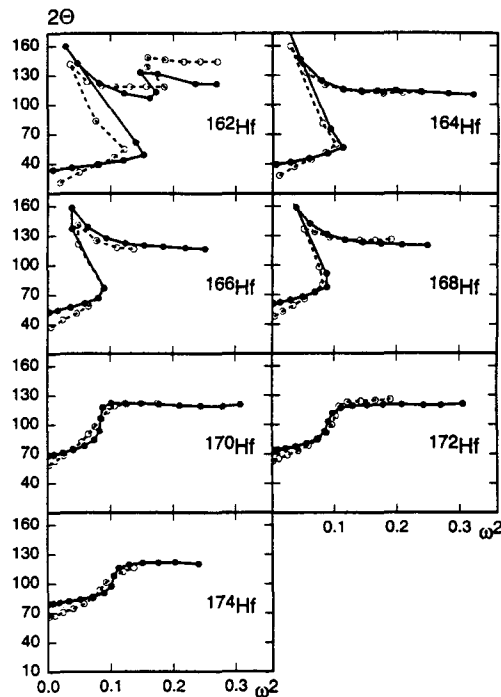


Fig. 16. Backbending plots for Hf isotopes. The dots represent the theoretical predictions and the circles the experimental results. The data are taken from Refs. 53–59.

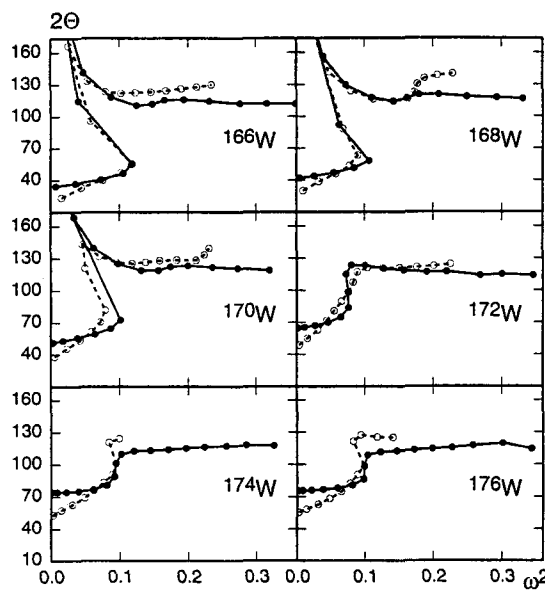


Fig. 17. Backbending plots for W isotopes. The dots represent the theoretical predictions and the circles the experimental results. The data are taken from Refs. 60–65.

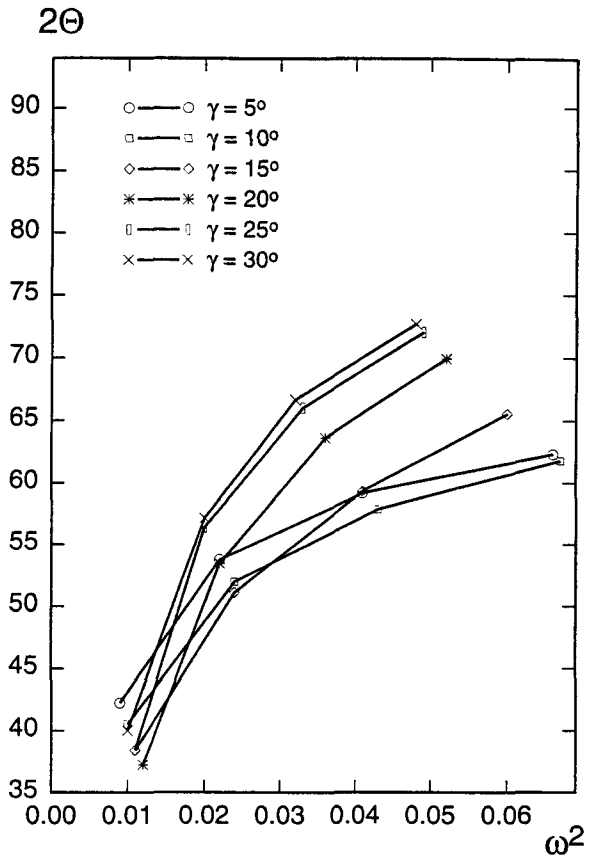


Fig. 18. Backbending plots of a triaxial rotor for various values of  $\gamma$ . The  $g$ -band moment of inertia in low-spin region ( $I < 10$ ) is plotted for  $\gamma = 5^\circ - 30^\circ$  in step of  $5^\circ$ . Note that the slope of the plot becomes steeper if the triaxiality increases.

of the W nuclei (Fig. 17), we see that the agreement between theory and experiment becomes worse as we move to heavier isotopes. All this seems to suggest that the discrepancy of the slope of the moment of inertia in the low spin region has to do with the presence of the triaxiality. This is one of the problems to be studied with the help of the triaxial projection code in the future.

Next, we examine the (first) band crossing region ( $I \approx 12 - 16$ ) where the plot shows backbending or upbending depending on the crossing condition. (The band diagrams for  $^{160}\text{Er}$  and  $^{164}\text{Er}$  were already shown in Figs. 11 and 12, respectively, which exhibit the signature dependence for some bands because of the choice  $\Delta I = 1$ .) We observe in Figs. 14–17 that the theoretical results “exaggerate” the backbending feature against the experiment. This discrepancy is due to the violation of the particle number in the BCS approximation and can be improved by applying the particle number projection in addition to the angular momentum pro-

jection, as we will see in Sec. 4.3. However, we should like to emphasize that the quantitative and qualitative modification caused by the additional particle number projection will not be very large. In particular, there will be no essential change in the physical interpretation of the mechanism leading to the backbending (or upbending) phenomenon.

As pointed out earlier, one of the most critical factors for the sharpness of the backbending is the crossing angle of the *g*- and *s*-band at the crossing spin. Since the angular frequency  $\omega$  is the slope of the rotational energy of a band in the band diagram, a good measure for the crossing angle is the ratio of their angular frequencies<sup>11</sup>

$$\rho_c = \left( \frac{\omega_g}{\omega_s} \right)_{I=I_c}, \quad (4.5)$$

where  $I_c$  is the spin at the crossing point. Table 4 shows this quantity for the Er isotopes and is to be compared with the trend of the backbending plots shown in Fig. 14.

Table 4. The Ratio (4.5) as a measure of the *g*-*s* crossing angle.

Nucleus	<sup>156</sup> Er	<sup>158</sup> Er	<sup>160</sup> Er	<sup>162</sup> Er	<sup>164</sup> Er	<sup>166</sup> Er	<sup>168</sup> Er	<sup>170</sup> Er
$I_c$	12	14	14	14	14	14	14	16
$\rho_c$	3.46	2.39	2.33	2.22	2.11	1.71	1.73	1.56

At this point, we comment on the role of the quadrupole pairing force. If this force is absent, the *g*-*s* crossing occurs around  $I_c = 8$  which is too early since we find  $I_c \approx 12$ –16 experimentally. This is due to the well-known fact that the theoretical *g*-band moment of inertia becomes 10 to 15% smaller than the experimental value if the monopole pairing force is adjusted to the observed energy gap. The quadrupole pairing force corrects this mishap and increases the moment of inertia to a proper value (another important effect is the attenuation of the rotation-particle coupling). We may also recall that the spin at which the *s*-band reaches its minimum ( $\omega_s = 0$ ) is the amount of the spin alignment; cf. (3.11). In effect, the occurrence of the spin alignment shifts the rotational spectrum of the (favored) band towards higher spins as a whole; cf. (3.9). This is the reason why the neutron *s*-band comes to the yrast region. The proton  $K = 1$  band plays a minor role due to a smaller alignment. It also means that the larger the spin alignment (i.e., the larger the intruder subshell), the larger the *g*-*s* crossing angle. Another quantity which affects the crossing angle is the size of the *g*-band moment of inertia. The smaller the *g*-band moment of inertia (i.e., the smaller the deformation), the larger the *g*-*s* crossing angle. This explains the reason why (sharply) backbending nuclei are found at the beginning and at the end of the deformed region while nuclei in the middle show upbending rather than backbending. The evidence for this can be found in Figs. 14–17. Namely, the moments of inertia of the backbending nuclei start from  $2\Theta \approx 40$  while those of the upbending nuclei start from  $2\Theta \approx 70$ .

Finally, we discuss the spin region beyond the first band crossing. The *s*-band, which crossed the *g*-band at the (first) band crossing, remains to be the yrast band (*s*-dominant) until it is crossed by another band (usually a  $2\nu\otimes2\pi$  4-*qp* band). As we can see in Fig. 16, the nucleus  $^{162}\text{Hf}$  exhibits both the first and second backbending while the nucleus  $^{170}\text{Hf}$  shows what is usually called upbending as well as a beautiful plateau for the moment of inertia (a horizontal line in the backbending plot) which already starts to develop at a moderate spin. By looking at their band diagrams, we can learn what makes these two nuclei so different. Figures 19 and 20 are the band diagrams (plotted only for even values of spin), respectively, for the nuclei  $^{162}\text{Hf}$  and  $^{170}\text{Hf}$ .

In the nucleus  $^{162}\text{Hf}$  (Fig. 19), a clear crossing between 2-*qp* (full line) and 4-*qp* (dashed line) bands is seen at  $I = 22$ , which causes the second backbending. However, in the nucleus  $^{170}\text{Hf}$  (Fig. 20), the band crossings take place one after

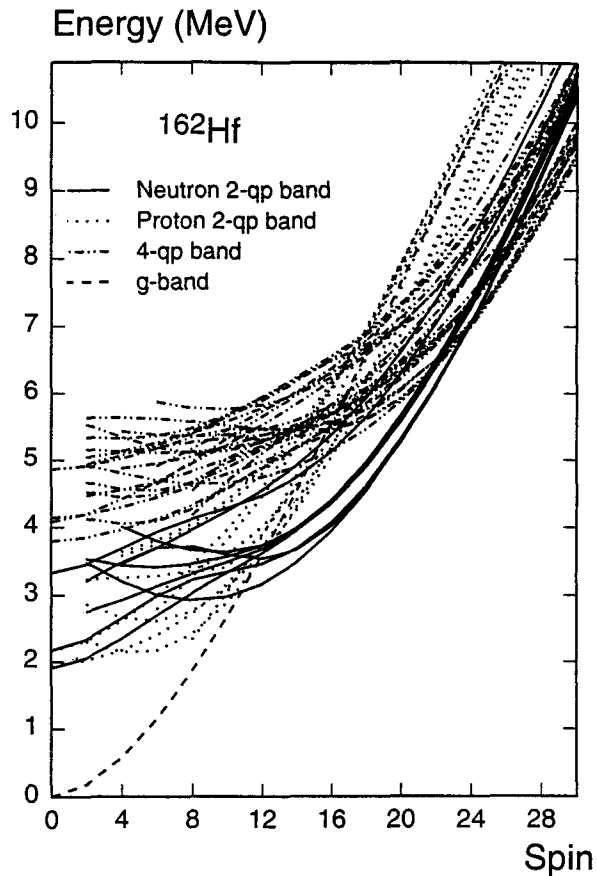


Fig. 19. A band diagram for  $^{162}\text{Hf}$ . The band energies are plotted only for even-values of the spin. Sharp band-crossing is seen at the first and second crossing points. See text for discussions.

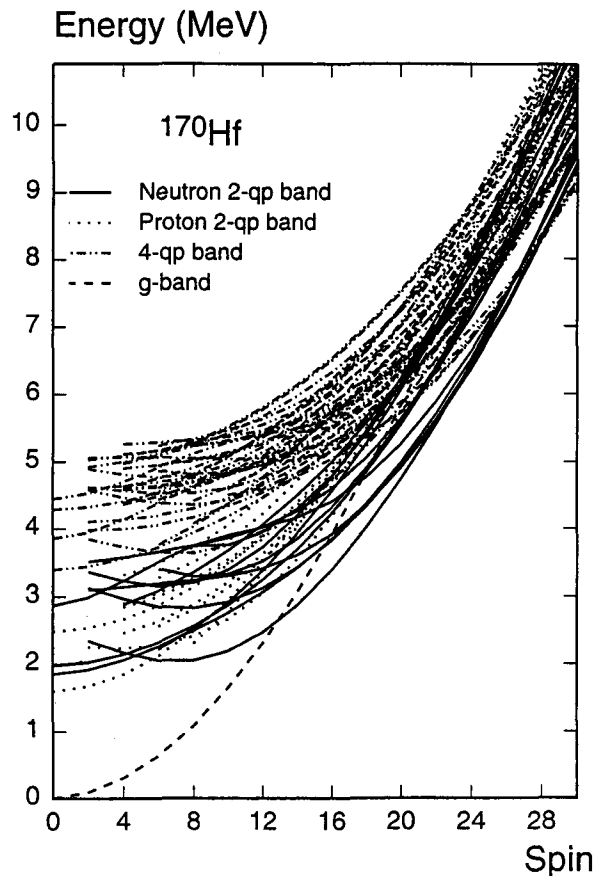


Fig. 20. A band diagram for  $^{170}\text{Hf}$ . The band energies are plotted only for even-values of the spin. Note that the band-crossing is not very sharp in this nucleus. See text for discussions.

the other with very small crossing-angle. This leads to the upbending and, in the higher spin region, to a plateau of moment of inertia. Actually, when one sees such a plateau in the backbending plot, one might conclude that the system reached the classical rotational limit having very large deformation (because of a large moment of inertia), but this is not correct. In the first place, as mentioned above, the plateau is produced by the successive band crossings which take place one after the other as the spin increases. In fact, the theoretical moment of inertia will decrease if this does not happen since the rotational spectrum of a (single) band in general develops faster than  $I^2$  (i.e., a stretched rotational spectrum) for the high spin region. This can be seen from the decrease in the moment of inertia immediately after the first band crossing in a strongly backbending nucleus (e.g.,  $^{162}\text{Hf}$  in Fig. 16) in which the  $s$ -band continues to be the yrast for a wide range of spin. Secondly, even if the moment of inertia becomes very large in the plateau region, one should not

conclude that the deformation is very large. This interpretation contradicts the fact that the measured  $BE2$  values are not much larger than those of the  $g$ -band. On the contrary, they are usually smaller and even decrease with spin, which may indicate the occurrence of successive band crossing.

It should be observed that the level density increases rapidly with spin, which is a common feature of all nuclei. In Figs. 19 and 20, we have plotted a group of high-lying bands to stress this point. There, we can see that many bands converge into the yrast region as the spin becomes high. The bands overlap and cross with each other in a complex manner and, as a result, produce a plateau in the moment of inertia. Even a sharply backbending nucleus such as  $^{162}\text{Hf}$  will eventually develop a plateau in the moment of inertia, although the spin at which this may happen differs from nucleus to nucleus. Thus, due to the increase of the level density with spin, it is most unlikely to happen in the very high spin region that a particular band crosses all the others with a sharp angle and becomes a unique yrast band. This is probably the reason why no backbending is observed beyond the second band crossing region.

Another consequence of the occurrence of a very high level density in the high spin region is that the variational approaches such as the Cranked HFB and VAM-PIR will encounter a serious convergence problem because there is no longer the unique (i.e., well separated) lowest energy state in this region. This is the potential difficulty mentioned in Sec. 1.3. Recall that the Cranked HFB becomes much less stable due to a large fluctuation already in the first band crossing region where only two (or at most three) levels come close to each other. This indicates that there is little hope of a variational type calculation being stable (and convergent) in the high spin region, where the degree of degeneracy is very high and the phase transition takes place at every spin increment of a few units. This is a serious problem which is usually overlooked. In contrast, the Projected Shell Model might have a better chance so long as one is prepared to take into account those multi-quasiparticle states which come down into the yrast region for very high spins. A criticism often addressed to the present approach is that it should be inapplicable since the theory does not take into account the spin dependence of the deformation. We do not share the opinion. In fact, this argument also implies that the standard (spherical) shell model should not apply to deformed nuclei, which is obviously not true. What happens is that, even if the static deformation is kept fixed (or set equal to zero as in the case of the standard shell model), the effective deformation develops dynamically with spin due to the configuration mixing since the intrinsic state changes from spin to spin. In practice, what really matters is the efficiency of the method and this may change depending on the energy and/or spin region of interest. In this respect, we admit that the present approach may eventually lose its efficiency in the sense that the number of quasiparticles in the configuration has to be drastically increased when the spin becomes extremely high. A better basis has to be sought in such a limiting case in order to reduce the required number of quasiparticles. We point out in this connection that the band diagram can provide us with good means of checking the adequacy of the actual multi-quasiparticle configurations.

#### 4.2. Side bands

When the Hamiltonian is diagonalized, a set of eigenstates is obtained for a given spin. This means that we obtain not only the yrast band but also many excited bands simultaneously. A number of positive and negative parity side bands is reported<sup>68</sup> for the nucleus  $^{168}\text{Yb}$  and an analysis of the data has been carried out in the framework of the present theory.<sup>69</sup> We will briefly present the result in the following.

Figure 21 shows the level schemes of three positive parity excited bands plotted relative to the yrast band (the left-most pair) which has already been presented as a backbending plot in the previous section (Fig. 15). Agreement with the experimental data is satisfactory. To indicate the bands that constitute these levels, in Fig. 22, we show a band diagram where the lowest few configurations (unperturbed bands) are plotted. As mentioned previously, the excitation energies of neutron 4-*qp*

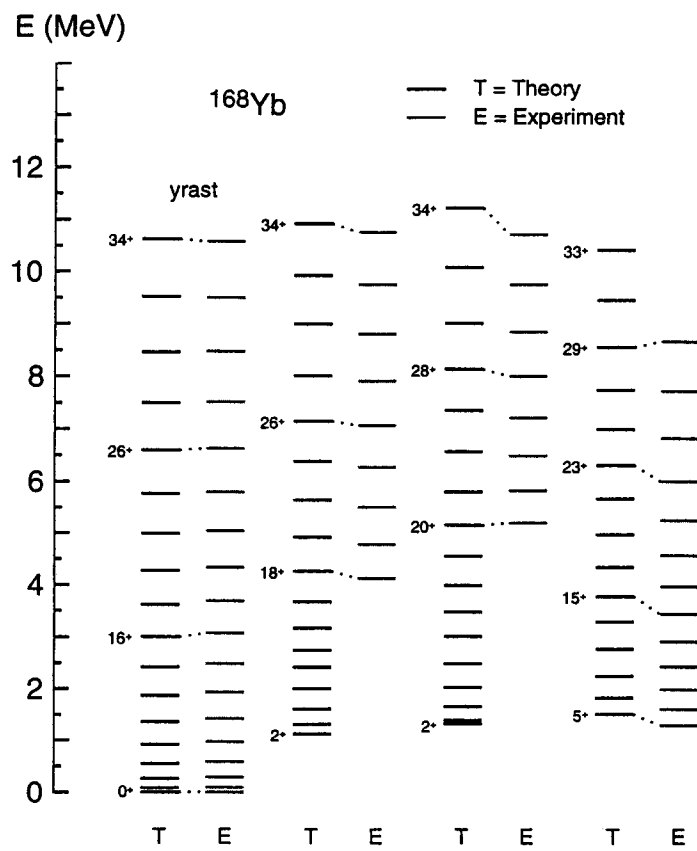


Fig. 21. Level schemes of positive parity side-bands in  $^{168}\text{Yb}$ . The first pair of level schemes (T for theory and E for experiment) shows the yrast band. The other three pairs of schemes are plotted relative to the yrast band.

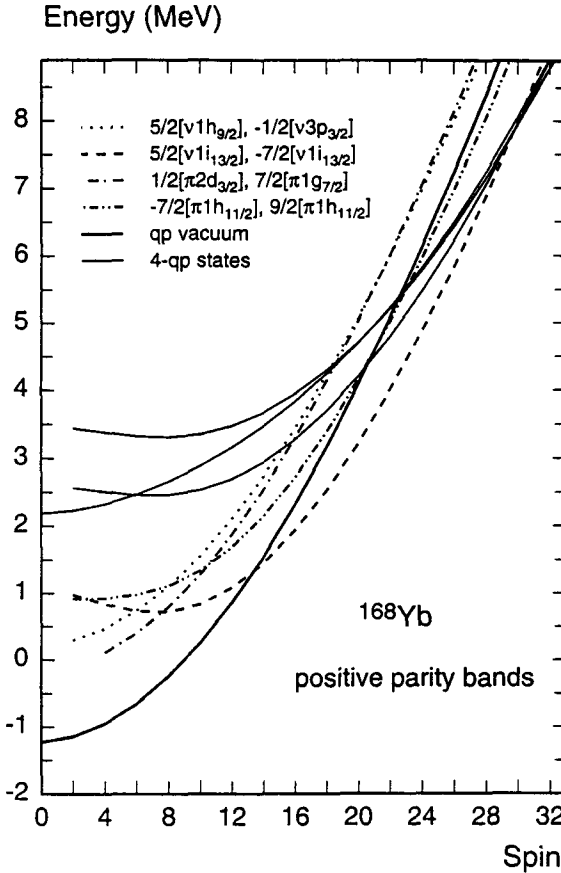


Fig. 22. A positive parity band diagram for  $^{168}\text{Yb}$ . Some of the lowest positive parity bands are plotted relative to the  $g$ -band.

configuration such as  $\nu[i_{13/2}^4]$  are high-lying due to the blocking of four low-lying single-particle levels and they are, therefore, still negligible in this spin region.

Figure 23 shows the level schemes of three negative parity excited bands also plotted relative to the yrast band which is not shown here. The main configurations in these cases are the neutron 2- $qp$  states of the configurations  $\nu[h_{9/2}i_{13/2}]$  (the 2 $\nu$ -2 $\pi$  4- $qp$  states play a minor role, see below). A band diagram for the lowest few configurations (bands) are shown in Fig. 24 (the  $g$ -band is plotted only for the sake of reference). We see that the spectra get more and more stretched as the spin increases and the theoretical prediction becomes worse. In contrast to the positive parity bands, it is most likely that this is due to the absence of neutron 4- $qp$  states in the configuration space. To clarify why this is so, let us compare the spin alignment diagrams of the (positive parity) yrast band and of the negative parity band that starts at spin  $6^-$ .

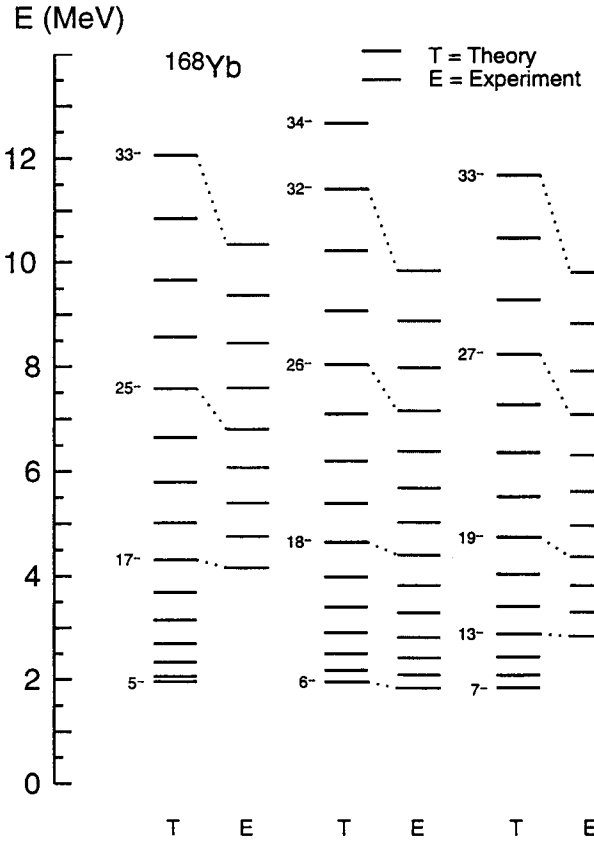


Fig. 23. Level schemes of negative parity side-bands in  $^{168}\text{Yb}$ . Three pairs of level schemes (T for theory and E for experiment) are plotted relative to the yrast band (not shown). The discrepancy of the theory with the data in the high-spin region is due to missing neutron 4-*qp* configurations. See text for the discussion.

In Fig. 25, we see that the yrast band shows a modest amount of spin alignment starting at spin 14. The theory explains this successfully in terms of the crossing of the *g*- (*0-qp*) and *s*- ( $K = 1 \nu[i_{13/2}^2]$  2-*qp*) bands, as we have seen in the previous section. In the negative parity band, the experimental data (dashed line) shows a very similar alignment effect which is totally absent in the theory (a small amount of alignment starting at spin 26 is due to a  $2\nu-2\pi$  4-*qp* band). It means that the missing alignment would come into play if we took the neutron 4-*qp* states of the configuration  $\nu[h_{9/2}i_{13/2}^3]$  into account since then a  $\nu[h_{9/2}i_{13/2}]$  2-*qp* band will play the role of the *g*-band and a  $\nu[h_{9/2}i_{13/2}^3]$  4-*qp* band that of the *s*-band. Note that the latter contains less blocking of low-lying single-particle levels compared to the positive parity neutron 4-*qp* band and can therefore already affect the spectrum in the modest spin region. Unfortunately, our present code does not take into account

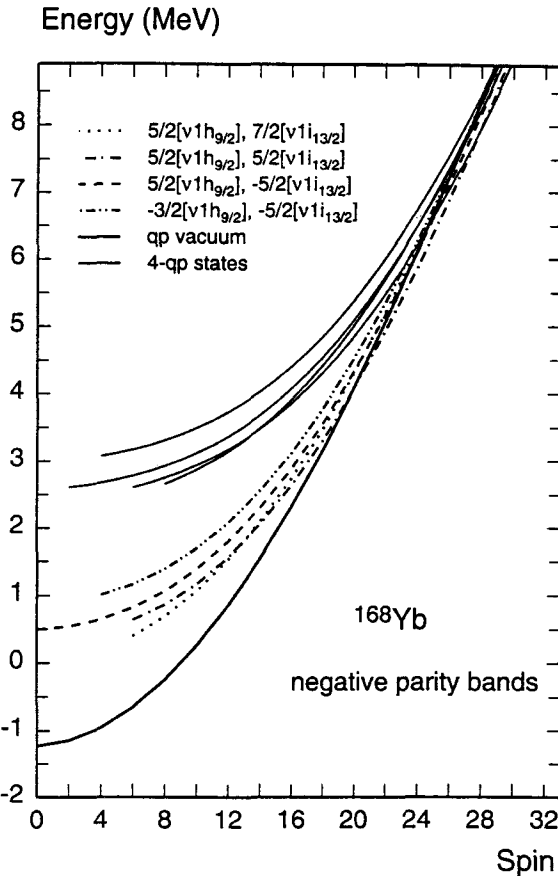


Fig. 24. A negative parity band diagram for  $^{168}\text{Yb}$ . Some of the lowest negative parity bands are plotted relative to the  $g$ -band. The latter is shown only for the sake of reference.

those configurations which consist of three and more like-nucleon states; cf. (4.4). We will lift this restriction in the future.

On the other hand, the theory describes the low spin part of the negative parity bands rather well, which justifies the assignment given to these bands ( $\nu[h_{9/2}i_{13/2}]$ ). In particular, the odd spin band that starts from  $5^-$  and the even spin band that starts from  $6^-$  belong to the same band and are actually the signature partners of each other according to the present analysis. We always expect such signature partners for a band with  $K \neq 0$ . They will exhibit the signature dependence if the  $K$ -value is small.

#### 4.3. Effect of particle number projection

Violation of the particle number caused by the BCS (or HFB) approximation is not so dangerous for the Projected Shell Model as usually believed, in the sense that

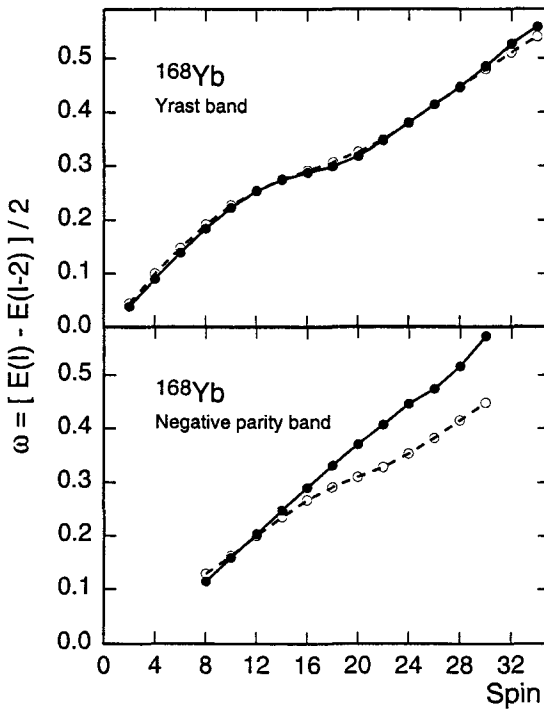


Fig. 25. Alignment diagrams for the yrast and a negative parity band of  $^{168}\text{Yb}$ . The upper figure is the alignment diagram for the (positive parity) yrast band and the lower one for the negative parity band that starts with the spin  $6^-$ . The experimental data (dashed lines with circles) show a similar alignment effect in both bands. The solid lines with dots are the theoretical results.

the essence of the physics obtained by the angular momentum projection alone is not altered even if particle number projection is carried out in addition. However, for a “perfectionist” who demands a more sophisticated treatment of the system, it may be worth carrying out a simultaneous particle number projection. In fact, there are cases where it leads to a considerable improvement in the results especially in the band crossing region. Although particle number projection may improve the agreement between theory and experiment, we nevertheless do not consider it to be of absolute necessity for understanding various phenomena related to nuclear rotational motion.

When carrying out particle number projection in a truncated space, one has to pay special attention to the treatment of the spurious state. Let us examine this problem by studying some concrete example. Figures 26 and 27 show, respectively, the usual and the particle number-projected band diagrams for the nucleus  $^{156}\text{Er}$ , in which the  $K = 0$  bands based on the neutron  $2qp$  self-conjugate states  $a_\nu^\dagger a_p^\dagger |0\rangle$  (referred to as  $qp$ -pair states hereafter) are represented by dotted lines. In Fig. 26, the lowest  $qp$ -pair state is seen to appear rather close to the yrast state at and beyond the first crossing point ( $I > 10$ ). Since this state contains a large admixture

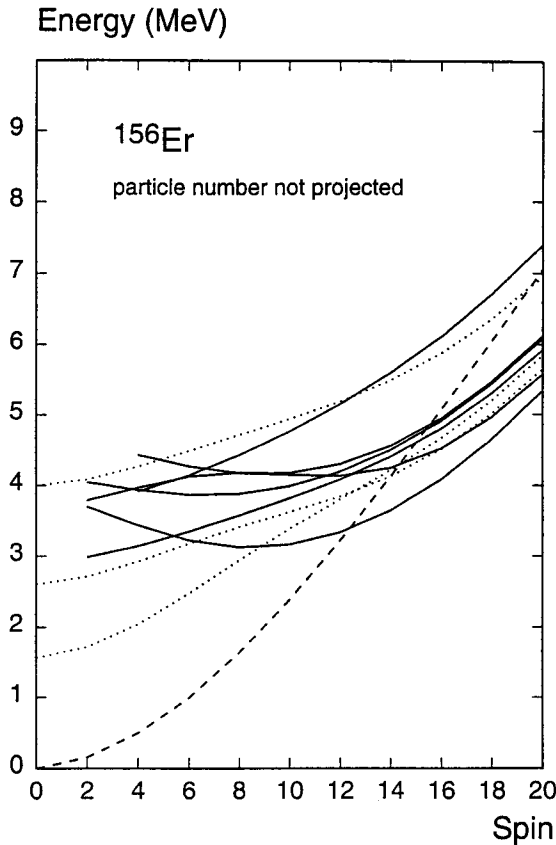


Fig. 26. A band diagram for  $^{156}\text{Er}$  without particle number projection. The figure is to be compared with Fig. 27. The number of bands is strongly reduced to emphasize the point of discussion.

of the spurious state, the final (shell model) wave function will inherit the spurious admixture. In principle, the spurious state will be removed automatically as a zero norm state when the Hamiltonian is diagonalized in the number projected basis. However, this mechanism works only if the diagonalization is carried out in the whole (i.e., untruncated) configuration space.<sup>67</sup> In practice, however, we do diagonalize the Hamiltonian by discarding those high-lying states which are far away from the yrast region since they are expected to be physically uninteresting. Consequently, the spurious state remains unremoved. This is a serious problem since the spurious state associated with particle number violation is mostly admixed in the low-lying  $qp$ -pair states. What is worse is that, if the particle number projection is performed, the energy of the lowest  $qp$ -pair (i.e., the most strongly contaminated) state becomes even lower. This is shown in Fig. 27. In the figure, we can also see that the  $g$ -band moment of inertia becomes slightly larger since particle number

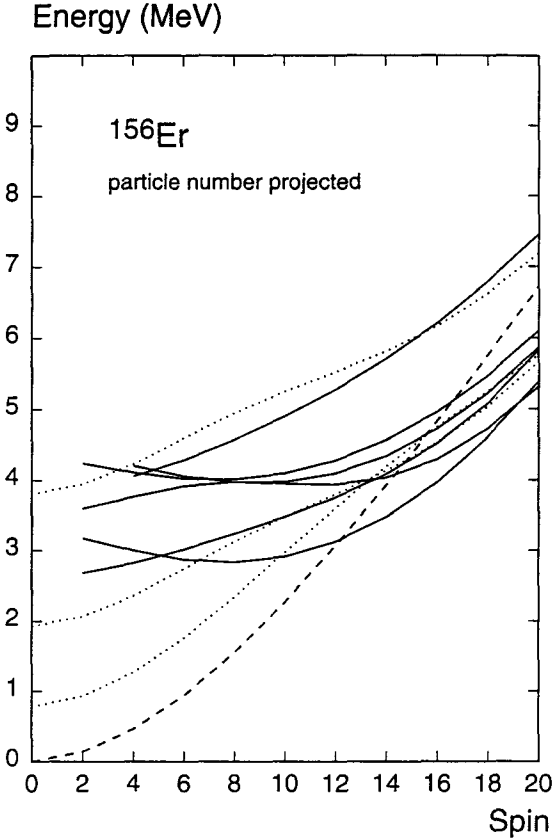


Fig. 27. A band diagram for  $^{156}\text{Er}$  with particle number projection. The figure is to be compared with Fig. 26. It reveals how the particle number projection affects the unprojected result.

projection makes the  $g-s$  crossing angle smaller, which will lead to a weaker backbending. Although this is not seen in the figure, the  $g-s$  coupling turns out to become slightly larger, which also makes the backbending weaker. However, the largest change is seen in the  $qp$ -pair bands (dotted lines). We find, in particular, that the lowest  $qp$ -pair state becomes closer to the yrast band and thus becomes even more dangerous when the particle number is projected. A “pragmatist” would therefore exclude it from the actual configuration space (the old pedestrian recipe), which is of course not quite satisfactory since the remaining  $qp$ -pair states are still contaminated although they may be less dangerous than the lowest one. In order to circumvent this problem, we propose a simple systematic way of separating the spurious state from the physical ones, which works consistently on the whole as well as in a truncated space. The details are described in Appendix D. The result of the particle number projection presented in this section is obtained by applying this method. We will see that, although the (additional) particle number projection

improves the (unprojected) result of the previous section, it does not alter the basic physical picture obtained by angular momentum projection alone.

Let us first see the effect of the basis transformation on the  $qp$ -pair bands discussed in Appendix D. This is shown in Figs. 28–31. We remark that the transformation does not affect other bands (dashed and solid lines), so we need not pay attention to them. When the transformation is carried out, the usual band diagrams Figs. 28 ( $^{156}\text{Er}$ ) and 29 ( $^{162}\text{Er}$ ) become, respectively, Figs. 30 and 31, which show the band diagrams in the new basis. We see, in the first place, that all  $qp$ -pair bands (dotted lines) are pushed upward in the new basis. Secondly, among the new  $qp$ -pair bands, there is one which comes rapidly down as the spin increases and penetrates deeply into the yrast region (see the third dotted line from below which starts at  $I = 0$  in Figs. 30 and 31) while the remaining bands develop monotonically with spin showing that they are strongly coupled to the rotating body. Loosely speaking,

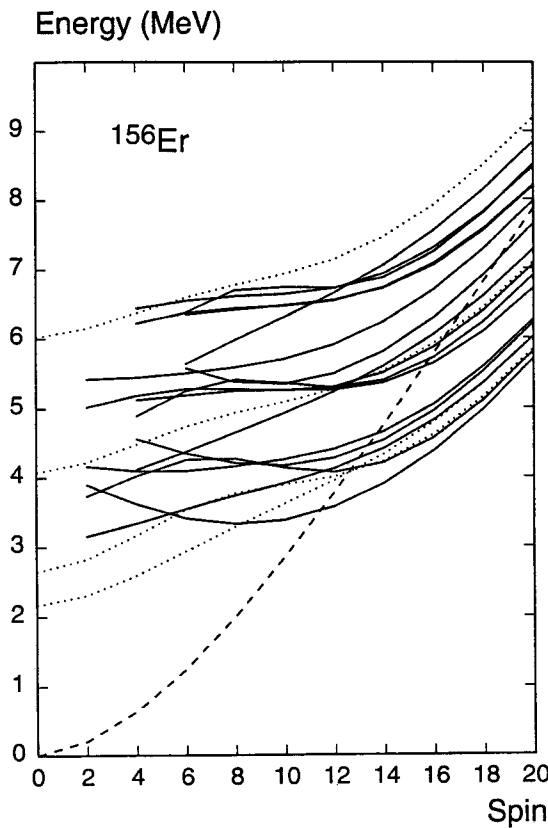


Fig. 28. A band diagram for  $^{156}\text{Er}$  before the basis transformation. The dashed line represents the  $g$ -band, the dotted lines the  $qp$ -pair bands, and the solid lines the  $2\text{-}qp$  bands of  $K \neq 0$ .

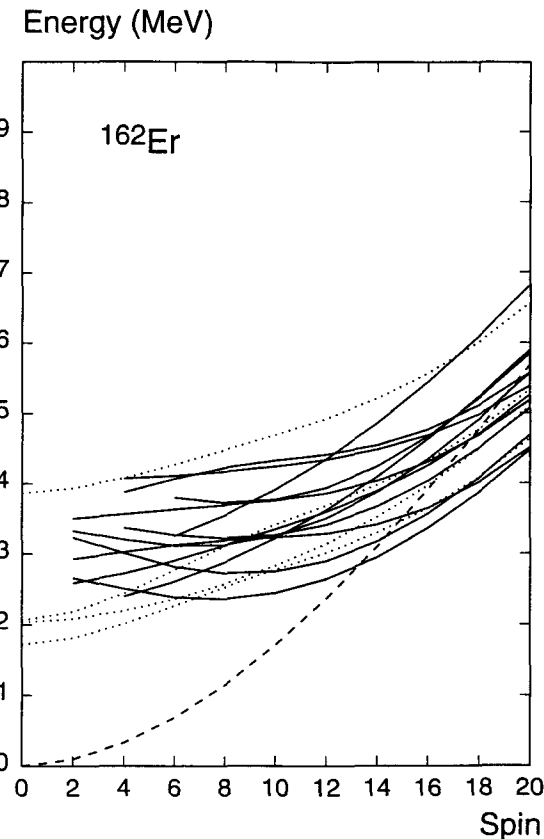


Fig. 29. A band diagram for  $^{162}\text{Er}$  before the basis transformation. The dashed line represents the  $g$ -band, the dotted lines the  $qp$ -pair bands, and the solid lines the  $2\text{-}qp$  bands of  $K \neq 0$ .

this state (i.e., the former which is decoupled from the body) is mostly spurious and will be removed when the diagonalization procedure is carried out. Therefore, if we want to use the above mentioned “pedestrian recipe”, we should apply it to this state by excluding it from the whole calculations. All this demonstrates the advantages of the new basis. We will now show the final result obtained by simultaneous angular momentum and particle number projection. The spurious state is treated by the method described in Appendix D.

Figure 32 compares the backbending plots obtained by the angular momentum and particle number projected shell model diagonalization procedure (dots) with the experimental data (circles) for some Er isotopes. The corresponding results of the previous section are also shown (diamonds) for the sake of comparison. The Hamiltonian used in both calculations is the same. Agreement between the present result and experimental data is clearly better in that the backbending features which were previously too strong become less sharp. Namely, particle number projection

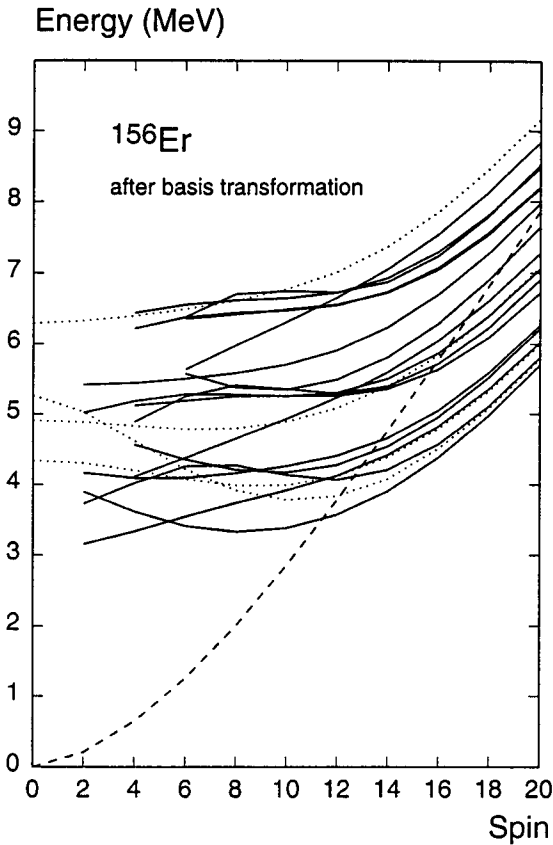


Fig. 30. A band diagram for  $^{156}\text{Er}$  after the basis transformation. The dashed line represents the  $g$ -band, the dotted lines the modified  $qp$ -pair bands, and the solid lines the  $2\text{-}qp$  bands of  $K \neq 0$ . The figure should be compared with Fig. 28. The  $qp$ -pair band which dives into the yrast region is mostly contaminated by the spurious state.

alters the result in the right direction. On the one hand, whether or not this can be achieved by fitting the force parameters is not the main issue here. What one should pay attention to in these examples is the way in which the particle number projection affects the unprojected result (i.e., it makes the  $g$ -band moment of inertia slightly larger and the  $g$ - $s$  band crossing less sharp). Actually, it would be rather difficult to correct the discrepancy in the number unprojected results simply by means of a parameter fitting without disturbing the overall agreement and the internal consistency of the theory. In this sense, particle number projection is essential for the quantitative improvement of the result. On the other hand, we notice that there is essentially no qualitative difference between the two results, in the sense that the mechanism of the backbending phenomenon discussed in the

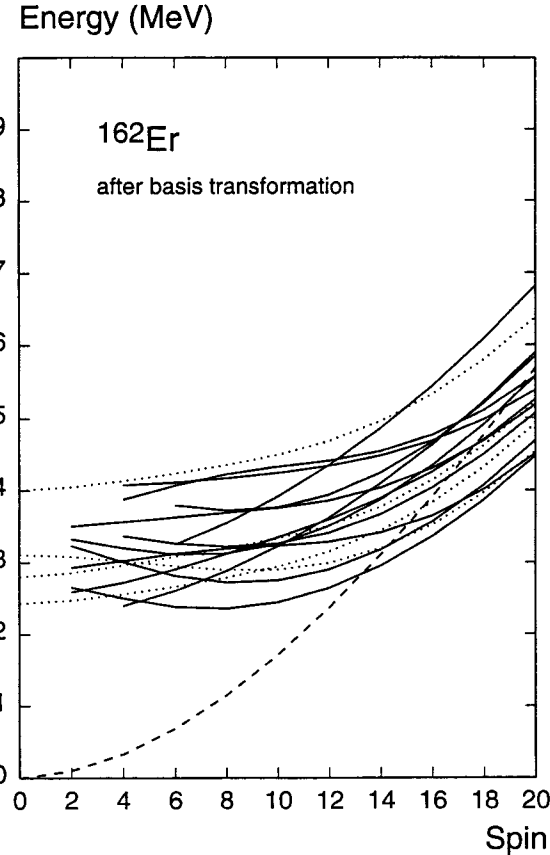


Fig. 31. A band diagram for  $^{162}\text{Er}$  after the basis transformation. The dashed line represents the  $g$ -band, the dotted lines the modified  $qp$ -pair bands and the solid lines the  $2\text{-}qp$  bands of  $K \neq 0$ . The figure should be compared with Fig. 29. The  $qp$ -pair band which dives into the yrast region is mostly contaminated by the spurious state.

previous section remains unaltered even if particle number projection is carried out in addition. All essential features of the phenomenon are already very well described by angular momentum projection alone and particle number projection adds no new physics except for some modifications in the numerical result.

#### 4.4. Magnetic moments and $E2$ transitions

The electromagnetic moments and transitions provide us with a test for the wave functions. In this section, we will present typical results<sup>70,71</sup> for the  $g$ -factors (gyro-magnetic ratios) and  $BE2$  values obtained by the Projected Shell Model and compare them with available experimental data for some doubly even rare-earth nuclei.

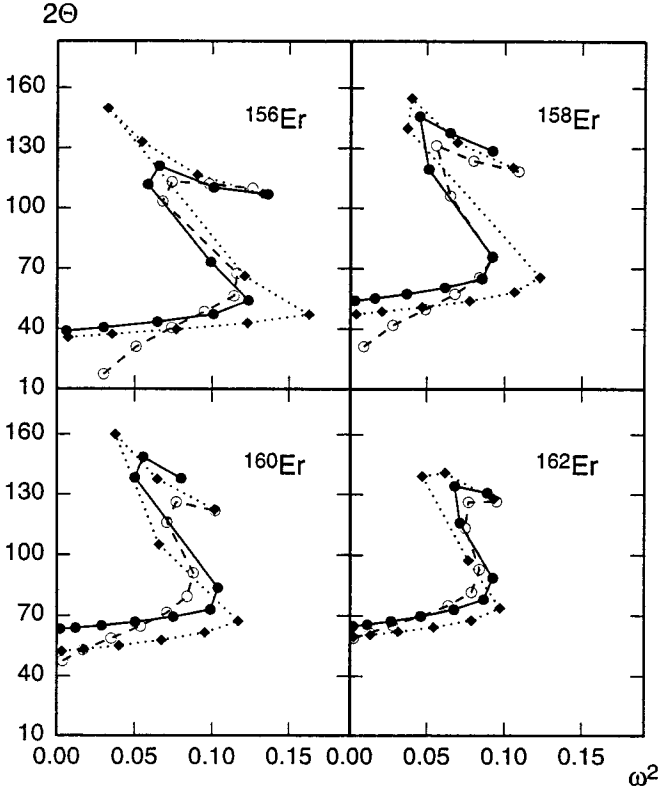


Fig. 32. Backbending plots for some Er isotopes with and without particle number projection. The particle number projected results (dots) are compared with the unprojected ones (diamonds) and with the experimental data (circles).

The matrix element of a multipole operator  $\hat{T}_{\lambda\mu}$  with respect to the (final) shell model wave functions can be evaluated by using the formula (2.39)

$$\langle \Psi_{I'M'} | \hat{T}_{\lambda\mu} | \Psi_{IM} \rangle = (IM, \lambda\mu | I'M') \langle \Psi_{I'} | \hat{T}_\lambda | \Psi_I \rangle, \quad (4.6)$$

where the reduced matrix element is defined by

$$\langle \Psi_{I'} | \hat{T}_\lambda | \Psi_I \rangle = \sum_\nu \left\{ \sum_{\kappa\kappa'} (IK' - \nu, \lambda\nu | I'K') \langle \Phi_{\kappa'} | \hat{T}_{\lambda\nu} \hat{P}_{K'-\nu K}^I | \Phi_\kappa \rangle F_{\kappa'}^{I'} F_\kappa^I \right\}. \quad (4.7)$$

Here,  $F_\kappa^I$  and  $F_{\kappa'}^{I'}$  are, respectively, the eigenvectors of the Projected Shell Model equation (2.38) for spins  $I$  and  $I'$ . For the purpose of analysis, it is recommended to study the contribution of each component ( $\nu$ ) to the reduced matrix element before adding over  $\nu$ , as indicated in (4.7). The so-called reduced transition probability is given by

$$B(E \text{ or } M\lambda; I \rightarrow I') = \frac{2I' + 1}{2I + 1} |\langle \Psi_{I'} | \hat{T}_\lambda | \Psi_I \rangle|^2. \quad (4.8)$$

In the present calculations, the effective spin  $g$ -factor for the magnetic dipole operator is taken to be 0.7 of the bare value and the effective charge for the electric quadrupole operator to be  $0.5e$ . Both of them are the standard values.

We use the usual definition for the  $g$ -factor (in unit of nuclear magneton)

$$g_I = \frac{\langle \Psi_{IM=I} | \hat{\mu}_z | \Psi_{IM=I} \rangle}{I} = \frac{\langle \Psi_I | \hat{\mu} | \Psi_I \rangle}{\sqrt{I(I+1)}}, \quad (4.9)$$

while the  $BE2$  value will be converted into the quantity (usual convention)

$$Q_t(I \rightarrow I') = \frac{1}{(I0, 20|I'0)} \sqrt{\frac{4\pi}{5} \frac{2I+1}{2I'+1} B(E2; I \rightarrow I')} = \frac{|\langle \Psi_{I'} | \hat{Q}_2 | \Psi_I \rangle|}{(I0, 20|I'0)} \quad (4.10)$$

which is meaningful only for the stretched transitions ( $\Delta I = 2$ ). Note that, in (4.10), we used the electric quadrupole moment operator  $\hat{Q}_{2\mu}$  which differs from the corresponding transition operator by a factor  $\sqrt{\frac{4\pi}{5}}$ . The electric quadrupole moment is thus given by

$$Q_I = \langle \Psi_{IM=I} | \hat{Q}_{20} | \Psi_{IM=I} \rangle = (II, 20|II) \langle \Psi_I | \hat{Q}_2 | \Psi_I \rangle \quad (4.11)$$

while the intrinsic (or static) electric quadrupole moment is defined by

$$Q_s(I) = \frac{\langle \Psi_I | \hat{Q}_2 | \Psi_I \rangle}{(I0, 20|I0)}, \quad (4.12)$$

so that the latter is related to the former (a measurable quantity) through

$$Q_s(I) = \frac{Q_I}{(I0, 20|I0)(II, 20|II)} = -\frac{2I+3}{I} Q_I. \quad (4.13)$$

A negative (positive) quadrupole moment corresponds to a positive (negative) intrinsic quadrupole moment due to the sign of the Clebsch–Gordan coefficients.

In an axially symmetric rotor model, the quantity (4.10) becomes equal to the usual static electric quadrupole moment (4.12) except for the sign and thus independent of spin, so that the ratio  $Q_t(I \rightarrow I-2)/Q_t(2 \rightarrow 0)$  is 1. As a rule, this ratio does not exceed unity either in the present theory. However, there are exceptional cases which may occur just before and after a band crossing point. At a band crossing point, on the other hand, we usually obtain a dip (sudden decrease of both the  $BE2$  value and  $g$ -factor) due to a strong destructive interference between crossing bands, which is also observed experimentally. However, in contrast to the  $\gamma$ -ray transition energies that can be measured very accurately, a precise determination of the  $g$ -factors and  $BE2$  values is difficult and their experimental data are usually associated with relatively large error bars. This is in particular the case in the high spin region.

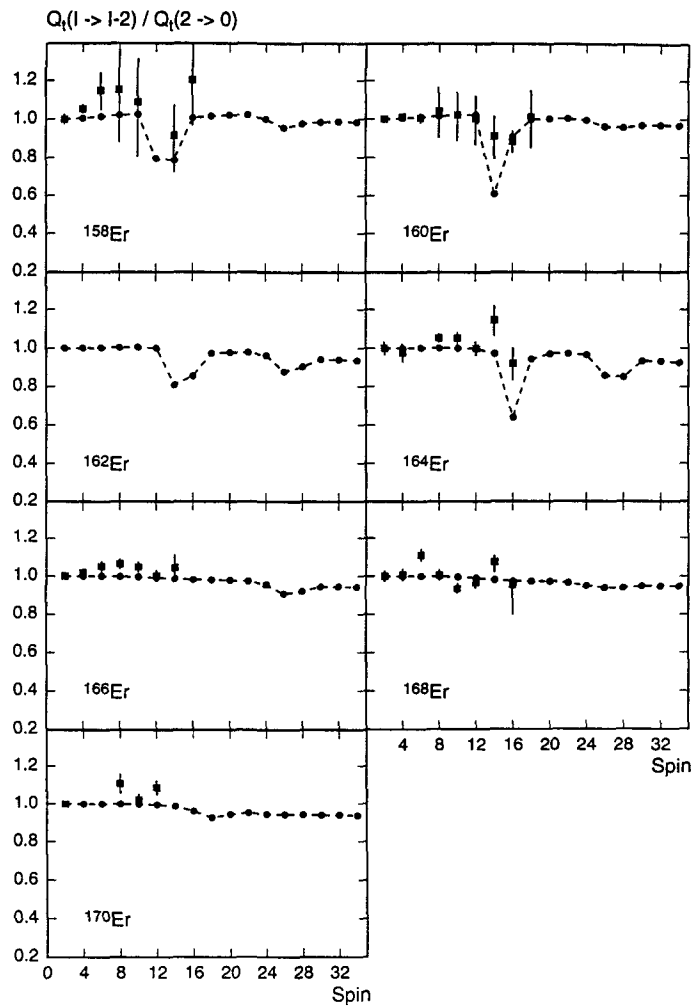


Fig. 33. The E2 transitions of  $^{158-170}\text{Er}$  isotopes. Theoretical results (dots) are compared with the experimental data (filled squares) taken from Refs. 72-77.

Figures 33 and 34 show the intra-yrast band  $BE2$  values for the nuclei  $^{158-170}\text{Er}$  and  $^{160-172}\text{Yb}$ , respectively. Theoretical results (dots) are connected through dashed lines while experimental data (filled squares) are presented together with their error bars. For the nucleus  $^{160}\text{Yb}$ , there are two independent measurements so that squares (low spin region) and triangles (high spin region) are used to distinguish them.

For three nuclei  $^{164}\text{Yb}$ ,  $^{166}\text{Yb}$ , and  $^{168}\text{Yb}$ , it is seen that the measured  $BE2$  values tend to decrease rapidly at higher spins while theoretical predictions remain almost constant. Evaluating the contribution from each component of the

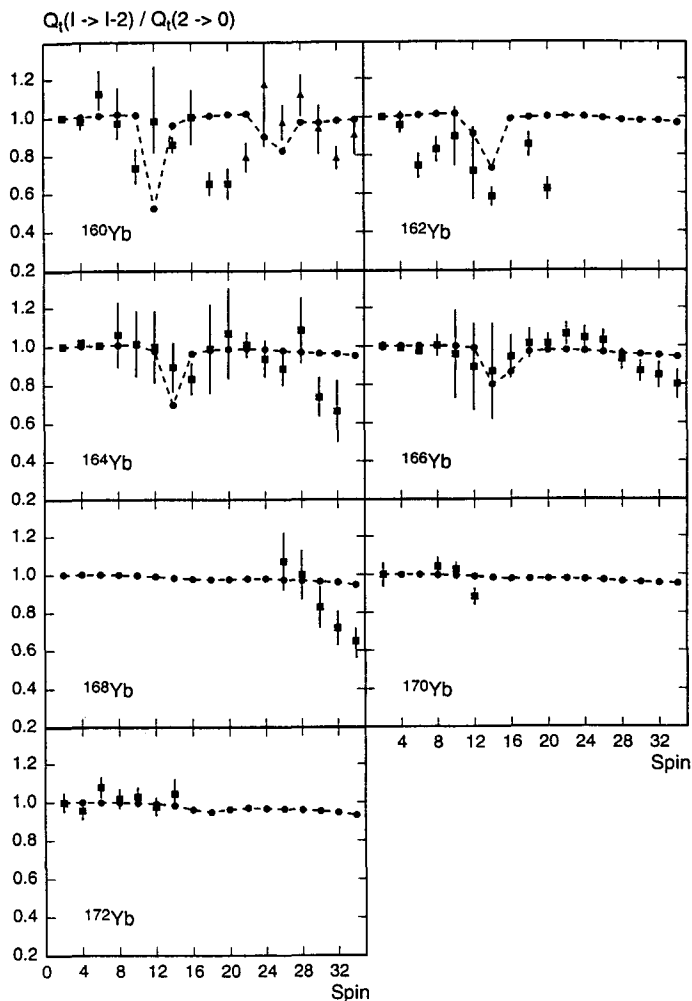


Fig. 34. The E2 transitions of  $^{160-172}\text{Yb}$  isotopes. Theoretical results (dots) are compared with the experimental data (filled squares) taken from Refs. 78–84. For the nucleus  $^{160}\text{Yb}$ , two independent measurements are marked by squares (the lower spin region) and triangles (the higher spin region).

electric quadrupole moment operator  $\hat{Q}_{2\nu}$  in the formula (4.7), we found that the contribution of the component  $\nu = 0$  decreases with spin while that of other components ( $\nu \neq 0$ ) increases, which indicates that the effective triaxiality of the nucleus increases dynamically with spin. As a result, the total value stays more or less constant. If one may conclude from the above three cases ( $^{164}\text{Yb}$ ,  $^{166}\text{Yb}$ , and  $^{168}\text{Yb}$ ) that the  $BE2$  values decrease strongly at higher spins, interesting questions arise as to whether or not this is a general trend in all other (yet unmeasured) nuclei and whether or not there is some failure in the present theory which shows no decrease

of the  $BE2$  values in the high spin region. We can only hope that more  $BE2$  values at higher spins will be measured systematically over a wider range of nuclei in the future to clarify these questions.

Figures 35 and 36 show the  $g$ -factors of the yrast states for the same series of isotopes considered above, namely, for the nuclei  $^{158-170}\text{Er}$  and  $^{160-172}\text{Yb}$ ,

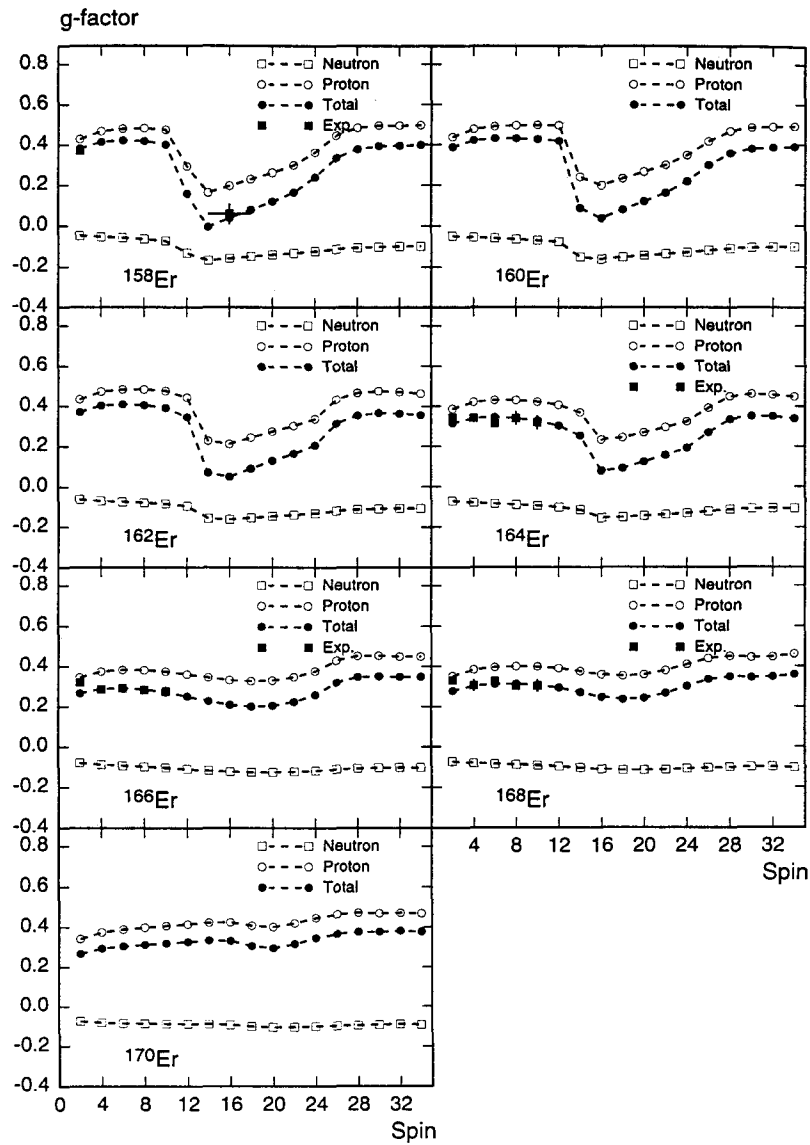


Fig. 35. The  $g$ -factors of  $^{158-170}\text{Er}$  Isotopes. Theoretical results (dots) are compared with the experimental data (filled squares) taken from Refs. 85-89. The total values are decomposed into the contributions from the neutron (circles) and proton (squares) degrees of freedom.

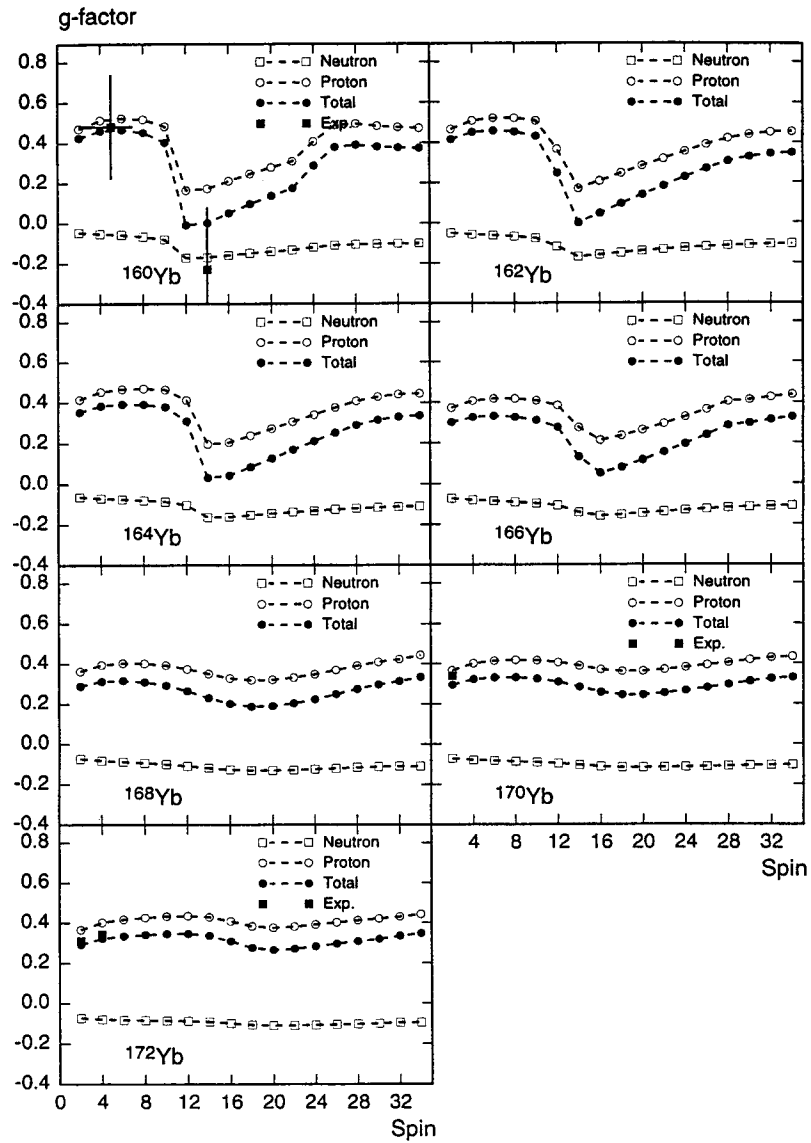


Fig. 36. The  $g$ -factors of  $^{160-172}\text{Yb}$  isotopes. Theoretical results (dots) are compared with the experimental data (filled squares) taken from Refs. 90–91. The total values are decomposed into the contributions from the neutron (circles) and proton (squares) degrees of freedom.

respectively. Theoretical results (dots) are decomposed further into the individual contribution from the neutron (squares) and proton (circles) degrees of freedom. It is seen that the  $g$ -factors originate mostly from the proton degrees of freedom. Needless to say, this is due to the magnetic moment associated with the proton

orbital angular momenta, which is absent in the case of neutrons. Experimental values (filled squares) are given whenever available. Although the number of measurements is not very large at the moment and those at higher spins in particular are still missing, one sees that the theoretical results agree well with the data. Another interesting quantity is the BM1 value of the magnetic dipole transition between two signature partners (the even- and odd-spin branches of a band) in doubly-even nuclei but no (systematic) data is available at the moment. Extensive measurements of such transitions would provide us with a very useful clue to identify the band structure.

## 5. Application to Doubly-Odd Nuclei

### 5.1. Nuclei in the mass region $A \approx 130$

For low-lying bands of doubly-odd nuclei, the quasiparticle configuration is taken as

$$|\Phi_\kappa\rangle = \{a_\nu^\dagger a_\pi^\dagger |0\rangle\} \quad (5.1)$$

where the quantum numbers for the neutron ( $\nu$ ) and proton ( $\pi$ ) run over the Nilsson states near the respective Fermi level; cf. (2.53). It should be noted that, although the configuration space spanned by (5.1) looks simple and its numerical treatment is indeed most straightforward, the level density is actually quite large (about ten times larger than that of odd-mass nuclei) so that several different configurations may contribute to the shell model wave functions with nearly equal weights even in the lowest energy region. This makes the numerical results very sensitive to the shell filling and is the reason why the theoretical predictions for doubly-odd nuclei are far more difficult than for any other types of nuclei.

A series of measurements on doubly-odd nuclei in the mass region  $A \approx 130$  has been carried out at the Pelletron Laboratory of the University of São Paulo and the data have been systematically analyzed within the framework of the present theory.<sup>70,92</sup> The analysis indicates that there are possible shape transitions in this mass region and that these nuclei may be classified in three different shapes (prolate, oblate, and triaxial) depending on the number of neutrons as shown in Table 5.

Table 5. Shape transitions in the mass region  $A \approx 130$ .

$N$	73	74	75	76	77	78	79
$^{60}\text{Nd}_N$	+0.22		+0.20		*		-0.16
$^{59}\text{Pr}_N$	+0.22	+0.21	+0.20	*	*	*	-0.16
$^{58}\text{Ce}_N$	+0.22		+0.20		*		-0.16
$^{57}\text{La}_N$	+0.22	+0.21	+0.20	*	*		

+: prolate deformation \*: presumably triaxial shape -: oblate deformation

The compilation of this table has been done according to the following criteria: On the one hand, if the theoretical result for a nucleus agreed with the experimental

data reasonably well by assuming a prolate or oblate shape, we accepted the corresponding deformation. On the other hand, if the theory failed to reproduce the data with any of the assumed axially symmetric deformation, we concluded that the nucleus in question has a triaxial shape. In this way, we found that the present theory suggests the shape transitions at the neutron numbers 76 and 78 as Table 5 shows. Since our computer code has been written assuming an axially symmetric system, this is the best we can do at the moment. Still, it is to be confirmed with the help of a triaxial projection code whether or not the spectra of the nuclei having the intermediate neutron numbers  $76 \sim 78$  are indeed consistent with the triaxial shapes. This is one of our future problems.

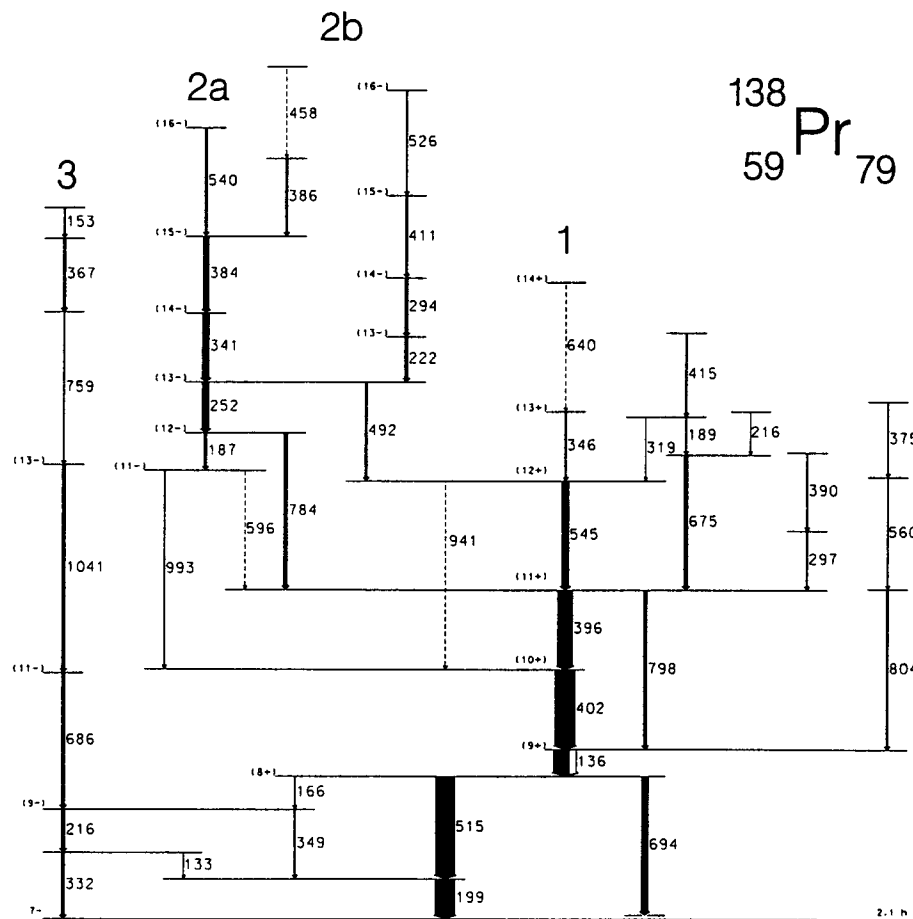


Fig. 37. The level scheme of  $^{138}\text{Pr}$ . Theoretical analysis of two low-lying bands designated as 1 (positive parity band that starts from  $8^+$ ) and 3 (negative parity band that starts from  $9^-$ ) is performed. They will be called symbolically as 55 and 54 band since the neutron and proton quasiparticles are in the major shells  $[N_\nu = 5, N_\pi = 5]$  and  $[N_\nu = 5, N_\pi = 4]$ , respectively.

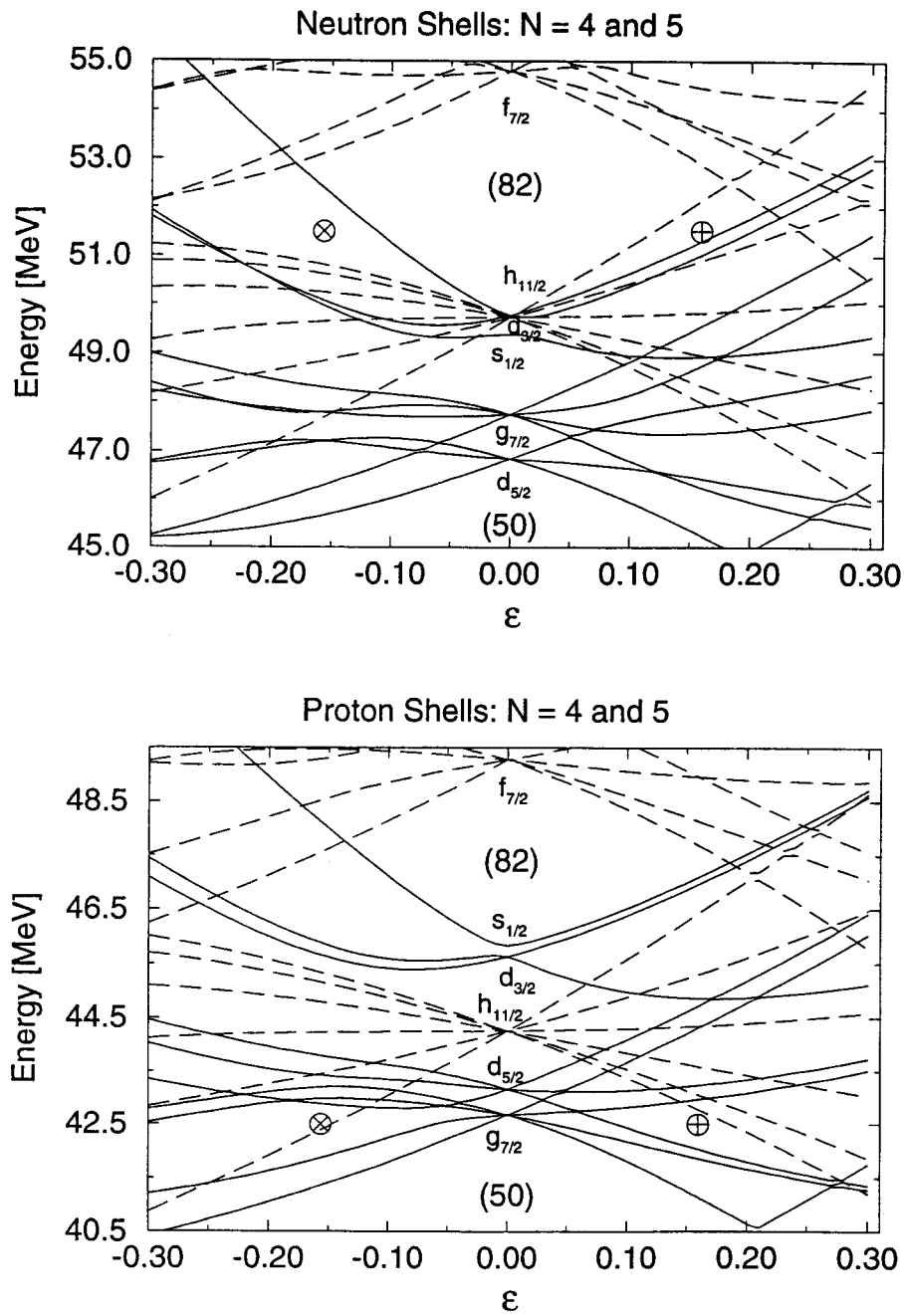


Fig. 38. Neutron and proton Nilsson diagrams for  $^{138}\text{Pr}$ . The symbol  $\oplus$  marks the location of the Fermi energy for the prolate ( $\epsilon = 0.16$ ) and  $\otimes$  for the oblate ( $\epsilon = -0.16$ ) deformation. They are roughly the mirror image of each other with respect to the vertical axis  $\epsilon = 0$ .

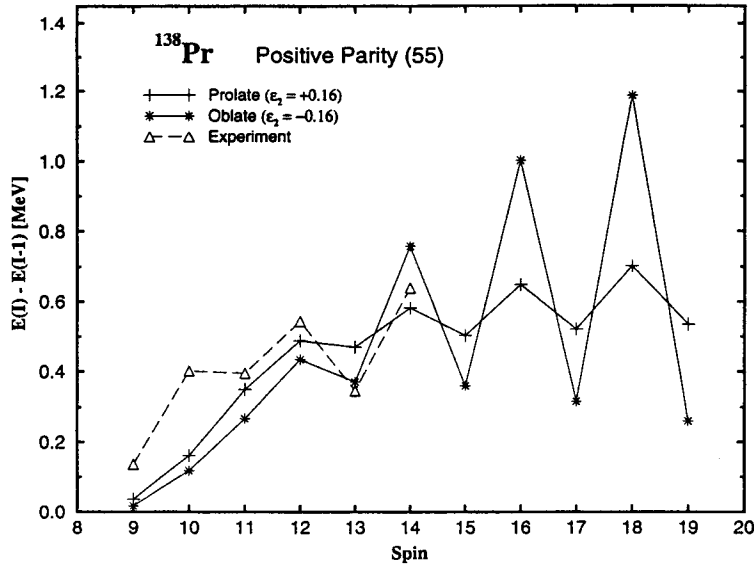


Fig. 39. Energy difference in the positive parity (55) band of  $^{138}\text{Pr}$ . The energy difference  $E(I) - E(I-1)$  of the 55 band for the prolate and oblate deformation is compared with experiment. Both shapes are consistent with data due to an accidental symmetry of the neutron and proton shell fillings against the sign flip of the deformation. Hence, no conclusion can be drawn about the shape of the nucleus  $^{138}\text{Pr}$ .

As a typical example, we will present here the analysis on the low-lying bands of the nucleus  $^{138}\text{Pr}$  and explain how we came to conclude that it has an oblate shape. The compiled level scheme of this nucleus<sup>93</sup> is shown in Fig. 37.

We concentrate on the low-lying two bands designated, respectively, as 1 (the positive parity band that starts at  $8^+$ ) and 3 (the negative parity band that starts at  $9^-$ ) in the figure. In these positive (negative) parity states, the neutron and proton quasiparticles are, respectively, in the major shells  $N_\nu = 5$  and  $N_\pi = 5$  ( $N_\nu = 5$  and  $N_\pi = 4$ ) which we refer to as the 55 (54) configuration for simplicity. In fact, the Nilsson diagram indicates that the main components consist of the configurations  $\nu h_{11/2} \otimes \pi h_{11/2}$  ( $\nu h_{11/2} \otimes \pi g_{7/2}$  and  $\nu h_{11/2} \otimes \pi d_{5/2}$ ). This is shown in Fig. 38.

To begin with, let us consider the 55 band. The analysis was done assuming the prolate shape because this was the commonly believed shape attributed to this band. As a matter of fact, the other band (54) was believed to belong to an oblate shape. Therefore, in addition, we have also done an extra calculation assuming an oblate shape for this band. Interestingly, we found that the spectra obtained by the prolate and oblate deformation are quite similar to each other. In particular, both calculations predicted the spin of the bandhead to be  $8^+$ , which is in agreement with experiment. The results of the prolate and oblate calculations performed with the deformation parameter  $|\epsilon| = 0.16$  are compared with data in Fig. 39.

We see that both the prolate and oblate shapes are compatible with the experiment. As a matter of fact, this can be understood easily from the particular shell filling of this nucleus. Namely, both the neutron and proton fill the  $h_{11/2}$  subshell which has roughly a point symmetry with respect to the zero deformation. This interchanges the role of the neutron and proton if the sign of the deformation is flipped. In fact, Fig. 39 shows that the lowest configuration is  $K_\nu = \frac{11}{2}(\nu h_{11/2}) \otimes K_\pi = \frac{1}{2}(\pi h_{11/2})$  for the prolate deformation, i.e., the neutron is in the high- $K$  orbit and the proton in the low- $K$  orbit ( $\oplus$  marks the Fermi energy). The situation is totally reversed in the oblate deformation since the lowest configuration becomes  $K_\nu = \frac{1}{2}(\nu h_{11/2}) \otimes K_\pi = \frac{11}{2}(\pi h_{11/2})$ , i.e., the neutron is in the low- $K$  orbit and the proton in the high- $K$  orbit ( $\otimes$  marks the Fermi energy). This means that the neutron and proton interchange their role if the sign of the deformation is flipped. As a result, the prolate spectrum becomes very similar to the oblate one, if not exactly the same, due among other thing to their different strengths of the neutron and proton spin-orbit force. It means that there is no definite clue as to the shape of the nucleus in the 55 band. The decisive information may be found in the 54 band where no such symmetry is expected.

Figure 40 compares the oblate and prolate spectra of the 54 configuration with experiment (the origin of the energy axis is arbitrary). It shows clearly that the data support the oblate deformation, so that one can exclude the prolate shape

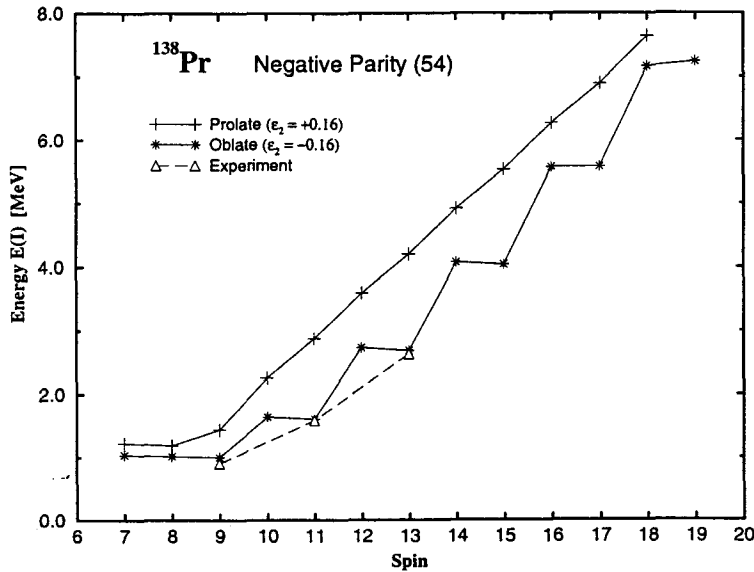


Fig. 40. Energy spectrum of the negative parity (54) band of  $^{138}\text{Pr}$ . The prolate and oblate spectra  $E(I)$  of the 54 band are compared with experiment. The origin of the energy axis is arbitrary. Only the oblate spectrum is consistent with data suggesting that the nucleus  $^{138}\text{Pr}$  is oblate. Moreover, the theory predicts the existence of the signature partners  $8^-$ ,  $10^-$ ,  $12^- \dots$ , which are degenerate respectively to the observed states  $9^-$ ,  $11^-$ ,  $13^- \dots$ .

from the consideration. According to the signature rule (3.21), the states with spins  $I = \text{odd}$  are favored in the oblate 54 configuration ( $\nu h_{11/2} \otimes \pi g_{7/2}$ ) leading to degeneracy between pairs of states  $(8^-, 9^-)$ ,  $(10^-, 11^-)$ ,  $(12^-, 13^-) \dots$ . This feature plays an important role in understanding why only the favored signature partners ( $9^-, 11^-$ , and  $13^-$ ) are observed experimentally as we will discuss in detail later. As mentioned above, the commonly believed shape for this band was in fact oblate. The present analysis shows that it is actually possible to understand both (55 and 54) spectra consistently by using the same deformation parameter if we accept the oblate shape and this is the reason why we were convinced that the nucleus  $^{138}\text{Pr}$  is oblate.

As mentioned earlier, the 55 band was believed to correspond to a prolate shape and the 54 band to an oblate shape. In fact, the present analysis does not exclude such a possibility. However, if we accept this interpretation, it will be difficult to understand the reason why such low-lying bands belong to entirely different nuclear shapes. Eventually, a legitimate investigation of the energy surface is expected to clarify this matter. Here, without going into such a study, we propose an oblate shape for this nucleus on the basis of the simplicity and consistency of the interpretation of the spectra.

We note that, in Fig. 40, the energy  $E(I)$  is plotted for the 54 band rather than the difference  $E(I) - E(I - 1)$ . This is because the measurement shows that these levels decay through the stretched  $E2$  transitions and thus the data were obtained only for a  $\Delta I = 2$  sequence although the theory predicts the  $\Delta I = 1$  sequence. It is easy to understand why this happens. The theory predicts that the signature partners  $(8^-, 9^-)$ ,  $(10^-, 11^-)$ , and  $(12^-, 13^-)$  are almost degenerate. This means that no electromagnetic transition within the partners (e.g.,  $13^- \rightarrow 12^-$ ) can take place (the vanishing photon energy). Therefore, it is due to this accidental degeneracy between the signature partner states that only the stretched  $E2$  transitions ( $13^- \rightarrow 11^- \rightarrow 9^-$ ) are observed experimentally. At the same time, this also justifies the spin assignment  $9^-, 11^-$ , and  $13^-$  made in the level scheme Fig. 37. In fact, if it were the sequence  $8^-, 10^-$ , and  $12^-$ , which is quite possible because of the predicted degeneracy, some  $\Delta I = 1$  decay such as  $12^- \rightarrow 11^-$  would have been observed. In this context, we should like to make the following remark. While the present theory predicts the states of the spin sequence  $8^-, 10^-$ ,  $12^-$ ,  $\dots$ , to be the signature partners of the observed states  $9^-, 11^-$ ,  $13^-$ ,  $\dots$ , the measurement failed to resolve them. Therefore, it remains to be seen whether these missing partners can indeed be found in the nucleus  $^{138}\text{Pr}$ . This poses the interesting technical question of how to detect those states which were “invisible” in the above experiment.

### 5.2. Signature inversion

The yrast spectrum of some doubly-odd nuclei shows the so-called inversion of the signature dependence (i.e., the phase inversion of the zigzag behavior) at moderate

spin. The observed bandhead spin usually ranges from 6 to 10, which means that the  $K$ -value of the (unperturbed) yrast band is large. This is one characteristic feature of this kind of inversion phenomenon. However, the rotational energy of such a high- $K$  band has no signature dependence as we have seen in Sec. 3; see Figs. 4 and 5. Therefore, it has to arise in the first place from the signature dependence of the high-lying decoupled low- $K$  bands which affect the smoothly behaving yrast band through the band coupling. The actual signature inversion takes place among such high-lying aligned bands through the band crossing.<sup>12</sup> This kind of mechanism is consistent with the observation that the signature dependence in such a doubly-odd nucleus is rather weak, which is another characteristic feature closely related to the first one. In most cases, it is so weak that one has to use a specially designed plot in order to disclose the presence of the signature dependence and the occurrence of the signature inversion.

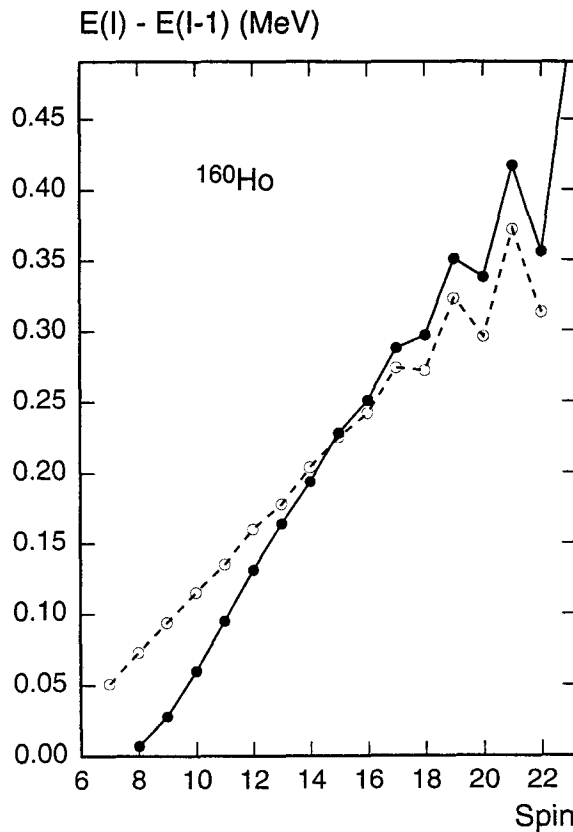


Fig. 41. The transition energies of  $^{160}\text{Ho}$ . The energy difference  $E(I) - E(I - 1)$  is compared between theory (dots) and experiment (circles). Data are taken from Ref. 94.

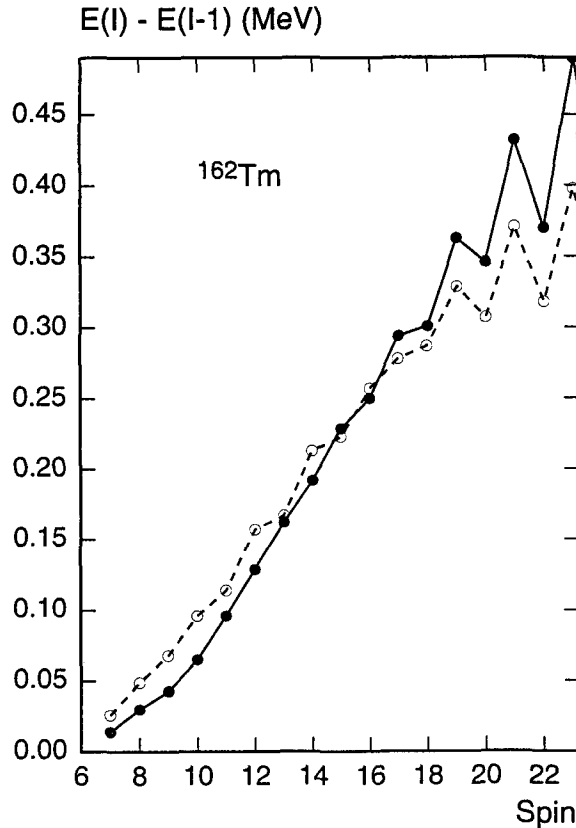


Fig. 42. The transition energies of  $^{162}\text{Tm}$ . The energy difference  $E(I) - E(I - 1)$  is compared between theory (dots) and experiment (circles). Data are taken from Ref. 95.

In this section, we present some examples from nuclei in the mass region  $A \approx 160$  and analyze the mechanism which leads to such an inversion phenomenon.<sup>12</sup> However, there is yet another possible mechanism which becomes available if a certain shell filling condition is met and may lead to another type of signature inversion. It is different from the former mechanism in that the inversion takes place without undergoing any band crossing. This will be discussed in the next section.

Figures 41 and 42 show the transition energies for the isotones  $^{160}\text{Ho}$  and  $^{162}\text{Tm}$  for the spin sequence  $\Delta I = 1$ , the dots being theory and the circles represent experiment. In order to make the signature inversion clearly visible, however, it is necessary to plot the quantity

$$F(I) - \frac{1}{2}[F(I + 1) + F(I - 1)] \quad (5.2)$$

which is proportional to the three point formula representing the second order derivative of the transition energy  $F(I) \equiv E(I) - E(I-1)$ , the proportionality constant being  $-\frac{1}{2}$ . In Fig. 43, we show this for the nucleus  $^{160}\text{Ho}$ .

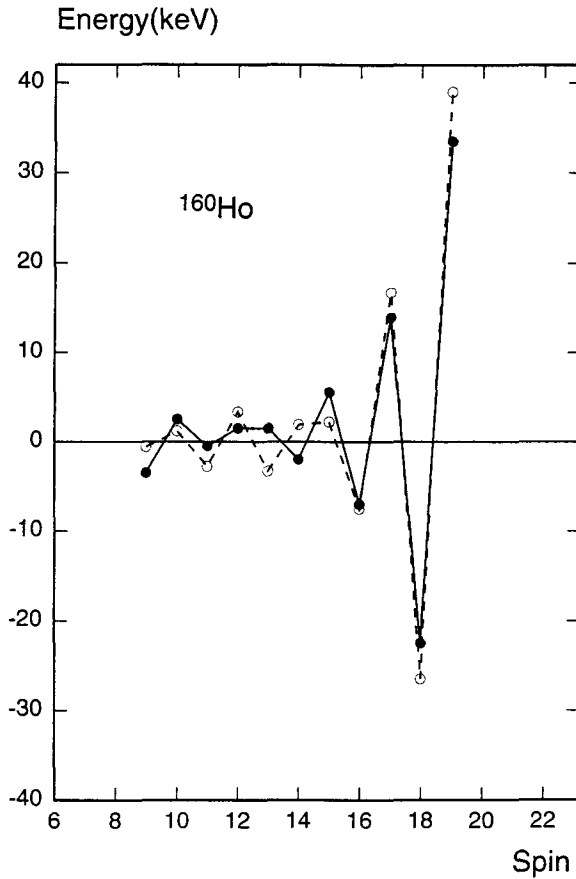


Fig. 43. The signature inversion in  $^{160}\text{Ho}$ . The signature inversion becomes clearly visible if the quantity (5.2) is plotted for theory (dots) and experiment (circles).

The actual inversion takes place at spin  $I = 15$  while the theory predicts it at  $I = 13$ . We believe that this discrepancy is due to a problem in our level scheme; see below for more details. It is best to study the corresponding band diagram in order to see the mechanism which leads to the signature inversion in question. In Fig. 44, we first show the shell filling (the neutron and proton Fermi energies) of the nucleus  $^{160}\text{Ho}$  which we obtain from the Nilsson + BCS scheme.

It shows that the lowest configuration is  $K_\nu = \frac{5}{2}i_{13/2} \otimes K_\pi = \frac{7}{2}h_{11/2}$ , so that there are two low-lying  $1\nu \otimes 1\pi$ -qp bands having  $K = 6$  and 1 ( $K = |\frac{5}{2} \pm \frac{7}{2}|$ ). Above these lowest-lying bands, there are many bands which are not of much interest

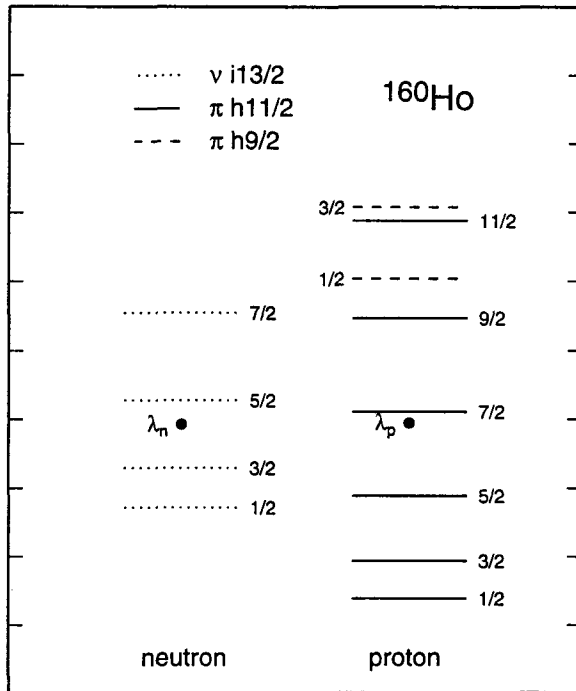


Fig. 44. Shell filling in  $^{160}\text{Ho}$ . The location of the neutron ( $\lambda_n$ ) and proton ( $\lambda_p$ ) Fermi energies are represented by dots in the Nilsson scheme.

because of their smooth behavior. Among them, however, one finds four strongly signature-dependent bands whose configurations are

$$\begin{aligned}
 1. K = 3 & \left[ \frac{3}{2} i_{13/2} \otimes \frac{3}{2} h_{11/2} \right], \quad 2. K = 2 \left[ \frac{1}{2} i_{13/2} \otimes \frac{3}{2} h_{11/2} \right], \\
 3. K = 2 & \left[ \frac{3}{2} i_{13/2} \otimes \frac{1}{2} h_{9/2} \right], \quad 4. K = 1 \left[ \frac{1}{2} i_{13/2} \otimes \frac{1}{2} h_{9/2} \right].
 \end{aligned} \tag{4.3}$$

The former two ( $\nu i_{13/2} \otimes \pi h_{11/2}$ ) and the latter two ( $\nu i_{13/2} \otimes \pi h_{9/2}$ ) have mutually opposite signature dependence with  $I =$  even and odd as favored bands, respectively. Figure 45 shows these four bands as well as the aforementioned two lowest-lying bands.

In the figure, dots represent the yrast levels obtained by the shell model diagonalization including all low-lying bands, most of which are not plotted in the band diagram Fig. 45 for clarity. Obviously, the signature dependence in the low (high) spin region originates from the excited bands #1 and #2 (#3 and #4) listed in (5.3) through their coupling to the lowest band. The influence of the bands  $\nu i_{13/2} \otimes \pi h_{11/2}$  (dotted lines) is larger in the low spin region while that of the bands  $\nu i_{13/2} \otimes \pi h_{9/2}$  (dashed lines) is larger in the high spin region. In other words, the inversion of

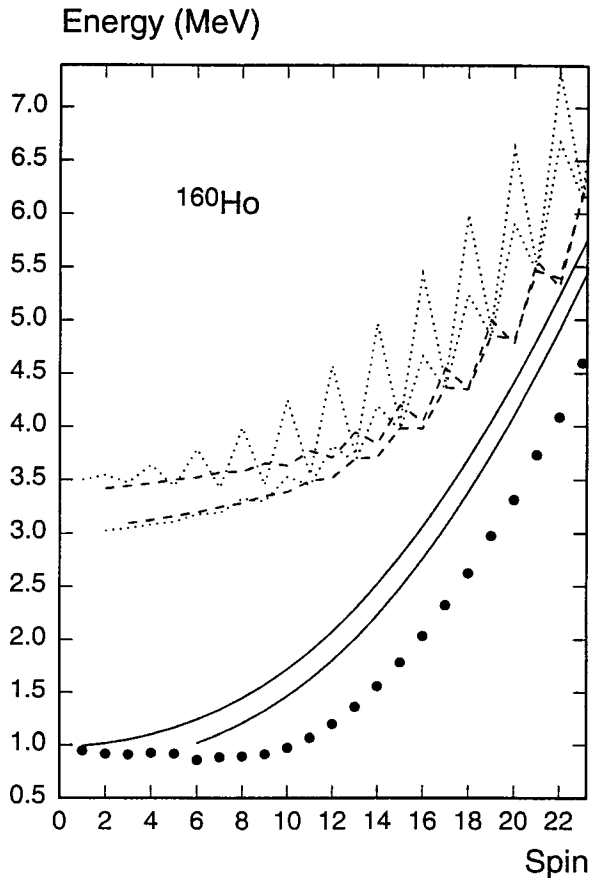


Fig. 45. A band diagram for  $^{160}\text{Ho}$ . The band energies are shown for the excited bands  $\nu i_{13/2} \otimes \pi h_{11/2}$  (dotted lines) and  $\nu i_{13/2} \otimes \pi h_{9/2}$  (dashed lines) as well as the lowest two bands (solid lines), see text for their detailed configurations.

the signature is caused by the crossing of these bands, which can be indeed seen in Fig. 45. If the proton subshell  $h_{9/2}$  was slightly far away from the subshell  $h_{11/2}$ , the crossing would have taken place somewhat later, shifting the inversion point to a larger spin. This is the reason why we have stated that the discrepancy between theory and experiment is due to a problem in the level scheme. One can also make another important observation. The experimental data seems to indicate that the signature dependence in the low spin region increases with the proton number, as can be seen in Figs. 41 ( $^{160}\text{Ho}$ ) and 42 ( $^{162}\text{Tm}$ ). This fact seems to contradict with the assumption that these nuclei are axially symmetric since an axially symmetric level scheme implies that the low  $K$ -valued orbitals of the subshell  $\pi h_{11/2}$  would move away from the proton Fermi level as the proton number increases (cf. Fig. 44), and as a consequence, the signature dependence in the low spin region would be

reduced. This is in fact what we see in the present calculation which is based on an axially symmetric scheme. Because of this fact, one may not fully exclude the possibility that triaxiality develops with the increasing proton number along this isotone chain.

### 5.3. Selfinversion

The present theory predicts that some  $1\nu \otimes 1\pi$ -qp bands show an appreciable signature dependence which undergoes selfinversion as demonstrated in Sec. 3; cf. Figs. 4 and 5. As we mentioned there, certain conditions have to be met for the occurrence of such a strongly signature dependent band. In the first place, both neutron and proton must be in the decoupled low- $K$  states (a doubly aligned band). Secondly, the  $K$ -values of the neutron ( $K_\nu$ ) and proton ( $K_\pi$ ) must have opposite signs so that it belongs to a low- $K$  configuration ( $K = K_\nu + K_\pi$ ). Consequently, such a band starts at a low spin ( $|K| \leq I$ ). If it happens to be the yrast band, the spectrum will undergo signature inversion without any band crossing.<sup>12</sup> Note that this kind of inversion phenomenon has rather opposite characteristics compared to that discussed in the previous section, namely, the spectrum starts at a low spin and shows an appreciable signature dependence. Unfortunately, appropriate examples are difficult to find among the measured doubly-odd nuclei, so that we will present a model calculation in order to demonstrate its typical feature. We will take a case where

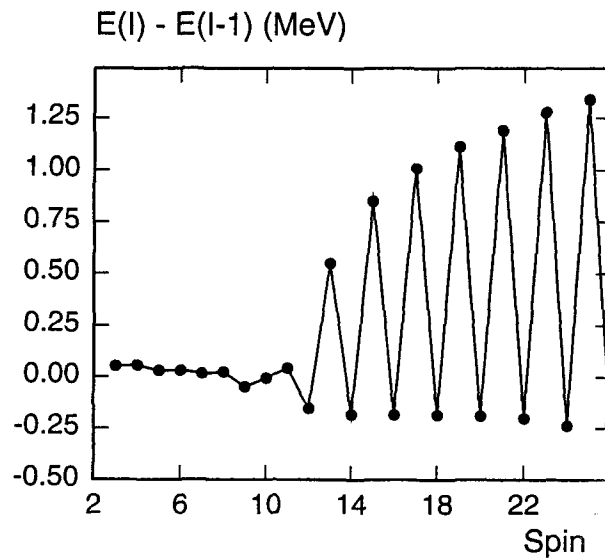


Fig. 46. The selfinversion of the signature dependence in the yrast levels of the nucleus  $^{150}\text{Pm}$ . The selfinversion of the signature dependence is demonstrated for the doubly aligned configurations. The lowest configuration is  $K_\nu = \frac{1}{2}(i_{13/2}) \otimes K_\pi = \frac{3}{2}(h_{11/2})$  where both neutron and proton states are well aligned.

the neutron and proton Fermi energies are, respectively, around the  $K_\nu = \frac{1}{2}i_{13/2}$  and  $K_\pi = \frac{3}{2}h_{11/2}$  orbits, which would correspond to the nucleus  $^{150}\text{Pm}$ . Figure 46 shows the result.

The smooth behavior below  $I = 9$  is due to the interference of many (self-inverting) bands causing a mutual cancellation of individual effect. Indeed, the occurrence of a high level density even in the vicinity of the ground state is a typical feature of a doubly-odd nucleus. The result therefore depends most sensitively on the level scheme used. Nevertheless, one can see a clear signature inversion at  $I = 10$  which is caused by a selfinversion mechanism. Beyond this spin, the signature dependence of all bands coincides with each other and thus the yrast level shows a very strong splitting. Note that the signature rule becomes  $I = \text{even}$  for the favored band and  $I = \text{odd}$  for the unfavored band ( $j_\nu + j_\pi = 12$ ) in the asymptotic (i.e., the high spin) region.

## 6. Application to Odd-Mass Nuclei

### 6.1. Odd-neutron nuclei

The quasiparticle configurations for odd-neutron nuclei are taken to be

$$|\Phi_\kappa\rangle = \{a_\nu^\dagger |0\rangle, a_\nu^\dagger a_{\pi_1}^\dagger a_{\pi_2}^\dagger |0\rangle\}. \quad (6.1)$$

However, in contrast to the odd-proton case to be discussed later, the  $3qp$  (i.e.,  $1\nu \otimes 2\pi$ ) configurations do not contribute very much to the results in the spin-energy region of interest because the spin alignment of the  $2\pi$ -qp  $K = 1$  state is rather small in comparison to the  $2\nu$ -qp  $K = 1$  state (the  $s$ -band) as we have seen in doubly-even nuclei. It should therefore be stated clearly that, even if we use the configuration (6.1), the following analysis corresponds essentially to that of the  $1\nu$ -qp configuration space. The use of the configuration space (6.1) is simply due to the technical reason that the odd-neutron code can be most easily generated from the odd-proton code in which the inclusion of the  $3qp$  (i.e.,  $1\pi \otimes 2\nu$ ) components is essential. As to the  $3\nu$ -qp configurations which are neglected, we point out that the experimental data presently stop at the beginning of the spin-energy region where the contribution of the  $3\nu$ -qp components is expected to become important. We also mention that the analysis of data within the  $1\nu$ -qp configuration space has been done over a large number of odd-neutron rare-earth nuclei,<sup>10</sup> taking also particle number projection into account. However, it was found that the results with and without particle number projection do not differ very much from each other. This again confirms that angular momentum projection alone describes the essence of the physics quite well.

We present the analysis of the positive parity states of the odd-neutron nuclei  $^{161-167}\text{Er}$  and  $^{163-169}\text{Yb}$ , respectively, in Figs. 47 and 48. The comparison is made for the theoretical results (dots) and experimental data (circles) of the energy difference  $E(I) - E(I - 1)$ . The bandhead spins are therefore one less than the starting spins

of these plots. The agreement is so good that in most cases the theoretical points overlap with the experimental ones. More examples including in addition some Hf isotopes can be found in Ref. 10.

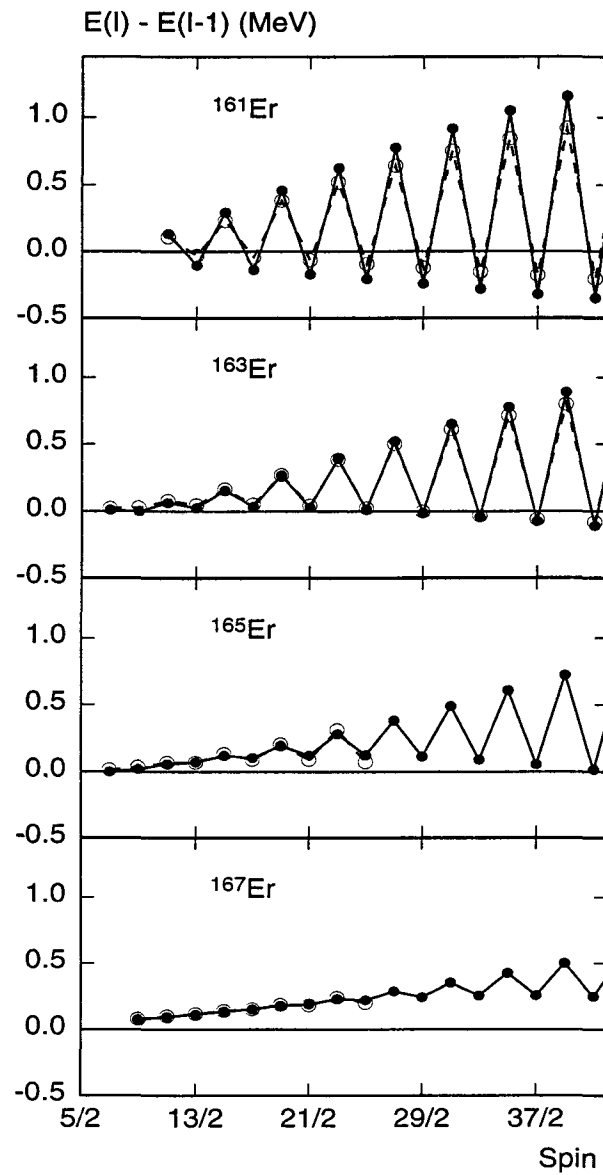


Fig. 47. The transition energies of the positive parity (yrast) states in some odd neutron Er isotopes. The transition energies  $E(I) - E(I - 1)$  are compared for the theoretical results (dots) and the experimental data (circles). The data are taken from Refs. 96–99. The agreement is so good that they overlap on top of each other and cannot be distinguished in most cases.

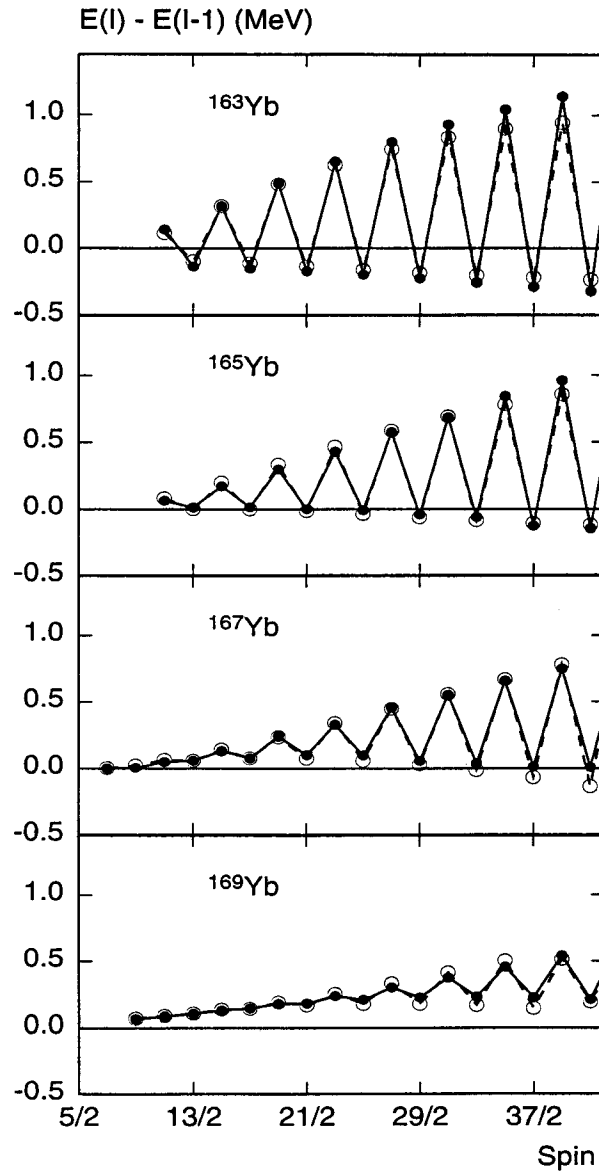


Fig. 48. The transition energies of the positive parity (yrast) states in some odd neutron Yb isotopes. The transition energies  $E(I) - E(I - 1)$  are compared for the theoretical results (dots) and the experimental data (circles). The data are taken from Refs. 100–103. The agreement is so good that they overlap on top of each other and cannot be distinguished in most cases.

We notice here the interesting phenomenon that the bandhead spin of the nucleus  $^{161}\text{Er}$  ( $^{165}\text{Yb}$ ) is  $\frac{9}{2}^+$  while that of the neighboring nucleus  $^{163}\text{Er}$  ( $^{167}\text{Yb}$ ) is  $\frac{5}{2}^+$ . This means that, when two more neutrons are added to the nucleus  $^{161}\text{Er}$  ( $^{165}\text{Yb}$ ),

there occurs a sudden change of the bandhead spin. In these neighboring isotopes, the neutron Fermi level is close to the  $K = \frac{5}{2}$  Nilsson orbit of the  $i_{13/2}$  subshell so that the  $K = \frac{9}{2}$  orbit lies much higher. Thus, one usually expects the band to start with the spin  $\frac{5}{2}$  according to the rule  $|K| \leq I$ . It is therefore interesting to establish what kind of mechanism is responsible for the occurrence of such a unexpected bandhead spin.

The occurrence of the lowest state of  $I = \frac{9}{2}^+$  in the region where we expect it to be  $I = \frac{5}{2}^+$  is anomalous. Actually, we can find many nuclei which exhibit similar spin anomalies in the present mass region. Table 6 shows the compilation of the empirical data<sup>104</sup> of some odd-neutron rare-earth nuclei.

Table 6. Empirical spin anomalies of the lowest positive parity states.

<i>N</i>	89	91	93	95	97	99	101
$^{64}\text{Gd}_N$	<b>9/2</b>	5/2	5/2	5/2			
$^{66}\text{Dy}_N$	<b>9/2</b>	<b>9/2</b>	5/2	5/2	5/2		
$^{68}\text{Er}_N$		<b>9/2</b>	<b>9/2</b>	5/2	5/2	7/2	
$^{70}\text{Yb}_N$			<b>9/2</b>	<b>9/2</b>	5/2	7/2	7/2

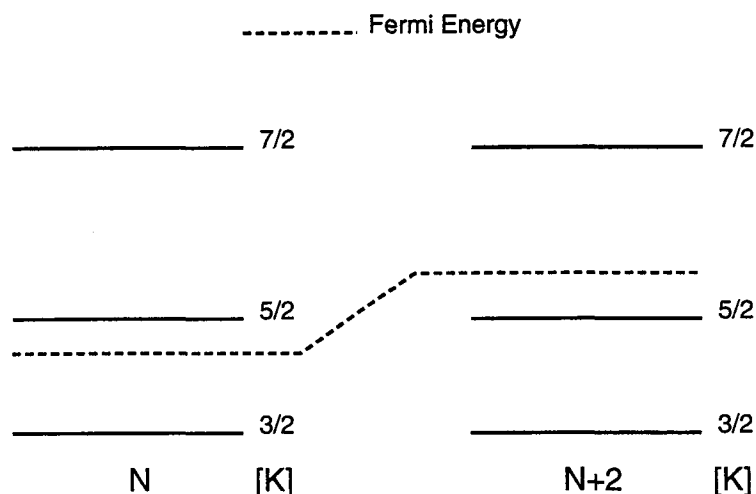


Fig. 49. Comparison of the neutron Fermi energies in the isotopes having the neutron number  $N$  and  $N + 2$ . The figure shows schematically how the neutron Fermi energy of the system of  $N$  neutrons (left) changes when two more neutrons are added to it (right). They correspond, for example, to the isotopes  $^{161}\text{Er}$  and  $^{163}\text{Er}$ , respectively. Compare Figs. 50 and 51 to see how the band diagrams of these isotopes differ from each other.

The mechanism leading to this spin anomaly is actually very simple. It is due to the  $K = \frac{3}{2}^+_1$  orbit, which is rather well aligned (i.e., signature dependent): cf. Fig. 3. This orbit will constitute the first excited band for those nuclei which have

a bandhead spin  $\frac{9}{2}^+$ . However, if two more neutrons are added to such a nucleus, the  $K = \frac{7}{2}i_{13/2}$  orbit will become the first excited band, which is not aligned and thus has no signature dependence. This situation is schematically shown in Fig. 49. In both cases, the neutron orbit  $K = \frac{5}{2}i_{13/2}$  is the yrast band whose rotational energy is a smoothly increasing function of spin showing no staggering.

In the first case, the  $I = \frac{9}{2}$  states of the  $K = \frac{5}{2}$  yrast band and the  $K = \frac{3}{2}$  first excited band come particularly close to each other because of the signature dependence of the latter. As a result, one of the spin  $\frac{9}{2}$  states is largely pushed down through the band coupling and becomes the lowest positive parity state after the shell model diagonalization. The states of  $I = \frac{5}{2}$  and  $\frac{7}{2}$  still belong to the same band but appear higher than that of  $I = \frac{9}{2}$ . In this way, the spin of the lowest

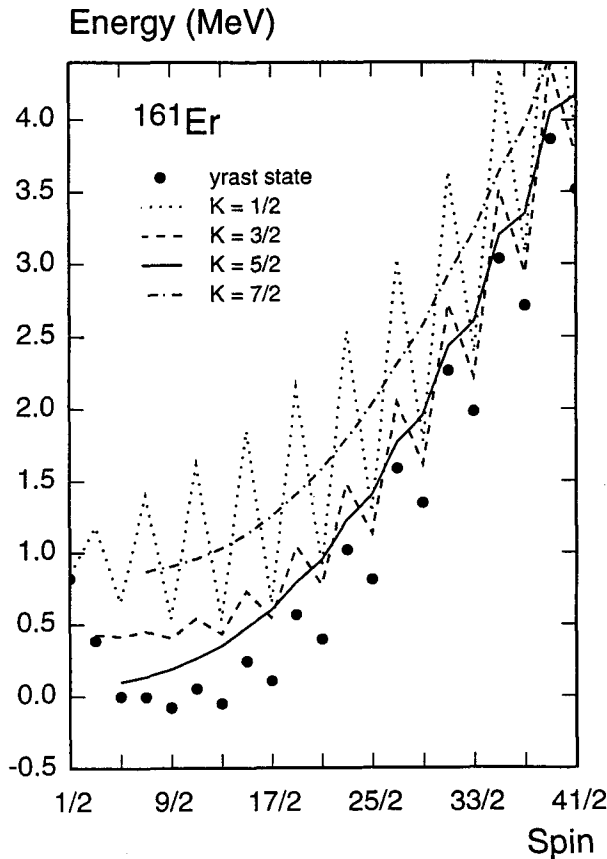


Fig. 50. A band diagram for the nucleus  $^{161}\text{Er}$ . In this nucleus, the shell filling is such that the  $K = \frac{5}{2}$  band is the yrast band and the  $K = \frac{3}{2}$  band the first excited band in the low-spin region. Due to the signature dependence of the latter, the lowest state in this band is  $I = \frac{9}{2}$  rather than  $\frac{3}{2}$ . A state with  $I = \frac{9}{2}$  is therefore pushed down when the shell model diagonalization is carried out and becomes the lowest state leading to the spin anomaly. The dots in the figure represent the yrast states thus obtained.

state becomes  $\frac{9}{2}$ . This mechanism is clearly demonstrated in Fig. 50 which shows the band diagram of a few low-lying rotational bands of the nucleus  $^{161}\text{Er}$ .

In the second case, where the  $K = \frac{3}{2}$  band is now the second excited band because of two more neutrons, the coupling between the  $K = \frac{5}{2}$  yrast band and  $K = \frac{7}{2}$  first excited band no longer produces such a prominent effect as in the first case since the latter is a smoothly behaving band due to a large  $K$ -value (no alignment). The bandhead spin therefore becomes  $\frac{5}{2}^+$  as expected from the rule  $|K| \leq I$ . We show this in Fig. 51 for the nucleus  $^{163}\text{Er}$ . Incidentally, if further neutrons are added, the  $K = \frac{7}{2}$  band will eventually become the yrast band leading to the bandhead spin  $\frac{7}{2}^+$ . This can be seen in Table 6.

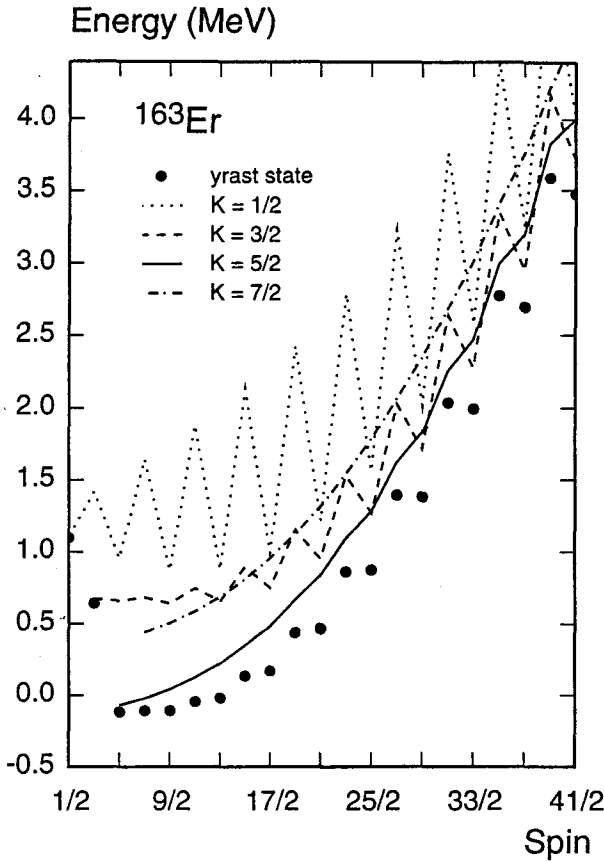


Fig. 51. A band diagram for the nucleus  $^{163}\text{Er}$ . In this nucleus, the shell filling is such that the  $K = \frac{5}{2}$  band is the yrast band and the  $K = \frac{7}{2}$  band the first excited band in the low-spin region. However, since the latter has no signature dependence (no alignment), nothing spectacular happens and the spin of the lowest state becomes  $I = \frac{5}{2}$  even after the shell model diagonalization. The dots in the figure represent the yrast states thus obtained. Namely, the spin of the lowest state is normal as dictated by the Nilsson scheme.

In both the cases discussed above, the most strongly signature-dependent band  $K = \frac{1}{2}i_{13/2}$  is rather far away from the Fermi level and has no appreciable influence on the bandhead spin. This was confirmed in Ref. 10 by repeating the same calculations excluding the  $K = \frac{1}{2}$  band. Therefore, it is the effect of the first excited band ( $K = \frac{3}{2}$  or  $\frac{7}{2}$ ) which determines whether the bandhead spin becomes anomalous ( $\frac{9}{2}$ ) or normal ( $\frac{5}{2}$ ) and this depends sensitively on the neutron shell filling.

The spin anomaly discussed above demonstrates clearly the importance of the signature dependence in the  $K = \frac{3}{2}$  band, which is a manifestation of the quantum mechanical features of the present theory. This kind of phenomenon may therefore provide us with a useful hint about the direction along which the refinement of the particle-rotor model should be attempted.

### 6.2. *M1 transitions*

In order to test the shell model wave functions obtained in the previous section, let us consider the *M1* transitions. The necessary formulas have already given in (4.6)–(4.8):

$$B(M1; I \rightarrow I') = \frac{3}{4\pi} \frac{2I' + 1}{2I + 1} |\langle \Psi_{I'} | \hat{\mu} | \Psi_I \rangle|^2 \quad (6.2)$$

which is measured in unit of (nuclear magneton)<sup>2</sup>.

Figure 52 shows the theoretical results (dots) of *BM1* values between the positive parity states for the nuclei <sup>163–169</sup>Yb. The experimental values (circles) are plotted so far as measurements are available. As we can see from Fig. 48, these nuclei show clear signature splitting. This reflects to the *BM1* values as Fig. 52 shows. The spins of the favored (unfavored) states are given by  $I = i \pm$  even (odd) according to the signature rule (3.13) in which  $i = \frac{13}{2}$  in the present nuclei. We see that the *BM1* value for the transition going from the favored to unfavored state is larger than that going from the unfavored to favoured state, namely, we find in most cases the relation

$$B(M1; I + 1 \rightarrow I) < B(M1; I \rightarrow I - 1) \quad (I = \text{spin of a favored state}). \quad (6.3)$$

In other words, the zigzag phase of  $B(M1; I \rightarrow I - 1)$  is opposite to that of  $E(I) - E(I - 1)$ . This is due to a similar interference effect of the aligned intrinsic states to the one which is responsible for the signature dependence of the spectrum discussed in Sec. 3.2. We notice however that there occurs an inversion of the zigzag phase in the theoretical *BM1* values in the low spin region for heavier isotopes (<sup>167</sup>Yb and <sup>169</sup>Yb), in which the relation (6.3) is reversed. This is a rather unexpected result. However, we will show in a moment that it is not an unique feature of the present theory.

We notice in Fig. 52 that the larger *BM1* values from favored ( $I_f$ ) to unfavored state  $B(M1; I_f \rightarrow I_f - 1)$  are observed in the nucleus <sup>163</sup>Yb but not in the neighboring nucleus <sup>165</sup>Yb, although the smaller *BM1* values from unfavored ( $I_u$ ) to favored state  $B(M1; I_u \rightarrow I_u - 1)$  are measured in both nuclei. The strange fact about the

nucleus  $^{165}\text{Yb}$  is that the larger  $BM1$  values are not observed experimentally even if the smaller ones are measured. Actually, this is quite easy to understand from the fact that the corresponding initial and final states in this nucleus are accidentally degenerate,  $E(I_f) - E(I_f - 1) = 0$ , as we can confirm in Fig. 48. These  $BM1$  values will thus remain unmeasured simply because no electromagnetic transition can take place between two degenerate states (i.e., the vanishing photon energy). The electromagnetic decay of such a favored state will therefore proceed to the next favored state through a stretched  $E2$  transition ( $\Delta I = 2$ ). We have encountered a similar example of this kind in the doubly-odd nucleus  $^{138}\text{Pr}$ ; see Sec. 5.3.

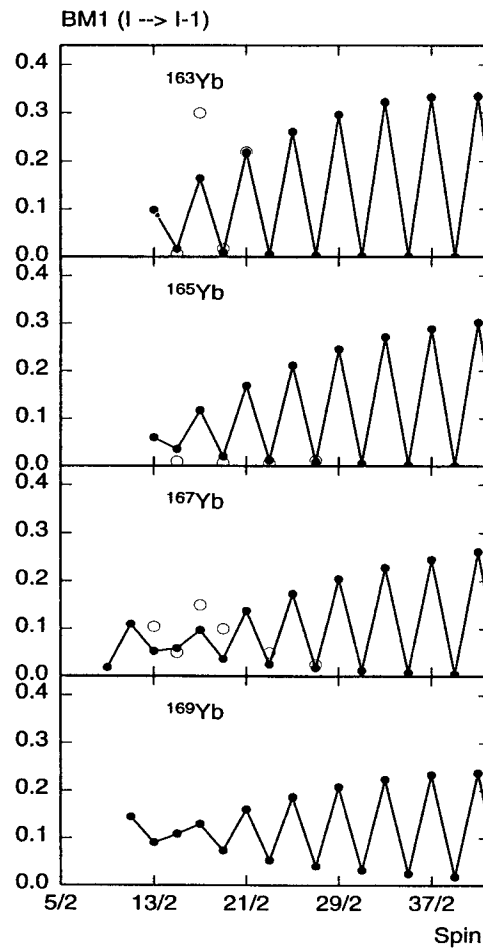


Fig. 52. The  $M1$  transitions between the positive parity (yrast) states in some odd neutron  $\text{Yb}$  isotopes. The theoretical  $BM1$  values (dots) are compared with the experimental data (circles) whenever available. The data are taken from Refs. 105 and 106. The spectra corresponding to these isotopes are shown in Fig. 48.

For the sake of comparison, we performed the corresponding calculations using the particle-rotor model in the  $i_{13/2}$  subshell. The particle part ( $p$ ) of the reduced matrix element of a multipole operator  $T_{\lambda\mu} = T_{\lambda\mu}^{(R)} + T_{\lambda\mu}^{(p)}$  for the transition  $I \rightarrow I'$  is given by

$$\begin{aligned} & \sqrt{\frac{2I+1}{2I'+1}} \langle \Phi_j | T_{\lambda}^{(p)} | \Phi_j \rangle \sum_{\nu KK'} (u_K u_{K'} + v_K v_{K'}) \{ (IK, \lambda\nu | I'K') (jK, \lambda\nu | jK') \\ & + (-)^{I-j} (I-K, \lambda\nu | I'K') (j-K, \lambda\nu | jK') \} F_K^I F_{K'}^{I'} \end{aligned} \quad (6.4)$$

where  $F_K^I$  and  $F_{K'}^{I'} (K = \frac{1}{2}, \dots, \min\{j, I\}$  and  $K' = \frac{1}{2}, \dots, \min\{j, I'\})$  are the eigenvectors of the particle-rotor model Hamiltonian (3.1). Note that the second product of the Clebsch-Gordan coefficients contributes only if  $K = K' = \frac{1}{2}$  and  $\nu = 1$ . In the case of the  $M1$  transitions, we have  $T_{1\nu} = \frac{3}{4\pi} \mu_\nu$  where the magnetic dipole operator is given by

$$\mu_\nu = g_R R_\nu + g_s s_\nu + g_l l_\nu = g_R I_\nu + \{(g_s - g_R) s_\nu + (g_l - g_R) l_\nu\} \equiv \mu_\nu^{(R)} + \mu_\nu^{(p)}.$$

Although (6.4) represents only the contribution from the (quasi-) particle degrees of freedom, it is in fact the only possible contribution for an  $M1$  transition ( $I \neq I'$ ), so that the spin independent factor  $\langle \Phi_j | \mu^{(p)} | \Phi_j \rangle$  is unimportant for the present discussion. The reduced transition probability  $B(M1; I \rightarrow I')$  of (6.2) is therefore proportional to the square of the factor consisting of the sum over  $\nu KK'$  in (6.4) with  $\lambda = 1$ , which we will refer to as the  $M1$  (transition) amplitude.

The results of various test calculations in the particle-rotor model can be summarized as follows. On the one hand, the energy difference  $E(I) - E(I-1)$  becomes small (large) for the spin  $I = j \pm \text{even} (\text{odd})$  which is nothing other than the classical signature rule (3.13). However, it should be mentioned that the quantitative comparison of the energy difference (or the spectrum itself) with the experimental data is so bad that it does not make any sense. This is one of the well-known failures of the particle-rotor model, to which we will return later. On the other hand, the staggering of  $B(M1; I \rightarrow I-1)$  in the high spin region becomes the opposite of this rule in accordance with (6.3) while, in the low spin region, the inversion of the zigzag phase may also occur in this model under certain circumstances. Namely, depending on the shell filling, the critical spin across which the inversion takes place may appear around  $I \approx j = \frac{13}{2}$ , so that the zigzag behavior of the  $BM1$  values and the energy differences becomes the same for  $I < \frac{13}{2}$  and the opposite for  $I \geq \frac{13}{2}$ . In passing, we note that the staggering of the energy spectrum and  $BM1$  values disappear if we exclude the  $K = \frac{1}{2}$  (aligned) band from the configuration. This indicates that they originate from the same mechanism.

To understand these results, we decomposed the  $M1$  transition amplitude into three ( $\nu = \pm 1, 0$ ) components and studied their behavior. On the one hand, the absolute value of the  $\nu = 0$  transition amplitude always increases smoothly with spin  $I$ . On the other hand, the magnitude of the  $\nu = -1$  component becomes small

(large) for spins  $I = j \pm$  even (odd) with decreasing zigzag amplitudes while that of the  $\nu = 1$  component behaves exactly opposite to the  $\nu = -1$  component with increasing zigzag amplitudes. The sign of the  $\nu = -1$  component is opposite to those of the  $\nu = 0$  and 1 components, so that there is always a partial cancellation between them causing the staggering of the  $M1$  transition amplitude (the sum of three components). In order to make the analysis easier, we fixed the signs of the  $M1$  amplitudes such that they oscillate between plus and minus values according to the usual signature rule. Note that such a sign convention can be introduced rather freely since the  $BM1$  value is the square of the amplitude. The main point of the present discussion is that, even if the  $M1$  amplitudes follow a regular signature

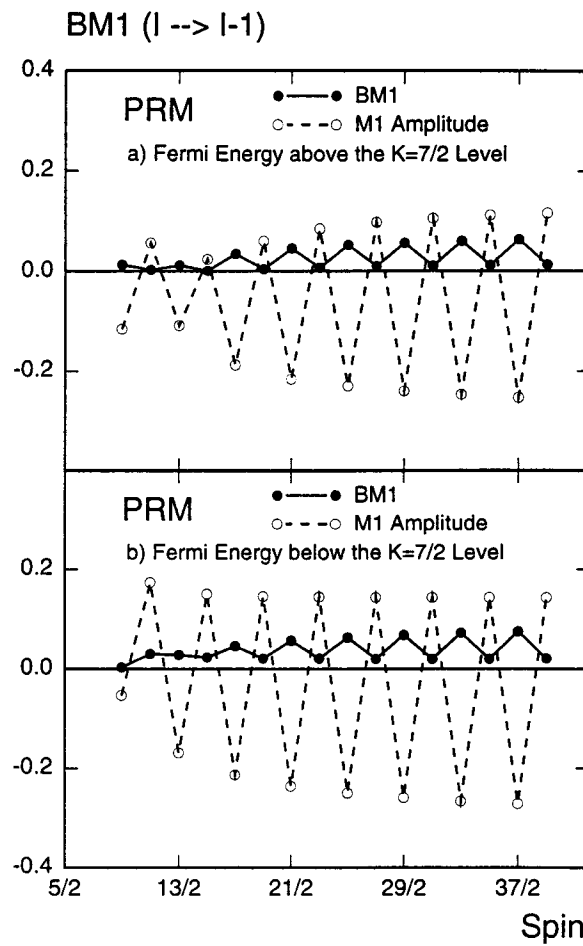


Fig. 53. The  $BM1$  values and the transition amplitudes in the particle-rotor model. The upper (lower) figure shows the  $BM1$  values and the corresponding  $M1$  transition amplitudes for the case of the Fermi energy lying just above (below) the  $K = \frac{7}{2}$  Nilsson level. See text for the phase (sign) convention of the amplitudes.

pattern, the inversion of the zigzag phase may occur when they are squared. We show two numerical examples in Fig. 53.

Although these results may seem suggestive, one should not proceed to find quantitatively when and where the inversion takes place since the answer to such questions may not necessarily be unique. It is known that the particle-rotor model fails to reproduce the observed spectra in many cases (e.g., even the spins of the lowest states are predicted incorrectly). This is mostly due to the fact that the Coriolis force, which is the term  $-\mathbf{J} \cdot \mathbf{j}/\Im$  in (3.1) originating from the kinematics of the particle and rotor, is actually too strong. In practice, this problem is circumvented phenomenologically by reducing the strength of the Coriolis coupling through the so-called attenuation factor.<sup>e</sup> However, such a modification of the Hamiltonian naturally affects the  $BM1$  values, so that the result becomes different depending on the attenuation factor or whether one introduces it or not. All in all, it was not possible to get satisfying results for both the spectrum and  $BM1$  values simultaneously. The prediction of the particle-rotor model should be understood to be qualitative rather than quantitative. Nevertheless, the above simple exercises demonstrate how the signature inversion of the  $BM1$  values may arise on the one hand and that it is not a special feature of the Projected Shell Model on the other. This observation does not depend on the use of the attenuation factor.

The notion of the signature dependence of the spectrum and of the electromagnetic moments and transitions in deformed odd-mass nuclei dates back to the work of Nilsson.<sup>4</sup> Specifically, the rotational disturbance on the  $M1$  transitions was later investigated qualitatively in terms of the cranked shell model<sup>107</sup> and of the particle-rotor model.<sup>108</sup> While no simultaneous analysis of the spectra has been attempted in these treatments, the present theory describes both the spectra and the  $BM1$  values consistently in terms of the same shell model wave functions. As we saw in Figs. 48 and 52, the results are in good agreement with the experimental data except for a minor discrepancy in the  $BM1$  value at  $I = \frac{13}{2}$  in the nucleus  $^{167}\text{Yb}$  where the present theory predicts signature inversion. It is quite possible that the predicted signature inversion might occur in the isotopes heavier than expected. Therefore, the measurement of the  $M1$  transitions down to the low spin region for the nucleus  $^{169}\text{Yb}$  is of great interest for testing the prediction of the present theory.

### 6.3. Odd-proton nuclei

The quasiparticle configurations for odd-proton nuclei are taken to be

$$|\Phi_\kappa\rangle = \{a_\pi^\dagger |0\rangle, a_\pi^\dagger a_{\nu_1}^\dagger a_{\nu_2}^\dagger |0\rangle\}. \quad (6.5)$$

The presence of the 3- $qp$  (i.e.,  $1\pi \otimes 2\nu$ ) configuration is very important in odd-proton nuclei because such a band will cross the lowest  $1\pi$ - $qp$  band at a moderate

---

<sup>e</sup>The Coriolis force receives a dynamical correction arising from the interplay between the particle and rotor,<sup>34,35</sup> which is a possible origin of the attenuation factor.

spin due to a large spin alignment of the  $2\nu\text{-}qp K = 1$  state (i.e., the *s*-band) exactly as in the case of the *g*-*s* band crossing in doubly-even nuclei. The  $\Delta I = 2$  plot of the yrast spectrum will indeed show a behavior very similar to the alignment diagram of a doubly-even nucleus. This feature is quite different in odd-neutron nuclei as we have seen before. What distinguishes odd-proton nuclei from odd-neutron nuclei is the amount of the spin alignment of the  $2\nu$ - and  $2\pi\text{-}qp$  states. However, as in the odd neutron case, the energy difference (or the transition energy)  $E(I) - E(I - 1)$  plotted against spin will again show the characteristic modulation due to the signature dependence of the last odd proton if it is in an aligned state.

A serious problem in the odd-proton (and also in the doubly-odd) nuclei is that the Nilsson scheme for protons seems to be not (yet) optimally adjusted and we plan to investigate this problem in a separate work. In this section, we will show explicitly what kind of problems it presents and how one can improve the results.

Figures 54–57 show the  $E(I) - E(I - 1)$  plot for the four isotones  $^{161}\text{Ho}$ ,  $^{163}\text{Tm}$ ,  $^{165}\text{Lu}$ , and  $^{167}\text{Ta}$ , respectively. The sudden drop of the diagrams at moderate spin is due to the crossing between the  $1\text{-}qp$  ( $\pi h_{11/2}$ ) and  $3\text{-}qp$  ( $\pi h_{11/2} \otimes \nu i_{13/2}^2$ ) band. In the nucleus  $^{167}\text{Ta}$ , the linking transition between the  $1\text{-}qp$  and  $3\text{-}qp$  band has not been measured, so that the experimental data shows discontinuity. At the moment, we do not know the reason for the discrepancy in the high spin region where the  $3\text{-}qp$  states are the dominant (yrast) configurations. In the low spin region, on the other hand, the theoretical results (dots) show that the amount of signature dependence

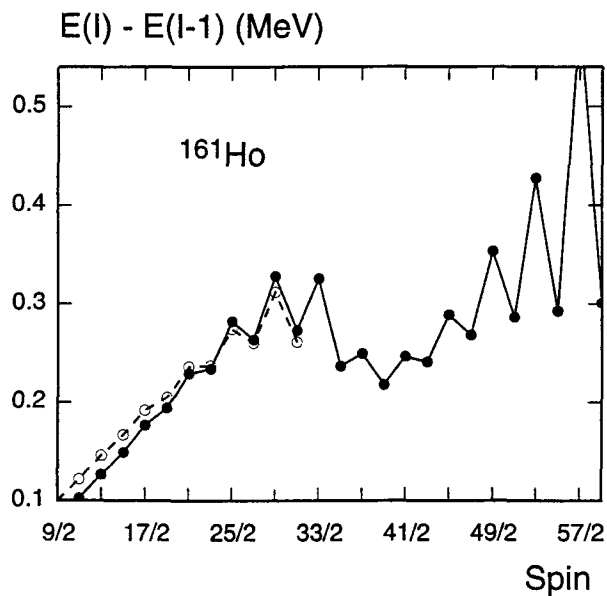


Fig. 54. The transition energies for the nucleus  $^{161}\text{Ho}$ . The transition energies  $E(I) - E(I - 1)$  are compared between theory (dots) and experiment (circles). The data are taken from Ref. 109.

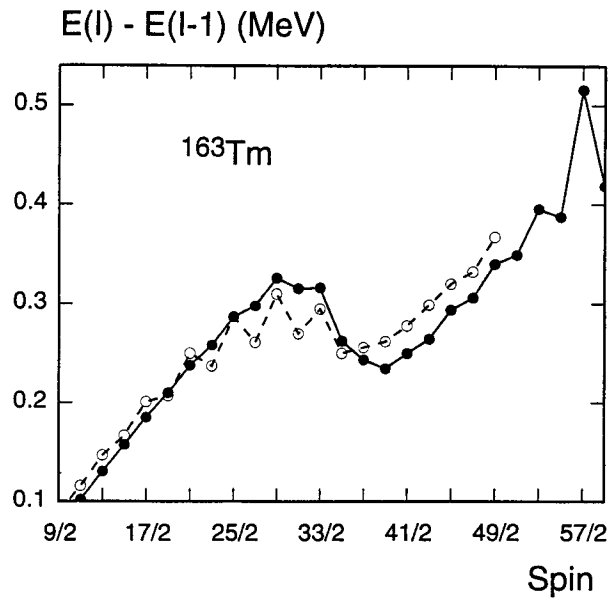


Fig. 55. The transition energies for the nucleus  $^{163}\text{Tm}$ . The transition energies  $E(I) - E(I - 1)$  are compared between theory (dots) and experiment (circles). The data are taken from Ref. 110.

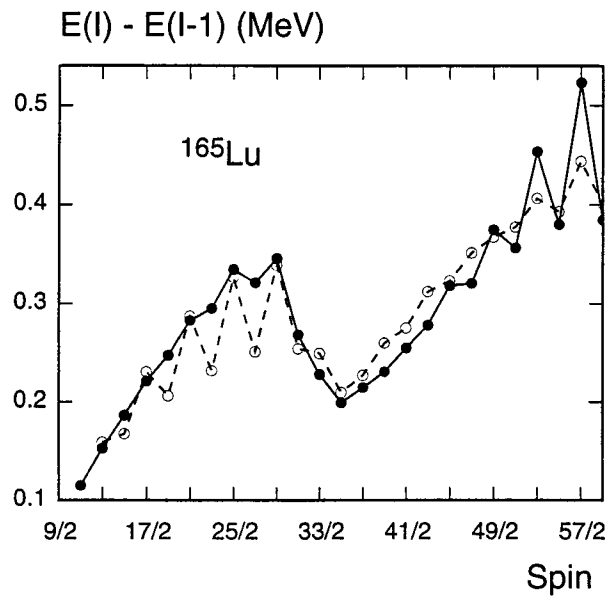


Fig. 56. The transition energies for the nucleus  $^{165}\text{Lu}$ . The transition energies  $E(I) - E(I - 1)$  are compared between theory (dots) and experiment (circles). The data are taken from Ref. 111.

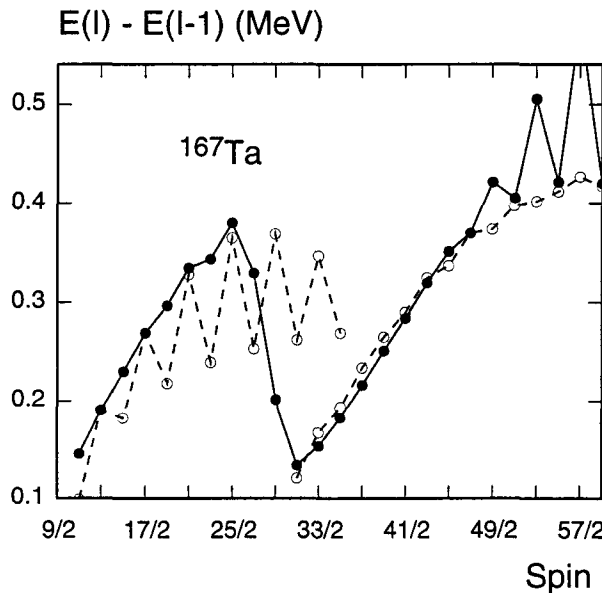


Fig. 57. The transition energies for the nucleus  $^{167}\text{Ta}$ . The transition energies  $E(I) - E(I - 1)$  are compared between theory (dots) and experiment (circles). The data are taken from Ref. 112.

decreases too rapidly as the proton number increases while the experimental data (circles) show that the signature dependence still continues to exist in the low spin region ( $1\pi$ -qp dominant region). This means that the alignment of the (proton) 1-qp band is too small in the theoretical prediction.

This discrepancy in the low spin region can be removed to a large extent by modifying the proton Nilsson scheme slightly, namely, we have simply multiplied a factor 0.9 to the standard Nilsson parameters ( $\kappa$  and  $\mu$ ) for the proton major shell  $N_\pi = 5$  in order to lift up the low- $K$  orbitals of the intruder subshell  $\pi h_{11/2}$  so that they come closer to the proton Fermi energy. Figures 58–61 show the result of this calculation.

Again, the signature dependence in the high spin region is predicted too strongly. It may mean that a more smoothly behaving (i.e., a less aligned) state which comes into the yrast region is missing in the configuration or that the nucleus is triaxial. As mentioned before, we do not know the real reason at the moment. However, for the heavier two isotones, the low spin regions are clearly improved. For the lighter two, on the other hand, use of slightly larger deformation parameters will greatly improve the agreement; see below for the choice of the deformation parameters. These are good examples which show the sensitivity of the calculations to the Nilsson scheme. However, it is not the purpose of the present work to achieve the best fit and we present the results as they are because we believe that this will be more informative to the reader.

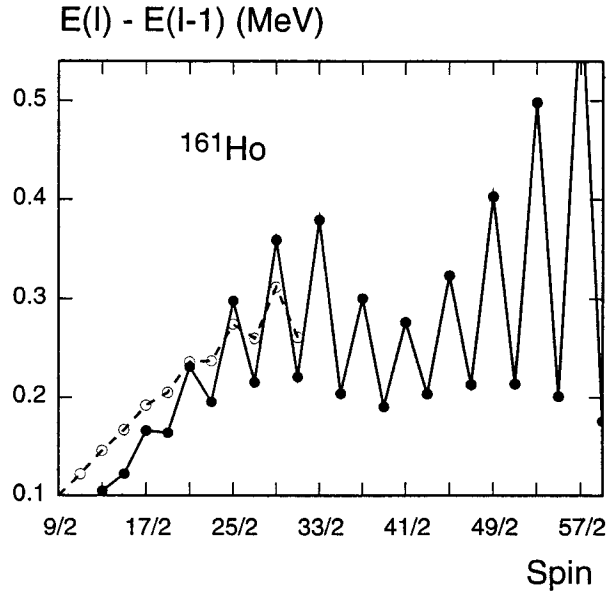


Fig. 58. The transition energies  $E(I) - E(I - 1)$  for the nucleus  $^{161}\text{Ho}$ . Same as Fig. 54 but the proton Nilsson scheme is modified by multiplying a factor 0.9 to the Nilsson parameters  $\kappa$  and  $\mu$  for the major shell  $N_\pi = 5$ .

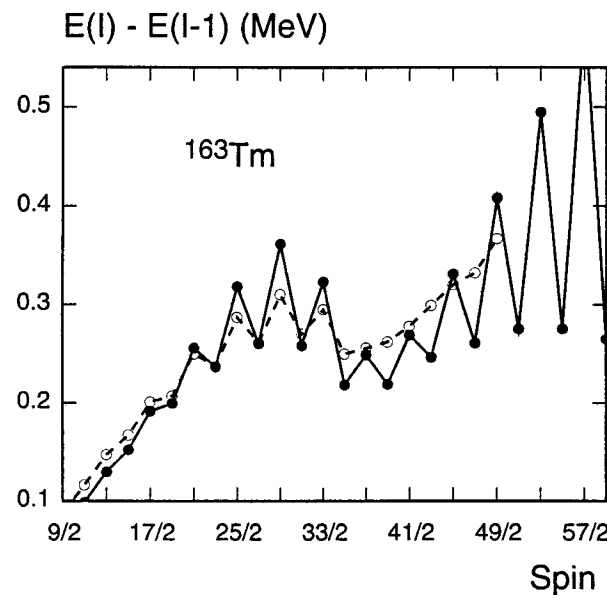


Fig. 59. The transition energies  $E(I) - E(I - 1)$  for the nucleus  $^{163}\text{Tm}$ . Same as Fig. 55 but the proton Nilsson scheme is modified by multiplying a factor 0.9 to the Nilsson parameters  $\kappa$  and  $\mu$  for the major shell  $N_\pi = 5$ .

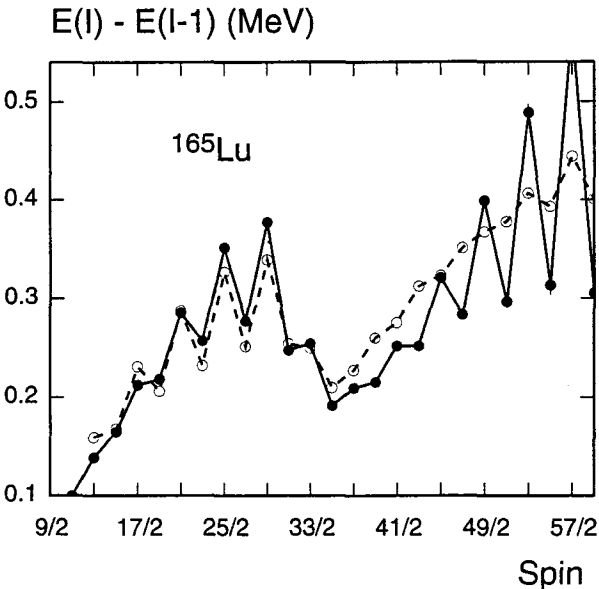


Fig. 60. The transition energies  $E(I) - E(I - 1)$  for the nucleus  $^{165}\text{Lu}$ . Same as Fig. 56 but the proton Nilsson scheme is modified by multiplying a factor 0.9 to the Nilsson parameters  $\kappa$  and  $\mu$  for the major shell  $N_\pi = 5$ .

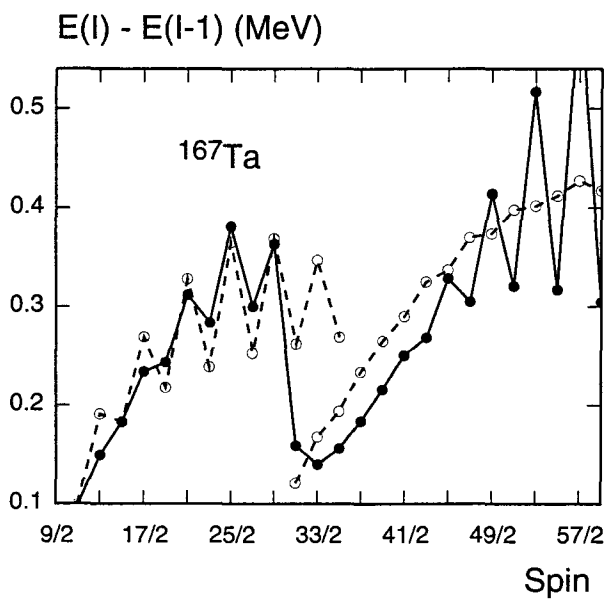


Fig. 61. The transition energies  $E(I) - E(I - 1)$  for the nucleus  $^{167}\text{Ta}$ . Same as Fig. 57 but the proton Nilsson scheme is modified by multiplying a factor 0.9 to the Nilsson parameters  $\kappa$  and  $\mu$  for the major shell  $N_\pi = 5$ .

All calculations in the present article have been carried out using the Nilsson parameters  $\kappa$  and  $\mu$ , which were compiled almost three decades ago,<sup>113</sup> in order to maintain the consistency with our earlier calculations. On the other hand, a new compilation<sup>114,115</sup> became available in the meantime. It takes into account some new data which were not available at that time. We have therefore repeated the same calculations using the new parametrization in order to see how the revised level scheme affects the results. However, the improvement was very small. In particular, the above-mentioned factor (0.9) was still necessary to obtain agreement with the data in the low spin region. Also, the problem in the high spin region persisted.

The deformation parameters in the above calculations were taken from Ref. 23 and Ref. 116 or from an interpolation along the isotone chain if the nucleus in question is not found in both works. Table 7 lists the deformation parameters used.

Table 7. Deformation parameters of four isotones.

Nucleus	$^{161}\text{Ho}$	$^{163}\text{Tm}$	$^{165}\text{Lu}$	$^{167}\text{Ta}$
Deformation Parameter	0.244	0.242	0.230	0.215

Normally, one expects the signature dependence to weaken as the particle number increases. This is because, as the Fermi energy (or the particle number) increases, the low  $K$ -valued orbitals move away from it (i.e., the states near the Fermi level become less aligned) if the deformation is prolate. In the present case, it persists in contrast to this expectation. This is due to the decreasing deformation as a function of the proton number; see Table 7. In fact, the low  $K$ -valued levels do not move away from the Fermi level so rapidly with increasing proton number if the deformation becomes smaller according to the Nilsson scheme and, in particular, if the Nilsson parameter is somewhat weakened (factor 0.9 for  $N_\pi = 5$ ) compared to the standard value. This shows the importance of proper single-particle level scheme.

Finally, we mention the “delay” in the band crossing observed in the nucleus  $^{175}\text{Ta}$ . In this nucleus, the crossing point between  $1\pi$ - and  $1\pi \otimes 2\nu$ -qp band occurs at a spin higher than that expected from the neighboring doubly-even nuclei  $^{174}\text{Hf}$  and  $^{176}\text{W}$ . This problem was investigated in Ref. 117 within the framework of the present theory. It was concluded that, in order to obtain good agreement with the data, the strength of the Quadrupole Pairing force has to be increased to  $\gamma = 0.24$  while the usual value is  $0.16 \sim 0.18$  for heavy nuclei, where  $\gamma$  measures its strength relative to the Monopole Pairing force; cf. (2.48). The alignment diagrams for the neighboring doubly-even nuclei  $^{174}\text{Hf}$  and  $^{176}\text{W}$  were confirmed to be compatible with the increased strength. However, this means that we have to trade in the excellent agreement shown in Sec. 4 and thus face a more serious problem if we accept this value since the  $g$ -s band crossing would then be shifted to a much larger

spin. As a matter of fact, the alignment diagrams for  $^{174}\text{Hf}$  and  $^{176}\text{W}$  should be relatively insensitive to the value of  $\gamma$  because these nuclei do upbend rather than backbend; see Figs. 16 and 17. It means that the  $g-s$  band crossing occurs with a very small angle so that the location of the crossing point does not significantly affect the result. Therefore, the fact that their alignment diagrams are compatible with those obtained from the standard  $\gamma$  value is not necessarily a strong support for the proposed  $\gamma$  value of 0.24. On the contrary, if one used the value  $\gamma = 0.24$  for strongly backbending nuclei, the conclusion would have been totally different. Therefore, we would rather attribute the origin of the  $^{175}\text{Ta}$  problem to an improper proton Nilsson parameters. Compare Figs. 57 and 61, for example. These figures show clearly that the  $1\text{-}qp$  and  $3\text{-}qp$  bands cross at  $I = \frac{25}{2}$  ( $\frac{29}{2}$ ) if the above mentioned factor for the Nilsson parameter is taken to be 1 (0.9). In other words, the modification of the Nilsson parameter can easily cause the delay of two spin unit for the band crossing. This is obviously due to an increased alignment in the (proton)  $1\text{-}qp$  band. Modification of the proton Nilsson parameters in the shell  $N_\pi = 5$  seems to be required from this point of view too. All in all, we feel strongly that more detailed investigation of the proton Nilsson scheme (and also of the deformation parameter) is necessary for a better description of odd-proton (and doubly-odd) nuclei.

### 7. Qualitative Discussion of the $\Delta I = 4$ Bifurcation

As we have seen in the previous chapters, all well decoupled aligned bands show the signature dependence of the  $\Delta I = 1$  spin sequence. Such a rotational band has been classified into favored and unfavored bands, so that a band splits into two bands for the spin sequence of  $\Delta I = 2$ . This is a  $\Delta I = 2$  bifurcation. Recently, a  $\Delta I = 4$  type bifurcation has been observed in some superdeformed rotational band which may be considered as an “ultrafine signature dependence” of the  $\Delta I = 2$  spin sequence.

This phenomenon seems to take place in a decoupled band involving the  $N_\nu = 7$  and  $N_\pi = 6$  intruder subshells but is not necessarily related to the spin alignment (i.e., the  $K$ -value of the band is supposedly not necessarily small). It has been suggested that the phenomenon is associated with the presence of a  $C_4$  type intrinsic symmetry<sup>118</sup> (an invariance under the  $90^\circ$  rotation with respect to an intrinsic axis). There is also some indication that a similar feature is present in certain rotational band belonging to the normal deformation<sup>119</sup> involving  $N_\nu = 6$  and  $N_\pi = 5$  intruder subshells.

One can in fact observe some regular perturbation in the dynamical moment of inertia (4.3) by plotting it as a function of spin or rotational frequency. However, the effect is in most cases so weak that it has been proposed<sup>120</sup> to study the quantity

$$\frac{3}{8} \left\{ F(I) - \frac{1}{6} [4F(I+2) + 4F(I-2) - F(I+4) - F(I-4)] \right\} \quad (7.1)$$

as a function of spin or rotational frequency in order to make it clearly visible. Here,

$$F(I) \equiv E(I) - E(I-2) = 2\omega \quad (7.2)$$

represents the transition energy or twice the rotational frequency. The quantity (7.1) is nothing other than the five point formula for the fourth order derivative of the function  $F(I)$  and indeed shows a  $\Delta I = 4$  bifurcation, in the sense that it oscillates with a period of  $\Delta I = 4$  when applied to the observed data. This means that the quantity (7.1) changes its sign at every spin increment of two units (the  $\Delta I = 2$  sequence) and the rotational spectrum (after the usual signature splitting if any) splits into two further classes of bands. The order of magnitude of the zigzag amplitude is indeed very small and ranges roughly from 10 to 100 eV. Such a detailed measurement represents a state-of-the-art experiment achieved with the help of modern  $\gamma$ -ray detector technology.

There have been several theoretical attempts to explain this phenomenon in terms of a  $C_4$  type symmetry by introducing the fourth order terms of the body-fixed angular momentum operator ( $I_{\pm}^4$ ) in the rotor model<sup>121-123</sup> or an additional  $Y_{4\pm 4}$  type deformation<sup>124,125</sup> in the mean field. Whether or not the introduction of this kind of  $C_4$  symmetries ( $\Delta K = 4$ ) is the natural answer to this problem is being heavily debated at present and there may still be other proposals<sup>126</sup> in the future.

Quite recently, it has been demonstrated numerically that the Projected Shell Model in its original form can account for a  $\Delta I = 4$  bifurcation without assuming any extra symmetry.<sup>127</sup> This is certainly an important observation and is quite interesting as it can provide us with an alternative view of the problem. Nevertheless, whether it is an explanation of the observed bifurcation or not must still be ascertained by further investigations and such work is in progress. Apart from such a cardinal question, there arises a basic theoretical question as to how such a (unexpected) feature can exist at all in the Projected Shell Model without assuming any extra intrinsic symmetry. We will clarify the origin of this mechanism qualitatively in this short section. It is in fact not too difficult to locate from where it comes.

For simplicity, we assume that the lowest two bands (band 1 and 2) cross each other at a certain spin. If the crossing angle is not too large, they will stay closely together for an appreciable range of spins across the crossing point. This is where the bifurcation in question will take place. Another assumption, which is essential, is that both bands are well decoupled (intruder subshells). They thus have a better chance of entering the yrast region if they are aligned ( $|K|$  small) although this is not necessarily required in the following discussion. It all hinges upon the actual shell filling of the nucleus in question. Let us see what happens to such closely lying decoupled bands.

The  $2 \times 2$  PSM eigenvalue equation (for a given spin) leads to the secular equation

$$\begin{vmatrix} H_{11} - EN_{11} & H_{12} - EN_{12} \\ H_{12} - EN_{12} & E_{22} - EN_{22} \end{vmatrix} = 0. \quad (7.3)$$

As the usual signature dependence ( $\Delta I = 1$ ) is excluded, all matrix elements in (7.3) are basically smooth functions of the spin  $I$  if we consider the  $\Delta I = 2$  sequence (i.e., they do not show staggering). However, if we look at a certain combination of them closely in terms of a quantity such as (7.1), we do find that it may have some regular spin dependence (oscillatory behavior). We will demonstrate this in the following.

Two solutions of the secular equation (7.3) are given by

$$\begin{aligned} E &= \frac{1}{1 - n_{12}^2} [E_0 - h_{12}n_{12} \pm \sqrt{D^2 + (E_1 n_{12} - h_{12})(E_2 n_{12} - h_{12})}] \\ &= \frac{1}{1 - n_{12}^2} [E_0 - h_{12}n_{12} \pm \sqrt{(1 - n_{12}^2)D^2 + (E_0 n_{12} - h_{12})^2}] \end{aligned} \quad (7.4)$$

where we have defined

$$E_k \equiv \frac{H_{kk}}{N_{kk}} \quad (k = 1, 2), \quad h_{12} \equiv \frac{H_{12}}{\sqrt{N_{11}N_{22}}}, \quad n_{12} \equiv \frac{N_{12}}{\sqrt{N_{11}N_{22}}}. \quad (7.5)$$

The quantity  $E_k$  is the rotational energy of the band  $k$  ( $k = 1, 2$ ) and

$$E_0 \equiv \frac{E_1 + E_2}{2}, \quad D \equiv \frac{E_1 - E_2}{2}. \quad (7.6)$$

The “-(+)" solution of (7.4) corresponds to the “yrast (yrare)" solution. The origin of the staggering is in this formula, in particular, in the square root term.

As mentioned earlier, all matrix elements are very smooth functions of spin in the  $\Delta I = 2$  sequence and show no staggering. However, when they are combined in a certain way, there occurs a regular dependence. In the formula (7.4), it is the term  $D^2$  in the square root. We now present a numerical example which demonstrates this.

Figures 62 and 63 show the quantity (7.1) evaluated by taking respectively the yrast solution of (7.4) and  $-|D|$  for  $E(I)$  in (7.2). Clearly, the results do not differ very much from each other. This is because the formula (7.1) filters out slowly varying part of a spin dependent function  $F(I) = E(I) - E(I - 2)$ . The two configurations in this example are  $K_\nu = \frac{5}{2}(\nu i_{13/2}) \otimes K_\pi = \frac{9}{2}(\pi h_{11/2})$  for band 1 and  $K_\nu = \frac{5}{2}(\nu i_{13/2}) \otimes K_\pi = \frac{1}{2}(\pi h_{9/2})$  for band 2 (with  $K = K_\nu + K_\pi = 7$  and 3, respectively). These states represent two normally deformed bands of the nucleus  $^{178}\text{Re}$  where two  $1\nu \otimes 1\pi$ -qp bands having  $K = 7$  (band 1) and 3 (band 2) cross with each other around spin  $I \sim 20$ . The staggering would have lasted longer if more than one crossing occurred one after the other.

On the other hand, for superdeformed bands, multi-qp states higher than two will be important in order to reach very high spins ( $I \sim 60$ ). Investigation of such a case has still to be done. This is one of the future problems.

The shell model basis of the PSM is not orthonormal. However, the non-orthogonality of the basis states plays a minor role in the present problem since

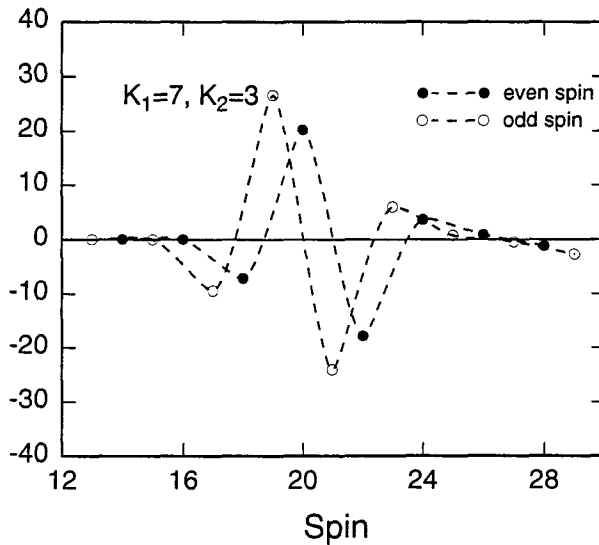


Fig. 62. The  $\Delta I = 4$  bifurcation in the nucleus  $^{178}\text{Re}$ . The solution (7.4) exhibits the  $\Delta I = 4$  bifurcation for the both spin sequences of  $I = \text{even}$  (dots) and  $\text{odd}$  (circles). See text for the  $1\nu \otimes 1\pi\text{-}qp$  configurations of  $^{178}\text{Re}$ . The ( $\Delta I = 2$ ) staggering would have lasted longer if two bands stayed close together for a more extended region of spin.

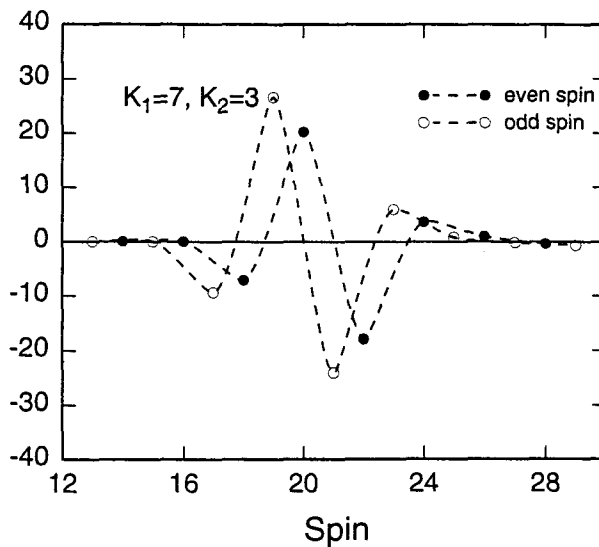


Fig. 63. The  $\Delta I = 4$  bifurcation due to the difference of the band energies. The same as Fig. 62 but taking only the essential term of (7.4),  $E \approx -|D|$ , for the evaluation of the quantity (7.1). It shows that the quantity  $|D|$  is indeed responsible for the present  $\Delta I = 4$  bifurcation.

the norm overlap  $n_{12}$  does not show the  $\Delta I = 2$  staggering. In the present example, the actual values of  $n_{12}$  are rather small (zero to the first approximation). According to the method presented in Appendix B, this can be easily understood from the fact that two bands are based on mutually different subshells ( $\nu i_{13/2} \otimes \pi h_{11/2}$  for band 1 and  $\nu i_{13/2} \otimes \pi h_{9/2}$  for band 2). On the other hand, two states on which two bands are based will no longer be linearly independent if  $|n_{12}|$  becomes very close to unity. The formula (7.4) has to be dealt with a special care in such a case.

The above result shows clearly that the  $\Delta I = 4$  bifurcation originates from the spin dependence of the difference of the rotational energies  $|D|$  of two closely lying decoupled bands, the condition being that two bands run almost parallel to each other for a certain spin interval. On the other hand, it should be noted that the quantity  $|D|$  in question can be evaluated by the method proposed in Appendix B. In fact, we have presented there a simple method of evaluating the band energies without going into the full complexity of angular momentum projection. It was shown that the usual signature dependence (i.e., the  $\Delta I = 2$  bifurcation) can be described also from this point of view. Moreover, one can confirm that the quantity  $|D|$  evaluated from the band energies of this method reproduces the present  $\Delta I = 4$  bifurcation. However, what is more important for the present problem is not the simplification of the treatment but the physical implication which the method suggests. In Appendix B, it was pointed out that this approach suggests that the spin dependence (shape) of the band energy is determined essentially by the kinematical aspect of the system and is rather independent of details of the Hamiltonian. This means that, as in the case of the  $\Delta I = 2$  bifurcation (the usual signature splitting), the present  $\Delta I = 4$  bifurcation is also a consequence of the quantum mechanical kinematics (coupling of angular momenta) of the quasiparticles and the rotating body. In other words, both ( $\Delta I = 1$  and  $\Delta I = 2$ ) types of staggering have a common physical origin and this establishes a unified picture of the two bifurcation phenomena. Nevertheless, we must admit at the same time that, although we have located from where the  $\Delta I = 2$  staggering comes, we have not yet understood the mathematical reason lying behind the fine staggering of the quantity  $|D|$ . At the moment, we can only guess that both bifurcations arise most likely from the properties of the relevant Clebsch-Gordan coefficients. This is another problem which has to be studied in greater depth in the future. The above-mentioned method will provide us with a useful hint when investigating this problem.

The result shown here should at present be considered independently from questions as to whether this is an explanation of the observed  $\Delta I = 4$  bifurcation or not. It is in fact too early to be able to give a conclusion to such a cardinal issue. In addition to the above-mentioned problems, there are other important questions to be clarified before one can make final conclusions. We point out only one of them. In the present qualitative discussion, we have considered two closely lying bands. This is done for the sake of simplicity to make it clear from where the effect comes. However, this is merely a sufficient condition and does not mean that such an assumption is absolutely necessary. Therefore, the study has to be further extended

to multiband cases higher than two. Such a study is important, in particular, for the case of superdeformed bands as we expect it to be the realistic situation.

To conclude the present section, we should like to state once again that, although we have not yet fully understood its mathematical ground, a potential mechanism which leads to a  $\Delta I = 4$  bifurcation is present in the Projected Shell Model. The discussion made in Appendix B shows that, as in the case of the usual signature dependence (i.e., the  $\Delta I = 2$  bifurcation), it is not due to the dynamics (details of the Hamiltonian) but is rather due to the quantum mechanical kinematics (coupling of angular momenta) of the decoupled quasiparticles and the rotating body, which we have not expected in the outset. It is well possible that the present theory may have still more unexpected features which we have not yet discovered.

### 8. Concluding Remarks

We have shown various aspects of the Projected Shell Model through a number of applications to the high-spin states of various axially symmetric nuclei. As it stands, the theory is fully quantum mechanical and is free from any uncontrollable approximations although several simplifying compromises have been made. Depending on the physics of interest, one may remove some of them. This is possible without undue difficulty. To conclude the present article, we will first summarize each chapter.

In Sec. 1, we pointed out the weakness of the spherical shell model and called attention to the advantage of the deformed shell model. The concept of the deformed shell model was first introduced by Elliott who developed the SU(3) shell model which applies to light nuclei where the spin-orbit force is negligible to the first approximation. However, the prominent phenomena discovered by high-spin experiments are closely connected to the presence of a strong spin-orbit force which leads to the decoupling and spin alignment of particles. Hence, the elegant group theoretical method used in the SU(3) model is inapplicable and thus the use of a numerical method becomes unavoidable. Our algorithm is presented in greater detail in Appendix A. We made a detailed comparison between the MONSTER and the present approach.

In Sec. 2, we investigated the semiclassical limit of the angular momentum projection method. The Projected Shell Model, which is valid in principle for any choice of the (spherically symmetric) Hamiltonian, was then formulated in full generality. The actual Hamiltonian used in our numerical applications was specified at the end of the chapter. The use of a schematic interaction makes the theory extremely powerful for practical applications. It is rather amazing that such simple schematic forces ( $Q \cdot Q +$  Monopole Pairing + Quadrupole Pairing Force) can describe a large number of different types of nuclei consistently and accurately. It may imply that they indeed represent the most important parts of the effective nucleon correlations in nuclei. The use of such a schematic interaction can be justified as shown in Appendix B. We will make further remarks about this point later.

In Sec. 3, the particle-rotor model and the Projected Shell Model were compared with each other to demonstrate the difference between a semiclassical and a quantum mechanical theory. A generalized signature rule for decoupled bands has been established numerically. Evidence indicating that this rule might not depend on the details of the Hamiltonian is given in Appendix B. We explained how to use the band diagram which has been applied in the subsequent chapters. It is a powerful and indispensable tool for understanding the basic mechanisms of various phenomena. The present theory predicts the existence of high- $K$  bands in some doubly-even nuclei. They occur as a consequence of the Nilsson + BCS scheme independently of the details of the residual interaction but are sensitive to the filling of the intruder subshell.

In Secs. 4 to 6, the actual applications to doubly-even (Sec. 4), doubly-odd (Sec. 5), and odd-mass (Sec. 6) nuclei were presented. All nuclei have been treated consistently using the same Hamiltonian. For doubly-even nuclei, we discussed the effect of (simultaneous) particle number projection. A simple way of separating the spurious state from the physical states was proposed in Appendix D. Although it improves the agreement between theory and experiment, the essence of physics can be well understood by angular momentum projection alone. We pointed out that the level density increases rapidly with spin, which leads to a plateau in moment of inertia. However, this does not mean that the system reached the classical rotational limit. It is due to the band crossings (or phase transitions in the terminology of mean field theory) that occur one after the other at every spin increment. For doubly-odd and odd-mass nuclei, the location of the Fermi energy is crucial in obtaining the correct result since the shell filling of the last particle(s) determines the basic feature of the spectrum. One may obtain unexpected result if the nucleus is not axially symmetric or if incorrect Nilsson parameters ( $\kappa$ ,  $\mu$ , and deformation) are used. Analysis of doubly-odd nuclei is particularly delicate and often difficult due to the fact that the level density is about ten times larger than that of odd-mass nuclei even near the ground state. While the signature dependence of doubly-odd nuclei is generally very weak, that of odd-mass nuclei is very pronounced. In fact, it can even lead to spin anomaly of the ground state (or the lowest state of a given parity) in some odd-mass nuclei. This is indeed observed in the positive parity states of lighter odd-neutron rare-earth nuclei. The present theory predicts the inversion of the  $BM1$  signature in heavier odd-neutron Yb nuclei in the lowest spin region. This has still to be confirmed experimentally. For odd-proton nuclei, the backbending caused by the two-neutron alignment occurs just like the  $g-s$  crossing of doubly-even nuclei. In odd-neutron nuclei, this does not occur since the two-proton alignment is not large enough to cause such an effect. However, it is possible that a similar phenomenon may occur in a higher spin region where the three-neutron configurations become important since then crossing between one- and three-neutron bands is possible. Although these are the next configurations to be included, the present data stop just before such a region.

In Sec. 7, we have shown that the Projected Shell Model is furnished with a mechanism which leads to a  $\Delta I = 4$  bifurcation. This result follows without assuming any  $C_4$  type symmetry. At the moment, however, we reserve judgement as to whether or not it is an explanation of the recently discovered one in some superdeformed nuclei. This has still to be investigated in the future.

Most of the prominent phenomena observed in high-spin experiments are closely related to the spin alignment which takes place in the decoupled bands. In fact, this was one of the main points which we emphasized in the examples presented in Secs. 4 to 6. It was shown in Appendix B that, once the HFB basis is fixed, the spin dependence of the rotational energies of decoupled bands does not depend on the quasiparticle residual interaction to a good approximation. In other words, the band energies are determined essentially by the kinematics of the rotational motion, whose quantum mechanical aspect can be seen from the probabilistic nature of the resulting formulas (B.8) and (B.10). In that formulation, the effect of the residual interaction appears first in the moment of inertia of the rotor, which is a scaling factor of the band energies, and in the off-diagonal matrix elements of the Hamiltonian, which describe the coupling between various bands. As we have shown in a number of examples, the band diagram, which is a collection of the band energies, plays a crucial role for the interpretation of the yrast states which result from the final band mixing procedure (the shell model diagonalization). It means that one can learn the basic features of the final result already from the band diagram. From this fact, one can understand the reason why the simple schematic forces used in the present theory work so well. There are two points to be remarked, namely, the band energies as functions of the spin (shapes) and the relative location of the bands (bandheads) in a band diagram. The latter depends on details of the Hamiltonian whilst the former does not. Let us elucidate these features in some detail.

In the first place, according to the discussion given in Appendix B, the shapes of the band energies are essentially determined by the fluctuation of the angular momentum  $\Delta J_y^2$  (responsible for the spin dependent features of the band energies) and the moment of inertia of the rotor  $\mathfrak{I}$  (responsible for the scaling of the band energies). Therefore, any (rotationally invariant) Hamiltonian which yields the same  $\Delta J_y^2$  and  $\mathfrak{I}$  leads to the same result. This justifies the use of a schematic interaction. In the present model, the main role of each schematic force is as follows. The  $Q \cdot Q$  and Monopole Pairing force, which are adjusted, respectively, to the known deformation and energy gap, determine the fluctuation of the angular momentum while the Quadrupole Pairing force is responsible for the correct moment of inertia of the rotor. In fact, the moment of inertia resulting from the former two forces alone is always 10 to 15% smaller than the right value.

Secondly, the relative location (bandhead) of the unperturbed rotational bands in the band diagram is determined by the shell filling, on which the features of individual nucleus depend sensitively. Therefore, the single-particle level scheme (the HFB basis) resulting from the assumed Hamiltonian has to be absolutely reliable

in reproducing the correct shell filling over the whole range of nuclei one wants to investigate. Obviously, the systematic description of nuclei along an isotope or isotone chain will fail if the empirical shell structure is not well reproduced. All this will naturally depend on details of the Hamiltonian and is therefore an important constraint on the Hamiltonian which may be used in nuclear structure problems. This aspect has also to be investigated for the so-called realistic Hamiltonian before applying it to actual structure calculations. The present model is designed to fulfill this requirement from the outset in that the resulting mean field is a sum of the (stretched) Nilsson and (BCS) pairing potential. After all, the Nilsson + BCS scheme is one of the most successful models in nuclear structure theories and has been used and tested since four decades. This is doubtlessly the main reason why the present model works so well for a wide range of different types of nuclei.

We should also remark on the (obvious) limitation of a schematic interaction. In fact, the schematic forces may make sense only when they are used in conjunction with a single-particle Hamiltonian which binds nucleons "tightly" in space, such as the harmonic oscillator. Such a Hamiltonian does not allow nucleons to travel far away from the rest of the nucleus and is therefore inappropriate for the description of nuclei near the drip lines. One might need a more realistic Hamiltonian if some nucleons are loosely bound. The framework of the present theory itself is valid even for such "exotic" nuclei.

As a perspective for the future, we will next comment on the treatment of triaxial nuclei. Although we considered exclusively the axially symmetric nuclei throughout the present article, the algorithm presented in Appendix A also applies to triaxial systems. There is no doubt that triaxial nuclei exist in nature and in fact many experimental data suggesting such nuclei are accumulating. They are the next target of our study. According to the usual HFB approach,<sup>128</sup> the (ground state) energy surface in the  $\beta-\gamma$  plane for transitional nuclei show only a shallow minimum (if it exists at all) leading to the  $\gamma$ -instability due to a very flat energy surface against the  $\gamma$ -deformation. On the other hand, it has been shown that the angular momentum projected energy surface can indeed lead to a pronounced minimum in the  $\gamma \neq 0$  region for some nuclei.<sup>31</sup> This implies that the existence of triaxial nuclei cannot be fully understood without angular momentum projection. This fact matches very well with the basic concept of the Projected Shell Model. Accordingly, the investigation of triaxial nuclei should proceed in two steps. First, in order to fix the nuclear shapes, a systematic search of the amount of triaxiality over the entire transitional nuclei has to be carried out in terms of the projected energy surface. Only after this process can one investigate the excited states of each nucleus in the Projected Shell Model using the triaxial basis established in the first step. In comparison to the axial case, the triaxiality makes the resulting shell model space larger since each  $qp$ -state is projected into several states of different  $K$ -values. A finer description of the nucleus thus becomes possible.

Finally, we comment on the domain of the applicability of the Projected Shell Model. It can be used almost everywhere in the nuclear chart (except for those

"exotic" nuclei mentioned above) since most nuclei are deformed. However, there is no reason why the method cannot be applied to the zero deformation limit (spherical nuclei). In this case, angular momentum projection works just as an efficient way of carrying out the angular momentum algebra without going explicitly into the whole complexity of the multi-quasiparticle kinematics. It means that the method can be used to circumvent the formidable CFP formalism, which introduces a (physically less significant) quantum number in addition to the seniority for the classification of the shell model basis, and thus leads to an awkward labeling problem when distributing the whole active nucleons over various subshells. Moreover, the advantage of the (BCS) quasiparticle representation over the seniority scheme may not be overlooked. It shows shell filling simply via the Fermi energy and also establishes the hierarchy among the quasiparticle states through their excitation energies. This aspect will be essential for heavier nuclei since it enables us to truncate the shell model configuration space most efficiently.

We should like to stress that, although angular momentum projection can be carried out explicitly in closed form due to the relation (B.11) of Appendix B

$$\hat{P}_{M'K'}^{I'} a_{j_1 k_1}^\dagger \cdots a_{j_n k_n}^\dagger = \sum (j_n k_n, IK | J_{n-1} K_{n-1}) (j_n m_n, IM | J_{n-1} M_{n-1}) \cdots \\ (j_1 k_1, J_1 K_1 | I' K') (j_1 m_1, J_1 M_1 | I' M') a_{j_1 m_1}^\dagger \cdots a_{j_n m_n}^\dagger \hat{P}_{MK}^I$$

which is now valid rigorously, the use of the present numerical method will be more advantageous from the computational point of view (a single integral instead of multiple summations as the above relation shows) since the spherical basis not only conserves the  $K$ -quantum number (i.e., a single integral over the Euler angle  $\beta$ ) but also simplifies most of the formulas given in Appendix A drastically (e.g., among others the contractions  $A$  and  $B$  vanish identically if the particle number is not projected). The latter accelerates the whole numerical process of angular momentum projection.

This kind of approach may be of practical use, for example, in the investigation of the multiphonon problems in spherical nuclei. One of its advantages over the usual approach based on the RPA type formalism is that the Pauli Principle, whose effect has never been estimated properly although no one denies its importance, can be taken into account strictly. Particle number projection can also be taken into account if necessary (the contractions  $A$  and  $B$  will then no longer vanish). The main difference to the rotational problems discussed in the present article lies in the choice of the configuration space. Such a potential domain of applications is not yet fully exploited at present.

### Acknowledgments

The first author (K. H.) is indebted to his Brazilian colleagues, especially to Prof. E. W. Cybulska and Dr. M. A. Rizzutto for preparing the figures related to the nucleus  $^{138}\text{Pr}$  and to Prof. R. V. Ribas for providing us with the latest  $g$ -factor

measurement of the isotopes  $^{164-168}\text{Er}$  prior to publication. The second author (Y. S.) expresses his sincere thanks to Prof. D. H. Feng for the warm hospitality extended to him during his stay at Drexel University. Last but not least, we are most grateful to Dr. R. R. Hilton and Mrs. R. Hilton for kindly reading and carefully checking this lengthy manuscript.

#### Note Added to Proof

There has been doubt raised as to whether or not one may interpret the  $\Delta I = 2$  staggering discussed in Sec. 7 as a  $\Delta I = 4$  bifurcation. This is because it might be due to an artifice caused by using a five-point formula (7.1) based on finite differences. In fact, we have in the meantime noticed that both the left and right outermost oscillations shown in Figs. 62 and 63 disappear if we use the three-point formula

$$F(I) - \frac{1}{2} [F(I+2) + F(I-2)],$$

which is proportional to the second derivative of the function  $F(I) = E(I) - E(I-2)$ . In contrast, the strongest oscillation seen around the center (i.e., around the crossing point  $I \sim 20$ ) continues to exist even in the case of the three-point formula. This may indicate that the  $\Delta I = 2$  staggering in question is simply caused by a band crossing. Note that the difference of the two band energies  $D$  defined in (7.6) changes its sign at the crossing point, so that derivatives of  $|D|$  become discontinuous. Obviously, the larger the crossing angle (and/or the weaker the band coupling), the larger the discontinuity. The present  $\Delta I = 2$  staggering is induced by such a discontinuity (which determines the amplitude of the oscillation), whose effect propagates over other spin values due to the use of finite differences and should not therefore be interpreted as a  $\Delta I = 4$  bifurcation. Instead, it should be considered as a manifestation of a band crossing. Accordingly, this kind of analysis is still useful for detecting the occurrence of band crossings, which cannot be observed directly from experiment. Details will be reported elsewhere.

#### Appendix A: Algorithm of the Projection Method

##### A.1. Deformed quasiparticle basis

We denote the annihilation operator in the spherical harmonic oscillator basis by  $c_\alpha = c_{Njm}$  and its time-reversal by  $c_\alpha = \hat{T}c_\alpha\hat{T}^\dagger = (-)^{j-m}c_{Nj-m}$ . We note that, under this phase convention and in the real representation, the time-reversal transformation  $\hat{T}$  is equivalent to the unitary operator  $e^{-i\pi\hat{J}_y}$ . Note also that, because of the identity

$$e^{-i\pi\hat{J}_x} = e^{-i\pi\hat{J}_y}e^{-i\pi\hat{J}_x}, \quad (\text{A.1})$$

$e^{-i\pi\hat{J}_x}$  and  $e^{-i\pi\hat{J}_z}$  do not represent mutually independent operations if the time-reversal is preserved. The former is the so-called signature operator. We will use

the latter to classify the basis states and thus define a symmetry operator  $\hat{S}$  by

$$\hat{S} = e^{-i\pi J_z}. \quad (\text{A.2})$$

This operator is convenient since it is diagonal in the spherical basis while the signature operator is not. The whole set of operators is classified into two classes according to

$$\hat{S}c_\alpha\hat{S}^\dagger = e^{im\pi}c_\alpha = \pm i c_\alpha, \quad \hat{S}c_{\bar{\alpha}}^\dagger\hat{S}^\dagger = e^{im\pi}c_{\bar{\alpha}}^\dagger = \pm i c_{\bar{\alpha}}^\dagger. \quad (\text{A.3})$$

Here, the sign  $+(-)$  applies to  $m = \frac{1}{2}, -\frac{3}{2}, \frac{5}{2}, \dots (-\frac{1}{2}, \frac{3}{2}, -\frac{5}{2}, \dots)$  and such a quantum number is denoted as  $\alpha > 0$  ( $\alpha < 0$ ) or referred to as of the class  $S$  ( $\bar{S}$ ). There is a one-to-one correspondence between the operators in the class  $S$  and  $\bar{S}$  which are related to each other through the time-reversal transformation. Note that, for a given quantum state  $\alpha$ , the operators  $c_\alpha$  and  $c_\alpha^\dagger$  belong to the same class whereas  $c_{\bar{\alpha}}$  and  $c_{\bar{\alpha}}^\dagger$  belong to the other. The HFB transformation should be done within the same class of operators in order to preserve the symmetry described by (A.2). For the sake of generality, the following discussions will be made to cover not only the axially symmetric (spheroidal) deformation but also the triaxial (ellipsoidal) one. However, for the sake of convenience, we will keep referring to the corresponding deformed single-particle basis as a “Nilsson basis”.

The HFB quasiparticle operators which preserve the time-reversal invariance and the symmetry described by  $\hat{S}$  take (in the real representation) the form

$$\begin{aligned} a_\nu &= \sum_{\alpha>0} \{U_{\alpha\nu}c_\alpha + V_{\alpha\nu}c_{\bar{\alpha}}^\dagger\}, \\ a_\nu^\dagger &= \sum_{\alpha>0} \{-V_{\alpha\nu}c_\alpha + U_{\alpha\nu}c_{\bar{\alpha}}^\dagger\}, \end{aligned} \quad (\text{A.4})$$

where the summations run over the class  $S$  only. The quasiparticle operators (A.4) then belong to the class  $S$  ( $\nu > 0$ ) and those which belong to the class  $\bar{S}$  ( $\nu < 0$ ) are obtained by applying the time-reversal transformation to (A.4). The inverse of (A.4) is given by

$$\begin{aligned} c_\alpha &= \sum_{\nu>0} \{U_{\alpha\nu}a_\nu - V_{\alpha\nu}a_\nu^\dagger\}, \\ c_{\bar{\alpha}}^\dagger &= \sum_{\nu>0} \{V_{\alpha\nu}a_\nu + U_{\alpha\nu}a_\nu^\dagger\}. \end{aligned} \quad (\text{A.5})$$

In summary, the HFB transformation is carried out among the operators belonging to the same class to ensure invariance with respect to the operator  $\hat{S}$  and those belonging to different classes are mutually related with each other by the time-reversal transformation  $\hat{T}$ . The HFB vacuum state has the symmetry properties

$$\hat{S}|0\rangle = |0\rangle \quad \text{and} \quad \hat{T}|0\rangle = |0\rangle. \quad (\text{A.6})$$

In passing, we note that the identity  $\sum_{\alpha>0} (c_\alpha^\dagger c_\alpha + c_{\bar{\alpha}}^\dagger c_{\bar{\alpha}}) = \sum_{\nu>0} (a_\nu^\dagger a_\nu + a_{\bar{\nu}}^\dagger a_{\bar{\nu}})$ , i.e.,

$$\sum_{\alpha>0} (c_\alpha^\dagger c_\alpha - c_{\bar{\alpha}}^\dagger c_{\bar{\alpha}}) = \sum_{\nu>0} (a_\nu^\dagger a_\nu - a_{\bar{\nu}}^\dagger a_{\bar{\nu}}) \equiv 2\hat{M} \quad (\text{A.7})$$

follows from the unitarity of the HFB transformation. It is an invariant operator which counts the difference between the number of particles (or quasiparticles) occupying the class  $S$  and  $\bar{S}$  states. Since the HFB procedure inherently violates the conservation of the total number of particles

$$\hat{N} = \sum_{\alpha>0} (c_\alpha^\dagger c_\alpha + c_{\bar{\alpha}}^\dagger c_{\bar{\alpha}}),$$

the operator  $\hat{M}$  represents the “next best” conserved quantity. It commutes with  $\hat{J}_z$  but not with  $\hat{J}_x$  or  $\hat{J}_y$  and changes sign under the time-reversal transformation,  $\hat{T}\hat{M}\hat{T}^\dagger = -\hat{M}$ . We will refer to its eigenvalue as character; cf. (A.70).

If we define the quasiparticle basis by the Nilsson + BCS instead of the HFB procedure for the sake of simplicity (i.e., if we do not take the Quadrupole Pairing field into account when defining the quasiparticle basis), the HFB transformation amplitudes become

$$U_{\alpha\nu} = W_{\alpha\nu} u_\nu \quad \text{and} \quad V_{\alpha\nu} = W_{\alpha\nu} v_\nu, \quad (\text{A.8})$$

where  $W_{\alpha\nu}$  is the Nilsson amplitude and  $u_\nu$  and  $v_\nu$  the BCS amplitudes:

$$a_\nu = u_\nu b_\nu + v_\nu b_\nu^\dagger, \quad b_\nu = \sum_{\alpha>0} W_{\alpha\nu} c_\alpha. \quad (\text{A.9})$$

In practice, the final results obtained in the Nilsson + BCS basis do not differ very much from those obtained in the HFB basis. This is because the final shell model diagonalization can take into account properly the main effect of the Quadrupole Pairing force including the influence on the moment of inertia as well as on the coupling between the intrinsic (quasi-) particles and the rotating body. It is therefore possible to use the standard Nilsson + BCS basis without introducing much error. We will not make our theory any more sophisticated than is necessary in accordance with our basic philosophy.

The amplitudes  $W_{\alpha\nu}$  in (A.9) are obtained by diagonalizing the (ellipsoidal) Nilsson Hamiltonian for a given set of deformation parameters  $\epsilon$  and  $\epsilon'$

$$\hat{H}_0 - \frac{3}{2}\hbar\omega \left\{ \epsilon \hat{Q}_0 + \epsilon' \frac{\hat{Q}_{+2} + \hat{Q}_{-2}}{\sqrt{2}} \right\} \rightarrow \sum_{\nu>0} \varepsilon_\nu (b_\nu^\dagger b_\nu + b_{\bar{\nu}}^\dagger b_{\bar{\nu}}) \quad (\text{A.10})$$

where the operators  $\hat{H}_0$  and  $\hat{Q}_\mu$  are defined, respectively, by (2.41) and (2.42). For an axially symmetric system, we have  $\epsilon' = 0$ . It should be noticed that the unitary operator

$$e^{-i\frac{\pi}{2}\hat{J}_z} \quad (\text{A.11})$$

transforms the Hamiltonian (A.10) into that of the opposite triaxiality ( $\epsilon' \rightarrow -\epsilon'$ ) but does not change the eigenvalues  $\epsilon_\nu$ , since it simply represents the transformation of the intrinsic axis ( $x \rightarrow y$  and  $y \rightarrow -x$ ). We will show later that it is sufficient to consider only the case of  $\epsilon' \geq 0$  if we project out the angular momentum. On the other hand, volume conservation<sup>4</sup> requires the deformation dependence of the oscillator frequency

$$\omega = \overset{\circ}{\omega} \left[ \left( 1 + \frac{\epsilon}{3} + \frac{\epsilon'}{\sqrt{3}} \right) \left( 1 + \frac{\epsilon}{3} - \frac{\epsilon'}{\sqrt{3}} \right) \left( 1 - \frac{2\epsilon}{3} \right) \right]^{-\frac{1}{3}} \quad (> 0)$$

which limits the allowed range of the deformation parameters to

$$-3 < \epsilon < \frac{3}{2} \quad \text{and} \quad |\epsilon'| < \sqrt{3} \left( 1 + \frac{\epsilon}{3} \right). \quad (\text{A.12})$$

Thus, in the  $(\epsilon, \epsilon')$ -plane, the actual domain corresponds to the inside of the rectangular triangle  $\Delta ABC$  including the bottom line  $\overline{AB}$  as shown schematically in Fig. 64.

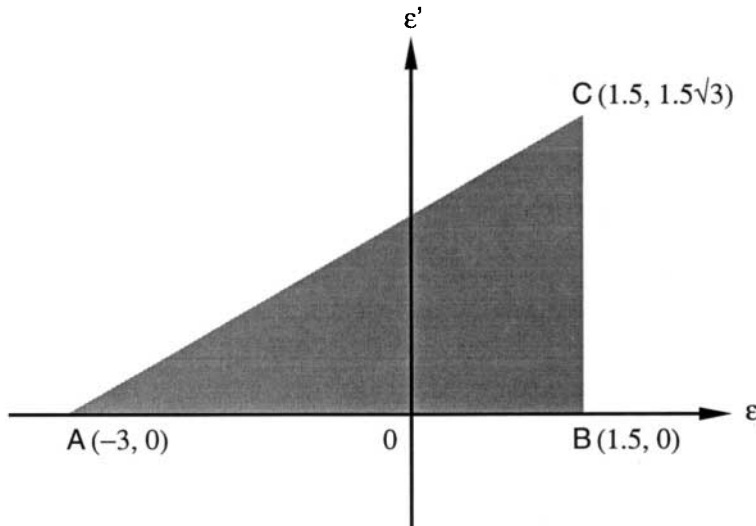


Fig. 64. The domain of the deformation parameters  $\epsilon$  and  $\epsilon'$ . In order for the oscillator frequency  $\omega$  to be positive, the domain of the deformation parameters is limited to the inside of the triangle  $\Delta ABC$  including the bottom line  $\overline{AB}$ .

It is convenient to write the relation (A.5) in the matrix form

$$\text{Class } S : \begin{bmatrix} c \\ c^\dagger \end{bmatrix} = \begin{bmatrix} U & -V \\ V & U \end{bmatrix} \begin{bmatrix} a \\ a^\dagger \end{bmatrix}. \quad (\text{A.13})$$

Note that this matrix relation holds among the operators of class  $S$ . For the operators of class  $\bar{S}$ , we have the relation

$$\text{Class } \bar{S} : \begin{bmatrix} c \\ c^\dagger \end{bmatrix} = \begin{bmatrix} U & V \\ -V & U \end{bmatrix} \begin{bmatrix} a \\ a^\dagger \end{bmatrix} \quad (\text{A.14})$$

which follows from (A.5) by applying the time-reversal transformation  $\hat{T}$ . Note also that the relations  $U_{\alpha\bar{\nu}} = U_{\alpha\nu}$  and  $V_{\alpha\bar{\nu}} = V_{\alpha\nu}$  hold, representing the time-reversal symmetry of the HFB transformation.

As we will see in the next section, the rotation operator mixes the class  $S$  and  $\bar{S}$ . It is therefore convenient to write the above two relations in a “large” form. We define

$$U = \begin{bmatrix} U & 0 \\ 0 & U \end{bmatrix} \quad \text{and} \quad V = \begin{bmatrix} 0 & -V \\ V & 0 \end{bmatrix} \quad (\text{A.15})$$

so that (A.13) and (A.14) can be combined together as

$$\begin{bmatrix} c \\ c^\dagger \end{bmatrix} = \begin{bmatrix} U & V \\ V & U \end{bmatrix} \begin{bmatrix} a \\ a^\dagger \end{bmatrix}, \quad (\text{A.16})$$

where the operator arrays are arranged as  $(c_\alpha, c_{\bar{\alpha}}, c_\alpha^\dagger, c_{\bar{\alpha}}^\dagger)$  and  $(a_\nu, a_{\bar{\nu}}, a_\nu^\dagger, a_{\bar{\nu}}^\dagger)$ . Since the transformation is unitary (with real matrix elements), the inverse of (A.16) is given by

$$\begin{bmatrix} a \\ a^\dagger \end{bmatrix} = \begin{bmatrix} U & V \\ V & U \end{bmatrix}^t \begin{bmatrix} c \\ c^\dagger \end{bmatrix}, \quad (\text{A.17})$$

where  $t$  denotes the transpose of a matrix. The “large” form is convenient for theoretical studies and the “small” form for numerical works. Decomposition of the former into the latter can be done by using (A.15).

### A.2. Evaluation of contractions and overlap

Let us now consider the rotation of the deformed quasiparticle basis, which is one of the basic ingredients of the projection method. For this purpose, we first note that the rotation of the spherical basis is attained on using the irreducible representation

$$\hat{R}(\Omega)c_\alpha\hat{R}^\dagger(\Omega) = \sum_{\alpha'} D_{\alpha\alpha'}(\Omega)c_{\alpha'}, \quad (\text{A.18})$$

where  $D_{\alpha\alpha'}(\Omega) \equiv \delta_{NN'}\delta_{jj'}D_{mm'}^j(\Omega)$ . The summation extends over all possible  $m'$ , so that the rotation mixes two classes  $S$  and  $\bar{S}$ . In matrix form, we can write

$$\hat{R}(\Omega) \begin{bmatrix} c \\ c^\dagger \end{bmatrix} \hat{R}^\dagger(\Omega) = \begin{bmatrix} D(\Omega) & 0 \\ 0 & D^*(\Omega) \end{bmatrix} \begin{bmatrix} c \\ c^\dagger \end{bmatrix}. \quad (\text{A.19})$$

It is convenient to decompose the “large” matrix  $D_{\alpha\alpha'}(\Omega)$  into the “small” form. This can be achieved by noting the property  $D_{\bar{\alpha}\bar{\alpha}'}(\Omega) = D_{\alpha\alpha'}^*(\Omega)$

$$D(\Omega) = \begin{bmatrix} D(\Omega) & \bar{D}(\Omega) \\ -\bar{D}^*(\Omega) & D^*(\Omega) \end{bmatrix}, \quad (\text{A.20})$$

where  $\bar{D}_{\alpha\alpha'}(\Omega) \equiv D_{\alpha\bar{\alpha}'}(\Omega) = \delta_{NN'}\delta_{jj'}(-)^{j-m'}D_{m-m'}^j(\Omega)$ .

Action of the rotation operator on the quasiparticles (A.17) can be evaluated by using (A.19) and (A.16). The result is

$$\hat{R}(\Omega) \begin{bmatrix} a \\ a^\dagger \end{bmatrix} \hat{R}^\dagger(\Omega) = \begin{bmatrix} X(\Omega) & Y(\Omega) \\ Y^*(\Omega) & X^*(\Omega) \end{bmatrix} \begin{bmatrix} a \\ a^\dagger \end{bmatrix}, \quad (\text{A.21})$$

where

$$X(\Omega) = U^t D(\Omega) U + V^t D^*(\Omega) V, \quad Y(\Omega) = U^t D(\Omega) V + V^t D^*(\Omega) U. \quad (\text{A.22})$$

The “small” forms of these matrices can be obtained by using (A.15) and (A.20), i.e.,

$$X(\Omega) = \begin{bmatrix} X(\Omega) & \bar{X}(\Omega) \\ -\bar{X}^*(\Omega) & X^*(\Omega) \end{bmatrix}, \quad Y(\Omega) = \begin{bmatrix} \bar{Y}(\Omega) & -Y(\Omega) \\ Y^*(\Omega) & \bar{Y}^*(\Omega) \end{bmatrix}, \quad (\text{A.23})$$

where

$$\begin{aligned} X(\Omega) &= U^t D(\Omega) U + V^t D(\Omega) V, \quad \bar{X}(\Omega) = U^t \bar{D}(\Omega) U + V^t \bar{D}(\Omega) V, \\ Y(\Omega) &= U^t D(\Omega) V - V^t D(\Omega) U, \quad \bar{Y}(\Omega) = U^t \bar{D}(\Omega) V - V^t \bar{D}(\Omega) U. \end{aligned} \quad (\text{A.24})$$

In the Nilsson + BCS representation, (A.24) reduces to

$$\begin{aligned} X_{\nu\nu'}(\Omega) &= x_{\nu\nu'} Z_{\nu\nu'}(\Omega), \quad \bar{X}_{\nu\nu'}(\Omega) = x_{\nu\nu'} \bar{Z}_{\nu\nu'}(\Omega), \\ Y_{\nu\nu'}(\Omega) &= y_{\nu\nu'} Z_{\nu\nu'}(\Omega), \quad \bar{Y}_{\nu\nu'}(\Omega) = y_{\nu\nu'} \bar{Z}_{\nu\nu'}(\Omega), \end{aligned} \quad (\text{A.25})$$

where

$$x_{\nu\nu'} = u_\nu u_{\nu'} + v_\nu v_{\nu'}, \quad y_{\nu\nu'} = u_\nu v_{\nu'} - v_\nu u_{\nu'} \quad (\text{A.26})$$

and

$$Z(\Omega) = W^t D(\Omega) W, \quad \bar{Z}(\Omega) = W^t \bar{D}(\Omega) W. \quad (\text{A.27})$$

Because of the reason previously mentioned, the Nilsson + BCS basis may be used instead of the HFB basis, so that the formulas (A.25)–(A.27) will be used in practice.

We now derive basic relations using the result (A.21) which can be written in the form

$$\begin{aligned} \hat{R}(\Omega) a_\nu &= \sum_\mu [X_{\nu\mu}(\Omega) a_\mu + Y_{\nu\mu}(\Omega) a_\mu^\dagger] \hat{R}(\Omega), \\ \hat{R}(\Omega) a_\nu^\dagger &= \sum_\mu [Y_{\nu\mu}^*(\Omega) a_\mu + X_{\nu\mu}^*(\Omega) a_\mu^\dagger] \hat{R}(\Omega). \end{aligned} \quad (\text{A.28})$$

Taking the matrix element of the first equation of (A.28) with respect to  $\langle 0|$  and  $a_{\nu'}^\dagger |0\rangle$ , we can derive the relation (using the abbreviation  $>\equiv |0\rangle$ )

$$\langle a_\nu \hat{R}(\Omega) a_{\nu'}^\dagger \rangle = \langle \hat{R}(\Omega) \rangle [X^{-1}(\Omega)]_{\nu\nu'} . \quad (\text{A.29})$$

Similarly, on taking the matrix element with respect to  $\langle 0|a_{\nu'}|0\rangle$ , we derive

$$\langle a_\nu a_{\nu'} \hat{R}(\Omega) \rangle = \langle \hat{R}(\Omega) \rangle [X^{-1}(\Omega) Y(\Omega)]_{\nu\nu'} . \quad (\text{A.30})$$

Finally, we take the matrix element of the second equation of (A.28) with respect to  $\langle 0|$  and  $a_{\nu'}^\dagger |0\rangle$  to derive

$$\langle \hat{R}(\Omega) a_\nu^\dagger a_{\nu'}^\dagger \rangle = \langle \hat{R}(\Omega) \rangle [Y^*(\Omega) X^{-1}(\Omega)]_{\nu\nu'} . \quad (\text{A.31})$$

It will be convenient to introduce the operator

$$[\Omega] = \frac{\hat{R}(\Omega)}{\langle \hat{R}(\Omega) \rangle} \quad (\text{A.32})$$

so that the above relations can be written as

$$\begin{aligned} C_{\nu\nu'}(\Omega) &\equiv \langle a_\nu [\Omega] a_{\nu'}^\dagger \rangle = [X^{-1}(\Omega)]_{\nu\nu'} , \\ B_{\nu\nu'}(\Omega) &\equiv \langle a_\nu a_{\nu'} [\Omega] \rangle = [X^{-1}(\Omega) Y(\Omega)]_{\nu\nu'} , \\ A_{\nu\nu'}(\Omega) &\equiv \langle [\Omega] a_\nu^\dagger a_{\nu'}^\dagger \rangle = [Y^*(\Omega) X^{-1}(\Omega)]_{\nu\nu'} . \end{aligned} \quad (\text{A.33})$$

Note that the operator (A.32) is the three-dimensional generalization of the operator

$$[\beta] = \frac{e^{-i\beta \hat{J}_y}}{\langle e^{-i\beta \hat{J}_y} \rangle}$$

which we introduced in (2.24) when dealing with an axially symmetric system.

Once the unitary coefficients  $X(\Omega)$  and  $Y(\Omega)$  are obtained, the “Contractions”  $A(\Omega)$ ,  $B(\Omega)$  and  $C(\Omega)$  can be evaluated by

$$\begin{aligned} C(\Omega) &= X^{-1}(\Omega) = \begin{bmatrix} C(\Omega) & \bar{C}(\Omega) \\ -\bar{C}^*(\Omega) & C^*(\Omega) \end{bmatrix} , \\ B(\Omega) &= C(\Omega) Y(\Omega) = \begin{bmatrix} B(\Omega) & \bar{B}(\Omega) \\ -\bar{B}^*(\Omega) & B^*(\Omega) \end{bmatrix} , \\ A(\Omega) &= Y^*(\Omega) C(\Omega) = \begin{bmatrix} A(\Omega) & \bar{A}(\Omega) \\ -\bar{A}^*(\Omega) & A^*(\Omega) \end{bmatrix} , \end{aligned} \quad (\text{A.34})$$

where the last forms of (A.34) are their “small” forms which can be expressed in terms of small matrices of  $X(\Omega)$  and  $Y(\Omega)$ .

Next, we consider how to evaluate the overlap  $\langle \hat{R}(\Omega) \rangle$ . It is well-known that an arbitrary finite rotation is equivalent to a single rotation around a properly chosen axis. This means that the rotation operator can be written in terms of a single exponent<sup>27</sup>

$$\hat{R}(\Omega) = \exp\{-i\mathbf{q}\cdot\hat{\mathbf{J}}\}.$$

Furthermore, in the case of a simultaneous angular momentum and particle number projection, the transformation becomes

$$\hat{R}(\Omega, \phi) = \exp\{-i(\mathbf{q}\cdot\hat{\mathbf{J}} + \phi\hat{N})\}.$$

In what follows, we will therefore consider a unitary transformation of the form

$$\exp(-it\hat{G}), \quad (\text{A.35})$$

where  $\hat{G}$  is a sum of Hermitian one-body operators,  $\hat{G} \equiv \sum_i g_i \hat{G}_i$ . The parameter  $t$  will be set to 1 at the end of the derivation. We may write the operator  $\hat{G}$  in the form

$$\hat{G} = \hat{G}^\dagger = \sum_{\alpha\alpha'} c_\alpha^\dagger G_{\alpha\alpha'} c_{\alpha'} = G^{(0)} + \sum_{\nu\nu'} \left\{ a_\nu^\dagger G_{\nu\nu'}^{(1)} a_{\nu'} + \frac{1}{2} [a_\nu^\dagger G_{\nu\nu'}^{(2)} a_{\nu'}^\dagger + \text{h.c.}] \right\}, \quad (\text{A.36})$$

where  $G_{\alpha\alpha'} = G_{\alpha'\alpha}^*$  is the matrix element in the spherical single-particle basis and

$$G^{(0)} = \langle \hat{G} \rangle, \quad G_{\nu\nu'}^{(1)} = \langle a_\nu [\hat{G}, a_{\nu'}^\dagger] \rangle = G_{\nu\nu'}^{(1)*}, \quad G_{\nu\nu'}^{(2)} = \langle a_\nu [\hat{G}, a_{\nu'}] \rangle = -G_{\nu'\nu}^{(2)} \quad (\text{A.37})$$

are those in the quasiparticle basis. We note that the following relations hold:

$$\begin{aligned} G^{(1)} &= U^\dagger G U - V^t G^* V^*, & G^{(2)} &= U^\dagger G V - V^t G^* U^*, \\ \text{Tr}\{G\} &= 2G^{(0)} + \text{Tr}\{G^{(1)}\}. \end{aligned} \quad (\text{A.38})$$

Now consider the transformation (A.21) which, in the present case, takes the form

$$a_\nu(t) = e^{-it\hat{G}} a_\nu e^{it\hat{G}} = \sum_\mu \left\{ X_{\nu\mu}(t) a_\mu + Y_{\nu\mu}(t) a_\mu^\dagger \right\}. \quad (\text{A.39})$$

From  $\dot{a}_\nu(t) \equiv \frac{d}{dt} a_\nu(t) = i[a_\nu(t), \hat{G}]$ , we then obtain the relation

$$\sum_\mu \left\{ \dot{X}_{\nu\mu}(t) a_\mu + \dot{Y}_{\nu\mu}(t) a_\mu^\dagger \right\} = i \sum_\mu \left\{ X_{\nu\mu}(t) [a_\mu, \hat{G}] + Y_{\nu\mu}(t) [a_\mu^\dagger, \hat{G}] \right\}. \quad (\text{A.40})$$

Taking matrix element of this equation between  $\langle 0 |$  and  $a_{\nu'}^\dagger | 0 \rangle$ , we find the relation

$$B(t) G^{(2)*} = G^{(1)} + i X^{-1}(t) \dot{X}(t), \quad (\text{A.41})$$

where we used (A.37) and definition (A.33) of the contraction

$$B_{\nu\mu}(t) = [X^{-1}(t)Y(t)]_{\nu\mu} = \frac{\langle a_\nu a_\mu e^{-it\hat{G}} \rangle}{\langle e^{-it\hat{G}} \rangle}.$$

We use (A.41) and the last relation of (A.38) in the following passage:

$$\begin{aligned} i\frac{d}{dt}\langle e^{-it\hat{G}} \rangle &= \langle \hat{G}e^{-it\hat{G}} \rangle = \langle e^{-it\hat{G}} \rangle G^{(0)} + \frac{1}{2} \sum_{\nu\mu} \langle a_\nu a_\mu e^{-it\hat{G}} \rangle G_{\mu\nu}^{(2)*} \\ &= \langle e^{-it\hat{G}} \rangle \left[ G^{(0)} + \frac{1}{2} \text{Tr}\{B(t)G^{(2)*}\} \right] \\ &= \langle e^{-it\hat{G}} \rangle \left[ \frac{1}{2} \text{Tr}\{G\} + \frac{i}{2} \text{Tr}\{X^{-1}(t)\dot{X}(t)\} \right]. \end{aligned}$$

This “differential equation” can be integrated to obtain the result (with  $t = 1$ )

$$\langle \exp(-i\hat{G}) \rangle = \exp \left[ -\frac{i}{2} \text{Tr}\{G\} + \frac{1}{2} \text{Tr}\{\ln X\} \right] = \{\det X\}^{\frac{1}{2}} \exp \left[ -\frac{i}{2} \text{Tr}\{G\} \right]. \quad (\text{A.42})$$

The matrix  $X$  depends on the real coefficients  $\{g_i\}$  (group parameters) contained in the operator  $\hat{G} = \sum_i g_i \hat{G}_i$ . It should be noted that, if the time-reversal properties

$$\hat{T}|0\rangle = |0\rangle \quad \text{and} \quad \hat{T}\hat{G}\hat{T}^\dagger = -\hat{G} \quad (\text{A.43})$$

are satisfied, the overlap (A.42) is a real quantity,

$$\langle \exp(-i\hat{G}) \rangle = \langle \hat{T}^\dagger \hat{T} \exp(-i\hat{G}) \hat{T}^\dagger \hat{T} \rangle = \langle \exp(-i\hat{G}) \rangle^*.$$

For the angular momentum projection, we have  $\hat{G} = \mathbf{q} \cdot \hat{\mathbf{J}}$  ( $\text{Tr}\{G\} = 0$ ) which satisfies the second relation of (A.43). In the present theory (with or without triaxiality but without particle number projection), both conditions of (A.43) are fulfilled so that  $\langle \hat{R}(\Omega) \rangle$  is a real quantity. Moreover, using the small form (A.23) for  $X(\Omega)$ , we find that it is a positive quantity

$$\begin{aligned} \langle \hat{R}(\Omega) \rangle &= \{\det X(\Omega)\}^{\frac{1}{2}} = |\det X(\Omega)|\{\det(1 + DD^*)\}^{\frac{1}{2}}, \\ D &\equiv X^{-1}(\Omega)\bar{X}(\Omega). \end{aligned} \quad (\text{A.44})$$

The overlap (A.42) will be a complex quantity if one of the conditions of (A.43) is not satisfied. For example, if  $|0\rangle$  is a Cranked HFB state, the first condition is not satisfied since the time-reversal is broken. In the case of a simultaneous angular momentum and particle number projection, the second condition is not fulfilled since the operator  $\hat{G} = \mathbf{q} \cdot \hat{\mathbf{J}} + \phi \hat{N}$  ( $\text{Tr}\{G\} = \phi \text{Tr}\{1\}$ ) is a sum of odd and even operator and has no definite time-reversal transformation property. The overlap is therefore a complex quantity even if the other condition may be satisfied. It means that, in such

a case, the determinant of the matrix  $X$  is a complex quantity. Consequently, it is necessary to ensure that the right branch be selected when evaluating its square root numerically since the computer always takes the principal branch by convention, which is not necessarily the right one. If the wrong branch is picked at a mesh point, the integration (summation) over the group parameters may not be done properly since it leads to a subtraction instead of an addition. Geometrically speaking, the overlap traverses as a function of the group parameters along a trajectory<sup>19</sup> in the complex plane which goes through the point  $(1, 0)$  corresponding to the identity transformation, while the wrong branch constitutes the trajectory that goes through the point  $(-1, 0)$ .

### A.3. Evaluation of rotated matrix elements

Using the contractions  $A(\Omega)$ ,  $B(\Omega)$ , and  $C(\Omega)$  obtained in the previous section, the operator (A.32) can be expressed in the form

$$[\Omega] = \exp \left\{ -\frac{1}{2} \sum_{\nu\nu'} a_\nu^\dagger B_{\nu\nu'} a_{\nu'}^\dagger \right\} \exp \left\{ \sum_{\nu\nu'} a_\nu^\dagger (\ln C)_{\nu\nu'} a_{\nu'} \right\} \exp \left\{ -\frac{1}{2} \sum_{\nu\nu'} a_\nu A_{\nu\nu'} a_{\nu'} \right\},$$

as one can easily verify. Based on this relation, we can prove a generalized contraction theorem<sup>7</sup> which takes the form ( $n + n' = \text{even}$  with  $m \equiv \max\{0, \frac{n-n'}{2}\}$ )

$$\langle a_{n'} \cdots a_1 [\Omega] a_1^\dagger \cdots a_n^\dagger \rangle = \sum_{k=m}^{\lfloor \frac{n}{2} \rfloor} \sum_P (\pm)(B)^{k-(n-n')/2} (C)^{n-2k} (A)^k. \quad (\text{A.45})$$

Here, the right-hand side is a “permuted sum” of products of  $(n+n')/2$  contractions with all possible combinations of pairs of  $n + n'$  indices and  $(\pm)$  is the parity of the permutation. The type of the contraction between a pair of operators is  $A$  ( $B$ ) if both of them stand on the right (left) side of  $[\Omega]$  and is  $C$  if one of them stands on the left and the other on the right side of  $[\Omega]$ . The notation such as  $(A)^k$  implies a product of  $k$  contractions of type  $A$ . This contraction rule can be intuitively understood by studying some examples. We give below those which involve four quasiparticle operators:

$$\begin{aligned} \langle a_1 a_2 a_3 a_4 [\Omega] \rangle &= B_{12}(\Omega) B_{34}(\Omega) - B_{13}(\Omega) B_{24}(\Omega) + B_{14}(\Omega) B_{23}(\Omega), \\ \langle a_1 a_2 a_3 [\Omega] a_4^\dagger \rangle &= B_{12}(\Omega) C_{34}(\Omega) - B_{13}(\Omega) C_{24}(\Omega) + C_{14}(\Omega) B_{23}(\Omega), \\ \langle a_1 a_2 [\Omega] a_3^\dagger a_4^\dagger \rangle &= B_{12}(\Omega) A_{34}(\Omega) - C_{13}(\Omega) C_{24}(\Omega) + C_{14}(\Omega) C_{23}(\Omega), \\ \langle a_1 [\Omega] a_2^\dagger a_3^\dagger a_4^\dagger \rangle &= C_{12}(\Omega) A_{34}(\Omega) - C_{13}(\Omega) A_{24}(\Omega) + C_{14}(\Omega) A_{23}(\Omega), \\ \langle [\Omega] a_1^\dagger a_2^\dagger a_3^\dagger a_4^\dagger \rangle &= A_{12}(\Omega) A_{34}(\Omega) - A_{13}(\Omega) A_{24}(\Omega) + A_{14}(\Omega) A_{23}(\Omega). \end{aligned}$$

Thus, the evaluation of the “rotated” matrix element can be made by first writing

$$\langle a_{n'} \cdots a_1 \hat{R}(\Omega) a_1^\dagger \cdots a_n^\dagger \rangle = \langle \hat{R}(\Omega) \rangle \langle a_{n'} \cdots a_1, [\Omega] a_1^\dagger \cdots a_n^\dagger \rangle \quad (\text{A.46})$$

and then expressing the right-hand side in terms of overlap (A.44) and contractions (A.34) with the help of the rule (A.45).

As an example, let us consider a one-body operator  $\hat{O}$ . There are four kinds of “basic” contractions, namely,

$$\langle \hat{O}[\Omega] \rangle, \quad \langle \hat{O}[\Omega] a_1^\dagger a_2^\dagger \rangle, \quad \langle a_1 \hat{O}[\Omega] a_2^\dagger \rangle, \quad \langle a_1 a_2 \hat{O}[\Omega] \rangle.$$

We can express any (higher order) contractions of  $\hat{O}$  in terms of these basic ones. It will be convenient to write them in the form

$$\begin{aligned} \langle \hat{O}[\Omega] a_1^\dagger a_2^\dagger \rangle &= \langle \hat{O}[\Omega] \rangle \langle [\Omega] a_1^\dagger a_2^\dagger \rangle + \langle \hat{O}[\Omega] a_1^\dagger a_2^\dagger \rangle, \\ \langle a_1 \hat{O}[\Omega] a_2^\dagger \rangle &= \langle \hat{O}[\Omega] \rangle \langle a_1 [\Omega] a_2^\dagger \rangle + \langle a_1 \hat{O}[\Omega] a_2^\dagger \rangle, \\ \langle a_1 a_2 \hat{O}[\Omega] \rangle &= \langle \hat{O}[\Omega] \rangle \langle a_1 a_2 [\Omega] \rangle + \langle a_1 a_2 \hat{O}[\Omega] \rangle. \end{aligned} \quad (\text{A.47})$$

The symbol  $(\cdots [\Omega] \cdots)$  will be referred to as “linked” contraction, which implies that contractions between external indices (quantum numbers 1 and 2) should not be taken. Linked contractions will vanish identically when external indices are contracted:

$$\langle [\Omega] a_1^\dagger a_2^\dagger \rangle = \langle a_1 [\Omega] a_2^\dagger \rangle = \langle a_1 a_2 [\Omega] \rangle = 0.$$

In fact, since  $\langle [\Omega] \rangle = 1$ , the above properties follow from (A.47) by taking  $\hat{O} = 1$ . The vacuum contraction  $\langle \hat{O}[\Omega] \rangle$  is identical to  $\langle \hat{O}[\Omega] \rangle$  as there is no external index. Below, we present formulas for the linked contractions of a general one-body operator  $\hat{O}$  which we separate into a *c*-number part and an operator part as  $\hat{O} = \langle \hat{O} \rangle + : \hat{O} :$

$$: \hat{O} : = \sum_{\nu\nu'} \left\{ a_\nu^\dagger O_{\nu\nu}^{(1)} a_{\nu'} + \frac{1}{2} [a_\nu^\dagger O_{\nu\nu}^{(2)} a_\nu^\dagger - a_\nu O_{\nu\nu}^{(3)} a_{\nu'}] \right\}. \quad (\text{A.48})$$

Matrices  $O^{(2)}$  and  $O^{(3)}$  are antisymmetric. If  $\hat{O}$  is a Hermitian operator, then  $O^{(1)}$  is Hermitian and  $O^{(3)} = O^{(2)*}$ . In practice, we may assume that they are real matrices.

The linked contractions of  $: \hat{O} :$  become

$$\begin{aligned} \langle : \hat{O} : [\Omega] \rangle &= -\frac{1}{2} \text{Tr}\{O^{(B3)}\}, \quad (a_1 : \hat{O} : [\Omega] a_2^\dagger) = O_{12}^{(1C)} + O_{12}^{(B3C)}, \\ (: \hat{O} : [\Omega] a_1^\dagger a_2^\dagger) &= O_{12}^{(C3C)}, \quad (a_2 a_1 : \hat{O} : [\Omega]) = O_{12}^{(2)} - O_{12}^{(1B)} - O_{12}^{(B3B)}, \end{aligned} \quad (\text{A.49})$$

where the following matrices are introduced

$$\begin{aligned} O^{(1B)} &= O^{(1)}B(\Omega) - B^t(\Omega)O^{(1)t}, & O^{(1C)} &= O^{(1)}C(\Omega), & O^{(B3)} &= B^t(\Omega)O^{(3)}, \\ O^{(B3B)} &= O^{(B3)}B(\Omega), & O^{(B3C)} &= O^{(B3)}C(\Omega), & O^{(C3C)} &= C^t(\Omega)O^{(3)}C(\Omega). \end{aligned} \quad (\text{A.50})$$

Similarly, for the operator

$$:\hat{O}^\dagger:=\sum_{\nu\nu'}\left\{a_\nu^\dagger O_{\nu\nu'}^{(1)t}a_{\nu'}+\frac{1}{2}[a_\nu^\dagger O_{\nu\nu'}^{(3)}a_{\nu'}^\dagger-a_\nu O_{\nu\nu'}^{(2)}a_{\nu'}]\right\}, \quad (\text{A.51})$$

we obtain

$$\begin{aligned} \langle :\hat{O}^\dagger: [\Omega] \rangle &= -\frac{1}{2}\text{Tr}\{O^{(B2)}\}, & (a_1 :\hat{O}^\dagger: [\Omega] a_2^\dagger) &= O_{12}^{(0C)} + O_{12}^{(B2C)}, \\ \langle :\hat{O}^\dagger: [\Omega] a_1^\dagger a_2^\dagger \rangle &= O_{12}^{(C2C)}, & (a_2 a_1 :\hat{O}^\dagger: [\Omega]) &= O_{12}^{(3)} - O_{12}^{(0B)} - O_{12}^{(B2B)}, \end{aligned} \quad (\text{A.52})$$

where

$$\begin{aligned} O^{(0B)} &= O^{(1)t}B(\Omega) - B^t(\Omega)O^{(1)}, & O^{(0C)} &= O^{(1)t}C(\Omega), & O^{(B2)} &= B^t(\Omega)O^{(2)}, \\ O^{(B2B)} &= O^{(B2)}B(\Omega), & O^{(B2C)} &= O^{(B2)}C(\Omega), & O^{(C2C)} &= C^t(\Omega)O^{(2)}C(\Omega). \end{aligned} \quad (\text{A.53})$$

These formulas are of much practical importance. Since the two-body interaction of the present model is a sum of separable forces, the direct matrix elements can be expressed in terms of the quantities such as (A.49) and (A.52). This will save much memory and computing time and is one of the advantages of the present model. On the other hand, the exchange matrix elements of separable forces are less important due to the absence of the coherence (which has been confirmed numerically in our earlier work<sup>8</sup>) and will be neglected in accordance with the usual treatment of separable forces.

Let us consider a Hermitian two-body operator representing a separable force

$$\hat{H} = \hat{O}^\dagger \hat{O} = \langle \hat{O} \rangle^2 + \langle \hat{O} \rangle \{ :\hat{O}^\dagger: + :\hat{O}: \} + :\hat{O}^\dagger: :\hat{O}: \equiv H^{(0)} + \hat{H}^{(1)} + \hat{H}^{(2)}, \quad (\text{A.54})$$

where  $H^{(0)}$  is a  $c$ -number and  $\hat{H}^{(1)}$  ( $\hat{H}^{(2)}$ ) is that part which contains 2 (4) quasi-particle operators. Evaluation of  $\hat{H}^{(1)}$  proceeds in the same way as for the one-body operator, namely, its vacuum contraction is given by

$$\langle H^{(1)}[\Omega] \rangle = \langle \hat{O} \rangle \{ \langle :\hat{O}^\dagger: [\Omega] \rangle + \langle :\hat{O}: [\Omega] \rangle \}, \quad (\text{A.55})$$

while linked contractions become

$$\begin{aligned} \langle \hat{H}^{(1)}[\Omega] a_1^\dagger a_2^\dagger \rangle &= \langle \hat{O} \rangle \{ \langle :\hat{O}^\dagger: [\Omega] a_1^\dagger a_2^\dagger \rangle + \langle :\hat{O}: [\Omega] a_1^\dagger a_2^\dagger \rangle \}, \\ (a_1 \hat{H}^{(1)}[\Omega] a_2^\dagger) &= \langle \hat{O} \rangle \{ (a_1 :\hat{O}^\dagger: [\Omega] a_2^\dagger) + (a_1 :\hat{O}: [\Omega] a_2^\dagger) \}, \\ (a_2 a_1 \hat{H}^{(1)}[\Omega]) &= \langle \hat{O} \rangle \{ (a_2 a_1 :\hat{O}^\dagger: [\Omega]) + (a_2 a_1 :\hat{O}: [\Omega]) \}. \end{aligned} \quad (\text{A.56})$$

The treatment of  $\hat{H}^{(2)}$  is more complex. First, the vacuum contraction is given by

$$\langle H^{(2)}[\Omega] \rangle = \langle : \hat{O}^\dagger : [\Omega] \rangle \langle : \hat{O} : [\Omega] \rangle. \quad (\text{A.57})$$

There are eight possible linked contractions for  $\hat{H}^{(2)}$ . The first three are 2-qp type which are similar to those of  $\hat{H}^{(1)}$  (and may be combined with (A.56)):

$$\begin{aligned} (\hat{H}^{(2)}[\Omega]a_1^\dagger a_2^\dagger) &= \langle : \hat{O}^\dagger : [\Omega] \rangle \langle : \hat{O} : [\Omega] a_1^\dagger a_2^\dagger \rangle + \langle : \hat{O} : [\Omega] \rangle \langle : \hat{O}^\dagger : [\Omega] a_1^\dagger a_2^\dagger \rangle, \\ (a_1 \hat{H}^{(2)}[\Omega]a_2^\dagger) &= \langle : \hat{O}^\dagger : [\Omega] \rangle (a_1 : \hat{O} : [\Omega] a_2^\dagger) + \langle : \hat{O} : [\Omega] \rangle (a_1 : \hat{O}^\dagger : [\Omega] a_2^\dagger), \quad (\text{A.58}) \\ (a_2 a_1 \hat{H}^{(2)}[\Omega]) &= \langle : \hat{O}^\dagger : [\Omega] \rangle (a_2 a_1 : \hat{O} : [\Omega]) + \langle : \hat{O} : [\Omega] \rangle (a_2 a_1 : \hat{O}^\dagger : [\Omega]). \end{aligned}$$

The remaining five are 4-qp type:

$$\begin{aligned} (\hat{H}^{(2)}[\Omega]a_1^\dagger a_2^\dagger a_3^\dagger a_4^\dagger) &= \langle : \hat{O}^\dagger : [\Omega] a_1^\dagger a_2^\dagger \rangle \langle : \hat{O} : [\Omega] a_3^\dagger a_4^\dagger \rangle + \langle : \hat{O} : [\Omega] a_1^\dagger a_2^\dagger \rangle \langle : \hat{O}^\dagger : [\Omega] a_3^\dagger a_4^\dagger \rangle \\ &\quad - \langle : \hat{O}^\dagger : [\Omega] a_1^\dagger a_3^\dagger \rangle \langle : \hat{O} : [\Omega] a_2^\dagger a_4^\dagger \rangle - \langle : \hat{O} : [\Omega] a_1^\dagger a_3^\dagger \rangle \langle : \hat{O}^\dagger : [\Omega] a_2^\dagger a_4^\dagger \rangle \\ &\quad + \langle : \hat{O}^\dagger : [\Omega] a_1^\dagger a_4^\dagger \rangle \langle : \hat{O} : [\Omega] a_2^\dagger a_3^\dagger \rangle + \langle : \hat{O} : [\Omega] a_1^\dagger a_4^\dagger \rangle \langle : \hat{O}^\dagger : [\Omega] a_2^\dagger a_3^\dagger \rangle, \quad (\text{A.59}) \end{aligned}$$

$$\begin{aligned} (a_1 \hat{H}^{(2)}[\Omega]a_2^\dagger a_3^\dagger a_4^\dagger) &= (a_1 : \hat{O}^\dagger : [\Omega] a_2^\dagger) \langle : \hat{O} : [\Omega] a_3^\dagger a_4^\dagger \rangle + (a_1 : \hat{O} : [\Omega] a_2^\dagger) \langle : \hat{O}^\dagger : [\Omega] a_3^\dagger a_4^\dagger \rangle \\ &\quad - (a_1 : \hat{O}^\dagger : [\Omega] a_3^\dagger) \langle : \hat{O} : [\Omega] a_2^\dagger a_4^\dagger \rangle - (a_1 : \hat{O} : [\Omega] a_3^\dagger) \langle : \hat{O}^\dagger : [\Omega] a_2^\dagger a_4^\dagger \rangle \\ &\quad + (a_1 : \hat{O}^\dagger : [\Omega] a_4^\dagger) \langle : \hat{O} : [\Omega] a_2^\dagger a_3^\dagger \rangle + (a_1 : \hat{O} : [\Omega] a_4^\dagger) \langle : \hat{O}^\dagger : [\Omega] a_2^\dagger a_3^\dagger \rangle, \quad (\text{A.60}) \end{aligned}$$

$$\begin{aligned} (a_2 a_1 \hat{H}^{(2)}[\Omega]a_3^\dagger a_4^\dagger) &= (a_2 a_1 : \hat{O}^\dagger : [\Omega]) \langle : \hat{O} : [\Omega] a_3^\dagger a_4^\dagger \rangle + (a_2 a_1 : \hat{O} : [\Omega]) \langle : \hat{O}^\dagger : [\Omega] a_3^\dagger a_4^\dagger \rangle \\ &\quad - (a_2 : \hat{O}^\dagger : [\Omega] a_3^\dagger) (a_1 : \hat{O} : [\Omega] a_4^\dagger) - (a_2 : \hat{O} : [\Omega] a_3^\dagger) (a_1 : \hat{O}^\dagger : [\Omega] a_4^\dagger) \\ &\quad + (a_2 : \hat{O}^\dagger : [\Omega] a_4^\dagger) (a_1 : \hat{O} : [\Omega] a_3^\dagger) + (a_2 : \hat{O} : [\Omega] a_4^\dagger) (a_1 : \hat{O}^\dagger : [\Omega] a_3^\dagger), \quad (\text{A.61}) \end{aligned}$$

$$\begin{aligned} (a_3 a_2 a_1 \hat{H}^{(2)}[\Omega]a_4^\dagger) &= (a_2 a_1 : \hat{O}^\dagger : [\Omega]) (a_3 : \hat{O} : [\Omega] a_4^\dagger) + (a_2 a_1 : \hat{O} : [\Omega]) (a_3 : \hat{O}^\dagger : [\Omega] a_4^\dagger) \\ &\quad - (a_3 a_1 : \hat{O}^\dagger : [\Omega]) (a_2 : \hat{O} : [\Omega] a_4^\dagger) - (a_3 a_1 : \hat{O} : [\Omega]) (a_2 : \hat{O}^\dagger : [\Omega] a_4^\dagger) \\ &\quad + (a_1 : \hat{O}^\dagger : [\Omega] a_4^\dagger) (a_3 a_2 : \hat{O} : [\Omega]) + (a_1 : \hat{O} : [\Omega] a_4^\dagger) (a_3 a_2 : \hat{O}^\dagger : [\Omega]), \quad (\text{A.62}) \end{aligned}$$

$$\begin{aligned}
& (a_4 a_3 a_2 a_1 \hat{H}^{(2)}[\Omega]) \\
&= (a_2 a_1 : \hat{O}^\dagger : [\Omega])(a_4 a_3 : \hat{O} : [\Omega]) + (a_2 a_1 : \hat{O} : [\Omega])(a_4 a_3 : \hat{O}^\dagger : [\Omega]) \\
&\quad - (a_3 a_1 : \hat{O}^\dagger : [\Omega])(a_4 a_2 : \hat{O} : [\Omega]) - (a_3 a_1 : \hat{O} : [\Omega])(a_4 a_2 : \hat{O}^\dagger : [\Omega]) \\
&\quad + (a_4 a_1 : \hat{O}^\dagger : [\Omega])(a_3 a_2 : \hat{O} : [\Omega]) + (a_4 a_1 : \hat{O} : [\Omega])(a_3 a_2 : \hat{O}^\dagger : [\Omega]). \quad (\text{A.63})
\end{aligned}$$

Note that, in evaluating the contractions of  $\hat{H}^{(2)}$ , only those terms which factorize to two one-body contractions are retained since they are the terms which benefit from the maximal coherence. They represent the direct type matrix elements. All other matrix elements are neglected since they are of exchange types.

Let us now consider the matrix elements of the operators  $\hat{H}^{(1)}$  and  $\hat{H}^{(2)}$  in (A.54) between two multi-quasiparticle states

$$|\Phi\{n\}\rangle = a_1^\dagger \cdots a_n^\dagger |0\rangle \quad \text{and} \quad |\Phi\{n'\}\rangle = a_1^\dagger \cdots a_{n'}^\dagger |0\rangle, \quad (\text{A.64})$$

where the sum of the number of quasiparticles in these states ( $n + n'$ ) has to be an even number. We obtain for the operator  $\hat{H}^{(1)}$ :

$$\begin{aligned}
\langle \Phi\{n'\} | \hat{H}^{(1)}[\Omega] | \Phi\{n\} \rangle &= \langle \hat{H}^{(1)}[\Omega] \rangle \langle \Phi\{n'\} | [\Omega] | \Phi\{n\} \rangle \\
&+ \sum (\pm) (\hat{H}^{(1)}[\Omega] a_i^\dagger a_j^\dagger) \langle \Phi\{n'\} | [\Omega] | \Phi\{n; i, j\} \rangle \\
&+ \sum (\pm) (a_{i'} \hat{H}^{(1)}[\Omega] a_i^\dagger) \langle \Phi\{n'; i'\} | [\Omega] | \Phi\{n; i\} \rangle \\
&+ \sum (\pm) (a_{j'} a_{i'} \hat{H}^{(1)}[\Omega]) \langle \Phi\{n'; i', j'\} | [\Omega] | \Phi\{n\} \rangle \quad (\text{A.65})
\end{aligned}$$

where  $|\Phi\{n; i, j\}\rangle$ , etc. means a state which is obtained by removing the quasiparticles  $a_i^\dagger$  and  $a_j^\dagger$  from the state  $|\Phi\{n\}\rangle$ . Similarly, we obtain for the operator  $\hat{H}^{(2)}$ :

$$\begin{aligned}
\langle \Phi\{n'\} | \hat{H}^{(2)}[\Omega] | \Phi\{n\} \rangle &= \langle \hat{H}^{(2)}[\Omega] \rangle \langle \Phi\{n'\} | [\Omega] | \Phi\{n\} \rangle \\
&+ \sum (\pm) (\hat{H}^{(2)}[\Omega] a_i^\dagger a_j^\dagger) \langle \Phi\{n'\} | [\Omega] | \Phi\{n; i, j\} \rangle \\
&+ \sum (\pm) (a_{i'} \hat{H}^{(2)}[\Omega] a_i^\dagger) \langle \Phi\{n'; i'\} | [\Omega] | \Phi\{n; i\} \rangle \\
&+ \sum (\pm) (a_{j'} a_{i'} \hat{H}^{(2)}[\Omega]) \langle \Phi\{n'; i', j'\} | [\Omega] | \Phi\{n\} \rangle \\
&+ \sum (\pm) (\hat{H}^{(2)}[\Omega] a_i^\dagger a_j^\dagger a_k^\dagger a_l^\dagger) \langle \Phi\{n'\} | [\Omega] | \Phi\{n; i, j, k, l\} \rangle \\
&+ \sum (\pm) (a_{i'} \hat{H}^{(2)}[\Omega] a_i^\dagger a_j^\dagger a_k^\dagger) \langle \Phi\{n'; i'\} | [\Omega] | \Phi\{n; i, j, k\} \rangle \\
&+ \sum (\pm) (a_{j'} a_{i'} \hat{H}^{(2)}[\Omega] a_i^\dagger a_j^\dagger) \langle \Phi\{n'; i', j'\} | [\Omega] | \Phi\{n; i, j\} \rangle
\end{aligned}$$

$$\begin{aligned}
& + \sum (\pm)(a_{k'} a_{j'} a_{i'} \hat{H}^{(2)}[\Omega] a_i^\dagger) \langle \Phi\{n'; i', j', k'\} | [\Omega] | \Phi\{n; i\} \rangle \\
& + \sum (\pm)(a_{l'} a_{k'} a_{j'} a_{i'} \hat{H}^{(2)}[\Omega]) \langle \Phi\{n'; i', j', k', l'\} | [\Omega] | \Phi\{n\} \rangle. \quad (\text{A.66})
\end{aligned}$$

The summations are over permutations. The contractions appearing in these formulas can be evaluated by using (A.55)–(A.63) and overlaps of two states by (A.45).

#### A.4. Evaluation of projected matrix elements

The last step is the integration over the group parameters. According to (2.35), the projected matrix element between two intrinsic states in general takes the form

$$\begin{aligned}
& \langle \Phi\{n'\} | \hat{P}_{K'M'}^{I'} \hat{T}_{\lambda\mu} \hat{P}_{KM}^I | \Phi\{n\} \rangle \\
& = (IM, \lambda\mu | I'M') \sum_\nu (IK' - \nu, \lambda\nu | I'K') \langle \Phi\{n'\} | \hat{T}_{\lambda\nu} \hat{P}_{K'-\nu K}^I | \Phi\{n\} \rangle. \quad (\text{A.67})
\end{aligned}$$

The operator  $\hat{T}_{\lambda\mu}$  was originally considered to be a one-body (multipole) operator but the formula (2.35) is actually valid for any spherical tensor operators. For example, we could also take it to be 1 (norm) or  $\hat{H}$  (Hamiltonian) in which case we have  $\lambda = \mu = 0$ . In what follows, we will thus examine the three-fold integration in the projected matrix element (using the abbreviations  $|\Phi\rangle \equiv |\Phi\{n\}\rangle$  and  $|\Phi'\rangle \equiv |\Phi\{n'\}\rangle$ ):

$$\langle \Phi' | \hat{T}_{\lambda\nu} \hat{P}_{K'-\nu K}^I | \Phi \rangle = \frac{2I+1}{8\pi^2} \int d\Omega D_{K'-\nu K}^I(\Omega) \langle \Phi' | \hat{T}_{\lambda\nu} \hat{R}(\Omega) | \Phi \rangle. \quad (\text{A.68})$$

In order to accelerate the computation, it is essential to use an efficient algorithm to evaluate the rotated matrix element  $\langle \Phi' | \hat{T}_{\lambda\nu} \hat{R}(\Omega) | \Phi \rangle$  since it has to be computed at each mesh point of  $\Omega$  for all possible quasiparticle configurations taken into account. This aspect was discussed in the previous section. Moreover, the same rotated matrix element is used to compute the projected matrix elements for different spins (i.e., the dependence on  $I$ ,  $K$ , and  $K'$  comes only from the  $D$ -function) so that we can take the advantage of this feature to speed up the computation. Another important strategy is to reduce the range of the integrations (i.e., the number of mesh points of  $\Omega$ ) by using the symmetry properties of the integrand. Such a consideration is especially important when carrying out a triaxial projection (three-fold integration over complex functions) which can be quite time-consuming. We will therefore examine this aspect below.

Using the symmetry operator (A.2), we obtain the relation

$$\hat{P}_{MK}^I |\Phi\rangle = \hat{P}_{MK}^I \hat{S}^\dagger \hat{S} |\Phi\rangle = e^{i\pi(K-\kappa)} \hat{P}_{MK}^I |\Phi\rangle, \quad (\text{A.69})$$

where  $\hat{S}|\Phi\rangle = e^{-i\pi\kappa} |\Phi\rangle$ . If the configuration  $\{n\}$  of the  $n$ -qp state  $|\Phi\rangle = |\Phi\{n\}\rangle$  is a product of  $m$ -qp states of class  $S$  and  $(n-m)$ -qp states of class  $\bar{S}$ , we have

$$\kappa = \frac{1}{2}m - \frac{1}{2}(n-m) = m - \frac{n}{2}, \quad (\text{A.70})$$

which we refer to as character of the intrinsic state  $|\Phi\rangle$ ; cf. (A.7). The relation (A.69) means that the projected state  $\hat{P}_{MK}^I |\Phi\rangle$  vanishes unless  $K = \kappa \pm$  even. For axially symmetric systems, this is trivial since only a definite  $K$  is allowed. For triaxial systems, however, it serves to select possible (allowed) values of  $K$  for a given state  $|\Phi\rangle$ . For example,  $K = 0, \pm 2, \pm 4, \dots$  are the allowed  $K$ -values for selfconjugate states ( $\kappa = 0$ ). Consequently, for an allowed value of  $K$ , the relation  $\hat{S}|\Phi\rangle = e^{-i\pi\kappa}|\Phi\rangle$  implies

$$e^{-i\pi(j_z - K)}|\Phi\rangle = |\Phi\rangle. \quad (\text{A.71})$$

A similar relation holds also for  $|\Phi'\rangle$  with an allowed  $K'$ . These properties can be used to reduce the range of the  $\alpha$ - and  $\gamma$ -integration. The original range  $[0, 2\pi]$  reduces simply to  $[0, \pi]$  in both integrations if  $K$  and  $K'$  in (A.68) are allowed values. In fact, by separating the integral into two parts  $[0, \pi]$  and  $[\pi, 2\pi]$ , we find

$$4 \int_0^\pi d\beta \sin \beta d_{K'-\nu K}^I(\beta) \int_0^\pi d\alpha \int_0^\pi d\gamma e^{i(K'-\nu)\alpha} e^{iK\gamma} \langle \Phi' | \hat{T}_{\lambda\nu} \hat{R}(\alpha, \beta, \gamma) | \Phi \rangle \quad (\text{A.72})$$

since the second part becomes just equal to the first one due to (A.71) and the property

$$\hat{S}^\dagger \hat{T}_{\lambda\nu} \hat{S} = e^{i\pi\nu} \hat{T}_{\lambda\nu} = (-)^{\nu} \hat{T}_{\lambda\nu}. \quad (\text{A.73})$$

Let us further try to reduce the range  $[0, \pi]$  of the  $\alpha$ - and  $\gamma$ -integration to  $[0, \frac{\pi}{2}]$ :

$$\begin{aligned} \int_0^{\frac{\pi}{2}} d\alpha \int_0^{\frac{\pi}{2}} d\gamma \{ & e^{i(K'-\nu)\alpha} e^{iK\gamma} \langle \Phi' | \hat{T}_{\lambda\nu} \hat{R}(\alpha, \beta, \gamma) | \Phi + e^{-i\frac{\pi}{2}(j_z - K)} \Phi \rangle \\ & + e^{-i(K'-\nu)\alpha} e^{-iK\gamma} \langle \Phi' | \hat{T}_{\lambda\nu} \hat{R}(-\alpha, \beta, -\gamma) | \Phi + e^{i\frac{\pi}{2}(j_z - K)} \Phi \rangle \}. \end{aligned}$$

The second integrand is the complex conjugate of the first one because of the relation

$$\langle \Phi' | \hat{T}_{\lambda\nu} \hat{R}(-\alpha, \beta, -\gamma) | \Phi \rangle = \langle \Phi' | \hat{T}_{\lambda\nu} \hat{R}(\alpha, \beta, \gamma) | \Phi \rangle^* \quad (\text{A.74})$$

and the fact that the matrix elements of  $\hat{T}_{\lambda\nu}$  are real (or can be made real in a time-reversal preserving representation). Therefore, the above two-fold integral becomes

$$2 \int_0^{\frac{\pi}{2}} d\alpha \int_0^{\frac{\pi}{2}} d\gamma \operatorname{Re} \{ e^{i(K'-\nu)\alpha} e^{iK\gamma} \langle \Phi' | \hat{T}_{\lambda\nu} \hat{R}(\alpha, \beta, \gamma) | \Phi + e^{-i\frac{\pi}{2}(j_z - K)} \Phi \rangle \}.$$

The role of the linear combination in the ket state is to eliminate those components of  $|\Phi\rangle$  which correspond to  $K \pm 2 \times$  odd integers. It has a simple physical meaning. The operator  $e^{-i\frac{\pi}{2}j_z}$  transforms a given state  $|\Phi\rangle$  into that of the opposite triaxiality ( $\epsilon' \rightarrow -\epsilon'$ ); see the discussion following (A.11). The state  $|\Phi + e^{-i\frac{\pi}{2}(j_z - K)} \Phi\rangle$  is therefore a superposition of two states corresponding to  $+\epsilon'$  and  $-\epsilon'$ . Although

the eigenvalues of (A.10) are the same for  $\pm\epsilon'$ , the eigenstates have no obvious symmetry against the sign flip of  $\epsilon'$ . They are not the eigenstates of the operator (A.11) and we have to evaluate the state  $e^{-i\frac{\pi}{2}(j_z-K)}|\Phi\rangle$  explicitly. We do this by going back to the range  $[0, \pi]$  again for the  $\gamma$ -integration. Thus, the above two-fold integration becomes

$$2 \int_0^{\frac{\pi}{2}} d\alpha \int_0^\pi d\gamma \operatorname{Re} \left\{ e^{i(K'-\nu)\alpha} e^{iK\gamma} \langle \Phi' | \hat{T}_{\lambda\nu} \hat{R}(\alpha, \beta, \gamma) | \Phi \rangle \right\}.$$

Incidentally, these discussions prove that the result does not depend on the sign of the triaxiality parameter  $\epsilon'$ . This justifies the restriction to  $\epsilon' \geq 0$ ; cf. Fig. 64.

The range of the  $\beta$ -integration can also be halved as in the axially symmetric case; cf. (3.14). In the triaxial case, however, the derivation is slightly more complex and it is necessary to resort to the property (A.73) and the relation

$$e^{i\beta j_z} = \hat{S}^\dagger e^{-i\beta j_z} \hat{S}, \quad (\text{A.75})$$

which is intuitively understandable because the symmetry operator  $\hat{S}$  transforms the  $x$ -axis into  $-x$  and  $y$ -axis into  $-y$ . Although the rotated amplitudes are not real quantities in the triaxial case, the time-reversal operator  $\hat{T}$  and  $e^{-i\pi j_y}$  are still equivalent to each other. This can be proved as follows:

$$\begin{aligned} \langle e^{-i\pi j_y} \Phi' | \hat{T}_{\lambda\nu} \hat{R}(\alpha, \beta, \gamma) | e^{-i\pi j_y} \Phi \rangle &= \langle \Phi' | (-)^{\lambda-\nu} \hat{T}_{\lambda-\nu} \hat{R}(-\alpha, \beta, -\gamma) | \Phi \rangle \\ &= \langle \Phi' | \hat{T}_{\lambda\nu} \hat{R}(\alpha, \beta, \gamma) | \Phi \rangle^* \\ &= \langle \hat{T} \Phi' | \hat{T}_{\lambda\nu} \hat{R}(\alpha, \beta, \gamma) | \hat{T} \Phi \rangle, \end{aligned} \quad (\text{A.76})$$

where we used (A.74) and the properties

$$e^{i\pi j_y} \hat{T}_{\lambda\nu} e^{-i\pi j_y} = (-)^{\lambda-\nu} \hat{T}_{\lambda-\nu} = \hat{T}_{\lambda\nu} = \hat{T}^\dagger \hat{T}_{\lambda\nu} \hat{T}.$$

Collecting all this, the final result becomes (on using the notation  $|\bar{\Phi}\rangle \equiv \hat{T}|\Phi\rangle$ )

$$\begin{aligned} 8 \int_0^{\frac{\pi}{2}} d\beta \sin \beta \left[ d_{K'-\nu K}^I(\beta) \int_0^{\frac{\pi}{2}} d\alpha \operatorname{Re} \left\{ e^{i(K'-\nu)\alpha} \int_0^\pi d\gamma e^{iK\gamma} \langle \Phi' | \hat{T}_{\lambda\nu} \hat{R}(\Omega) | \Phi \rangle \right\} \right. \\ \left. + (-)^{I-K} d_{K'-\nu-K}^I(\beta) \int_0^{\frac{\pi}{2}} d\alpha \operatorname{Re} \left\{ e^{i(K'-\nu)\alpha} \int_0^\pi d\gamma e^{-iK\gamma} \langle \Phi' | \hat{T}_{\lambda\nu} \hat{R}(\Omega) | \bar{\Phi} \rangle \right\} \right]. \end{aligned} \quad (\text{A.77})$$

The whole domain of the integrations is therefore reduced to 1/16 of the original one. For axially symmetric systems, the result becomes (after integrating over  $\alpha$  and  $\gamma$ )

$$\begin{aligned} 4\pi^2 \int_0^{\frac{\pi}{2}} d\beta \sin \beta \left[ d_{K'-\nu K}^I(\beta) \langle \Phi' | \hat{T}_{\lambda\nu} e^{-i\beta j_y} | \Phi \rangle \right. \\ \left. + (-)^{I-K} d_{K'-\nu-K}^I(\beta) \langle \Phi' | \hat{T}_{\lambda\nu} e^{-i\beta j_y} | \bar{\Phi} \rangle \right]. \end{aligned} \quad (\text{A.78})$$

The matrix element (A.68) is obtained by multiplying the factor  $\frac{2I+1}{8\pi^2}$  by these results. This factor is essential for the matrix elements of a multipole operator since it is a part of the projection operator. In contrast, a common multiplication factor for the Hamiltonian and norm matrix is unimportant (except for testing the sum rules, see the next section) since the eigenvalue equation remains unchanged.

The integrations in (A.77) and (A.78) are evaluated by using appropriate quadratures (e.g., the Gauß-Legendre for  $\beta$ - and trapezoidal formulas for  $\alpha$ - and  $\gamma$ -integration). They are the standard problems of the numerical analysis and will not be discussed.

#### A.5. Solution of the PSM eigenvalue equation

When a new Projected Shell Model code is written, one might wish to test it before applying it to actual problems. In particular, the test of that part which is related to the PSM eigenvalue equation will be essential among other parts of the programme. In this sense, the most important quantities are the Hamiltonian and norm matrix elements

$$H_{\kappa K \kappa' K'}^I = \langle \Phi_\kappa | \hat{H} \hat{P}_{KK'}^{IN} | \Phi_{\kappa'} \rangle \quad \text{and} \quad N_{\kappa K \kappa' K'}^I = \langle \Phi_\kappa | \hat{P}_{KK'}^{IN} | \Phi_{\kappa'} \rangle$$

which constitute the basic ingredients of the PSM eigenvalue equation.

To test the coding and check the numerical accuracy, two sum rules

$$\sum_{IM} H_{\kappa M \kappa' M}^I = \langle \Phi_\kappa | \hat{H} \hat{P}^N | \Phi_{\kappa'} \rangle \quad \text{and} \quad \sum_{IM} N_{\kappa M \kappa' M}^I = \langle \Phi_\kappa | \hat{P}^N | \Phi_{\kappa'} \rangle \quad (\text{A.79})$$

which follow from the second relation of (2.8) are most useful. Make the replacements  $\hat{P}_{KK'}^{IN} \rightarrow \hat{P}_{KK'}^I$  and  $\hat{P}^N \rightarrow 1$  if the particle number projection is to be omitted. The summation over  $I$  may be terminated at a sufficiently large value since the magnitudes of the projected matrix elements decrease rapidly beyond a certain value of  $I$ .

For an axially symmetric system, the Hamiltonian and norm elements are written as

$$H_{\kappa \kappa'}^I = \langle \Phi_\kappa | \hat{H} \hat{P}_{KK'}^{IN} | \Phi_{\kappa'} \rangle \quad \text{and} \quad N_{\kappa \kappa'}^I = \langle \Phi_\kappa | \hat{P}_{KK'}^{IN} | \Phi_{\kappa'} \rangle$$

where  $K$  and  $K'$  are, respectively, the conserved (intrinsic)  $K$ -quantum number of  $|\Phi_\kappa\rangle$  and  $|\Phi_{\kappa'}\rangle$ , so that the summation over  $M$  reduces to a single term with  $M = K = K'$ . If the particle number projection is omitted, for example, the sum rules become

$$\sum_I H_{\kappa \kappa'}^I = \langle \Phi_\kappa | \hat{H} | \Phi_{\kappa'} \rangle \quad \text{and} \quad \sum_I N_{\kappa \kappa'}^I = \langle \Phi_\kappa | \Phi_{\kappa'} \rangle. \quad (\text{A.80})$$

Note that both sides vanish if  $K \neq K'$ . It means unfortunately that nontrivial sum rules exist only for the matrix elements of  $K = K'$  in the axially symmetric case.

Let us now turn to the discussion of how to solve the PSM eigenvalue equation

$$\sum_{\kappa' K'} \{H_{\kappa K \kappa' K'}^I - EN_{\kappa K \kappa' K'}^I\} F_{\kappa' K'}^I = 0. \quad (\text{A.81})$$

We introduce and work in the representation in which the norm matrix is diagonal

$$\sum_{\kappa' K'} N_{\kappa K \kappa' K'}^I U_{\kappa' K'}^\sigma = n_\sigma U_{\kappa K}^\sigma. \quad (\text{A.82})$$

The norm eigenvalues  $n_\sigma$  are non-negative quantities since the norm is a positive semidefinite matrix. However, it is quite possible that some of them vanish. This happens under the circumstances that the multi- $qp$  states become linearly dependent when they are projected. It implies that the projected shell model basis contains some redundant states. Such redundant states can be removed simply by discarding the zero-eigenvalue solutions of (A.82) since the norm (length) of such a state becomes zero. In fact, we find that  $\langle U^\sigma | U^\sigma \rangle = n_\sigma$ , namely,  $|U^\sigma\rangle \equiv \sum_{\kappa K} U_{\kappa K}^\sigma \hat{P}_{MK}^{IN} |\Phi_\kappa\rangle = 0$  if  $n_\sigma = 0$ , which implies nothing other than the linear dependence of the projected multi- $qp$  states. We may exclude all solutions of (A.82) corresponding to  $n_\sigma = 0$  since  $|U^\sigma\rangle$  vanishes.

In the basis of  $\{|U^\sigma\rangle, n_\sigma \neq 0\}$ , the PSM eigenvalue equation takes the form

$$\sum_{\sigma'} G_{\sigma \sigma'}^I V_{\sigma'}^E = EV_\sigma^E, \quad G_{\sigma \sigma'}^I = \frac{\sum_{\kappa K \kappa' K'} U_{\kappa K}^\sigma H_{\kappa K \kappa' K'}^I U_{\kappa' K'}^{\sigma'}}{\sqrt{n_\sigma n_{\sigma'}}} \quad (\text{A.83})$$

from which the eigenvector  $V_\sigma^E$  and the energy  $E$  are obtained. In the original multi- $qp$  basis, the PSM amplitude corresponding to the energy  $E$  takes the (nonunitary) form

$$F_{\kappa K}^I = \sum_\sigma \frac{V_\sigma^E U_{\kappa K}^\sigma}{\sqrt{n_\sigma}}, \quad (\text{A.84})$$

which satisfies automatically the normalization condition (2.32),

$$\sum_{\kappa K \kappa' K'} F_{\kappa K}^I N_{\kappa K \kappa' K'}^I F_{\kappa' K'}^I = 1, \quad (\text{A.85})$$

provided that the eigenvectors of (A.82) and (A.83) are normalized to unity. For axially symmetric systems, we remove all summations over the  $K$ -quantum numbers and omit  $K$  in the amplitude  $F_{\kappa K}^I$ , as described in Sec. 2; cf. (2.38).

## Appendix B: Kinematics of Decoupled Particles

The signature dependence of decoupled bands discussed in Sec. 3.2 deserves more considerations. In particular, whether or not it depends on details of the Hamiltonian is an important question. This problem will be investigated in this Appendix. We prove first an important operator identity on which our discussions will be based.

In the following derivation, the transformation rule of a tensor operator

$$\hat{R}^\dagger(\Omega)\hat{T}_{\lambda\mu}\hat{R}(\Omega) = \sum_\nu D_{\mu\nu}^\lambda(\Omega)\hat{T}_{\lambda\nu} \quad \text{or} \quad \hat{R}^\dagger(\Omega)\hat{T}_{\lambda\mu} = \sum_\nu D_{\mu\nu}^\lambda(\Omega)\hat{T}_{\lambda\nu}\hat{R}^\dagger(\Omega),$$

the reduction theorem for a product of two  $D$ -functions

$$D_{M_1 K_1}^{J_1}(\Omega)D_{M_2 K_2}^{J_2}(\Omega) = \sum_{JMK} (J_1 M_1, J_2 M_2 | JM)(J_1 K_1, J_2 K_2 | JK) D_{MK}^J(\Omega)$$

and the property  $D_{\mu\nu}^\lambda(\Omega) = (-)^{\mu-\nu} D_{-\mu-\nu}^{\lambda*}(\Omega)$  are used:

$$\begin{aligned} & \hat{P}_{M'K'}^{I'\dagger}\hat{T}_{\lambda\mu} \\ &= \frac{2I'+1}{8\pi^2} \int d\Omega D_{M'K'}^{I'*}\hat{R}^\dagger\hat{T}_{\lambda\mu} = \sum_\nu \frac{2I'+1}{8\pi^2} \int d\Omega D_{M'K'}^{I'*} D_{\mu\nu}^\lambda \hat{T}_{\lambda\nu}\hat{R}^\dagger \\ &= \sum_{IMK\nu} (-)^{\mu-\nu}(I'M', \lambda-\mu|IM)(I'K', \lambda-\nu|IK)\hat{T}_{\lambda\nu} \frac{2I'+1}{8\pi^2} \int d\Omega D_{MK}^{I*}\hat{R}^\dagger \\ &= \sum_{IMK\nu} (-)^{\mu-\nu}(I'M', \lambda-\mu|IM)(I'K', \lambda-\nu|IK)\hat{T}_{\lambda\nu} \frac{2I'+1}{2I+1} \hat{P}_{MK}^{I\dagger}. \end{aligned}$$

With the help of the symmetry property of the Clebsch–Gordan coefficient

$$(-)^{\lambda-\mu}(I'M', \lambda-\mu|IM) = \sqrt{\frac{2I+1}{2I'+1}} (\lambda\mu, IM|I'M')$$

and the relation  $\hat{P}_{MK}^{I\dagger} = \hat{P}_{KM}^I$ , the above result can be rewritten in the form<sup>8</sup>

$$\hat{P}_{K'M'}^{I'}\hat{T}_{\lambda\mu} = \sum_{IMK\nu} (\lambda\mu, IM|I'M') (\lambda\nu, IK|I'K') \hat{T}_{\lambda\nu} \hat{P}_{KM}^I. \quad (\text{B.1})$$

This relation represents a kind of commutation rule ( $\hat{P}\hat{T} \rightarrow \hat{T}\hat{P}$ , e.g.,  $\hat{P}_{MK}^I \hat{H} = \hat{H}\hat{P}_{MK}^I$  for a scalar operator  $\hat{H}$  of  $\lambda = 0$ ) and is an operator identity valid independently of the basis. It can be used in various ways. An example is the relation (2.35) which follows immediately from (B.1) by multiplying  $\hat{P}_{MK}^I$  from the right side and using the second relation of (2.9). We will present another important application in what follows.

In Sec. 3.2, we have shown how the signature dependence of the band energy may arise in the present theory; see (3.17). In that formalism, however, the signature dependence may seem to depend explicitly on the Hamiltonian being used while it does not in the particle-rotor model; see (3.5). This is the basic problem we want to clarify. Obviously, it is necessary to investigate the property of the band energy from a different point of view. In fact, the use of the identity (B.1) opens such a possibility. The following discussion is valid for any (rotationally invariant) Hamiltonian.

To begin with, we consider a 1-*qp* band in a decoupled subshell *j*. The quasi-particle operator is nearly a spherical tensor in such a case. We thus obtain from (B.1)

$$\hat{P}_{M'K'}^{I'} a_{jk}^\dagger = \sum_{IMKm} (jk, IK|I'K')(jm, IM|I'M') a_{jm}^\dagger \hat{P}_{MK}^I \quad (\text{B.2})$$

which is valid to a good approximation if the *j*-mixing of the Nilsson wave function is weak. We will evaluate the rotational energy of the band  $a_{jK}^\dagger |0\rangle$  using this relation. The diagonal element of the norm matrix can be evaluated immediately as

$$\langle a_{jK} \hat{P}_{KK}^I a_{jK}^\dagger \rangle = \sum_{L=\text{even}} q_L^I(K), \quad q_L^I(K) \equiv \langle \hat{P}_{00}^L \rangle (jK, L0|IK)^2. \quad (\text{B.3})$$

Since  $\sum_I (jK, L0|IK)^2 = 1$  and  $\sum_L \langle \hat{P}_{00}^L \rangle = 1$ , we have  $\sum_{IL} q_L^I(K) = 1$ . Therefore, the second sum rule of (A.80) is fulfilled,

$$\sum_I \langle a_{jK} \hat{P}_{KK}^I a_{jK}^\dagger \rangle = 1 = \langle a_{jK} a_{jK}^\dagger \rangle.$$

In passing, we note that there is also no problem in evaluating the off-diagonal elements

$$\langle a_{jK} \hat{P}_{KK'}^I a_{jK'}^\dagger \rangle = \sum_{L=\text{even}} \langle \hat{P}_{00}^L \rangle (jK, L0|IK)(jK', L0|IK'). \quad (\text{B.4})$$

To evaluate the diagonal element of the Hamiltonian matrix, we write

$$\hat{H} a_{jm}^\dagger = [\hat{H}, a_{jm}^\dagger] + a_{jm}^\dagger \hat{H}$$

after the transformation (B.2) and then make a drastic approximation that the residual interaction between quasiparticles is negligible ( $E_{jm} \equiv$  HFB quasiparticle energy)

$$[\hat{H}, a_{jm}^\dagger] \approx [\hat{H}_{HFB}, a_{jm}^\dagger] = E_{jm} a_{jm}^\dagger. \quad (\text{B.5})$$

Using this approximation, we obtain the diagonal elements in the form

$$\langle a_{jK} \hat{H} \hat{P}_{KK}^I a_{jK}^\dagger \rangle = \sum_{L=\text{even}} (E_{jK} \langle \hat{P}_{00}^L \rangle + \langle \hat{H} \hat{P}_{00}^L \rangle) (jK, L0|IK)^2.$$

We remark that the approximation like (B.5) should not be used for the evaluation of the off-diagonal elements because it conflicts with the rotational symmetry and will consequently lead to a non Hermitian Hamiltonian matrix. Nevertheless, for the diagonal elements, it is compatible with the first sum rule of (A.80),

$$\sum_I \langle a_{jK} \hat{H} \hat{P}_{KK}^I a_{jK}^\dagger \rangle = E_{jK} + \langle \hat{H} \rangle = \langle a_{jK} \hat{H} a_{jK}^\dagger \rangle.$$

The present approximation implies that the last particle plays the role of a “spectator” which supplies the angular momentum to the system in order to conserve (quantum mechanically) the total angular momentum but does not interact with the rotating body. In other words, we take into account the kinematical aspect of the last particle properly but neglect the dynamical influence of the rotating body on the single-particle motion. It should be noticed that a similar assumption is made also in the particle-rotor model (i.e., the Coriolis force is of a kinematical origin), which uses in addition a “semiquantal” treatment for the rotational degree of freedom to define the spin of the system; cf. Sec. 3.1. In this way, we obtain the expression for the band energy

$$\begin{aligned} \frac{\langle a_{jK} \hat{H} \hat{P}_{KK}^I a_{jK}^\dagger \rangle}{\langle a_{jK} \hat{P}_{KK}^I a_{jK}^\dagger \rangle} &= E_{jK} + \sum_{L=\text{even}} E_L p_L^I(K), \\ p_L^I(K) &\equiv \frac{q_L^I(K)}{\sum_{L=\text{even}} q_L^I(K)}, \quad E_L \equiv \frac{\langle \hat{H} \hat{P}_{00}^L \rangle}{\langle \hat{P}_{00}^L \rangle}. \end{aligned} \quad (\text{B.6})$$

The first term  $E_{jK}$  is the quasiparticle energy which does not depend on spin  $I$ . It determines the location (bandhead) of the band energy for a given shell filling. The interpretation of the second term is as follows. The quantity  $\langle \hat{P}_{00}^L \rangle$  in  $q_L^I(K)$  of (B.3) is the probability of finding the rotor angular momentum  $L$  ( $L = \text{odd}$  is forbidden for a symmetric rotor,  $\langle \hat{P}_{00}^L \rangle = 0$  if  $L = \text{odd}$ ). Therefore, the quantity  $p_L^I(K)$  is the probability of finding the angular momentum of the quasiparticle ( $j$ ) and the rotor ( $L$ ) being coupled to the spin of the system ( $I$ ). The spin dependent part of the band energy is thus obtained by averaging the rotor energy  $E_L$  over possible  $L$  ( $|j - I| \leq L \leq j + I$ ). The probabilistic nature of the result (B.6) shows the quantum mechanical feature of the present theory. For a well deformed nucleus, we may estimate  $E_L$  and  $\langle \hat{P}_{00}^L \rangle$  by the formula (2.29) without performing the numerical projection,

$$E_L \approx E_0 + \frac{L(L+1)}{2\Im} \quad \text{and} \quad \langle \hat{P}_{00}^L \rangle \approx Q_L \equiv \frac{2L+1}{\Delta J_y^2} \exp \left\{ -\frac{L(L+1)}{2\Delta J_y^2} \right\}. \quad (\text{B.7})$$

Thus, apart from the bandhead  $E_{jK}$ , the spin dependent part of (B.6) becomes

$$\begin{aligned} E_I(K) &= \frac{1}{2\Im} \sum_{L=\text{even}} L(L+1) p_L^I(K), \\ p_L^I(K) &= \frac{q_L^I(K)}{\sum_{L=\text{even}} q_L^I(K)}, \quad q_L^I(K) \approx Q_L(jK, L0|IK)^2. \end{aligned} \quad (\text{B.8})$$

The probability  $Q_L$  depends only on a single parameter  $\Delta J_y^2$  ( $\approx 40$ ; see Table 2) while the rotor moment of inertia  $\Im$  may depend on the Hamiltonian but it is a

common scaling factor. The remaining quantities on the right-hand side are of the kinematical origin. The formula (B.8) describes the whole features of Figs. 2 and 3 quite accurately. The confirmation is left to the reader as a simple numerical exercise (one gets exactly the same figures without knowing the value of  $\Im$  if  $E_I(K)$  is scaled properly in the plot). Note that any Hamiltonian which yields the same  $\Im$  and  $\Delta J_y^2$  will lead to the same result (B.8). This indicates that the signature rule does not depend on details of the Hamiltonian and accordingly justifies the use of a schematic model.

We can play a similar game with a 2-*qp* band in the decoupled subshells  $j_1 \otimes j_2$ ; cf. Sec. 3.4. In this case, it is advantageous to use an irreducible tensor operator  $\hat{A}_{JK}^\dagger = \sum_{K_1 K_2} (j_1 K_1, j_2 K_2 | JK) a_{j_1 K_1}^\dagger a_{j_2 K_2}^\dagger$  and write the 2-*qp* operator in the form  $a_{j_1 K_1}^\dagger a_{j_2 K_2}^\dagger = \sum_J (j_1 K_1, j_2 K_2 | JK) \hat{A}_{JK}^\dagger$  so that the relation (B.1) can be used on  $\hat{A}_{JK}^\dagger$ . The rest is very similar to the 1-*qp* case, e.g., the norm matrix element becomes

$$\begin{aligned} \langle a_{j_2 K_2} a_{j_1 K_1} \hat{P}_{KK'}^I a_{j_1 K'_1}^\dagger a_{j_2 K'_2}^\dagger \rangle &= \sum_J [1 + (-)^J \delta_{j_1 j_2}] (j_1 K_1, j_2 K_2 | JK) \\ &\times \left\{ \sum_{L=\text{even}} \langle \hat{P}_{00}^L \rangle (JK, L0 | IK) (JK', L0 | IK') \right\} (j_1 K'_1, j_2 K'_2 | JK'). \end{aligned} \quad (\text{B.9})$$

Using an approximation like (B.5) and the simplification (B.7), we obtain an analogous formula for the 2-*qp* band energy (apart from the bandhead  $E_{j_1 K_1} + E_{j_2 K_2}$ )

$$\begin{aligned} E_I(K_1, K_2) &= \frac{1}{2\Im} \sum_{L=\text{even}} L(L+1) p_L^I(K_1, K_2), \\ p_L^I(K_1, K_2) &= \frac{q_L^I(K_1, K_2)}{\sum_{L=\text{even}} q_L^I(K_1, K_2)}, \\ q_L^I(K_1, K_2) &\approx Q_L \sum_J [1 + (-)^J \delta_{j_1 j_2}] (j_1 K_1, j_2 K_2 | JK)^2 (JK, L0 | IK)^2. \end{aligned} \quad (\text{B.10})$$

The interpretation is very similar to (B.8). However, there are two important differences. In the first place, two nucleons can couple to various intermediate angular momenta ( $J$ ) which should be summed over. Secondly, there is a factor  $[1 + (-)^J \delta_{j_1 j_2}]$  which arises from the exchange symmetry of two like-nucleons. It should be removed for nucleons of different kinds (i.e.,  $1\nu \otimes 1\pi$ ). For like-nucleons, this factor excludes their angular momenta to be coupled to  $J = \text{odd}$  if  $j_1 = j_2$ . This selection rule forbids in turn the total spin  $I = \text{odd}$  if the identical particles (like-nucleons in the same subshell) have  $K_1 + K_2 = K = 0$ , which corresponds to a selfconjugate state  $a_\nu^\dagger a_\nu^\dagger |0\rangle$  discussed in Sec. 3.3; see (3.25). In the present point of view, it is the parity Clebsch–Gordan coefficient ( $J0, L0 | I0$ ) which forbids the spin  $I = \text{odd}$  for a selfconjugate band. The formula (B.10) reproduces Figs. 4–7 quite

nicely including all the anomalous signature dependence such as the selfinversion. The verification is again left to the reader. It is already done for bands having  $|K| > 2$  (compare Figs. 8 and 9). Again, this suggests that the signature rule does not depend on details of the Hamiltonian.

More generally, an  $n$ -qp band in the decoupled subshells  $j_1 \otimes \cdots \otimes j_n$  can be treated in a similar fashion since a repeated use of (B.2) leads to the relation

$$\begin{aligned} \hat{P}_{M'K'}^{I'} a_{j_1 k_1}^\dagger \cdots a_{j_n k_n}^\dagger = & \sum (j_n k_n, IK | J_{n-1} K_{n-1}) (j_n m_n, IM | J_{n-1} M_{n-1}) \cdots \\ & (j_1 k_1, J_1 K_1 | I' K') (j_1 m_1, J_1 M_1 | I' M') a_{j_1 m_1}^\dagger \cdots \\ & a_{j_n m_n}^\dagger \hat{P}_{MK}^I, \end{aligned} \quad (\text{B.11})$$

where the summation is taken over those angular momenta which do not appear on the left-hand side. We will give another representation for a general multi-qp case at the end. It is clear from the above discussions and (B.11) that the spin dependence of the band energies will not depend on details of the Hamiltonian if the residual interaction between quasiparticles is negligible. The validity of this and the corresponding signature rule (3.19)

$$I - j_1 - \cdots - j_n + \sigma = \pm \begin{cases} \text{even} & \text{favored} \\ \text{odd} & \text{unfavored} \end{cases} \quad (\text{B.12})$$

can be tested numerically against the exact projection calculations, as we have done above for the case of  $n = 1$  and 2. In the generalized signature rule (B.12), the value of  $\sigma$  takes either 0 (normal signature) or 1 (anomalous signature) but would in general depend dynamically on spin (occurrence of selfinversion). Note that we have studied it only numerically so far. In this sense,  $\sigma$  in the rule (B.12) is empirical. Its rigorous mathematical derivation is still missing and is an open problem at present.

Finally, we present a convenient way of treating a general multi-qp case. The method is valid for any quasiparticle states which are well decoupled ( $n$ -qp states in the intruder subshells  $j_1 \otimes \cdots \otimes j_n$ ) but are not necessarily aligned ( $K$ -value arbitrary).

In the first place, we note that the decoupled quasiparticles satisfy the relation

$$a_{jm} \hat{P}_{M0}^L = 0, \quad (\text{B.13})$$

which can be proved from the Hermitian conjugate of the relation (B.2). It means that not only the deformed body  $|0\rangle$  but also the rotating body  $\hat{P}_{M0}^L |0\rangle$  is the vacuum of the decoupled quasiparticles and therefore that the rotation of the deformed body is generated only by those quasiparticles which are coupled strongly to the body.

One can express a decoupled  $n$ -qp state in the form ( $K = K_1 + \cdots + K_n$ )

$$\begin{aligned} a_{j_1 K_1}^\dagger \cdots a_{j_n K_n}^\dagger \rangle &= \sum_{\alpha J} A_{\alpha JK}^\dagger (j_1, \dots, j_n) \langle A_{\alpha JK} (j_1, \dots, j_n) | a_{j_1 K_1}^\dagger \cdots a_{j_n K_n}^\dagger \rangle, \quad (\text{B.14}) \end{aligned}$$

where  $\{A_{\alpha JK}^\dagger(j_1, \dots, j_n)\}$  is an orthonormal set of irreducible  $n$ -qp states,  $\alpha$  being a set of additional quantum numbers (if any) which is necessary to specify a quantum state uniquely for given  $J$  and  $K$ . Application of (B.1) leads to the relation

$$\begin{aligned} \hat{P}_{MK}^I a_{j_1 K_1}^\dagger \cdots a_{j_n K_n}^\dagger \rangle &= \sum_{\alpha JLM'} (JK, L0|IK)(JM', LM - M'|IM) \\ &\quad \times A_{\alpha JM'}^\dagger(j_1, \dots, j_n) \hat{P}_{M-M'0}^L \rangle \\ &\quad \times \langle A_{\alpha JK}(j_1, \dots, j_n) | a_{j_1 K_1}^\dagger \cdots a_{j_n K_n}^\dagger \rangle. \end{aligned} \quad (\text{B.15})$$

The norm matrix element is therefore given by

$$\begin{aligned} &\langle a_{j_n K_n} \cdots a_{j_1 K_1} \hat{P}_{KK'}^I a_{j_1 K'_1}^\dagger \cdots a_{j_n K'_n}^\dagger \rangle \\ &= \sum_{\alpha J} g_J^I(K, K') \langle a_{j_n K_n} \cdots a_{j_1 K_1} | A_{\alpha JK}^\dagger(j_1, \dots, j_n) \rangle \\ &\quad \times \langle a_{j_n K'_n} \cdots a_{j_1 K'_1} | A_{\alpha JK'}^\dagger(j_1, \dots, j_n) \rangle \end{aligned} \quad (\text{B.16})$$

while the band energy by

$$\begin{aligned} &\frac{\langle a_{j_n K_n} \cdots a_{j_1 K_1} \hat{H} \hat{P}_{KK'}^I a_{j_1 K_1}^\dagger \cdots a_{j_n K_n}^\dagger \rangle}{\langle a_{j_n K_n} \cdots a_{j_1 K_1} \hat{P}_{KK'}^I a_{j_1 K_1}^\dagger \cdots a_{j_n K_n}^\dagger \rangle} \\ &= E_{j_1 K_1} + \cdots + E_{j_n K_n} + \frac{1}{2\Im} \sum_{\alpha J} f_J^I(K) \\ &\quad \times \langle a_{j_n K_n} \cdots a_{j_1 K_1} | A_{\alpha JK}^\dagger(j_1, \dots, j_n) \rangle^2 \end{aligned} \quad (\text{B.17})$$

if the whole (quasiparticle) residual interactions are neglected, where we have defined

$$\begin{aligned} g_J^I(K, K') &= \sum_{L=\text{even}} Q_L(JK, L0|IK)(JK', L0|IK'), \\ f_J^I(K) &= \sum_{L=\text{even}} L(L+1)Q_L(JK, L0|IK)^2. \end{aligned} \quad (\text{B.18})$$

Note that these formulas reduce to the previous ones for  $n = 1$  and 2. In a more general case ( $n \geq 3$ ), the evaluation of the (real) coefficients

$$\langle a_{j_n K_n} \cdots a_{j_1 K_1} | A_{\alpha JK}^\dagger(j_1, \dots, j_n) \rangle \quad (\text{B.19})$$

can be done by using the technique well-known in the ordinary shell model method. In fact, it can be expressed in terms of the CFP's of the quasiparticle seniority

scheme so that it is purely of a kinematical origin (coupling of the angular momenta).

In the limit of vanishing deformation (i.e., in the spherical single-particle basis), the rotating body disappears since the quasiparticle vacuum carries no angular momentum,

$$\hat{P}_{M0}^L |0\rangle = \delta_{L0} \delta_{M0} |0\rangle. \quad (\text{B.20})$$

This implies that the Projected Shell Model reduces essentially to the  $M$ -scheme shell model based on the (spherical) quasiparticle representation.

The formula (B.16) depends only on the fluctuation of the angular momentum  $\Delta J_y^2$  in the quasiparticle vacuum state while (B.17) on the rotor moment of inertia  $\Im$  as well as on the bandhead energy  $E_{j_1 K_1} + \dots + E_{j_n K_n}$ . The quantities  $\Delta J_y^2$  and  $\Im$  are rather independent of details of the Hamiltonian and whether the Hamiltonian is schematic or realistic plays no role for them. On the other hand, the bandhead energy sensitively depends on the level scheme resulting from the mean field potential of the assumed Hamiltonian. It represents nothing other than the shell filling of individual nucleus, so that the resulting level scheme has to be absolutely consistent with the empirical shell structure in order to obtain satisfying results. This indeed poses a critical condition on a Hamiltonian to be used in nuclear structure calculations (irrespective of whether it is schematic or realistic).

In summary, the shape of a band energy does not depend on details of the Hamiltonian while its location (relative to other bands) in the band diagram does depend on them quite sensitively. The latter reflects the shell filling of the nucleus.

As the number of quasiparticles becomes larger, the exact numerical projection will become more time consuming and harder, if not impossible. In such a case, the formulas derived here should be quite useful. In particular, the relation (B.17) can be used to evaluate band energies, from which one can plot the band diagram and study the features of the system qualitatively.

### Appendix C: Three-Level Crossing Model

Consider three levels  $E_1$ ,  $E_2$ , and  $E_3$  interacting through the coupling matrix elements  $V_{12}$ ,  $V_{23}$ , and  $V_{31}$ . For the sake of simplicity, let us assume that the basis is orthonormal. Denoting the eigenvalue by  $x$ , we obtain the secular equation

$$\begin{vmatrix} E_1 - x & V_{12} & V_{13} \\ V_{21} & E_2 - x & V_{23} \\ V_{31} & V_{32} & E_3 - x \end{vmatrix} = 0. \quad (\text{C.1})$$

We are interested in the solutions of (C.1) at the three-band crossing point where three unperturbed levels become mutually degenerate. Our task is thus to find the condition for the yrare-yrast degeneracy to occur for the equation (C.1) with  $E_1 = E_2 = E_3 \equiv E_0$

$$S(x) \equiv (E_0 - x)^3 - (V_{12}^2 + V_{23}^2 + V_{31}^2)(E_0 - x) + 2V_{12}V_{23}V_{31} = 0. \quad (\text{C.2})$$

Graphically, the cubic function  $S(x)$  must touch the  $x$ -axis from above if the lowest two (i.e., yrast and yrare) solutions should be degenerate. Therefore, two conditions

$$\frac{dS(x)}{dx} = 0 \quad \text{and} \quad \frac{d^2S(x)}{dx^2} > 0 \quad (\text{C.3})$$

have to be met by such solutions. The first condition gives two possible solutions

$$x = E_0 - F_{\pm} \quad \text{where} \quad F_{\pm} \equiv \pm \sqrt{\frac{V_{12}^2 + V_{23}^2 + V_{31}^2}{3}} \quad (\text{C.4})$$

while the second condition selects the “+” solution. Inserting  $x = E_0 - F_+$  into (C.2), we obtain the relation which has to be fulfilled by the coupling matrix elements

$$V_{12}V_{23}V_{31} = F_+^3 \quad (\text{C.5})$$

from which the condition (3.37) results. In fact, (C.5) implies that the product of three matrix elements must be positive. Moreover, (C.5) also means that the equality

$$\frac{V_{12}^2 + V_{23}^2 + V_{31}^2}{3} = \sqrt[3]{V_{12}^2 V_{23}^2 V_{31}^2} \quad (\text{C.6})$$

must hold. This is the case only if  $V_{12}^2$ ,  $V_{23}^2$ , and  $V_{31}^2$  are equal to each other.

Actually, the basis of the Projected Shell Model is not orthonormal. However, since the unperturbed states are degenerate, one can take an appropriate set of their linear combinations to construct an orthonormal basis. The coupling matrix elements should then be understood to be those with respect to the corresponding basis.

#### Appendix D: Broken Symmetry and Spurious State

A symmetry breaking basis is admixed with spurious state(s). When we diagonalize the Hamiltonian in the projected basis which restores the broken symmetry, the spurious state(s) will be automatically eliminated as the zero norm state(s). However, this is the case only if the diagonalization is carried out in the whole configuration space. In practice, we usually truncate those high-lying states which are physically not interesting. Indeed, the very aim of using a symmetry breaking basis is to carry out the truncation of the configuration space efficiently. Therefore, in principle, it is necessary to remove the spurious admixtures out of the truncated basis to obtain the physical states. In particular, the spurious state originating from the particle number violation deserves a special consideration because it is mostly the low-lying states which are contaminated by the spurious admixture. In what follows, we will therefore develop a systematic method to separate the spurious state from the physical ones in a truncated space. For simplicity, we will concentrate on

the space spanned by the  $K = 0$  selfconjugate 2- $qp$  states (referred to as 2- $qp$  pair states hereafter). This is justified due to the fact that the lowest order spurious state in question appears only in this channel and all states in other channels can be excluded from the consideration.

The starting point of our discussion is the identity

$$\hat{P}^N(\hat{N} - N)|0\rangle = 0. \quad (\text{D.1})$$

For the BCS vacuum state satisfying the number condition  $\langle 0|\hat{N}|0\rangle = \sum_\nu v_\nu^2 = N$ , the relation (D.1) reduces to

$$\sum_\nu u_\nu v_\nu \hat{P}^N a_\nu^\dagger a_\nu^\dagger |0\rangle = 0. \quad (\text{D.2})$$

It shows that there is a linear dependence among the 2- $qp$  pair states

$$|\Phi_\nu\rangle \equiv a_\nu^\dagger a_\nu^\dagger |0\rangle \quad (\text{D.3})$$

when projected onto the good particle number.

In passing, we remark that there also exists higher order linear dependence among multi- $qp$  pair states. For example, a relation containing 4- $qp$  pair states follows from the second order identity<sup>67</sup>

$$\hat{P}^N(\hat{N} - N)^2|0\rangle = 0.$$

The method described below can be easily generalized to such a case but restriction to the 2- $qp$  pair space is sufficient for our present purpose.

Let us consider the diagonalization in the projected 0- $qp$  and 2- $qp$  pair states

$$\sum_{\nu'} \{H_{\nu\nu'} - EN_{\nu\nu'}\} F_{\nu'} = 0, \quad (\text{D.4})$$

$$H_{\nu\nu'} = \langle \Phi_\nu | \hat{H} \hat{P}^N | \Phi_{\nu'} \rangle, \quad N_{\nu\nu'} = \langle \Phi_\nu | \hat{P}^N | \Phi_{\nu'} \rangle,$$

where the quantum number  $\nu$  runs over all possible 2- $qp$  pair states (the number of such states is equal to the number of levels which are taken into account in the BCS procedure) including  $\nu = 0$  for the 0- $qp$  state  $|\Phi_0\rangle \equiv |0\rangle$ . Obviously, an eigenvector  $F = (0, u_\nu v_\nu)$  fulfills the equation (D.4) for any eigenvalue  $E$  due to the relation (D.2). It is an eigenvector of the norm matrix  $N$  corresponding to the eigenvalue (norm) 0 and is the so-called spurious solution. Accordingly, the number of physical states (for each kind of nucleons) is one less than the dimension of the original space. As a consequence, the (original) lowest excited state will disappear from the resulting eigenstates. The diagonalization in the projected basis thus automatically removes the spurious state as a norm 0 state. However, it should be remarked that this mechanism works only if the whole 2- $qp$  pair states (untruncated ones) are

taken into account. For example, if three major shells for each kind of nucleons are taken into account as in our case, there are 64 (46) neutron (proton) 2-*qp* pair states for rare-earth nuclei. Obviously, many (as a matter of fact, most) of them are highly excited and are physically uninteresting since they are far away from the yrast region. However, since the amplitude of the spurious admixture is  $u_\nu v_\nu$ , the lower the 2-*qp* pair state, the stronger the contamination. Thus, if we truncate the configuration space to the low-lying states, most of them are largely contaminated, so that it is necessary (in principle) to remove the spurious admixtures in some way since the diagonalization procedure fails to achieve this task.

We will now develop a method to remove the spurious state consistently out of a truncated space. Some preparation is necessary for this purpose. Let us first define

$$|\Phi_{sp}\rangle \equiv \sum_\nu u_\nu v_\nu |\Phi_\nu\rangle \quad (\text{D.5})$$

which projects to 0 because of (D.2). We introduce a new set of basis states by

$$\begin{aligned} |\Phi'_0\rangle &= |\Phi_0\rangle, \\ |\Phi'_\nu\rangle &= |\Phi_\nu\rangle - C_\nu |\Phi_{sp}\rangle. \end{aligned} \quad (\text{D.6})$$

The constant  $C_\nu$  is determined by the condition that  $|\Phi'_\nu\rangle$  is orthogonal to  $|\Phi_{sp}\rangle$

$$C_\nu = \frac{\langle \Phi_{sp} | \Phi_\nu \rangle}{\langle \Phi_{sp} | \Phi_{sp} \rangle} = \frac{u_\nu v_\nu}{\sum_\nu u_\nu^2 v_\nu^2}. \quad (\text{D.7})$$

The transformation from  $\{|\Phi_0\rangle, |\Phi_\nu\rangle\}$  to  $\{|\Phi'_0\rangle, |\Phi'_\nu\rangle\}$  is done by the matrix

$$M = \begin{bmatrix} 1 & 0 \\ 0 & L \end{bmatrix}, \quad L_{\nu\nu'} = \delta_{\nu\nu'} - \frac{u_\nu v_\nu u_{\nu'} v_{\nu'}}{\sum_\nu u_\nu^2 v_\nu^2}, \quad (\text{D.8})$$

where the indices of  $M$  run over the 0-*qp* and 2-*qp* pair states while those of  $L$  only over the latter. Note that  $M$  is a projector ( $M^2 = M = M^\dagger$ ), so that its eigenvalues are either 1 or 0. Since  $\text{Trace}\{M\}$  is one less than the dimension of the space (of the 0-*qp* and 2-*qp* pair states), there is only one eigenvalue 0, the rest being 1. In the new basis, the eigenvalue equation takes the form

$$\sum_{\nu'} \{H'_{\nu\nu'} - EN'_{\nu\nu'}\} F'_{\nu'} = 0, \quad H'_{\nu\nu'} = (M H M)_{\nu\nu'}, \quad N'_{\nu\nu'} = (M N M)_{\nu\nu'}. \quad (\text{D.9})$$

We now show that this form of the eigenvalue equation can be safely truncated.

So far, we have performed only the basis transformation. Note, however, that the new basis allows us to remove the spurious state through the projector  $M$  since the eigenvector  $F = (0, u_\nu v_\nu)$  corresponding to the eigenvalue 0 is the same for the

matrices  $M$  and  $N$ . Moreover, two sets of basis states are equal to each other when projected in the whole configuration space because of the relation (D.2). Therefore, it does not matter whether we write the eigenvalue equation in the form (D.4) or (D.9). However, the former should not be used in a truncated space. This is because the norm matrix  $N$  becomes then a submatrix of the original one and no longer has the eigenvalue 0. It means that the equation (D.4) fails to remove the spurious state. On the other hand, the matrix  $M$  is a projector even in a truncated space by its construction. This makes the new basis advantageous because the equation (D.9) removes the spurious (i.e., the most contaminated) state as the zero norm solution of the matrix  $N'$ . This is what we can at best do in a truncated space. It becomes exact in the full space.

The method applies independently to the neutron and proton degrees of freedom and can be generalized to the configuration space up to and including the  $2\nu \otimes 2\pi$   $4\text{-}qp$  states in a straightforward manner. It also applies to the angular momentum projected case since two projection operators  $\hat{P}_{MK}^I$  and  $\hat{P}^N$  commute with one another.

## References

1. M. G. Mayer, *Phys. Rev.* **75**, 1968 (1949); O. J. Haxel, J. H. D. Jensen and H. E. Suess, *Phys. Rev.* **75**, 1766 (1949); M. G. Mayer and J. H. D. Jensen, *Elementary Theory of Nuclear Shell Structure* (John Wiley & Sons, New York, 1955); A. de-Shalit and I. Talmi, *Nuclear Shell Theory* (Academic Press, New York and London, 1963); see M. Vallières and H. Wu, *The Nuclear Shell Model*, eds. K. Langanke, J. A. Maruhn and S. E. Koonin, *Computational Nuclear Physics*, Vol. 1 (Springer-Verlag, Berlin and Heidelberg, 1991), for an overview of recent shell model codes.
2. R. R. Whitehead, A. Watt, B. J. Cole and I. Morrison, *Adv. Nucl. Phys.* **9**, 123 (1977); see M. Vallières and H. Wu in Ref. 1 for further references.
3. J. P. Elliott, *Proc. Roy. Soc.* **245**, 128 and 557 (1968).
4. S. G. Nilsson, *Dan. Mat. Fys. Medd.* **29**, nr.16 (1955).
5. A. Johnson, H. Ryde and J. Sztarkier, *Phys. Rev. Lett.* **B34**, 605 (1971).
6. A. Johnson, H. Ryde and S. A. Hjorth, *Nucl. Phys.* **A179**, 753 (1972).
7. K. Hara and S. Iwasaki, *Nucl. Phys.* **A332**, 61 (1979).
8. K. Hara and S. Iwasaki, *Nucl. Phys.* **A348**, 200 (1980).
9. S. Iwasaki and K. Hara, *Prog. Theor. Phys.* **68**, 1782 (1982).
10. K. Hara and S. Iwasaki, *Nucl. Phys.* **430**, 175 (1984).
11. K. Hara and Y. Sun, *Nucl. Phys.* **A529**, 445 (1991).
12. K. Hara and Y. Sun, *Nucl. Phys.* **A531**, 221 (1991).
13. K. Hara and Y. Sun, *Nucl. Phys.* **A537**, 77 (1992).
14. M. Hamermesh, *Group Theory and its Application to Physical Problems*, Chapter 3, Section 18, (Addison-Wesley, Reading, Massachusetts, 1964).
15. A. Bohr and B. R. Mottelson, *Nuclear Structure* Vol. I, Appendix 1A (Benjamin, Inc., London, 1969).
16. A. Bohr and B. R. Mottelson, *Nuclear Structure* Vol. II, Chapter 4 (Benjamin, Inc., London, 1975).
17. R. E. Pierls and I. Yoccoz, *Proc. Phys. Soc.* **A70**, 381 (1957).
18. N. Onishi and S. Yoshida, *Nucl. Phys.* **80**, 367 (1966).
19. N. Onishi, R. K. Sheline and S. Yoshida, *Phys. Rev.* **C3**, 1304 (1970).

20. M. Abramowitz and I. A. Segun (eds.), *Handbook of Mathematical Functions* (Dover Publications, Inc., New York, 1968) p. 486.
21. K. Hara and S. Iwasaki, unpublished calculations (1982).
22. S. Iwasaki and K. Hara, *Phys. Lett.* **B144**, 9 (1984).
23. I. L. Lamm, *Nucl. Phys.* **A125**, 504 (1969).
24. K. Allaart, E. Boeker, G. Bonsignori, M. Soria and Y. K. Gambhir, *Phys. Rep.* **169**, 209 (1988).
25. K. W. Schmid, F. Grümmer and A. Faessler, *Phys. Rev.* **C29**, 291 (1984).
26. K. W. Schmid, F. Grümmer and A. Faessler, *Phys. Rev.* **C29**, 308 (1984).
27. K. W. Schmid, F. Grümmer and A. Faessler, *Nucl. Phys.* **A436**, 417 (1985).
28. K. W. Schmid, F. Grümmer and A. Faessler, *Nucl. Phys.* **A431**, 205 (1984).
29. K. W. Schmid and F. Grümmer, *Rep. Prog. Phys.* **50**, 731 (1987).
30. K. Hara, A. Hayashi and P. Ring, *Nucl. Phys.* **A385**, 14 (1982).
31. A. Hayashi, K. Hara and P. Ring, *Phys. Rev. Lett.* **4**, 337 (1984).
32. H. J. Mang, *Phys. Rep.* **16**, 325 (1975).
33. D. R. Bes and R. A. Broglia, *Phys. Rev.* **C3**, 2349 (1971).
34. I. Hamamoto, *Nucl. Phys.* **A232**, 445 (1974).
35. K. Hara and S. Kusuno, *Nucl. Phys.* **A245**, 147 (1975).
36. R. Bengtsson, I. Hamamoto and B. R. Mottelson, *Phys. Lett.* **B73**, 259 (1978).
37. R. G. Helmer, *Nucl. Data Sheets* **49**, 398 (1986).
38. M. A. Lee, *Nucl. Data Sheets* **56**, 223 (1989).
39. J. Simpson, M. A. Riley, J. R. Cresswell, D. V. Elenkov, P. D. Forsyth, G. B. Hagemann, D. Howe, B. M. Nyakó, S. Ogaza, J. C. Lisle and J. F. Sharpey-Schafer, *J. Phys.* **G13**, 847 (1987).
40. R. G. Helmer, *Nucl. Data Sheets* **64**, 103 (1991).
41. E. N. Shurshikov, *Nucl. Data Sheets* **47**, 464 (1986).
42. A. E. Ignatochkin, E. N. Shurshikov and Yu. F. Jaborov, *Nucl. Data Sheets* **52**, 376 (1987).
43. V. S. Shirley, *Nucl. Data Sheets* **53**, 231 (1988).
44. C. M. Zhou, *Nucl. Data Sheets* **50**, 360 (1987).
45. C. Baktach, Y. Schutz, I. Y. Lee, F. K. McGowan, N. R. Johnson, M. L. Halbert, D. C. Hensley, M. P. Fewell, L. Courtney, A. J. Larabee, L. L. Riedinger, A. W. Sunyar, E. der Mateosian, O. C. Kistner and D. G. Sarantites, *Phys. Rev. Lett.* **54**, 978 (1985).
46. T. Byrski, F. A. Beck, J. C. Merdinger, A. Nourreddine, H. W. Granmer-Gordon, D. V. Elenkov, P. D. Forsyth, D. Howe, M. A. Riley, J. F. Sharpey-Schafer, J. Simpson, J. Dudek and W. Nararewicz, *Nucl. Phys.* **A474**, 183 (1987).
47. R. G. Helmer, *Nucl. Data Sheets*, **64**, 112 (1991).
48. E. N. Shurshikov, *Nucl. Data Sheets* **47**, 469 (1986).
49. A. E. Ignatochkin, E. N. Shurshikov and Yu. F. Jaborov, *Nucl. Data Sheets* **52**, 380 (1987).
50. V. S. Shirley, *Nucl. Data Sheets* **53**, 237 (1988).
51. C. M. Zhou, *Nucl. Data Sheets* **50**, 366 (1987).
52. G. Q. Wang, *Nucl. Data Sheets* **51**, 587 (1987).
53. R. G. Helmer, *Nucl. Data Sheets* **64**, 115 (1991).
54. J. N. Mo, S. Sergiwa, R. Chapman, J. C. Liste, E. Paul, J. C. Willmott, J. Hattula, M. Jääskeläinen, J. Simpson, P. M. Walker, J. D. Garrett, G. B. Hagemann, B. Herskind, M. A. Riley and G. Sletten, *Nucl. Phys.* **A472**, 295 (1987).
55. A. E. Ignatochkin, E. N. Shurshikov and Yu. F. Jaborov, *Nucl. Data Sheets* **52**, 383 (1987).

56. V. S. Shirley, *Nucl. Data Sheets* **53**, 241 (1988).
57. C. M. Zhou, *Nucl. Data Sheets* **50**, 370 (1987).
58. G. Q. Wang, *Nucl. Data Sheets* **51**, 595 (1987).
59. E. Browne, *Nucl. Data Sheets* **62**, 23 (1991).
60. J. Simpson, F. Hanna, M. A. Riley, A. Alderson, M. A. Bentley, A. M. Bruce, D. M. Cullen, P. Fallon and L. Walker, *J. Phys.* **G18**, 1207 (1992).
61. K. Theine, A. P. Byrne, H. Hübel, M. Murzel, R. Chapman, D. Clarke, F. Khazaie, J. C. Lisle, J. N. Mo, J. D. Garrett, H. Ryde and R. Wyss, *Nucl. Phys.* **A548**, 71 (1992).
62. C. M. Zhou, *Nucl. Data Sheets* **50**, 371 (1987).
63. J. Espino, J. D. Garrett, G. B. Hagemann, P. O. Tjom, C.-H. Yu, M. Bergström, L. Carlén, L. P. Ekström, J. Lyttkens-Lindén, H. Ryde, R. Bengtsson, T. Bengtsson, R. Chapman, D. Clarke, F. Khazaie, J. C. Lisle and J. N. Mo, *Nucl. Phys.* **A567**, 377, (1994).
64. E. Browne, *Nucl. Data Sheets* **62**, 28 (1991).
65. E. Browne, *Nucl. Data Sheets* **54**, 227 (1988).
66. A. S. Davydov and F. G. Filippov, *Nucl. Phys.* **8**, 237 (1958).
67. K. Hara, S. Iwasaki and K. Tanabe, *Nucl. Phys.* **A332**, 69 (1979).
68. J. R. B. Oliveira, S. Frauendorf, M. A. Deleplanque, R. M. Diamond, F. S. Stephens, C. W. Beausang, J. E. Draper, C. Duyer, E. Rubel, J. A. Becker, E. A. Henry and N. Roy, *Phys. Rev.* **C47**, R926 (1993).
69. Y. Sun and J. L. Egido, *Phys. Rev.* **C50**, 1893 (1994).
70. K. Hara, *Nucl. Phys.* **A557**, 449c (1993).
71. Y. Sun and J. L. Egido, *Nucl. Phys.* **A580**, 1 (1994).
72. M. Oshima, N. R. Johnson, F. K. McGowan, C. Baktash, I. Y. Lee, Y. Schulz, R. V. Ribas and J. C. Wells, *Phys. Rev.* **C33**, 1988 (1986).
73. B. Bochev *et al.*, *Sov. J. Nucl. Phys.* **30**, 305 (1979).
74. S. W. Yates, I. Y. Lee, N. R. Johnson, E. Eichler, L. L. Riedinger, M. W. Guidry, A. C. Kahler, D. Cline, R. S. Simon, P. A. Butler, P. Colombani, F. S. Stephens, R. M. Diamond, R. M. Ronningen, R. D. Hichwa, J. H. Hamilton and E. L. Robinson, *Phys. Rev.* **C21**, 2366 (1980).
75. C. Fahlander, I. Thorslund, B. Varnestig, A. Bäcklin, L. E. Svensson, D. Dissdier, L. Kraus, I. Linck, N. Schulz, J. Pedersen and D. Cline, *Nucl. Phys.* **A537**, 183 (1992).
76. B. Kotliński, D. Cline, A. Bäcklin, K. G. Helmer, A. E. Kavka, W. J. Kernan, E. G. Vogt, R. M. Diamond, A. O. Macchiavelli and M. A. Deleplanque, *Nucl. Phys.* **A517**, 365 (1990).
77. M. J. A. de Voigt, J. Dudek and Z. Szymański, *Rev. Mod. Phys.* **55**, 949 (1983).
78. M. P. Fewell, N. R. Johnson, F. K. McGowan, J. S. Hattula, I. Y. Lee, C. Baktash, Y. Schutz, J. C. Wells, L. L. Riedinger, M. W. Guidry and S. C. Pancholi, *Phys. Rev.* **C37**, 101 (1988).
79. C. W. Reich (ed.), *Nucl. Data Sheets* **68**, 405 (1993).
80. F. K. McGowan, N. R. Johnson, C. Baktash, I. Y. Lee, Y. Schutz, J. C. Wells and A. Larabee, *Nucl. Phys.* **A539**, 276 (1992).
81. B. Bochev, S. A. Karamian, T. Kutsarova, E. Nadjakov and Yu. Ts. Oganessian, *Nucl. Phys.* **A267**, 344 (1976).
82. J. C. Lisle, D. Clarke, R. Chapman, F. Khazaie, J. N. Mo, H. Hübel, W. Schmitz, K. Theine, J. D. Garrett, G. B. Hagemann, B. Herskind and K. Schiffer, *Nucl. Phys.* **A520**, 451c (1990).

83. J. C. Bacelar, R. M. Diamond, E. M. Beck, M. A. Deleplanque, J. Draper and F. S. Stephens, *Phys. Rev.* **C35**, 1170 (1987).
84. C. Fahlander, B. Varnestig, A. Bäcklin, L. E. Svensson, D. Disdier, L. Kraus, I. Linck, N. Schulz and J. Pedersen, *Nucl. Phys.* **A541**, 157 (1992).
85. E. Münck *et al.*, *Phys. Lett.* **B24**, 392 (1967).
86. A. Alzner, E. Bodenstedt, B. Gemünden, J. van den Hoff and H. Reif, *Z. Phys.* **A322**, 467 (1985).
87. C. E. Doran, H. H. Bolotin, A. E. Stuchbery and A. P. Byrne, *Z. Phys.* **A325**, 285 (1986).
88. C. E. Doran, A. E. Stuchbery, H. H. Bolotin, A. P. Byrne and G. J. Lampard, *Phys. Rev.* **C40**, 2035 (1989).
89. F. Brandolini, C. Cattaneo, R. V. Ribas, D. Bazzacco, M. De Poli, M. Inonescu-Bujor, P. Pavan, C. Roosi-Alvarez, to be published.
90. E. Lubkiewicz, H. Emling, H. Grein, R. Kulessa, R. S. Simon, H. J. Wollersheim, C. Ender, J. Gerl, D. Habs and D. Schwahn, *Z. Phys.* **A335**, 369 (1990).
91. C. M. Lederer and V. S. Shirley (eds.), *Table of Isotopes*, 7th Edition (John Wiley & Sons, New York, 1978).
92. M. A. Rizzutto, E. W. Cybulski, L. G. R. Emediato, N. H. Medina, R. V. Ribas, K. Hara and C. L. Lima, *Nucl. Phys.* **A569**, 547 (1994).
93. M. A. Rizzutto, E. W. Cybulski, V. R. Vanin, J. R. B. Oliveira, L. G. R. Emediato, R. V. Ribas, W. A. Seale, M. N. Rao, N. H. Medina, S. Botelho and C. L. Lima, *Z. Phys.* **A344**, 221 (1992).
94. J. L. Salicio, M. Délèze, S. Drissi, J. Kern, S. J. Mannanal, J. P. Vorlet and I. Hamamoto, *Nucl. Phys.* **A512**, 109 (1990).
95. S. Drissi, A. Bruder, J.-Cl. Dousse, V. Ionescu, J. Kern, J.-A. Pinston, S. André, D. Barnéoud, J. Genevey and H. Frisk, *Nucl. Phys.* **451**, 313 (1986).
96. R. G. Helmer, *Nucl. Data Sheets* **59**, 22 (1990).
97. T. Burrows, *Nucl. Data Sheets* **56**, 332 (1989).
98. L. K. Peker, *Nucl. Data Sheets* **65**, 450 (1992).
99. V. S. Shirley, *Nucl. Data Sheets* **58**, 882 (1989).
100. T. Burrows, *Nucl. Data Sheets* **56**, 343 (1989).
101. L. K. Peker, *Nucl. Data Sheets* **65**, 456 (1992).
102. V. S. Shirley, *Nucl. Data Sheets* **58**, 894 (1989).
103. V. S. Shirley, *Nucl. Data Sheets* **64**, 526 (1991).
104. K. Hara, in *Nuclear Collective Motion and Nuclear Reaction Dynamics*, eds. K.-I. Kubo, M. Ichimura, M. Ishihara and S. Yamaji, (World Scientific, 1990) p. 308.
105. N. Roy, S. Jónsson, H. Ryde, W. Waluś, J. J. Gaardhoje, J. D. Garrett, G. B. Hagemann and B. Herskind, *Nucl. Phys.* **A382**, 125 (1982).
106. J. Kownacki, J. D. Garrett, J. J. Gaardhoje, G. B. Hagemann, B. Herskind, S. Jónsson, N. Roy, H. Ryde and W. Waluś, *Nucl. Phys.* **A394**, 269 (1983).
107. I. Hamamoto, *Phys. Lett.* **B102**, 225 (1981).
108. I. Hamamoto, *Phys. Lett.* **B106**, 281 (1981).
109. R. G. Helmer, *Nucl. Data Sheets* **59**, 17 (1990).
110. H. J. Jensen *et al.*, *Z. Phys.* **A340**, 351 (1991).
111. L. K. Peker, *Nucl. Data Sheets* **65**, 459 (1992).
112. K. Theine, C.-X. Yang, A. P. Byrne, H. Hübel, R. Chapman, D. Clarke, F. Khazaie, J. C. Lisle, J. N. Mo, J. D. Garrett and H. Ryde, *Nucl. Phys.* **A536**, 418 (1992).
113. S. G. Nilsson, C. F. Tsang, A. Sobiczewski, Z. Szymanski, S. Wycech, C. Gustafson, I. Lamm, P. Möller and B. Nilsson, *Nucl. Phys.* **A131**, 1 (1969).
114. T. Bengtsson and I. Ragnarsson, *Nucl. Phys.* **A436**, 14 (1985).

115. J.-Y. Zhang, A. J. Larabee and L. L. Riedinger, *J. Phys.* **G13**, L75 (1987).
116. R. Bengtsson, S. Frauendorf and F.-R. May, *Atomic Data and Nuclear Data Tables*, **35**, 15 (1986).
117. Y. Sun, S. Wen and D. H. Feng, *Phys. Rev. Lett.* **72**, 3483 (1994).
118. S. Flibotte *et al.*, *Phys. Rev. Lett.* **71**, 4299 (1993).
119. L. Riedinger *et al.*, to be published.
120. B. Cederwall *et al.*, *Phys. Rev. Lett.* **72**, 3150 (1994).
121. I. Hamamoto and B. Mottelson, *Phys. Lett.* **B333**, 294 (1994).
122. A. O. Macchiavelli, B. Cederwall, R. M. Clark, M. A. Deleplanque, R. M. Diamond, P. Fallon, I. Y. Lee, F. S. Stephens and S. Asztalos, *Phys. Rev.* **C51**, R1 (1995).
123. I. M. Favlichenkov and S. Filbotte, *Phys. Rev.* **C51**, R460 (1995).
124. S. Frauendorf, J. Meng and J. Reif, Proceedings on *Physics from Large  $\gamma$ -Ray Arrays*, Berkeley, 2–6 August 1994, p. 52.
125. P. Magierski, P.-H. Heenen and W. Nazarewicz, *Phys. Rev.* **C51**, R2880 (1995).
126. I. N. Mikhailov and P. Quentin, *Phys. Rev. Lett.* **74**, 3336 (1995).
127. Y. Sun, J.-Y. Zhang and M. Guidry, *Phys. Rev. Lett.*, in press.
128. K. Kumar and M. Baranger, *Nucl. Phys.* **A110**, 529 (1968).



**Kenji Hara**, born in January 1935 in Kobe Japan, received his Ph.D. degree in March 1963 from the Tokyo University of Education.\* He was then stationed at the Research Institute for Fundamental Physics of the

Kyoto University until he went abroad to Italy in October 1964 as a research fellow at the International Center for Theoretical Physics in Trieste. In September 1965, he became an Alexander-von-Humboldt fellow and an assistant at the University of Heidelberg until he was invited to Brazil in October 1967 to fill the vacancy of a chair at the University of São Paulo. In October 1970, he returned to the University of Heidelberg as a guest professor. Since July 1972, he is a permanent staff at the Technical University of Munich. His main field of research is the microscopic theory of nuclear structure. In fact, theory of nuclear reactions in his view point is an extension of nuclear structure theories in the sense that the correlations of nucleons in the colliding nuclei have been always emphasized in the description of the reaction processes, which can be clearly seen from the works such as RPA including the continuum, nuclear Josephson effect and deep inelastic collision treated as a non-Markovian process.



**Yang Sun**, born in 1954 in Xuzhou, P. R. China, completed his university study both at Xuzhou Normal University and Suzhou University. Between 1986 and 1991, he was awarded the German Konrad-Adenauer-Foundation fellowship

to pursue a diploma and a doctorate in theoretical nuclear physics at the Technical University of Munich, under the advisorship of Professor Peter Ring. He was a post-doctoral research fellow at the Universidad Autonoma de Madrid, Spain (1991/1993) and this was followed by a short stay at Lund Institute of Technology, Sweden. In 1994, he was appointed by the Physics Department of Drexel University as an instructor post-doctoral fellow and adjunct assistant professor. Currently, he is a research fellow at the Joint Institute for Heavy Ion Research in Oak Ridge National Laboratory. His current interest is in all facets of nuclear many-body theories, and in particular, the microscopic description of high-spin structure of rapidly rotating nuclei.

\*The Tokyo University of Education was displaced to Tsukuba, 60 km north east of Tokyo, and became the present Tsukuba University in October 1973. From the late fifties to the early sixties, its President had been the late Professor S. Tomonaga.